Quantifying Uranium Isotope Ratios Using Resonance Ionization Mass Spectrometry: The Influence of Laser Parameters on Relative Ionization Probability

by

Brett Hallen Isselhardt

A dissertation submitted in partial satisfaction of the
requirements for the degree of
Doctor of Philosophy

in

Engineering - Nuclear Engineering

in the

Graduate Division
of the
University of California, Berkeley

Committee in charge:

Professor Stanley G. Prussin, Chair
Professor Kai Vetter
Professor Heino Nitsche
Dr. Ian D. Hutcheon
Dr. Michael R. Savina

Fall 2011

Quantifying Uranium Isotope Ratios Using Resonance Ionization Mass Spectrometry: The Influence of Laser Parameters on Relative Ionization Probability

Abstract

Quantifying Uranium Isotope Ratios Using Resonance Ionization Mass Spectrometry:
The Influence of Laser Parameters on Relative Ionization Probability

by

Brett Hallen Isselhardt
Doctor of Philosophy in Engineering - Nuclear Engineering

University of California, Berkeley

Professor Stanley G. Prussin, Chair

Resonance Ionization Mass Spectrometry (RIMS) has been developed as a method to measure relative uranium isotope abundances. In this approach, RIMS is used as an element-selective ionization process to provide a distinction between uranium atoms and potential isobars without the aid of chemical purification and separation. We explore the laser parameters critical to the ionization process and their effects on the measured isotope ratio. Specifically, the use of broad bandwidth lasers with automated feedback control of wavelength was applied to the measurement of $^{235}U/^{238}U$ ratios to decrease laser-induced isotopic fractionation. By broadening the bandwidth of the first laser in a 3-color, 3-photon ionization process from a bandwidth of 1.8 GHz to about 10 GHz , the variation in sequential relative isotope abundance measurements decreased from >10% to less than 0.5%. This procedure was demonstrated for the direct interrogation of uranium oxide targets with essentially no sample preparation. A rate equation model for predicting the relative ionization probability has been developed to study the effect of variation in laser parameters on the measured isotope ratio. This work demonstrates that RIMS can be used for the robust measurement of uranium isotope ratios.

Professor Stanley G. Prussin
Dissertation Committee Chair

This dissertation is dedicated to all those who have invested in me, especially my wife and son who have given the most.

Contents

List of Figures

List of Tables

Acknowledgments

I must gratefully acknowledge my dissertation committee for their excellent guidance and sustained support of this work. Particularly, my faculty advisor Professor Stanley Prussin has been a patient and gracious guide throughout this process. His heart for teaching and his passion for understanding are truely inspiring. Dr. Ian Hutcheon has been tireless in supporting this research. His direction and discernment have provided for its completion. I acknowlegde Dr. Michael Savina for graciously teaching me the experimental methods of RIMS and for the countless hours of his time that he invested in me and this work.

I acknowledge the assistance of Dr. Kimberly Knight in preparing target materials, performing experiments, and interpreting results. Vast technical assistance and numerous discussions were provided by Dr. Sid Neimeyer, Dr. Doug Phinney, Dr. Daniel Chivers, Dr. Michael Pellin, Dr. Jonathan Levine, Dr. Igor Veryovkin, and the Chemical and Isotopic Signatures group at Lawrence Livermore National Laboratory.

All of my colleagues in Professor Prussin's research group were essential to my success at Berkeley. I am especially thankful for the assistance of Jonathan Dreyer in the preparation of this dissertation and in the development of the computational model presented here.

I would like to ackowledge Lawrence Livermore National Laboratory, Argonne National Laboratory, and the National Technical Nuclear Forensics Center of the Department of Homeland Security for the facilities and research support provided.

None of this would have been possible without the love and encouragement from my family. Particularly my mother, who has been a constant source of support and motivation for all of my pursuits. Finally, and most importantly, I must acknowledge my wife. Kelly, your love and partnership have sustained me through these years.

This work performed under the auspices of the U.S. Department of Energy by Lawrence Livermore National Laboratory under Contract DE-AC52-07NA27344. LLNL-TH-500731.

Chapter 1

Introduction

1.1 Introduction

After the discovery of fission in 1938, physicists immediately understood that the sizable energy released by fission had two world-changing applications. The potential for a new, plentiful source of electric power and the potential for unparalleled explosive destruction. Unfortunately, with the world at war, the latter application was pursued first and with more zeal. The destructive capacity of fissile materials, such as ^{235}U and ^{239}Pu, was demonstrated for the first time on July 16, 1945 when the United States detonated the first nuclear weapon, Trinity, in the desert of New Mexico[2].

Since that day, there have been many concerted efforts to control and protect fissile materials and the knowledge of their use for the construction of weapons. Quantifying uranium isotope abundances in nuclear materials is an integral component of these efforts[3, 4, 5]. These efforts include nuclear safeguards, non-proliferation, environmental monitoring and forensic investigations of nuclear materials[1]. All share similar questions: Is this material natural or anthropogenic? What was the material's intended use? How was it produced? Was it exposed to a significant neutron flux? While the determination of uranium isotope ratios alone may not answer these questions completely, it often provides important insights.

Relative isotope abundances of uranium in nuclear materials are diagnostic of production and/or irradiation histories. For example, the $^{235}\mathrm{U}/^{238}\mathrm{U}$ ratio is useful for identifying intended use[5], the $^{234}\mathrm{U}/^{235}\mathrm{U}$ ratio can be indicative of the production process[5], and the ratios $^{236}\mathrm{U}/^{235}\mathrm{U}/^{238}\mathrm{U}$ can reveal a history of neutron irradiation[6]. Measurements of these isotope abundances by mass spectrometry are common, but typically require dissolution and chemical separation to ensure that contamination from interfering species (e.g., ^{238}Pu in the case of ^{238}U) is reduced or eliminated[7]. In situations where time is a critical parameter, or when sample size is limited and background correction for chemical blanks influences detection limits and accuracy, alternative approaches may be useful. Resonance Ionization Mass Spectrometry (RIMS) can, in principle, distinguish isotopes of interest from isobaric interferences without the need for chemical processing. RIMS uses photons tuned to atomic transitions to selectively excite and ionize neutral atoms vaporized from a sample while leaving other atomic species largely unionized[8, 9]. RIMS is now routinely used for high-sensitivity and high-selectivity measurements of trace element and isotope composition in environmental[10, 11, 12] and extraterrestrial samples[13, 14].

[1] The field of nuclear safeguards aims to ensure that the nuclear materials and processes used in nuclear power applications are not used the development of nuclear weapons. Nuclear non-proliferation is the attempt to prevent the spread of weapons-grade nuclear materials and the technical capabilities necessary to fabricate nuclear weapons. Nuclear environmental monitoring is the observation of nuclear materials released into the environment. It serves to protect people from exposure to contamination and to detect clandestine nuclear activities. Nuclear forensics is the technical means by which nuclear materials are characterized as to understand the age, history, and provenance of the material.

1.2 Current Approaches

Traditional methods for quantifying the relative isotope ratios of uranium, such as Inductively Coupled Plasma Mass Spectrometry (ICP-MS)[6, 15] or Thermal Ionization Mass Spectrometry (TIMS)[16, 17], rely on time consuming and labor intensive chemical processing prior to analysis to provide accurate isotopic abundances. The chemical processing methods are designed to provide concentrated samples essentially free of isobaric interferences. These processes generally involve mulitiple steps of ion exchange chromatography with selective exchange resins, each of which take on the order of hours to complete. Intermediate to the succesive separation steps, the sample solutions must often be heated to dryness. The procedure must include a step to remove any organic material that could interfere with the ion signals. If only a single step of separation and drying are required, both techniques may be completed in approximately 24 hours [R.Williams, *personal communication*, May 31, 2011]

The great majority of samples to be analyzed are solid and often contained within a matrix of some other material. Solid samples must be dissolved to prepare the sample for chemical purifcation. Dissolution of solid samples often takes at least 24 hours. Partial dissolution, known as sample leaching, can provide material for separation in as little as tens of minutes using modern techniques, but may be sensitive to sample heterogeneity or incomplete mixing of different reservoirs of an element (*e.g.*, different mineral phases). Samples held in organic matrices must be liberated, typically by thermal ashing, to destroy the matrix containing the sample and its organic molecules that may provide isobaric interferences. Thermal ashing typically requires at least 12 hours. Taken together and performed in rapid succession, the suite of chemical processing can provide a purified sample, ready for analysis, in as little as approximately three days [R.W. Williams, *personal communication*, May 31, 2011]. A recent review of current analytical techniques for quantifying radionuclides by Hou and Roos[7] describes the required separation time of 3-5 days for chemical purification of Pu, which is analogous to the separation processes required for U. Martinelli *et al.*[18] provides an example of the analytical procedures applied to the separation of U in environmental samples in preparation for mass spectrometric analysis.

Modern, rapid means of performing chemical separation and purification are in development and can, in principle, lead to reductions of the total processing time of samples prior to analysis of only a few hours. However, these methods are not yet developed to the point of providing results with accuracy rivaling the traditional techniques.

Secondary Ion Mass Spectrometry (SIMS) is the only technique that can acquire data on a similar time scale as RIMS. However, SIMS is not very efficient and is, in general, effective only for U-rich particles. The efficiency of SIMS suffers from the fact that, generally, the yield of secondary ions produced in SIMS is a small fraction of the total material removed from the sample. SIMS can analyze isotopic abundances for a wide range of elements, often without chemical preprocessing, but must resolve the effect of potential isobaric interferences on the basis of mass-to-charge ratio alone. This is often limited by the ability of a SIMS instrument to distinguish between an isotope (say $^{236}\mathrm{U} = 236.046\,\mathrm{amu}$) and a molecule of a neighboring isotope bound to a hydrogen atom ($^{235}\mathrm{UH} = 236.052\,\mathrm{amu}$). This requires very high resolving power, defined as $R = \frac{M}{\Delta M}$, where M is the mass to be measured and ΔM is the smallest mass

Technique	Typical Relative Measurement Uncertainty
TIMS	$0.05-1\,\%$
ICP-MS	$0.1-2\,\%$
SIMS	$1-10\,\%$

Table 1.1: Typically achieved uncertainties for nuclear forensic applications by traditional mass spectrometric techniques[1].

difference that can be distinguished. Operating with high mass resolution causes a reduction in efficiency and more of a sample must be consumed. Typical SIMS analysis often use mass resolving powers on the order of 3×10^3[19]. In the example of ^{236}U and ^{235}UH, a mass resolving power on the order of 4×10^4 is required.

TIMS and ICP-MS techniques provide measurements with the highest accuracy achievable for isotopic compositions, better than $\pm 0.001\%$ relative standard deviation. RIMS cannot yet compete with this level of accuracy and precision, but the lack of chemical processing and purification in RIMS procedures would lead to useful information on U isotopic composition within hours of sample receipt. The high level of precision offered by TIMS and ICP-MS is often not required for many nuclear forensics applications. Table 1.1 presents a summary of the typical relative measurement uncertainties achieved for nuclear forensic applications by current techniques[1]. If RIMS can provide uranium isotope ratio information with uncertainties on the order of 1 %, but in a fraction of the analysis time, it may compliment the use of the traditional mass spectrometric methods. The dramatic reduction in response time directly addresses a major issue identified in the recent study by the Nuclear Forensics Working Group of the American Physical Society and the American Association for the Advancement of Science[20].

1.3 RIMS

RIMS overcomes the limitations of traditional mass spectrometric analytical techniques through the use of element- or isotope-specific, laser ionization[21, 22, 9, 23]. First, atoms are desorbed from a sample surface using a focused laser or ion beam. This generates a cloud of ions, molecules and neutral atoms above the sample surface containing all elements originally present in the desorbed volume. Secondary ions generated during the desorption process are ejected from the cloud by applying a large voltage pulse to the sample holder. Neutral atoms of the element of interest are then selectively excited to an element-specific intermediate excited state by a laser beam tuned[2] to the excitation energy of that state. The excited atoms are then

[2]We commonly use the term "tune" to refer to the arrangement of a laser cavity to produce a laser beam of a defined mean wavelength. This wavelength is usually near the wavelength of a resonance transition we intend to excite. We use the term "detune" to mean altering of the mean wavelength of a laser beam to no longer be

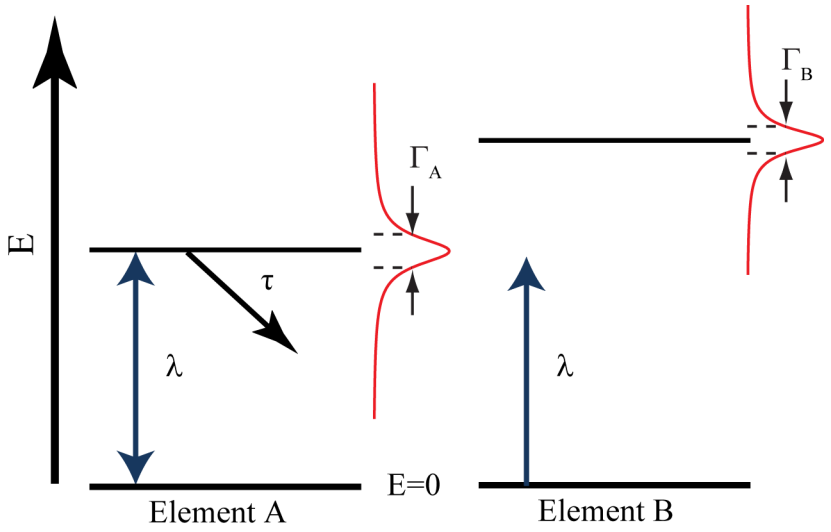

Figure 1.1: Energy level diagrams of two imaginary two-state atoms of different elements. Each atom has a single excited state with finite lifetimes and the states are characterized in energy by Γ_A and Γ_B. Photons of wavelength λ will have a high probability of exciting the atom of element A, while having a negligible probability of exciting the other atom.

photoionized from their resonant state by an additional laser tuned to provide enough energy to place the excited atoms over the ionization threshold for that element. The use of additional resonant excitation steps prior to ionization can improve the selectivity of the ionization process. Finally, the photoions are accelerated into a mass spectrometer and analyzed.

The concept of resonance excitation relies on the orders of magnitude difference in excitation probability for different species (atoms or molecules) depending on the energy of the incident photons. Consider an atom of element A, shown in Figure 1.1, this simplified atom has only two states: a ground state and an excited state with non-zero energy. The excited state has a finite lifetime given by τ. There is a probability distribution for finding the excited state in energy, characterized by Γ_A, the full-width at half of the maximum (FWHM) of the distribution. There is a high probability for exciting (and de-exciting) the excited state if λ is close to the energy difference between the states. If the wavelength differs significantly from the energy difference between states, as is shown for an atom of element B, there is a very low probability for excitation. Thus, that element is left largely unexcited.

One of the advantages of using a resonant process for ionization of the specified species is the capability to in effect "turn off" the resonance ionization process by changing the wavelength of just a single resonance laser by a small amount while maintaining all other experimental conditions. A change in wavelength of only a few parts in 10^4 is equivalent to moving 10 times the width of a typical resonance. This allows for a direct measurement of the background

near the resonance transition by an amount several times larger than the width of the resonance (*e.g.*, changing the wavelength by 50 pm away from the centroid of a resonance with a width of 2 pm, FWHM).

contribution to the total ion signal, which is unavailable for other mass spectrometric methods that do not perform selective ionization. This detuning of a laser away from the resonance transition wavelength is referred to as "off-resonance ionization conditions". When the ion signal generated from off-resonance ionization conditions is compared to the ion signal obtained when all of the resonance conditions of the scheme are satisfied ("on-resonance" for short), the only difference will be in the resonance ionization of the desired atoms. This difference between the on-resonance and the off-resonance ion signal is referred to as the resonant enhancement of the ion signal. This measure helps to quantify the signal-to-noise for our measurements, and positively identifies the ion signal of the resonant species.

The instrument used to perform RIMS in these studies is known as the Chicago-Argonne Resonant Ionization Spectrometer for Microbeam Analysis (CHARSIMA)[24, 13]. CHARISMA combines imaging capabilities ($< 1\,\mu$m spatial resolution) with the ability to measure element concentrations below one part per billion (ng/g). The instrument consists of a desorption laser system, primary ion guns for sample cleaning and/or analysis, a solid state tunable laser ionization system, advanced ion extraction and focusing optics, a reflectron time-of-flight (TOF) mass analyzer, and a fast data acquisition system. Analysis with CHARISMA is as follows: (1) a pulse of energetic ions impact the surface of a target producing a cloud of neutral atoms, ions and molecules; (2) a voltage pulse is applied to the target to electrostatically separate ions from neutrals in the cloud; (3) photons from two or more Ti:Sapphire lasers intersect the cloud of neutral atoms above the sample, resonantly ionizing the element of interest with close to 100 % efficiency; (4) a high voltage pulse extracts and accelerates the photo-ions into a TOF mass spectrometer for analysis. Generally, the combination of high ionization efficiency and high elemental selectivity gives an overall detection efficiency (ratio of ions detected to atoms removed for a given species) of $> 2.5\,\%$.

RIMS is based on the assumption that other potentially interfering species will mostly remain unexcited in the irradiation volume of the laser beams. That is, the excitation of these species would occur not through strong single-photon resonances but through low-probability pathways such as multi-photon absorption through virtual states. Literature indicates no known excited states within 0.05 nm of the wavelengths used to excite uranium in this work for the isotopes of Th, Pa, Np, or Pu with lifetimes greater than a few seconds[25, 26]. A wavelength difference of 0.05 nm is sufficient to reduce the excitation probability in uranium by many orders of magnitude and thus, we assume that the laser beam wavelengths used in this work are sufficiently far from any known resonances in potentially interfering atoms. The other source for high-probability excitation of species we do not intend to ionize would come from accidental resonances with molecules or unknown levels in atoms with masses near the atomic uranium masses. The electronic structure for uranium is very complex because of the large number of electrons, thus we will use it as an example for exciting an atom of a random element. The number of known electronic excited states in uranium (not including high-lying Rydberg states) is on the order of 2100 levels[27]. The first ionization limit of uranium is about 6.2 eV. Thus, the level density is approximately 1 level for every 3 meV, if we assume the levels are evenly distributed over the entire energy range below the ionization limit. Considering the natural width of a typical excited state is on the order of 1 μeV and the Doppler broadened width is on the

order of 30 μeV then the probability of randomly choosing a wavelength with energy less than the ionization potential that is within a few μeV of the mean energy of an excited state is on the order of 10^{-2}. If the absorption of three photons is required for ionization of the atom then the probability for three wavelengths to all be accidentally near an excited state is on the order of 10^{-6}, very small indeed.

1.4 Prior Work - Measuring U Isotope Ratios by RIMS

RIMS has been shown to be a potential tool for quantifying uranium isotope ratios [28, 29, 30, 31, 32]. Early approaches used a single pulsed broadband dye laser (0.063 – 0.1 nm bandwidth) tuned to a one-color (591 nm), three-photon ionization scheme. Donohue, *et al.*[28] obtained RIMS spectra from U adsorbed onto ion exchange beads covered with colloidal graphite and reported a relative standard deviation (RSD) of 0.65 % in the $^{235}U/^{238}U$ ratio, and an elemental selectivity against Pu of 3400 (U^+ ions/Pu^+ ions). When tuned for plutonium, a Pu/U selectivity of only 150 was found. Green and Sopchyshyn [29], under very similar experimental conditions, obtained RIMS spectra from metallic uranium and $UO_2(NO_3)_2$ coated with colloidal graphite (to aid in the formation of neutral U atoms during thermal desorption) and demonstrated that the U^+ ion signal from uranyl nitrate was a combination of both resonantly ionized U atoms and non-resonant U ions attributed to the photodissociation of UO_X. Green and Sopchyshyn did not observe a resonant U^+ signal from U_3O_8 deposited from a nitric acid slurry, possibly due to the lack of a colloidal graphite coating. They reported a RSD of 0.4 % for non-resonant ionization of $UO_X{}^+$. Erdmann, *et al.*[30] combined resonant and non-resonant ionization in the analysis of depleted uranium to obtain a precision in the $^{235}U/^{238}U$ ratio of 4.6 % from a sub-micron particle containing less than 6×10^6 atoms of ^{235}U.

More recent RIMS studies have used chemical purification and isotope-specific ionization schemes using narrow bandwidth (1-3 MHz) continuous wave lasers that are sequentially tuned to each isotope of interest (i.e., only a single uranium isotope was ionized and detected at a time). This technique is well suited for measurements requiring a large dynamic range ($> 10^6$), and provides $^{235}U/^{238}U$ ratios with precision ranging from 2 to 7 % [10, 32], limited mainly by the time dependence of sample atomization and laser parameters such as power and pointing stability. The potential of RIMS for measuring uranium isotope ratios with high accuracy in samples of unknown composition without the need for chemical preparation, has not been demonstrated by any of these prior studies.

1.5 The Challenge of Measuring Uranium Isotope Ratios by RIMS

The challenge of isotope ratio measurements by resonance ionization is to minimize the laser-induced isotope bias, induced by isotope shifts or angular momentum differences, that can be severe and must be moderated [33]. Levine et al. reported success in stabilizing measured

Cr isotope ratios to ~1 % using power broadening to overcome small isotope shifts (~1 pm), the effects of Doppler broadening, and small pulse-to-pulse fluctuations in wavelength [14]. However, the isotope shift between uranium isotopes is much larger and the need to maximize the ratio of resonant to non-resonant ionization has prevented this approach from providing high precision in the measurement of isotope ratios. Another option for stabilizing isotope ratio measurements in the presence of large shifts is the application of spectrally broadened lasers as initially demonstrated by Donohue, *et al.* [28].

The difficulty posed by the presence of large isotope shifts is clearly exemplified in the electric dipole transition for atomic uranium from its ground level ($E = 0\,\text{cm}$, $J = 6$) to an excited state near $E = 24{,}066\,\text{cm}^{-1}$ ($J = 7$)[3]. Figure 1.2 shows the calculated cross sections for this resonance transition in ^{235}U and ^{238}U. The cross section peaks are approximately 2 pm wide (FWHM) which includes both the natural width of the resonance ($\sim$ 1 fm) and the estimated Doppler broadening of the transition ($\sim 2\,\text{pm}$)[4]. The mean wavelengths of the resonances are separated by approximately 7 pm. Also shown in the figure, are two Gaussian models for the laser spectral distribution (dashed lines). The 1 pm laser model represents the nominal laser spectral distribution produced by our laser system at this wavelength. The 5 pm laser model represents a broadened spectral distribution, which provides improved overlap of both resonances. The consequence is that the broad spectral distribution can sufficiently excite this transition in both isotopes simultaneously at practical laser intensities while the 1 pm distribution cannot. Additionally, with the 5 pm distribution the excitation probability for both isotopes will be less dependent on small changes in mean wavelength of the laser distribution from pulse to pulse.

This work explores many avenues of improving the precision and accuracy of measured uranium isotope ratios. These measurements are demonstrated for resonant uranium ion signals obtained by ion sputtering of unprocessed uranium oxide samples. We investigated a few schemes for ionization, choosing a scheme involving three photons of different wavelength, which provides high ionization probability while minimizing the influence of non-resonant species. The dependence of the measured $^{235}\text{U}/^{238}\text{U}$ ratio as a function of many system parameters was studied and analyzed for improved efficiency and reproducibility. An approach using spectrally-broad laser beams to simultaneously ionize multiple isotopes of uranium with almost equal efficiency is described. This approach was combined with the use of automated feedback systems to overcome long-term variation in critical laser parameters. The results show a marked reduction in the response of the measured isotope ratios to the wavelength of the first resonance laser when the bandwidth is increased from 1 to 5 pm, along with significantly improved internal precision in the measured isotope ratios for $^{235}\text{U}/^{238}\text{U}$ and $^{234}\text{U}/^{238}\text{U}$.

1.6 Dissertation Outline

In Chapter 2, we explore the fundamental physics of resonance excitation and ionization processes. This includes a discussion of the challenges in ionizing different isotopes of ura-

[3] Conveniently, this is the transition we will focus on most closely in the present work.

[4] The detailed calculation of the cross sections is described in Sec. 5.1.2.

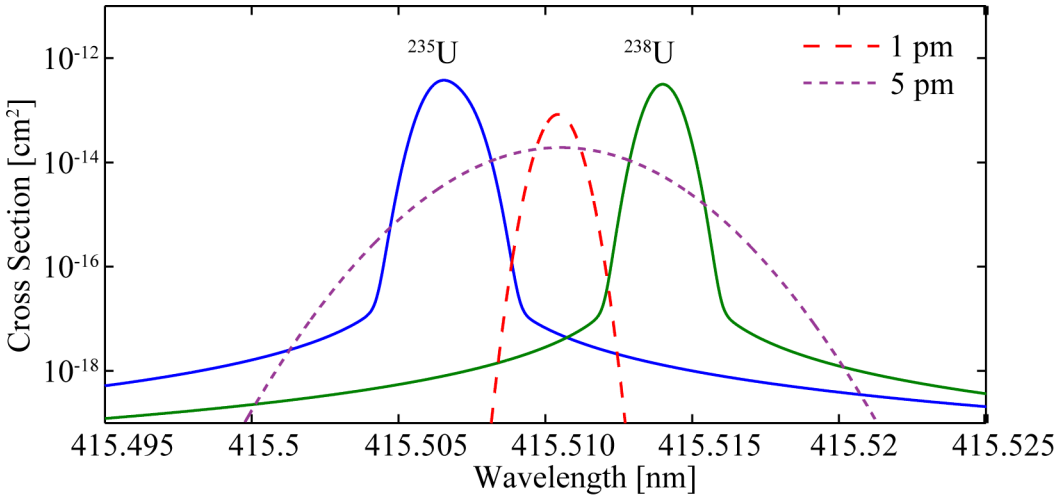

Figure 1.2: Cross sections for ^{235}U and ^{238}U as a function of wavelength for a resonance transition from the ground level to a level near $E = 24,066\,\mathrm{cm}^{-1}$. The resonances are approximately 2 pm wide (FWHM) and are separated by about 7 pm. Superimposed on these resonances are two Gaussian models for the spectral distribution of the resonance laser with FWHM of 1 and 5 pm, both of the same total intensity. The amplitudes of the laser models are arbitrary relative to the resonance cross sections.

nium. This chapter also introduces the processes responsible for generating photoions by means other than resonant excitation, and lastly a brief description of the processes involved in the mass spectrometry component of RIMS. Chapter 3 is a detailed description of CHARISMA, the analytical instrument used in this work and its various components. Chapter 3 is focused on describing and characterizing the laser systems used to provide the resonance photons required for RIMS. Chapter 3 also describes the material standards and data analysis techniques employed in the experiments. Chapter 4 presents the description of experiments designed to explore the utility of RIMS for measuring U isotope ratios. This chapter begins with a description of the basic ion signals observed in CHARISMA and then goes on to describe the study of the effects of variation of laser parameters on the relative ionization probability of the uranium isotopes. Finally, experimental results are presented that demonstrate the measurement of the ^{235}U/^{238}U ratio to a reproducibility of better than 0.5 %. Chapter 5 presents a rate equation model for calculating the relative ionization probability of uranium isotopes that has been developed. This is used to support our understanding of the empirical results as well as to study relative ionization probability outside of the parameter space explored experimentally. Chapter 6 is a summary of the conclusions of this work and a discussion of future research, some of which are already in progress. Appendix A provides a summary of experiment conditions for each of the experiments described in Chapter 4. Appendix B is included to document the MATLAB code used in the rate equation model, discussed in Chapter 5. Appendix C provides the calculated Clebsch-Gordan coefficients for the first resonance transition in ^{235}U.

Chapter 2

Theory

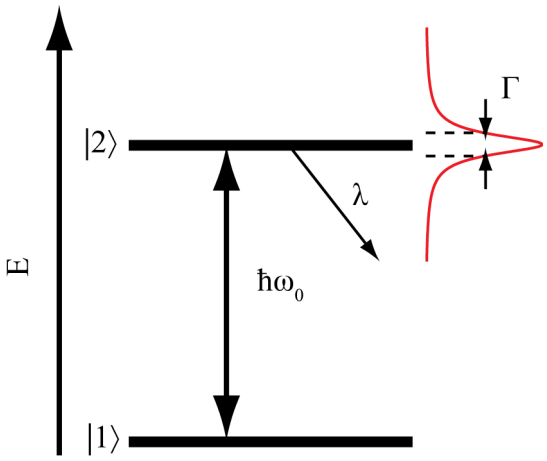

Figure 2.1: Two-state atomic model.

2.1 Introduction

Our goal here is to construct a knowledge of the theory relevant to the measurement of isotope ratios by RIMS. We begin by briefly introducing the two main components of our system, the states of atomic electrons and photon field of the laser. Then we will explore the interactions necessary to perform resonance ionization, the response of an ideal atomic system to a resonant photon field via the electric dipole moment. We then translate the probability for resonant excitation into cross sections using the Einstein coefficients. A few considerations necessary to study real atoms are introduced and the probabilities for ionization of excited atoms is then discussed. The challenge of measuring isotope ratios by resonance ionization is then introduced including, understanding the differences in the probability of excitation and ionization of different isotopes of an element that is required for reliable measurements. Once we have built up the full picture involved in the probabilities for excitation and ionization of the selected isotopes, the theoretical description of a system in terms of a rate equation approximation of the kinetics involved is presented. Other ion-generating processes that may be present in our experiments, such as non-resonant multi-photon ionization in atomic species and multi-photon disassociation/ionization in molecules are then discussed. Finally, we will conclude by introducing a few other processes necessary to perform our experiments such as mass spectrometry, ion sputtering, and the physics of laser cavities.

2.1.1 Atomic States - Behavior of Time Dependent States

We begin by considering two electronic states of an atomic system, the lower state being designated $|1\rangle$ and the upper state $|2\rangle$, characterized by energies E_1 and E_2, where $E_2 - E_1 = \hbar\omega_0 > 0$ as shown in Figure 2.1. An atomic state that can decay, by definition, must be time-dependent. From the time-dependent Schrödinger equation, it can be shown that for a normalized wave function ψ_0, which is a stationary state solution for the time-independent Schrödinger

equation, the time dependent wave function $\Psi(t)$ is of the form

$$\Psi(t) = \psi_0 \cdot \mathrm{e}^{-i\frac{E}{\hbar}t} \tag{2.1}$$

When an atom is in the upper state it may spontaneously decay by photon emission to the lower state with a characteristic average lifetime τ, where $\tau = \frac{1}{\lambda}$. In general the decay constant for a state i is the sum of all partial decay constants $\lambda_i = \sum_j \lambda_{ij}$, where j denotes each possible final state of the decay pathways. If the state can decay, then the probability of finding the atom in the state Ψ at a time t after it has been created will be given by

$$\langle \Psi \mid \Psi \rangle = \mathrm{e}^{-\lambda t} \tag{2.2}$$

This requires that the energy of the wavefunction be complex. If we define the energy for an atomic state which can undergo decay as $E = E_0 + i\gamma$, then to satisfy Eq. 2.2, -2γ must be equal to $\lambda\hbar$ $(= \hbar/\tau)$. We introduce

$$\Gamma = \frac{\hbar}{\tau} \tag{2.3}$$

as a notation for the complex component of the energy. Γ represents the uncertainty in energy, defined as the full-width-at-half-maximum (FWHM) of the energy distribution about the mean energy E_0. This equality can be derived from the Heisenberg Uncertainty Principle, $\Delta E \cdot \Delta t \approx \hbar$. When Γ is expressed as a function of the angular frequency, Eq. 2.3 becomes $\Gamma = 1/\tau$, because $E = \hbar\omega$. We see from Eq. 2.3 that $\gamma = -\frac{\Gamma}{2}$, and can now write the time-dependent wave function for an excited state as

$$\Psi(t) = \psi_0 \cdot \mathrm{e}^{-\frac{i}{\hbar}(E_0 - \frac{i\Gamma}{2})t} \tag{2.4}$$

It is illustrative to inquire about the effect that this complex energy has on the description of the wavefunction as a function of energy. Knowing that the Fourier transform allows for the description of a function of time in terms of a function of frequency, and remembering that $E = \hbar\omega$ and $\mathrm{d}E = \hbar\,\mathrm{d}\omega$, it can be shown that normalized probability for finding a time-dependent state in energy is

$$P(E) = \frac{1}{2\pi}\frac{\Gamma}{(E+E_0)^2 + (\frac{\Gamma}{2})^2} \tag{2.5}$$

$P(E))$ is a Lorentzian distribution centered at E_0, and with a full width at half maximum of Γ. Figure 2.2 shows a normalized Lorentzian lineshape centered around E_0 with $\Gamma = 0.2$ representing the wave function of a time-dependent atomic state.

In addition to spontaneous decay, the excited states in our system may be de-excited by a photon-induced transition. The simplest and most probable type of such a transition is an electric dipole transition wherein an atomic electron may absorb or emit energy and angular momentum through interaction with the electromagnetic field. Because the electromagnetic field is quantized, the resulting difference in the energy of the electromagnetic field must be equal to some integral number of photons, $n \cdot \hbar\omega = E_2 - E_1$.

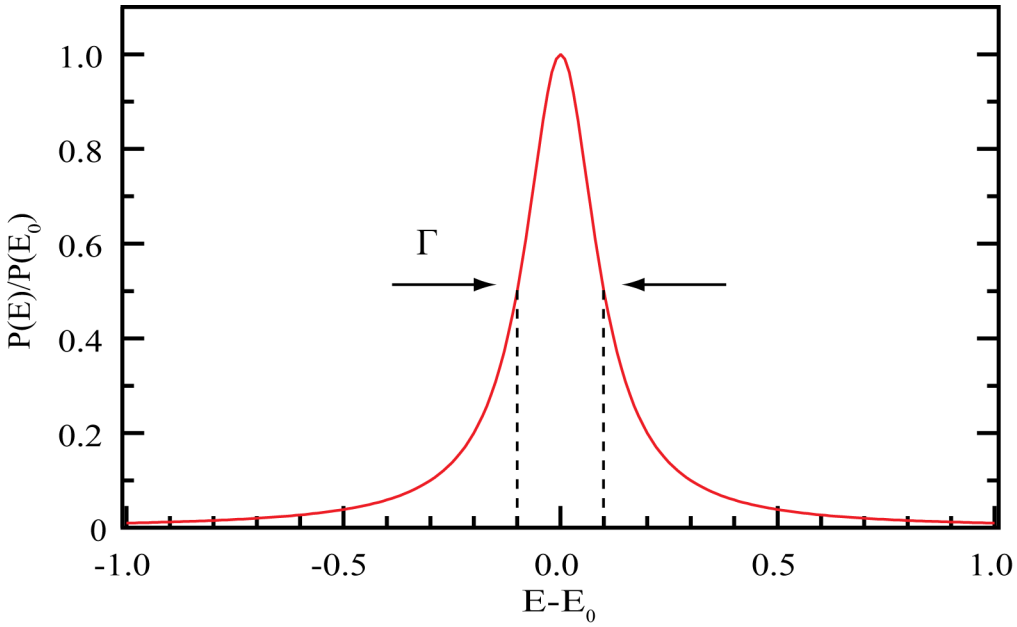

Figure 2.2: Normalized Lorentzian Function in units of $E - E_0$ with Γ =0.2

2.1.2 Laser Light

It is well known that for large numbers of photons in a mode (*i.e.*, with the same energy) of a radiation field, the classical and quantum mechanical descriptions of light agree very well[34]. This enables us to use a semi-classical model of the photo-atomic interaction when considering laser light, where the number of photons in the radiation field is almost always very high. Using the semi-classical model, laser light can be described as a plane wave of photons propagating in the $\hat{k}$-direction whose electric field is given by:

$$\vec{\mathrm{E}}(t) = \hat{e} \cdot \mathrm{E}_0 \cdot \cos(\omega_L t - \vec{k} \cdot \vec{r}) = \hat{e} \cdot \mathrm{E}_0 \cdot \frac{1}{2}(\mathrm{e}^{-i(\vec{k}\cdot\vec{r}-\omega_L t)} + \mathrm{e}^{i(\vec{k}\cdot\vec{r}-\omega_L t)}) \tag{2.6}$$

where $\hat{e}$ is the polarization vector (defined as $\vec{\mathrm{E}}/\mathrm{E}_0$), E_0 is the amplitude of the electric field (we reserve the italic E_0 for energy), and $\vec{r}$ is the radial unit vector. ω_L is the angular frequency of the laser light (or the average frequency when considering non-monochromatic light). It is helpful to note that E_0 is often a function of time, and that photon beams from broadband multimode lasers can be expressed as the sum of several plane waves with individual amplitudes and central frequencies. Some workers use what is known as the phase diffusion model of the laser for incorporating phase fluctuations between modes of a multimode laser that can affect the coherence of excitation [35, 36, 8]. We neglect this contribution in our models due to the incoherent nature of our system as we will discuss later. Because the size of an atom is small relative to the wavelengths of light considered here, we can neglect the spatial dependence of the electric field as it relates to the photon-atomic interactions and therefore the term $\mathrm{e}^{i(\vec{k}\cdot\vec{r})}$ will

be ignored going forward. The neglect of spatial variations is referred to as the electric dipole approximation. Likewise, because $\mu \mathrm{E}_0 \ll \hbar\omega_0$ where μ is the dipole moment (defined in the next section) and $|\delta| \equiv |\omega_0 - \omega_L| \ll \omega_0, \omega_L$, we also assume that frequencies on the order of 2ω (very fast oscillations) average to 0 on the timescale of $1/\delta$. This is known as the rotating wave approximation. We therefore ignore terms in the description of the electric field that are the sum of two frequencies (*i.e.* when the electric field term is $\mathrm{e}^{i\omega_L t}$). This leaves us with a practical description of the electric field as:

$$\vec{\mathrm{E}}(t) = \hat{e} \cdot \frac{\mathrm{E}_0}{2} \cdot \mathrm{e}^{-i\omega_L t} \tag{2.7}$$

The Poynting vector (S) is given by

$$S = \varepsilon_0 c(\vec{\mathrm{E}} \times \vec{\mathrm{B}}) \tag{2.8}$$

and its expectation value is related to the electric field amplitude by

$$\langle S \rangle = \varepsilon_0 c \frac{\mathrm{E}_0^2}{2} = I \tag{2.9}$$

Thus, the average of the Poynting vector over several optical cycles leads to,

$$I = \int_{\nu} I(\nu)\mathrm{d}\nu = \phi \cdot c \cdot h\nu = \frac{\varepsilon_0}{2} \cdot c \cdot |\mathrm{E}_0|^2 \tag{2.10}$$

where I is the irradiance of the light (power per unit area), ν is the frequency of the light, ϕ is the photon flux in photons/cm^{2}s, and ε_0 is the permittivity of free space. Later, we will use $I(\nu)$ as a frequency dependent description of the irradiance known as the spectral irradiance (power per unit area per unit frequency).

2.2 Resonance Ionization (Atom-Photon Interactions)

2.2.1 The Dipole Moment

Photons primarily interact with atoms via the electromagnetic field of the electrons in orbit around the nucleus. Of course, because the electrons are not free, they are strongly influenced by the presence of the nucleus and their surrounding electrons. The electric dipole moment is a measure of the separation between positive and negative electric charge. The simplest example of a dipole moment, μ, is that of two charged (point) particles with charges $+q$ and -q separated by a radial distance r. It is given by the product $\vec{\mu} = q \cdot \vec{r}$, where, by convention, μ points in the direction of positive charge as described in Figure 2.3. The electrons bound in an atom are not localized to a specific $\vec{r}$ relative to the nucleus but rather have a probability for being found at all radial dimensions. It is then the expectation value of $\hat{\mu}$, $\langle \hat{\mu} \rangle = e \langle \vec{r} \rangle = e \int \psi_i^* \vec{r} \psi_i \mathrm{d}q$, that is important.

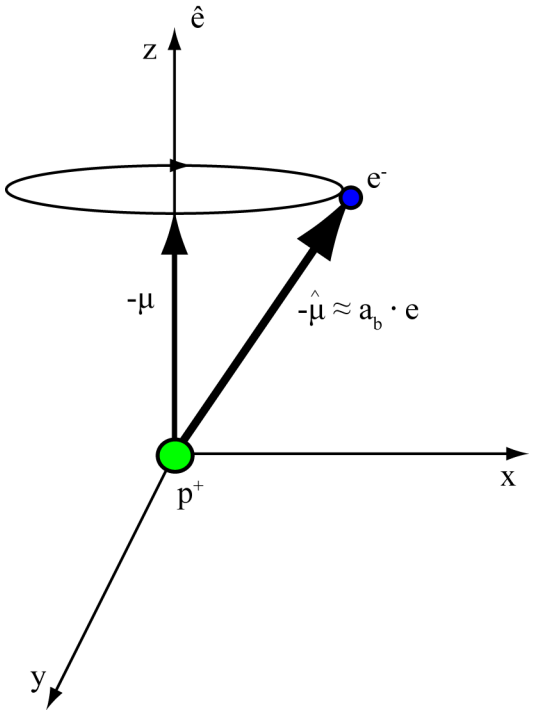

Figure 2.3: Dipole Moment

We are concerned specifically with the likelihood that a photon induces a change in the energy of a single atomic electron and so are interested in the *transition* dipole moment matrix element [34] which is defined as,

$$\langle \hat{\mu}_{ik} \rangle = e \int \psi_k^* \vec{r} \psi_i \mathrm{d}q = D_{ik} \tag{2.11}$$

where dq represents integration over all spatial dimensions. For example, strong dipole moments for valence shell electrons typically have expectation values of $r \approx a_b$, where a_b is the Bohr radius ($\sim$53 pm). If we use this as an order of magnitude estimate for a typical atomic dipole moment, we find $D \approx e a_b = 8.5 \times 10^{-30}$ C m.

2.2.2 Resonant Excitation of Discrete Transitions (Bound-Bound)

We need to understand the probability for a transition between two bound excited states of the atom induced by the photon field. We first consider the interaction between atoms and laser light by examining the model of an ideal two state system ($|1\rangle$ and $|2\rangle$) under the influence of a perfectly resonant light field, and which is free from relaxation by radiative decay. That is, we assume the time-dependent amplitudes of the atomic wave function will be dominated by the interaction with laser light. Of course the Hamiltonian of the atomic system ($\hat{H}_0$) acting on the

stationary wave function Ψ_0 will give the energy of the system,

$$\hat{H}_0\Psi_0 = E_0\Psi_0 \tag{2.12}$$

but we want to investigate the time dependence of the system wave function under the influence of the laser field so we are seeking solutions to the time-dependent Schrödinger equation,

$$\hat{H}\Psi = i\hbar\frac{\partial\Psi}{\partial t} \tag{2.13}$$

where $\hat{H}$ is the Hamiltonian of the system. Using first-order perturbation theory, we define $\hat{H}$ as,

$$\hat{H} = \hat{H}_0 + \hat{V} \tag{2.14}$$

and $\hat{V}(t)$ is the interaction term for the influence of the laser on the atomic electrons. Assuming that $\hat{V}(t)$ is only due to the electric dipole interaction,

$$\hat{V}(t) = -\hat{\mu}\cdot\vec{\mathrm{E}}(t) \tag{2.15}$$

where

$$\hat{\mu} = e\sum_i \vec{r}_i \tag{2.16}$$

Here, $\vec{\mathrm{E}}(t)$ is the electric field vector of the laser, $\hat{\mu}$ is the dipole moment of the atom, and $\vec{r}_i$ is the radial vector of electron i in a multi-electron atom. By the principle of superposition the wave function of the time-dependent system can be written as,

$$\Psi = a_1(t)\Psi_1\mathrm{e}^{-iE_1t/\hbar} + a_2(t)\Psi_2\mathrm{e}^{-iE_2t/\hbar} \tag{2.17}$$

where $a_i(t)$ is an amplitude and we've made use of Eq. 2.1. By substitution of Eq. 2.17 into Eq. 2.13 we can find the time evolution of the state amplitudes:

$$\begin{aligned} i\hbar\dot{a}_1 &= V_{21}a_2\mathrm{e}^{-i\omega_0t} \\ i\hbar\dot{a}_2 &= V_{12}a_1\mathrm{e}^{-i\omega_0t} \end{aligned} \tag{2.18}$$

where $\omega_0 = (E_2 - E_1)/\hbar$ and the interaction matrix element, V_{ij}, is given by

$$V_{ij} = \int \Psi_i V_{ij}\Psi_j \mathrm{d}q \tag{2.19}$$

Here q is a short-hand notation for the 3-space vectors. Note that, $V_{ij} = V_{ji}^*$. If we take Eq. 2.7 and Eq. 2.15 then we find

$$V_{12} = -\frac{\mu_{12}\mathrm{E}_0}{2}\mathrm{e}^{-i\omega_Lt} \tag{2.20}$$

then Eq. 2.18 becomes:

$$\begin{aligned} i\hbar\dot{a}_1 &= -\frac{\mu_{12}\mathrm{E}_0}{2}a_2\mathrm{e}^{-i\delta t} \\ i\hbar\dot{a}_2 &= -\frac{\mu_{12}\mathrm{E}_0}{2}a_1\mathrm{e}^{-i\delta t} \end{aligned} \tag{2.21}$$

where $|\delta| = |\omega_0 - \omega_L|$. If we assume that the system is initially in state $|1\rangle$ and that the dipole field is turned on at $t = 0$, then we can find simple analytical solutions to Eq. 2.21,

$$a_1(t) = \mathrm{e}^{\frac{1}{2}i\delta t}\left[\cos\left(\frac{\gamma}{2}t\right) - i\left(\frac{\delta}{\gamma}\right)\sin\left(\frac{\gamma}{2}t\right)\right]$$

$$a_2(t) = \mathrm{e}^{-\frac{1}{2}i\delta t} i\left(\frac{\mu\varepsilon_0}{\hbar\gamma}\right)\sin\left(\frac{\gamma}{2}t\right)$$

where γ is the generalized Rabi frequency [37], $\gamma^2 = \delta^2 + \left(\frac{\mu \mathrm{E}_0}{\hbar}\right)^2 = \delta^2 + \gamma_0^2$ and $\gamma_0 = \frac{\mu \mathrm{E}_0}{\hbar}$is the Rabi frequency when exactly on resonance. The Rabi frequency captures the strength or rate of the atomic amplitudes oscillating between the two states considered under the influence of a resonant photon field. The probability that the atom would be in the excited state as a function of time is given by:

$$|a_2|^2 = \left(\frac{\gamma_0}{\gamma}\right)^2 \sin^2\left(\frac{\gamma}{2}t\right)$$

This makes it clear that for two states interacting via the electric dipole moment with a photon field on or near resonance, the population of each state will change at a rate comparable to the Rabi frequency and the atomic system will not make a single transition but will be driven back and forth between the two states. Thus, when the population of atoms is able to oscillate several times between the two states within a single pulse of a resonant laser, we consider the transition to be *saturated*.

We include here for reference an estimate of the typical value of the Rabi frequency. For strong dipole transitions the dipole moment is on the order of ea_B. Then $|\gamma| \simeq ea_B \mathrm{E}_0/\hbar \simeq 10^8\sqrt{I}$ where, if I is in units of W/cm^2, the Rabi frequency is expressed in rad/s. Hence, for strong transitions and with a laser irradiance as low at 1 W/cm^2, the Rabi frequency is on the order of 100 MHz. The populations of states can change significantly in times on the order of 10 ns. The assumption of only considering the dipole moment interaction has been shown to be appropriate in all cases not near resonances for magnetic dipole or electric quadrupole moments[38].

This treatment of the discrete transition probability ignores the decay of an excited state by spontaneous decay or other phenomena that may shorten the lifetime of the state (such as collisions with other atoms). It is helpful when considering a stochastic process, such as the probability for decay of an atomic system, to use an ensemble of atoms and observe the behavior of the whole system. When considering a system consisting of a large number of atoms it is difficult to write down a single wave function equation which will describe the system in a well defined manner. However, when considering a collection of atoms we are really just interested in the average behavior of the atoms over a given period of time or volume of space. Density matrix theory has been developed for just such a purpose and aids in ensuring the proper averages are obtained. In using density matrix theory instead of observing the evolution of the amplitude of a given state $a_i(t)$, we will be interested in the average value of conjugate pairs of amplitudes and call those elements of the density matrix, $\rho_{ij} = \langle a_i^* a_j \rangle$, and the probability for finding the

atoms of the system in a given state i as a function of time will be given by the element of the density matrix $n_i = \rho_{ii}(t) = \langle a_i^* a_i \rangle$.

Our 2-state model then becomes a 2×2 system of matrix elements where the diagonal elements describe the populations of the two states and the off-diagonal elements describe the interactions between the states. We also choose here to include the possibility of radiative decay of the upper state at a rate $1/\tau = \Gamma$, which is valid for isolated atoms that are free from interactions with surrounding particles (no collisions). (In the case where interaction with surrounding particles needs to be considered this rate of relaxation would be higher. We would have to consider interactions that cause changes in the population of states at a rate $1/T_1$ and interactions that don't contribute to changes in the population of states but can alter the phase the atomic wavefunction at a rate $1/T_2$). So we obtain 4 equations defining the evolution of the average population of the two states as a function of time and electric field for our system,

$$\begin{aligned}
\frac{\mathrm{d}\rho_{11}}{\mathrm{d}t} &= \frac{\mathrm{d}n_1}{\mathrm{d}t} = \left(\frac{i}{\hbar}\right) \mathrm{E}_0 \left(\mu_{12}\rho_{21} - \mu_{21}\rho_{12}\right) - \Gamma\left(n_1 - n_1^0\right) \\
\frac{\mathrm{d}\rho_{22}}{\mathrm{d}t} &= \frac{\mathrm{d}n_2}{\mathrm{d}t} = \text{-}\left(\frac{i}{\hbar}\right) \mathrm{E}_0 \left(\mu_{12}\rho_{21} - \mu_{21}\rho_{12}\right) - \Gamma\left(n_2 - n_2^0\right) \\
\frac{\mathrm{d}\rho_{12}}{\mathrm{d}t} &= i\omega_0\rho_{12} + \left(\frac{i}{\hbar}\right) \mu_{12}\mathrm{E}_0 \left(n_2 - n_1\right) - \Gamma\rho_{12} \\
\frac{\mathrm{d}\rho_{12}}{\mathrm{d}t} &= \text{-}i\omega_0\rho_{21} - \left(\frac{i}{\hbar}\right) \mu_{21}\mathrm{E}_0 \left(n_2 - n_1\right) - \Gamma\rho_{21}
\end{aligned} \tag{2.22}$$

This result can be expanded to consider systems with a large number of states (N) by considering a matrix which includes N×N matrix elements resulting in N^2 equations describing the population change of each state and the interaction between states. In considering the excitation of an atomic system by coherent laser light it is important to consider the coherence of the resulting system and this density matrix formalism captures the coherent effects in the process. In cases of excitation that can be considered *incoherent,* we can reduce the number of equations needed to describe the system to N equations. Each equation simply describes the rate of change in population for a particular state. The terms of these equations are made up of the rate of excitation and de-excitation between states. For monochromatic light that is turned on and off instantaneously, the system is considered to be coherent when

$$2\gamma_0 = \frac{2\mu\mathrm{E}_0}{\hbar} \gg \Gamma \tag{2.23}$$

In this case the population difference between the two states will generally oscillate at the Rabi frequency, but the amplitude of the oscillation will decay exponentially at a rate given by Γ until the populations are equalized to the ratio of their degeneracies. When the light is no longer monochromatic, an additional condition for the coherence of the system is imposed in which the bandwidth of the laser (see Sec. 2.6.3), $\triangle\omega_L$, must be considered relative to the width of the state (Γ). If $\triangle\omega_L < \Gamma$ then the assumptions used above are still valid, but when the bandwidth of the laser is larger than the width of the state, $\triangle\omega_L > \Gamma$, then two factors become important: 1) only

part of the spectral distribution of the laser, $I(\nu)$, will contribute significantly to the resonant transition of the state, and 2) the presence of multiple modes in the broadband radiation field limit the coherence time of the laser light to $\tau_{\text{coherence}} = 1/\triangle\,\omega_L$. This limit to the coherence in the laser light limits the coherence of the photo-atomic system and when it exceeds the Rabi frequency the interaction must be considered to be incoherent regardless if Eq. 2.23 is satisfied. Therefore, to be considered a coherent interaction,

$$\gamma_0 \gg \Gamma \text{and} \, \gamma_0 \gg \triangle\omega_L$$

In addition, if the amplitude of the light pulse changes slowly in time (compared to an instantaneous change) then the interaction must again be considered incoherent due to the changing number of atoms influenced by the laser field. The time-dependent function of laser amplitude will create a time-dependent fraction of atoms participating in the interaction, therefore the ensemble of atoms as a whole will not behave coherently [1].

The experiments considered in this work will have a time-dependent pulse described by a Gaussian function with a FWHM of 10-20 ns. This is long compared to the time required for excitation to occur and therefore the experimental results will be considered in the limit of incoherent interactions. As a result, we will use the rate equation approximations to describe the ionization probability of atoms. It is important to note however, that the rate equation approximation is most effective when the lasers are tuned near the resonance frequencies and becomes less effective when studying atomic behavior in response to laser frequencies on the far wings of a resonance.

2.2.3 Stimulated Emission and Absorption

Now we will discuss the relative probability for the three types of transitions between states that we must consider. It is already clear from our discussion of the interaction matrix element that for a two-state system that stimulated emission and stimulated absorption must have the same probability for occurring, but we have not discussed the relationship between these induced transitions and spontaneous decay. In fact, as will be shown using the Einstein Coefficients, the line shapes for absorption, stimulated emission, and spontaneous emission are all very nearly identical and their probability distributions are closely related. Consider a black body cavity containing an atomic vapor in thermodynamic equilibrium . It is well known that the electromagnetic radiation density inside the cavity, regardless of the elemental composition of either the cavity walls or the atomic vapor, can be described by the Plank distribution,

$$u(\omega)\mathrm{d}\omega = \frac{u(\nu)}{2\pi}\mathrm{d}\nu = \left(\frac{\hbar\omega^3\mathrm{d}\omega}{\pi^2c^3}\right)\left[\frac{1}{\left(\mathrm{e}^{\frac{\hbar\omega}{kT}}-1\right)}\right] \tag{2.24}$$

[1] Consider the limit where a single photon arrives first in the interaction volume filled with ground state atoms and causes the excitation of a single atom. In the next instant when two photons arrive they will have a large probability for causing absorption in the other atoms but also a nonzero probability of causing stimulated emission in the atom that was previously excited. Therefore, it is not proper to consider the entire ensemble as behaving coherently any longer but only to ask what is occurring on the average (incoherent case).

where $u(\omega)\mathrm{d}\omega$ is the energy per unit volume with angular frequency in the range ω to $\omega+\mathrm{d}\omega$, $\hbar$ is the reduced Plank's constant, c is the speed of light, k is Boltzmann's constant, and T is temperature. In order for this distribution to be valid at thermal equilibrium, a balance is required between the energy absorbed within a given frequency range (*e.g.* near a resonance) by the atomic vapor and the energy emitted by that vapor within the same frequency range. We can then relate the populations of two states of an atom in this vapor ($|1\rangle$ and $|2\rangle$) which are connected by an allowed single-photon transition by the Boltzmann equation as,

$$\frac{N_2}{N_1} = \left(\frac{g_2}{g_1}\right) \mathrm{e}^{\frac{-\hbar\omega_0}{kT}} \tag{2.25}$$

where N_i is the population of the atomic state i, g_i is the statistical weight of state i ($g_i = 2J_i+1$, where J_i is the total angular momentum of the state) and $N_i = g_i n_i$. $\omega_o = (E_2 - E_1)/\hbar_0$ is the resonant photon frequency for the transition between the states $|1\rangle$ and $|2\rangle$. Logically, we can express the probability per unit time that a given atom will absorb a photon from the radiation field, or emit a photon into the radiation field by either spontaneous decay or stimulated emission by the following equations,

$$\frac{\mathrm{d}P_{\mathrm{abs}}}{\mathrm{d}t} = B_{12} \cdot u_\omega(\omega) \tag{2.26}$$

$$\frac{\mathrm{d}P_{\mathrm{emit}}}{\mathrm{d}t} = B_{21} \cdot u_\omega(\omega) \tag{2.27}$$

$$\frac{\mathrm{d}\,P_{\mathrm{decay}}}{\mathrm{d}t} = A_{21} \tag{2.28}$$

where $u_\omega(\omega)$ is the energy density of the radiation field expressed as a function of angular frequency and A_{21}, B_{21}, B_{12} are the Einstein coefficients for spontaneous decay, stimulated emission, and stimulated absorption respectively. These probabilities can also be expressed as transition rates (R_{ij}) by multiplying the probability by the number density of atoms (N_i) in the appropriate energy state. If state $|2\rangle$ can decay only to state $|1\rangle$, then we can see immediately that A_{21} must be equal to the inverse average lifetime of state $|2\rangle$ ($A_{21} = \frac{1}{\tau_2} = \Gamma_2$). We know at thermal equilibrium that these three quantities will describe a detailed balance of energy flow in the system and can be expressed as

$$(A_{21} + B_{21} \cdot u_\omega(\omega)) \cdot N_2 = B_{12} \cdot u_\omega(\omega) \cdot N_1 \tag{2.29}$$

by substituting Eq. 2.25 into Eq. 2.29 and solving for $u_\omega(\omega)$ we find,

$$u_\omega(\omega) = \frac{A_{21}}{\frac{g_1}{g_2}B_{12}} \frac{1}{\left[\mathrm{e}^{\frac{\hbar\omega}{kT}} - \left(\frac{g_2}{g_1}\frac{B_{21}}{B_{12}}\right)\right]} \tag{2.30}$$

and when this result is compared to Eq. 2.24 it is obvious that the following relationships for the Einstein coefficients must hold true:

$$g_2 B_{12} = g_1 B_{21} \tag{2.31}$$

$$A_{21} = \frac{\hbar\omega^3}{\pi^2 c^3} \cdot B_{21} \tag{2.32}$$

The cross sections for stimulated emission and absorption must be nearly equivalent, and will differ only by the statistical considerations of level degeneracies. This derivation assumes unpolarized light and that the absorption linewidth of a resonance is small compared to the bandwidth of the radiation field. This is true in the case of a black-body radiator at thermal equilibrium but is not always true for the interaction of atoms with laser beams. To consider the importance of narrow-band radiation, we must define a frequency-dependent Einstein B coefficient as

$$b_{12}(\omega) = B_{12} g(\omega)$$

where $g(\omega)$ is a normalized distribution function (lineshape) expressing the frequency dependence of the transition (*e.g.,* Eq. 2.5), and we must also include the directionality and polarization of the laser radiation. Because, as we'll see below, the dipole transition rate depends only on the square of the electric field *amplitude* in the vicinity of the dipole, as long as the directional beam results in the same energy density of the electric field near the atom as an isotropic light source, the transition rates will be the same (as long as polarization is accounted for). From Eq. 2.10 and considering the "spectral irradiance" (irradiance per frequency interval), then the power absorbed by atoms across a distance x (in the direction of propagation) in the range ω to $\omega + \mathrm{d}\omega$ is given by the energy of a photon times the rate of absorption as a function of frequency,

$$\Delta P(\omega) = \frac{\mathrm{d}I(\omega)}{\mathrm{d}x}\mathrm{d}\omega = \text{-}\hbar\omega \cdot R_{12}(\omega)\mathrm{d}\omega = \text{-}\hbar\omega \cdot N_1 B_{12} g(\omega) I(\omega)\mathrm{d}\omega/c = \text{-}N_1 I(\omega)\sigma_a(\omega)\mathrm{d}\omega \tag{2.33}$$

where R_{12} is the rate of stimulated absorption given by the Einstein B coefficient. We have used the fact that $I(\omega) = c \cdot u(\omega)$, and we have defined the cross section for absorption as $\sigma_a \equiv \hbar\omega B_{12} g(\omega)/c$. Using the relationships between the Einstein coefficients given above, we can express the cross section as a function of A_{21}

$$\sigma_a(\omega) = \frac{1}{4}\frac{g_2}{g_1}\lambda_0^2 A_{21} g(\omega) = \frac{1}{4}\frac{g_2}{g_1}\lambda_0^2 \Gamma_2 g(\omega) \tag{2.34}$$

This is remarkably close to the simple phenomenological estimate of the cross section obtained by guessing that the photon and atom must find each other in space ($\pi\lambda^2$), in energy (here $g(\omega)$), and must form the specific excited state $|2\rangle$, which must be proportional to A_{21}.

Dipole Moment in Terms of Einstein Coefficients

To be complete, we include a short discussion comparing the transition dipole matrix element for a transition with its Einstein coefficients . The classical description of the average power radiated by an oscillating electric dipole $\mu = qr$ is

$$\overline{P} = \frac{2}{3}\frac{\overline{\mu}^2 \omega^4}{4\pi\varepsilon_0 c^3} \tag{2.35}$$

where $\overline{\mu} = \frac{1}{2}\mu_0$. By invoking the correspondence principle, and using the quantum mechanical expectation value from the definition of the transition dipole matrix element (Eq. 2.43), we obtain

$$\langle P \rangle = \frac{4}{3}\frac{\omega_{ik}^4}{4\pi\varepsilon_0 c^3}|D_{ik}|^2 \tag{2.36}$$

. We also know, using the probability for emission from Eq. 2.28 and the energy of a photon, that we can describe the average power emitted by a single atom in an excited state as $\langle P \rangle = A_{ik}\hbar\omega_{ik}$. We then identify that

$$A_{ik} = \frac{2}{3}\frac{\omega_{ik}^3}{\varepsilon_0 hc^3}|D_{ik}|^2 \tag{2.37}$$

and using the relationship between the Einstein coefficients one finds,

$$B_{ik} = \frac{2\pi^2}{3\varepsilon_o h^2}|D_{ik}|^2 \tag{2.38}$$

Then from Eq. 2.34 we can show that the transition cross section is directly proportional to the square of the transition dipole matrix element[2],

$$\sigma_a(\omega) = \frac{1}{4}\frac{g_2}{g_1}\lambda_0^2 A_{21} g(\omega) = \frac{2\pi^2 g(\omega)}{3\varepsilon_0\hbar\lambda_0}\frac{g_2}{g_1}|D_{ik}|^2 \tag{2.39}$$

A particular dipole transition will be "saturated" as defined in Sec. 2.2.2 when the product of the absorption cross section and the laser flux in that frequency range exceeds the rate of decay

$$\sigma_a(\omega)\phi(\omega) \gg A_{21} = \frac{1}{\tau_2} \tag{2.40}$$

An additional condition for saturation, known as the fluence condition, requires that $\sigma F t_L = \sigma\phi \gg 1$, where $t_L$is the length of the laser pulse, which essentially just guarantees that the pulse length is shorter than the average lifetime of the state $t_L < \tau_2$[38].

Angular Momentum and the Degeneracy of States

We introduced in Eq. 2.25 the degeneracy of the ith level as $g_i = 2J+1$, the number of degenerate states within a given level (also called sublevels, see selection rules below). Of course it is well understood that the energy degeneracy for these states can be removed in the presence of electric or magnetic fields. For situations involving thermal equilibrium, in the absence of external fields, the total population of a given level N_i will equilibrate in relation to the total

[2]While we won't use it here, a quantity known as the oscillator strength $f_{i\to k}$ has been used historically to quantify the relative strength of a transition probability. It expresses the strength of a given transition relative to a classical Lorentz oscillating dipole. It helps to convey the partial shielding of the nuclear charge from the electron undergoing the transition. It can be used to define the dipole matrix element as well using $f_{i\to k} = 2m_e\omega_0|D_{ik}|^2/(3e^2\hbar(2J+1))$[39].

number of degenerate states within the level $\sum n_k = N_i$. It is clear in the context of our two-state model using the density matrix approach that the situation quickly becomes complicated when we must consider the presence of degenerate states within the two levels. All real atoms have a large number of states to be considered and instead of Rabi oscillations causing transitions between just two individual levels, the model must account for oscillations between individual states and all other permissible transitions (including the coupling between states within the same level) with specific rates for each transition. This requires expanding the density matrix approach to N^2 equations where N is the total number of states with allowed transitions. Under such conditions no simple analytical solutions are available. However, as long as all interactions can be considered incoherent, the situation is greatly simplified because of the applicability of the rate equation approximation. Instead of considering individual sublevel transitions to keep track of the evolution of the states involved, it is possible to simply track the total population of the level as long as the degeneracy of accessible states is considered. Therefore, under conditions of strong saturation,

$$\frac{N_2}{N_1} = \frac{g_2}{g_1} \tag{2.41}$$

and the distribution of atoms between the two states will be equal to the ratio of their level degeneracies. This condition permits the fraction of atoms in the excited state to exceed 50 % when $g_2 > g_1$, this is an important consideration for choosing a resonance ionization scheme as we will explore further when we discuss isotope dependent ionization factors.

2.2.4 Selection Rules for Electric Dipole Transitions

The conservation of angular momentum and parity impose rules on the transitions allowed by electric dipole interactions. Whenever the transition dipole matrix element D_{ik} between two states i and k is zero, we say that the transition is *dipole forbidden*. That is, the transition can not occur via the electric dipole interaction. Because the dipole operator has odd parity it follows that the parity of the wave functions of the levels involved in an electric dipole transition must have opposite parity. The parity selection rule can be written as $\triangle$parity = yes. As we have just seen that the transition rates are proportional to the square of the dipole matrix element let's examine a few simple cases in order to learn about the types of transitions that can occur. In order to simplify the mathematics we will not consider the contribution of electron spin to the wave functions which do not affect the result. Neglecting intrinsic spin, the wavefunction for an atomic electron can be written in spherical polar coordinates as

$$\psi_{n,l,m_l} = \frac{1}{\sqrt{2\pi}} R_{n,l}(r)\Theta^l_m(\theta)\mathrm{e}^{im_l\phi} \tag{2.42}$$

where $R_{n,l}$ is the radial component of the wavefunction and Θ^l_m is the polar angle component of the spherical harmonic function $Y^l_m(\theta,\phi)$. Through separation of variables it can be shown that one component of the dipole matrix element between two states must be non-zero in order to

have any probability for the transition to occur. Remember

$$|D_{ik}|_{\hat{e}} = \hat{e} \cdot e \int \psi_k^* \vec{r} \psi_i \mathrm{d}q \tag{2.43}$$

We begin exploring the interaction of an atom with linear polarized light, choosing the z-axis as the direction of polarization, $\vec{r} = r\cos(\theta)$. The only non-vanishing component of the transition dipole matrix element is the component along the z-axis

$$\begin{aligned} |D_{ik}|_z &= \frac{1}{2\pi} \int_{r=0}^{\infty} R_i R_k r^3 \mathrm{d}r \\ &\times \int_0^{2\pi} \Theta_{m_i}^{l_i} \Theta_{m_k}^{l_k} \sin(\theta)\cos(\theta)\mathrm{d}\theta \\ &\times \int_0^{\pi} \mathrm{e}^{i(m_k - m_i)\phi} \mathrm{d}\phi \end{aligned} \tag{2.44}$$

For circularly polarized light traveling in the direction of $\hat{z}$ and polarized in the x-y plane, the electric field would be described by $\mathrm{E} = \mathrm{E}_x \pm i\mathrm{E}_y$ depending on the direction of polarization, which would give for the dipole moment $\hat{e} \cdot \vec{r} = \mp r\sin(\theta)\mathrm{e}^{i\phi}$. The non-zero components of the transition dipole matrix element become the sum and difference of the x- and y- components

$$\begin{aligned} |D_{ik}|_x \pm \mathrm{i}\,|D_{ik}|_y &= \frac{1}{2\pi} \int_{r=0}^{\infty} R_i R_k r^3 \mathrm{d}r \\ &\times \int_0^{2\pi} \Theta_{m_i}^{l_i} \Theta_{m_k}^{l_k} \sin^2(\theta)\mathrm{d}\theta \\ &\times \int_0^{\pi} \mathrm{e}^{i(m_k - m_i \pm 1)\phi} \mathrm{d}\phi \end{aligned} \tag{2.45}$$

The radial part of the wave function remains unchanged, but the selection rules can be identified by examining the azimuthal and polar angle integrals separately. From the azimuthal part of the matrix element (third integral on the right hand side of Eqs. 2.44 & 2.45) one can see immediately that the only values for which $D_{ik}(\phi) \neq 0$ require that the exponent be zero. Therefore, for linearly polarized light $\triangle m_J = 0$, and for circularly polarized light $\triangle m_J = \pm 1$. Likewise, examining the polar angle part of the matrix element (second integral) reveals that $\triangle l = \pm 1$, and because the magnitude of the electron spin quantum number doesn't change but it can change orientation relative to the orbital angular momentum (if at least one of the states

Component	Rule
$\triangle m_J$	$0, \pm 1$
$\triangle J$	$0, \pm 1$ ($0 \leftrightarrow 0$ forbidden)
$\triangle$parity	yes

Table 2.1: Selection Rules for Dipole Transitions

has $l \neq 0$) then $\triangle J = 0, \pm 1$. To summarize, there are three relevant selection rules for allowed dipole transitions and they are displayed in Table 2.1. The selection rules for allowed dipole transitions using unpolarized light are ΔF$= 0, \pm 1$, Δm$_F = 0, \pm 1$. While for linear polarized light they are ΔF$= 0, \pm 1$, Δm$_F = 0$. The laser beams used in our experiments have been measured to be linearly polarized at a level $\geq$98%. Thus, in the following discussion, we will only consider transitions allowed by the selection rules for linearly polarized light.

2.2.5 Atomic Lineshape

Doppler Broadening

Now we must consider the fact that real atoms in our system are not stationary but in fact are generally moving in random directions in space. In the non-relativistic limit, an atom with a resonance at frequency ν_0 traveling with a velocity v parallel to the propagation direction of the laser beam will experience a shift in frequency known as the Doppler shift and described by

$$\nu_D = \nu_0(1 + \frac{\mathrm{v}}{c}) \tag{2.46}$$

(One should be aware not to confuse frequency (ν) with velocity (v) which look similar). If the distribution of atom velocities in the gas phase is thermal then it can be described by the Maxwell-Boltzmann probability distribution.

$$P(\mathrm{v})\mathrm{dv} = \sqrt{\frac{m}{2\pi kT}}\mathrm{e}^{-\frac{m\mathrm{v}^2}{2kT}}\mathrm{dv} \tag{2.47}$$

The frequency distribution about the central frequency ν_0 is then given by,

$$\mathscr{D}(\nu) = \frac{1}{\sqrt{2\pi\sigma}}\mathrm{e}^{-\frac{(\nu-\nu_0)^2}{2\sigma^2}} \tag{2.48}$$

which is a Gaussian distribution with a standard deviation given by,

$$\sigma_\nu = \sqrt{\frac{kT}{mc^2}}\nu_0 \tag{2.49}$$

This leads to a FWHM of the distribution, often called the Doppler width of

$$\triangle \nu_D = 2 \cdot \nu_0 \sqrt{\frac{2kT \cdot ln2}{mc^2}} \tag{2.50}$$

Substituting for the constants and converting to wavelength leads to the expression

$$\triangle \lambda_D = 7.16 \times 10^{-7} \cdot \lambda_0 \cdot \sqrt{\frac{T}{M}} \tag{2.51}$$

where T is in units of °K and M is the mass in amu. The Doppler width is in the same units used to expressed λ_0.

Collisional Rates

We discussed briefly our decision in the density matrix equations to ignore collisional broadening, also known as pressure broadening (reduced state lifetime and altered coherence due to collisions between atoms). We can estimate an average collisional time [34] for atoms in a Maxwell-Boltzmann distribution from the relation

$$\langle \tau_c \rangle = \frac{d}{\mathrm{v}} = \frac{1}{\mathrm{v} \cdot \sqrt[3]{n}} \tag{2.52}$$

where d is the average distance between atoms, v is the velocity of the atoms, and n is the atom density. In the experiments of interest here atoms are removed from the surface of a material via ion sputtering. Once atoms leave the surface of a target they freely expand in a high vacuum for a short time before the laser beams reach the ionization volume. Some collisions are bound to occur as atoms are being liberated from the target surface, but our interest is in the collisions that take place during the period in which atoms are being irradiated. As an example, we typically remove on the order of 10^5 atoms from a UO_2 target by ion sputtering in a single pulse (this has been confirmed by measuring crater volumes for a known number of ion pulses from materials of known density). If we conservatively assume that all the desorbed material occupies the ionization volume of about 0.5 mm^3, the atomic density would be about 2×10^{-4} atoms/m^3. The most probably energy for the sputtered material is about 2-4 eV (see Sec. 2.6.2). Therefore the most probable velocity of a uranium atom would be about $0.11c$ or 3.3×10^7 m/s ($\sim 1\,\mu$m/ns). From Eq. 2.52, the average predicted collision time would be $\langle \tau_c \rangle \sim 2.5\,\mu$s. The duration of a laser pulse used for excitation/ionization is about 20 ns long (FWHM) and thus the probability for collisions during the excitation process is clearly sufficiently small that it can be safely neglected.

Voigt Profile

With the assumption that the velocity distribution of the atoms interacting with a laser beam is Maxwell-Boltzmann, the natural Lorentzian lineshape of the interaction cross section must

be modified to account for the moving target atoms[3]. The proper convolution of the two distributions does not have an analytical form but can be expressed as the integral

$$\begin{aligned} \mathscr{V}(\nu) &= \int \mathscr{D}(\nu',\sigma)\cdot\mathscr{L}(\nu-\nu',\Gamma)\,\mathrm{d}\nu' \\ \mathscr{L}(\nu-\nu',\Gamma) &= \frac{1}{\pi}\frac{\Gamma}{(\nu-\nu')^2+\left(\frac{\Gamma}{2}\right)^2} \\ \mathscr{D}(\nu',\sigma) &= \frac{1}{\sqrt{2\pi\sigma}}\mathrm{e}^{-\frac{\nu'}{\sigma}} \end{aligned} \tag{2.53}$$

where $\mathscr{V}(\nu)$ is the convoluted distribution of the Lorentzian ($\mathscr{L}(\nu-\nu',\Gamma)$) and Gaussian ($\mathscr{D}(\nu',\sigma)$) profiles, known as a Voigt profile[34, 40], and the frequency (ν), width (Γ), and standard deviation (σ) have already been defined. The Voigt profile is dominated near the peak by the shape of the Gaussian function, but at the far wings is composed almost entirely of the Lorentzian function. Figure 2.4 is a diagram of the various lineshapes discussed above shown with characteristics typical of the first resonance of ^{238}U in our ionization scheme.

2.2.6 Ionization Processes

Many approaches may be used to carry out the resonant ionization of atoms. A feature common to all such schemes is an initial selective excitation by laser radiation of at least one intermediate atomic level followed by ionization of the excited atoms alone. Resonant excitation was explored in the previous section and the current section will explore the next step: ionization mechanisms of excited atoms. Two possibilities exist for effective ionization by laser radiation: direct non-resonant photoionization into the continuum and resonant photoionization via a transition to an autoionizing state. In addition, excited states near the ionization potential (Rydberg states) are comparatively easy to ionize by several other means: an electric field pulse which lowers the ionization potential of the electron, a pulse of infrared radiation, or collisions with other particles or surfaces[41, 42]. The excited states considered in this work are sufficiently far from the ionization limit that these later means of ionization are not of interest.

With proper selection of a resonant excitation scheme, it is possible to attain a situation in which all of the cross sections of successive bound-bound transitions lie in the region $\geq 10^{-15}\,\mathrm{cm}^2$. The energy fluxes of the laser pulse required to saturate these transitions are then in

[3]Often experimental discussions of resonance lineshape necessarily include a factor known as "power broadening" which is a critical component of the observed resonance shape in laser spectroscopy. It is due to the fact that the experimental lineshape is a product of the atomic resonance shape *and* the experimental laser lineshape and amplitude. The *apparent* width of a resonance will be different for two different values of laser power simply because of the increased number of photons on the resonance line wing allowing for excitation of a larger number of total atoms. This assumes that there is sufficient power in the laser beam to saturate the transition probability at the resonance wavelength. This is already included inherently in our estimation of resonance excitation by including the amplitude of the electric field of the laser. Estimating the contribution of power broadening to lineshape and the use of power broadening in helping to stabilize isotope ratios measured by RIMS is well discussed in Levine, *et al*. [14]. We will discuss the effects of power broadening on our system in our experimental results.

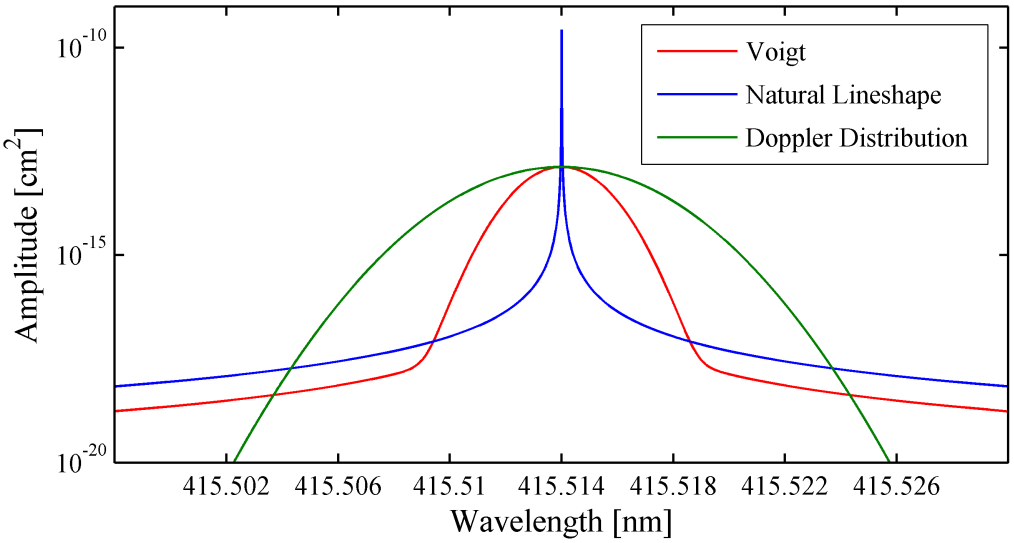

Figure 2.4: A Voigt lineshape composed of the natural lineshape (Lorentzian) and an approximate Doppler distribution of atoms (Gaussian) for first transition in ^{238}U. Resonance centered at 415.514 nm, natural average lifetime 57 ns, Doppler width 2.5 pm.

the range $10^{-4} - 10^{-5}$ J/cm^2. These are easily achieved with commercial laser systems. Direct photoionization of excited atoms to most states in the continuum have, on the average, very small cross sections (10^{-18}) compared to these bound-bound transitions and therefore are not ideal. Often, the ionization selectivity that can be achieved using a single resonant step is insufficient, and in these cases the use of resonant highly-excited states and autoionization are a particular help in gaining enhanced selectivity.

The photoionization yield, the fraction of target atoms in the ionization volume that are ionized, reaches a maximum when all successive transitions of a multilevel ionization process are simultaneously saturated by the lasers used to excite the individual transitions involved. If saturation of all excited states takes place during a laser pulse, and the final state of a multistep process lies in the continuum, it is possible to completely deplete the ground state through excitation and thus achieve an ionization yield of unity. These conditions can be achieved by ionization with laser radiation. Another approach occasionally employed for ionization is the use of an electric field which is turned on after the laser pulses are over. This method can only ionize atoms currently occupying the last excited state of the laser excitation process. The fraction of atoms ionized in this case would be determined by the equilibrium populations of all the levels involved and must always be less than unity. On the other hand, the use of a continuous electric field for ionization during the laser irradiation is complicated by a large Stark effect for highly excited states making this approach impractical[43]. Minimizing the required laser energy and maximizing selectivity of ionization can be best achieved simultaneously through the use of narrow autoionizing states.

When developing an ionization scheme to optimize the conversion of excited atoms into ions, two conditions are desired:

(1) Negligible relaxation of atoms from the excited states compared to excitation and ionization rates:

$$W_{12} \gg 1/\tau_{12} \text{ and } W_i \gg 1/\tau_{12}$$

(2) Matching of excitation and ionization rates, which can be derived from a simple rate equation model of two-state atom:

$$\frac{W_i}{2W_{12}} = \frac{\sigma_{2i} I_2}{2\sigma_{12} I_1} = 1$$

or

$$\frac{I_2}{I_1} = \frac{2\sigma_{12}}{\sigma_{2i}}$$

To ensure that all of the excited atoms can be ionized, the intensity of ionization radiation I_2 must be approximately $\frac{2\sigma_{12}}{\sigma_{2i}}$ times that of the exciting radiation[43]. Any increase in I_2 over this amount would not increase the ionization rate and may contribute to non-resonant ionization processes. This relation also demonstrates immediately the challenge of saturating the ionization transition because the ionization cross section is typically a few orders of magnitude smaller than the bound-bound transition cross sections.

2.2.6.1 Ionization into the Continuum

Photoionization is the process where an atom absorbs sufficient energy for a bound electron to escape into the continuum. The cross section for ionization, relative to the cross sections for exciting bound states, decreases sharply as one moves up in energy above the ionization potential[44]. We will represent the states of the ionization continuum in terms of an energy dE about the energy E_c, the angular momentum quantum number M_c, and its component along the axis of quantization m_c. Then the time-dependent wave function for our two state atom plus the ionization continuum becomes

$$|\psi(t)\rangle = a_1(t)\mathrm{e}^{-i\omega_1 t}|1\rangle + a_2(t)\mathrm{e}^{-i\omega_2 t}|2\rangle + \sum_{m_c}\int \mathrm{d}E_c \mathrm{e}^{-i\omega_c t} C(E_c, m_c, t)\,|E_c, M_c, m_c\rangle \qquad (2.54)$$

The inclusion of the final term on the right, which is a sum over all the continuum states, greatly complicates the equations of motion for the populations of levels in our model. It is often necessary and appropriate to approximate the continuum term as a constant over some small region about the energy E_c which allows the integral for each term in the sum to be divided into two portions. A small region over a constant value near the state of interest and the other over the remainder of the continuum. We assume that the magnitude of the cross section does not change in a small region of energy about a specific continuum state $|E_c, M_c, m_c\rangle$ and then assume an exponential form for the continuum outside this region. This approximation

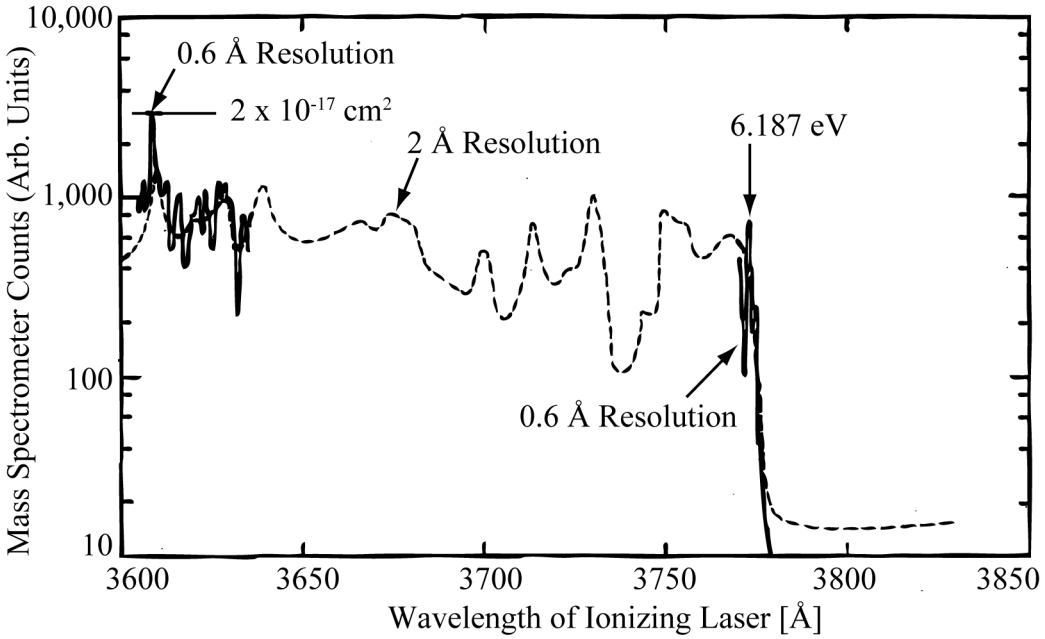

Figure 2.5: A Photoionization spectrum reproduced from Janes, *et al.*[46]. The exciting wavelength was 426.6 nm. The solid line indicates a bandwidth of the ionization laser of 0.6 Å , the dashed line was produced using a bandwidth of the ionization laser of 2 Å. The measured ionization limit was 6.187 eV.

is good in regions without any autoionizing resonances (see below)[8]. This allows the wave function to be evaluated at specific energies appropriate for specific ionization schemes. There are several useful references available for learning more about calculations involving ionization into the continuum [8, 45, 38]. We are here more interested in the magnitude and general energy dependence of the cross section for ionizing an atom from an excited state into the continuum. Mainly, that the cross section rapidly falls off as a function of energy as one moves up in energy above the ionization limit and is frequently found to be around $10^{-17} - 10^{-18}\,\mathrm{cm}^2$ near the ionization potential[38, 44].

The frequency dependence of the photoionization cross section was studied for uranium by Janes, *et al.*[46] using a two-photon ionization scheme. They excited an intermediate state at 2.905 eV above the ground state ($\lambda_1 = 426.6\,\mathrm{nm}$) using a narrowband dye laser (spectral width $\backsimeq 0.002\,\mathrm{nm}$). The excited atoms were then photoionized using a similar dye laser with variable wavelength in the range 360.5 - 383.0 nm (λ_2). The experimental results of relative ion count intensity as a function of ionization laser wavelength are reprinted in Fig. 2.5. The dashed curve represents a spectral width of the ionizing laser of 0.2 nm and the solid curve represents a spectral width of 0.06 nm. The ionization limit in the figure is at 3777 Å (377.7 nm) and when combined with the energy of the excitation laser gives an ionization potential for uranium of 6.187 ± 0.002 eV. There is a sharp peak at the wavelength 360.9 nm (above the ionization threshold) and its peak corresponds to an ionization cross section of $2 \times 10^{-17}\,\mathrm{cm}^2(\frac{\triangle\omega_L}{\triangle\omega_0})$, where

$\triangle\omega_L$ is the laser spectral width and $\triangle\omega_0$ is the natural linewidth of the transition. These data give a good estimate for the magnitude of ionization cross sections we can expect to encounter in the ionization of uranium. The presence of sharp peaks in the ionization spectrum demonstrates the presence of autoionizing resonances which will be the next topic of discussion. It is clear from these results that the highest ionization cross section observed (10^{-17} cm^2) is several orders of magnitude smaller than typical bound-state transition cross sections (10^{-12}-10^{-13} cm^2), which underscores the importance of attempts to maximize the probability of ionization through use of autoionization.

2.2.6.2 Autoionization

Autoionization states are bound states involving two excited electrons with total energy above the ionization potential. An atom in such a state can decay radiatively back to a state below the ionization limit or via non-radiative decay into a free electron and an ion (autoionization). The probability of a transition into the continuum shortens the lifetime of the discrete excited state and therefore causes broadening of its linewidth. Because autoionization can be considered a result of the superposition of discrete and continuous states, the probability for decay by this mechanism increases with an increase in the coupling of the autoionizing state and the continuum as will be apparent in the form of the lineshape discussed below. The theory of autoionization was first presented by Fano in 1961 and further explored in subsequent papers [47, 48]. The presence of discrete levels in the continuum region causes interference between the two types of states and the autoionizing resonance becomes asymmetric. The presence of relatively long-lived autoionizing states generates very sharp resonances in the ionization spectrum of atoms with peak ionization cross sections as high as 10^{-15} cm^2 [49, 43], which is several orders of magnitude higher than the ionization cross section in the continuum and greatly reduces the requirement for the laser intensity necessary to ionize all of the excited atoms.

In an independent-particle approximation, the autoionization decay can be represented as $i(n_1n_2) \rightarrow f(n_3k)$ where n_i is the bound state of the ith electron and k is the state of the free electron. $i(n_1n_2)$ is described as a doubly-excited discrete bound state with total energy above the ionization limit. The partial width of the autoionizing resonance then depends on the coupling of the states with the continuum as

$$\Gamma_{\text{ai}} = 2\pi |\langle i|V|f\rangle|^2$$

where V is the interaction matrix element between the initial and final states (i and f). The subscript "ai" is a shorthand notation for autoionizing. This partial width of decay to the continuum (Γ_{ai}) will dominate the total width of the decay of the resonance.

The lineshape of an autoionizing resonance is known as a Fano profile[47, 48] can be de-

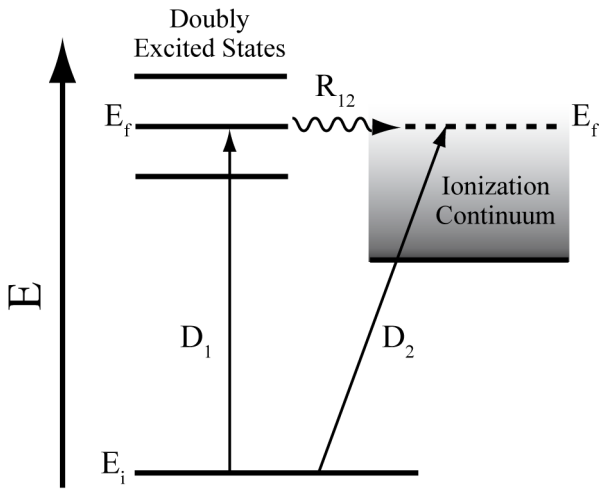

Figure 2.6: Autoionization schematic from an excited state E_i. D_1 is the transition amplitude to the doubly-excited bound state E_f, D_2 is the transition amplitude to a continuum state at energy equal E_f, R_{12} is the rate of the transition between bound and continuum states.

scribed by a function

$$\begin{aligned} \sigma_{\mathrm{ai}}(E) &= \sigma_a \tfrac{(q+\varepsilon)^2}{1+\varepsilon^2} + \sigma_b \\ \varepsilon &= \tfrac{2(E-E_0)}{\Gamma} \\ q &= -\tfrac{D_1^2}{D_2 R_{12}} \end{aligned} \tag{2.55}$$

where σ_a is the absorption cross section for forming the bound state, σ_b is the cross section for ionization into the continuum (background or non-resonant cross section), ε is the reduced energy of the doubly-excited bound state, q is the Fano parameter as described in Fano, 1961[47], where D_1 is the transition amplitude to a doubly-excited bound state, D_2 is the transition amplitude to the continuum state, and R_{12} is the rate of the transition between the discrete bound states and continuum states as shown schematically in Fig. 2.6. Further details of autoionizing states, particularly for cases of very strong laser fields can be found in Lambropoulos and Zoller[50].

Schumann, *et al.*[51] measured the ionization rate for uranium (^{238}U) with a three-photon excitation scheme as a function of frequency with high resolution. Their spectroscopy of the ionization transition from the last bound excited state (with $J = 8$) over the region near the ionization potential of $49,958\,\mathrm{cm}^{-1}$(6.195 eV) is included here as Fig. 2.7 Several peaks in the ionization probability with widths varying from < 100 to $30,000\,\mathrm{MHz}$ ($0.003-1\,\mathrm{cm}^{-1}$) are clearly identified in the spectrum and appear to have peak cross sections of as much as 5 orders of magnitude larger than the apparent ionization continuum (flat region near $49,966\,\mathrm{cm}^{-1}$). The very narrow and intense resonance, near $49,972\,\mathrm{cm}^{-1}$, identified in this spectrum with an asterisk was assigned an angular momentum of $J = 9$, and a width of 65 MHz ($0.002\,\mathrm{cm}^{-1}$),

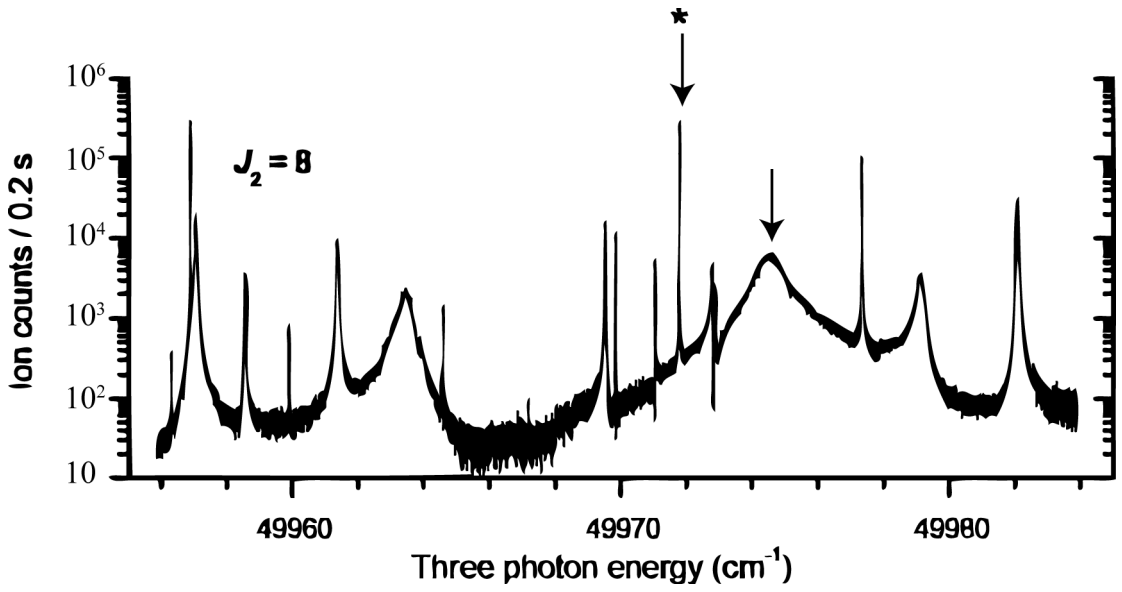

Figure 2.7: Ionization rate of ^{238}U as a function of wave number just above the ionization limit for excitation from a highly excited bound state with angular momentum $J_2 = 8$. Note the presence of very strong, narrow resonances and compare their peak amplitudes to the region near $49,966\,\mathrm{cm}^{-1}$. The arrows indicate the autoionizing states explored in the present work. The narrow resonance marked with an asterisk is described in the text. (Reproduced from Schumann, *et al.*[51])

that corresponds to a lifetime of ~ 3 ns, which is very long for an autoionizing state, indicating weak coupling between the discrete state and the ionization continuum. The two autoionizing resonances explored in this work, including the sharp long-lived state just discussed and the very broad peak just above $49,974\,\mathrm{cm}^{-1}$, are identified by arrows in the spectrum and will be further described in the experimental details of the resonance ionization scheme.

2.3 Isotope Dependent Factors

There are two differences between isotopes of a particular element that will give rise to different excitation and ionization probabilities. The first is due to the isotope shift in the energies of electronic states, and the other that only effects odd isotopes, is the hyperfine splitting due to the coupling of non-zero nuclear angular momenta (I) with electron angular momenta ($J = L + S$). We'll explore both of these effects in the context of resonance ionization and the resulting differences in isotope ionization probabilities.

2.3.1 Isotope Shift

There are two main factors that give rise to the isotope shift:

(1) Nuclear Mass Difference - This is the main source of the isotope shift in light isotopes because the additional mass from an extra neutron or two is a large fraction of the total nuclear mass. This results in a slight difference in the reduced mass of a bound electron that affects the energy of the excited states.

(2) Volume Difference - This effect is due to the differences in the electric charge distribution in the nucleus for different isotopes. It is the main contributor to the isotope shift in heavier nuclei because the mass difference between isotopes is a relatively small fraction of the total nuclear mass, but nuclear structure effects can cause large changes in nuclear radii and/or asymmetries in nuclear shape with each neutron added. This change in nuclear shape produces a change in the electric field of the atom experienced by the electrons.

Because uranium is one of the heavier naturally occurring elements, the majority of the isotope shift is not due to the change in mass, but rather is due to the change in shape of the deformed uranium nuclei. As an example of the magnitudes of such shifts, the isotope shift for the first transition in the 3-photon resonance ionization scheme used in the present work is +12.5 GHz for ^{235}U and +14.9 GHz for ^{234}U, relative to the frequency of the transition for ^{238}U of 7.2×10^5 GHz (see Sec. 3.2.1). In the presence of these shifts we should expect that the measured isotope ratio of any two isotopes will show a significant dependence on the relative overlap of the laser spectral irradiance (wavelength, bandwidth, power) for the saturation of the excitation and ionization transitions of each isotope.

2.3.2 Odd Isotopes

2.3.2.1 Nuclear Spin and Hyperfine Structure

Even-massed nuclei in their ground states always contain nucleon pairs and thus have nuclear angular momenta of 0. However, odd-massed nuclei always have one unpaired nucleon and thus have non-zero angular momenta generally represented by I. The nuclear angular momentum couples with the angular momentum of the atomic electrons in orbit around the nucleus. Instead of being able to describe the states completely by combining the orbital (L) and spin angular momentum numbers (S) of the electrons into a total electron angular momentum number (J), we must now couple the angular momenta of the nucleus (I) and the electrons in orbit (J) into states of total atomic angular momentum, F. Following the rules of angular momentum coupling, the total number of magnetic substates is $(2J+1)(2I+1)$ compared to $2J+1$ when $I=0$. The inclusion of the nuclear field in the description of the atomic states removes the energy degeneracy (in field-free space) of the states of different electron total angular momentum (J) or, because I is a constant for a given isotope, of different total angular momentum (F)[4]. Each F state is then composed of $2F+1$ degenerate substates described by magnetic total angular momentum quantum numbers m_F. This splitting of states in energy for odd isotopes is known as the Hyperfine-Structure (HFS). As an example, for the first-excited state considered in the present work at 7.2×10^5 GHz, the hyperfine states in ^{235}U cover a range of 4 GHz. This can be compared to the 12.5 GHz isotope shift between ^{235}U and ^{238}U for that level. It has been shown that the energy shifts of the individual F states follow a pattern of energy separation that is a consequence of their angular momenta components (F, I, and J) and the details of the atomic structure of a given isotope (mass and volume differences that lead to the isotope shift). The energy shifts for individual hyperfine states can be calculated from the Casmir Formula[51, 52]:

$$\triangle E(F) = \frac{A}{2}C + B\frac{3C(C+1) - 4IJ(I+1)(J+1)}{8IJ(2J-1)(2I-1)} \tag{2.56}$$

$$\text{where } C = F(F+1) - I(I+1) - J(J+1)$$

where $\triangle E(F)$ is the shift in energy of a hyperfine state relative to the average energy of a level weighted by the degeneracy. A and B are empirically-determined constants representing the different contributions to the isotope shift.

The selection rules for electric dipole transitions of odd isotopes are equivalent to those given previously for even isotopes if we replace J and m_J with F and m_F. Here m_F is the magnetic quantum number for a substate with total angular momentum F. A state with angular momentum F will have $2F+1$ magnetic substates ranging from $F, F-1, \ldots -F$. However, as we will see next the difference in the total number of atomic states connected by allowed

[4]Note, that for even isotopes that the terms level and state are equivalent, it is only for odd isotopes that the terms have a different meaning. This is due to the coupling of nuclear spin with the electrons angular momentum that removes the degeneracy of the states within a given level.

dipole transitions can have a large effect on the relative population of atomic energy levels at equilibrium.

Figure 2.8 contains two partial level diagrams for an even and an odd isotope of a model atom with a lower level ($J = 0$) and an upper level ($J = 1$). The left diagram (a) shows the states of the even isotope with $I = 0$, where the lower level consists of a single magnetic substate with $m_J = 0$ and three substates in the upper level with $m_J = -1, 0, 1$. Using the notation $|J, m_J\rangle$, the allowed dipole transition for linearly polarized light is from $|0,0\rangle \rightarrow |1,0\rangle$. The right diagram (b) shows the states of the odd isotope with nuclear spin angular momentum $I = 1/2$. The proper quantum number for describing the states is now F, where F is defined by the proper coupling of I and J. There are now two states, $F = 3/2$ and $1/2$ in the upper level ($J = 1$) whose mean energy is shifted from the energy of the level shown in (a) by the isotope shift, and their energy is split about their mean as described by the Casmir formula (Eq. 2.56). Each state has a number of magnetic substates equal to $2F + 1$. Transitions will now be defined between states described by $|F, m_F\rangle$. Following the selection rule of $\triangle m_F = 0$, there are four allowed transitions. While the ratio of the total level degeneracies ($\frac{g_2}{g_1} = \frac{3}{1}$) is the same for both isotopes, at equilibrium under resonant excitation by linearly polarized light the probability of being in the excited level will be $1/2$ for the even isotope and $4/6$ for the odd isotope. The differences in angular momenta of substates will effect the rate at which the atomic levels are populated, which can result in large differences in the ionization probabilities for even and odd isotopes known as the even-odd effect. In fact, the angular momenta differences between even and odd isotopes can cause population trapping due to polarization effects and has even been proposed as a method for performing isotope separation[53]. The use of ionization schemes where the orbital angular momentum is always increasing by $\triangle J = +1$, is sufficient to avoid fractionation effects as a result of the change in selection rules. This approach to choosing transitions of increasing electron angular momentum is detailed in Payne, *et al.*[35].

The hyperfine splitting thus causes a dilution of the oscillator strength that is related to the addition of nuclear angular momentum in the description of states for odd isotopes. The matrix elements for the allowed dipole transition probabilities in *odd* isotopes can be related to the matrix elements for even isotopes by the Wigner-Eckart Theorem [54, 35] in the form

$$\langle F_1, m_1 | D_{odd} | F_2, m_2 \rangle = C(j_1, j_2, j, m_1, m_2, m) \langle J_1 \| D_{even} \| J_2 \rangle \tag{2.57}$$

where $C(j_1, j_2, j, m_1, m_2, m)$ are the Clebsch-Gordan coefficients (C-G) and are written explicitly as $C(F_1, 1, F_1 + \triangle F, m, 0, m)$ because F_2 is fixed by the transition considered and also $m_1 = m_2$ because $\triangle m = 0$ for linearly polarized light. The C-G coefficients can be calculated using the Wigner 3-j symbols and are symmetric about $m_F = 0$ [55]. Thus, the oscillator strength of a transition for odd isotopes is distributed between the individual hyperfine transitions according to the ratios of the squares of the corresponding C-G coefficients. The electric dipole transition leaves the spin of the electron (S) untouched so it is just changing the orbital angular momentum of the electron (L).

Now we will explore how the angular momentum and C-G coefficients affect our investigation of ^{235}U. The resonance ionization scheme we use involves exciting the ground state atoms of uranium ($J = 6$) to an excited level at 24,066 cm^{-1} with $J = 7$. The nuclear spin of ^{235}U

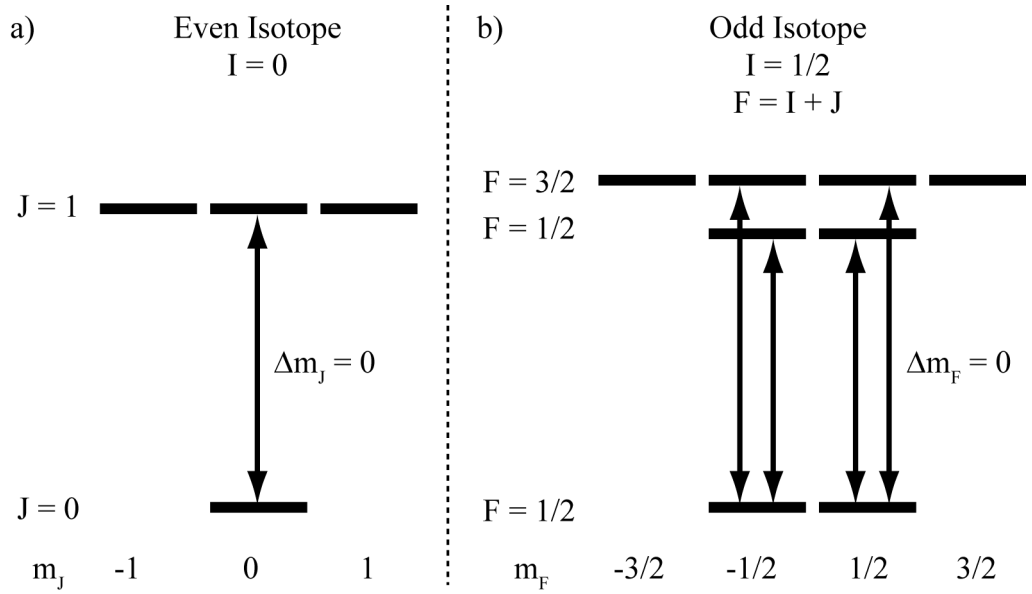

Figure 2.8: Partial level diagrams for an even and an odd isotope of a model atom with a lower level ($J = 0$) and an upper level ($J = 1$). a) Shows the states of the even isotope with $I = 0$, the result is a single magnetic substate with $m_J = 0$ in the lower level and three substates with $m_J = -1, 0, 1$. b) Shows the states of the odd isotope with nuclear spin angular momentum $I = 1/2$. There are now two states, $F = 3/2, 1/2$ in the upper level ($J = 1$) whose energy is split about their mean as described by the Casmir formula (Eq. 2.56). The arrows represent the allowed dipole transitions for linearly polarized light.

is $I = 7/2$. The coupling of atomic and nuclear spins leads to eight possible states (which are non-degenerate in energy) of total angular momentum with $F_g = [19/2, 17/2, ...5/2]$and $F_e = [21/2, 19/2, ...7/2]$ where the subscripts g and e refer to the ground state and excited state, respectively. In addition, each of these levels will be composed of $2(F+1)$ magnetic substates, m_F (which are degenerate in the absence of an external electromagnetic field). This leads to 104 total substates in the ground level and 120 total substates in the first excited level. The calculated C-G coefficients for this transition are included in Appendix C.

Figure 2.9 is an atomic energy level diagram of ^{235}U showing the 8 non-degenerate angular momentum states created by the inclusion of nuclear spin in the ground and first excited levels considered in our resonance ionization scheme. The individual F states are shown along with their energy in MHz relative to the average energy of the level, and are calculated by the Casmir formula with the empirically measured constants of Schumann, *et al.*[51]. Each state of total angular momentum F will have a set of $(2F+1)$ degenerate magnetic substates and thus there are 21 unique transition energies allowed by the selection rules for linearly polarized light. Each transition will have a probability proportional to its C-G coefficient. Each unique transition energy will have a different number of substates allowed to participate depending on the degeneracy of the levels involved. The figure uses three thin arrows to show the transitions from the $13/2$ state in the ground level to the $15/2$, $13/2$ and $11/2$ states in the first excited level as an example of the set of possible transitions from a given state. The 14 substates in the $13/2$ ground state would populate only 14 of 16 substates of the $15/2$ state, all 14 substates of the $13/2$ state, and all 12 substates of the $11/2$ state when using linearly polarized light.

2.3.2.2 Even-Odd Effect

There was an unanticipated observation of the differences in ionization probabilities of even and odd isotopes discovered by early experimenters [56, 35, 57, 36], even when the laser bandwidth exceeded the hyperfine splittings of odd isotopes. The even-odd isotope ratio for Sn was modeled by Lambropoulos and Lyras [36] as a function of excitation laser power. They studied the difference in ionization probability for the two types of isotopes due to the predicted rate of ionization and the hyperfine structure coupling time of the odd isotopes. No difference in ionization probability is expected from the isotope shift or the selection rules when the transitions are saturated. Their model agrees with the experimental observations [57] of an anomalous odd- to even-mass isotope ratio in Sn due to a "dynamic effect". This makes sense because resonance ionization is a dynamic process that must be described by the detailed time evolution of the atomic system interacting with the laser field. The different ionization probabilities can be traced to the two main differences in the isotopes: (1) the increased number of states of odd isotopes, and (2) the dilution of oscillator strength which decreases the dipole matrix elements of the individual transitions in odd isotopes. The difference noted in (1) results in a different number of states that can be involved in excitation due to the change in selection rules (F instead of J) and results in a different fraction of atoms (g_2/g_1, see Eq. 2.25) that can occupy the excited state while the transition is saturated. This fractionation is also enhanced however, by differences in the ionization probability for atoms with and without nuclear spin that arises from

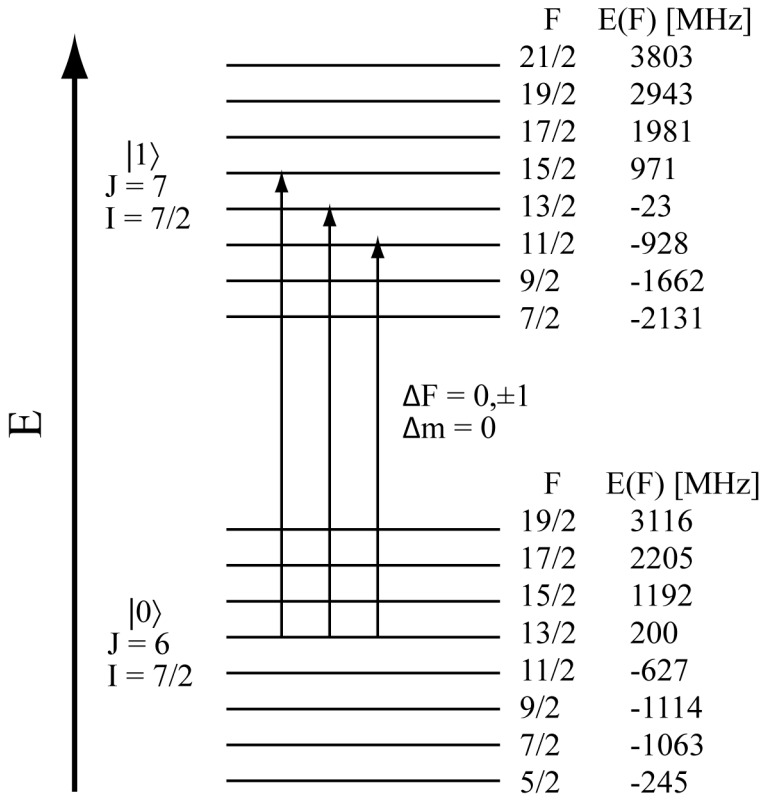

Figure 2.9: A level diagram of the first transition used in the resonant ionization of ^{235}U. The diagram shows the energy in MHz relative to the average of the 8 states within each level, the arrows show an example of the transitions allowed by the selection rules for dipole transitions. Each F state will have $2(F+1)$ degenerate substates.

changes in the discrete and continuum matrix elements produced by additional angular momentum coupling scheme needed to incorporate the presence of nuclear spin [33]. Two methods for circumventing these effects were suggested by Payne, Allman, and Parks [35]; the use of very fast excitation lasers (< 0.1 ns) or the changing the wavelength of the lasers to excite the wings of the resonances. Both methods require high fluences and cause a large increase in the probability of non-resonant ionization of undesired species. However, these dynamic effects should be minimized when all of the excitation and ionization steps are properly saturated. One must be careful then of the possibility of regions, on the edges of the ionization volume, where the transitions may be under-saturated and this dynamic effect may cause isotopic fractionation. This leads to a general rule-of-thumb for RIMS where the cross-sectional area of the laser responsible for ionization of the excited atoms is kept larger than the area of the excitation lasers to ensure that ions are created out of areas where the ionization process is saturated.

2.3.3 Summary of Isotopic Fractionation in the Ionization Process

The system of parameters required for calculating the even-odd effect in uranium isotopes is substantially more demanding than any discussed in the literature. Here we will summarize the causes and their corresponding parameters in our experiments. There are three main systematic causes of differences in ionization probability for isotope ratios measured by RIMS [58, 33]:

(1) Bandwidth and Tuning Effects − Ionization probabilities for individual isotopes will vary depending on the integrated laser irradiance over an isotope's resonance cross section. The critical laser beam parameters involved include the mean wavelength, the bandwidth, and the beam intensity. The stability in a measured isotope ratio will clearly depend on the behavior of these laser parameters as a function of time. The measured ratio of two even-massed isotopes will only experience fractionation due to these effects.

(2) Selection Rules and Polarization Effects − The difference in angular momentum quantum numbers of even and odd isotopes can lead to differences in the number of states accessible to the isotopes depending on the selection rules applicable for the polarization of the incident laser radiation. These effects are easily mitigated by an intelligent selection of the ionization scheme ($\triangle J = +1$) to ensure an equal ratio of degenerate substates are accessible for even and odd isotopes.

(3) Dynamic Effects − Volumes of ionization which are not saturated may result in fractionation of the isotope ratio because the fraction of odd isotopes in the excited states when saturated may exceed the fraction of even isotopes in the excited states [**?**]. In addition, the rates of ionization may differ due to differences in the angular momentum quantum numbers [36].

2.4 Rate Equation Description and Assumptions

Now we have covered all the aspects of resonant excitation and ionization necessary to build a description of our photon-atom system based on the rate equation approximation. In

summary we are considering three pathways for changing states in our system: (1) spontaneous decay (Γ), (2) stimulated absorption (σ_a), and (3) stimulated emission(σ_e). Here we will assume for simplicity that all spontaneous decay occurs within states considered in the system. That is the total lifetime of the state is equal to the partial lifetime due to this transition. This is a fairly safe assumption so long as we choose the states for which dipole transitions dominate the decay. This simplifies the conservation of the total number of atoms in our equations. We've discussed above the considerations necessary for calculating the cross sections for each of these pathways, including level degeneracy and the dipole transition selection rules, and have also discussed our model for calculating laser irradiance, which, for our system, we consider to be a function of wavelength and time ($I(\lambda,t)$) . Our system could be easily adapted to consider spatial effects of the laser beam profile if the atomic state populations and irradiance are described as functions of space. We have also discussed at least two pathways for ionization which have appreciable rates for our system, ionization into the continuum and ionization via a transition to an autoionizing state. With our model of the autoionizing state cross section we can treat the rate of ionization from our final bound state as a function of laser parameters in the same manner as the bound-bound transitions. We can also include the possibility of ionizing the atom from other states besides the final bound state. This simply requires the addition of a term containing the state population multiplied by a rate for the N-photon absorption process (Sec. 2.5.1) necessary to ionize from a given state that can be constrained empirically.

The rate equation approximation then will contain N equations for the rate of change of each state with terms for each allowed transition into and out of that state. From this description we can build an equation describing the rate of change of population for some state i within our system in the form

$$\frac{\mathrm{d}N_i}{\mathrm{d}t} = \text{-}N_i(\sigma_a I_{ii+1} + \sigma_e I_{ii-1} + \Gamma_i + W_{ion}) + N_{i-1}(\sigma_a I_{ii-1}) + N_{i+1}(\sigma_e I_{ii+1} + \Gamma_{i+1}) \qquad (2.58)$$

where $i+1$ and $i-1$ represent states above and below the state i, respectively, $I_{ii\pm1}$ is the irradiance of the laser that is resonant with the transition from i to $i\pm1$, and W_{ion} is the rate of ionization into the continuum by simultaneous multiphoton absorption (which we will describe next). Of course, the equations describing the ground and final states would include only the appropriate terms (*i.e.*, no term for spontaneous decay or for transitions between nonexistent states, see Sec. 5.1.1). For odd isotopes where we need to consider transitions to/from several hyperfine magnetic substates, the above equation would be expanded to consider terms of those transitions as well. Later we'll explore the ionization probabilities for uranium isotopes predicted by this description of the resonance ionization process.

2.5 Other Photoion Generating Processes to Consider

After considering the transition processes that are desired in our system (resonant excitation and ionization), we must consider that once a large number of photons are loosed upon a cloud of atomized material it is generally quite possible that other photon interactions may occur. We

are concerned only with processes that generate ions by means other than resonant excitation of the atoms selected for resonant ionization.

Before we delve into the details of non-resonant ionization processes, it is helpful to put their contribution to RIMS in perspective. The advantage of RIMS is that we don't need to predict the ionization behavior of all species within the ionization volume, but we can compare and contrast the sharp frequency response of resonant excitation with these other non-resonant processes and very easily identify their respective contributions to the total ion signal at any given mass/charge value. Thus by excluding ions which are not generated through the specific resonant process we can have confidence in the identity of resonant ions and can subtract the other "non-resonant" signal contributions if necessary.

2.5.1 Atomic Non-resonant Excitation (Multi-photon Absorption)

We first consider the possibility of absorption of more than a single photon nearly simultaneously (meaning within a time allowed by the uncertainty principle). We will explore the two-quantum excitation probability as it can easily be expanded to multi-photon processes. We begin by assuming two photon-fields whose frequencies sum in order to resonantly excite an atom, $\hbar(\omega_1+\omega_2) = E_{\text{final}} - E_{\text{intial}}$. It is possible for this process to occur with or without the presence of an intermediate state, $E_{\text{intermediate}} \sim \hbar\omega_1$ or $\hbar\omega_2$. Assume a photon-field composed of two frequencies:

$$\mathrm{E}(t) = \hat{e_1}\mathrm{E}_1\mathrm{e}^{-i\omega_1 t} + \hat{e_2}\mathrm{E}_2\mathrm{e}^{-i\omega_2 t} \tag{2.59}$$

with amplitudes E_1 and E_2, and frequencies ω_1 and ω_2. This could describe the electric field of a single laser composed of two modes, but here we will assume that these two components of the electric field are not correlated as would be the case for two independent laser cavities. Then, according to Letokhov [43], the rate for a two photon transition from i to f to occur will be defined by

$$W_{if} = \frac{\mathrm{E}_1\mathrm{E}_2\left|A_{if}\right|^2}{(\hbar^4\Gamma_f)} \tag{2.60}$$

where A_{if} is now a composite matrix element for the two photon transition, expressed as

$$A_{if} = \sum_n \left[\frac{(\hat{e}_1\vec{\mu})_{in}(\hat{e}_2\vec{\mu})_{nf}}{\omega_{ni}-\omega_1} + \frac{(\hat{e}_2\vec{\mu})_{in}(\hat{e}_1\vec{\mu})_{nf}}{\omega_{ni}-\omega_2}\right] \tag{2.61}$$

where the summation is extended over n, all the intermediate states associated with the initial and final states. From this it is clear that the probability for a two-quantum transition will be proportional to $\left[(\hat{e}\mu)^2\right]^2$. We can generalize this approach and show that the probability for N-photon transitions will depend on the square of the dipole matrix element to the Nth power. It is useful also to introduce a two-photon absorption cross section in the presence of two photon fields

$$\sigma^2(\omega_1) = \frac{32\pi^2\omega_1 I_2\hbar\omega_2}{\hbar^3c^2}g(\omega_1+\omega_2)\left|A_{if}\right|^2 \tag{2.62}$$

where I_2 is the irradiance of the second photon field and $g(\omega_1+\omega_2)$ is the normalized line-shape for the two-photon resonance. A_{if} will be proportional to the square of the dipole matrix elements.

Then, following Lambropoulos [45], the rate for a generalized N-photon absorption process can be written

$$W_{if}^{(\mathrm{N})} = \hat{\sigma}_{\mathrm{N}} \cdot I^{\mathrm{N}} \tag{2.63}$$

where $\hat{\sigma}_{\mathrm{N}}$ is the total generalized cross section given by

$$\hat{\sigma}_{\mathrm{N}} = \frac{(2\pi\alpha)^{\mathrm{N}}}{4\pi^2} \frac{\sqrt{2m_e^3 E_K}}{\hbar^2} \omega^{\mathrm{N}} \int \left| A_{if}^{(\mathrm{N})} \right|^2 \mathrm{d}\Omega_K \tag{2.64}$$

Here α is the fine structure constant ($\simeq$1/137), m_e is the electron mass, E_K represents the energy of the free photoelectron and the integral is over all directions of electron propagation. The composite matrix element is described by

$$A_{if}^{(\mathrm{N})} = \sum_{a_{\mathrm{N}-1}\cdots a_1} \frac{\left\langle f \left| A^{(\lambda)} \right| a_{\mathrm{N}-1} \right\rangle \cdots \left\langle a_2 \left| A^{(\lambda)} \right| a_1 \right\rangle \left\langle a_1 \left| A^{(\lambda)} \right| i \right\rangle}{(\omega_{a_{\mathrm{N}-1}} - \omega_i - (\mathrm{N}-1)\omega) \cdots (\omega_{a_2} - \omega_i - 2\omega)(\omega_{a_1} - \omega_i - \omega)} \tag{2.65}$$

where $A^{(\lambda)}$ is the matrix element for the transition between two states due to a photon of wavelength λ, and the final state f must be described by the methods discussed above (Eq. 2.54) for dealing with continuum states.

In summary, the multiphoton excitation rate is strongly dependent on the presence of the excited states in the atom summed over the bound and continuum states, and is always dominated by the contribution from the nearest resonance to the photon energy. But we can expect multiphoton processes to show a rate dependence of I^{N} where N is the order of the number of photons necessary for the transition. This power law dependence will be helpful later in identifying multi-photon absorption processes in our experiments.

2.5.2 Molecular Excitation

Multi-photon ionization of molecules, which may be present in the cloud of desorbed material, is another source of ions that could represent interferences in our measurements. The excitation and ionization of molecules is more complex than the situation for atoms for several reasons: (1) the density of excited states in molecules containing many atoms can be extremely high owing to the increased degrees of freedom (rotational and vibrational), and (2) molecules can undergo photodissociation to produce a mixture of fragments that may undergo further interactions with the photon field. In general, when discussing the excitation of molecules, it is necessary to consider rotational and vibrational modes of excitation. The high density of molecular excited states due to these additional excitation modes create "bands" of states on top of the discrete excitation of electrons. These bands of states make it much easier to excite molecules. These excited molecules can then disassociate to produce ions or ions and neutrals that continue to interact with the laser field. And although the typical cross section for molecular electronic

excitation is smaller than the atomic cross section, the presence of the bands of vibrational and rotational states makes the excitation of molecules generally less sensitive to wavelength. This also serves to make the ionization of molecules less selective than atoms.

Its impractical to try and predict the behavior of all possible molecular species, but that is not necessary when using RIMS due to the highly selective nature of the resonance ionization. Although a given resonance ionization scheme may produce ions from molecules present in the desorbed cloud, the fact that the resonant ions of the target element will be highly sensitive to wavelength allows for discrimination against potentially interfering species.

The dependence of ionization probability for simultaneous multi-photon absorption in atoms and molecules on the order of the number of photons involved is an important consideration for the selection of ionization schemes. The use of *excessive* power densities well-above those required to produce saturation of a resonance transition produces a relatively small increase in ionization probability (due to power broadening or an increase in saturated portion of the ionization volume), but may produce a marked increase in multi-photon ionization of other elements or molecules that have not been selected for ionization. Ideally, to minimize the non-resonant ionization of atoms and molecules, resonant ionization schemes would use a large number of low-energy photons. Under such conditions many photons have to be absorbed nearly simultaneously for non-resonant ionization, but each discrete step of the resonant ionization process could still have a high probability of being saturated. For example, increasing the number of photons required to be absorbed from 2 to 3 decreases the yield of non-resonant ionization while maintaining the possibility of 100 % resonant ionization yield as shown in Sec. 4.4.

2.6 Mass Spectrometry

Now that the excitation and ionization processes involved in RIMS have been outlined, the other half of RIMS is the mass spectrometry. There was no development of existing mass spectrometric methods in this work and we will explore the specific implementation in sufficient detail in the next chapter, but we will take the opportunity to discuss some of the fundamental principles involved in order to set the stage for the experimental details. Once the ions have been created, we wish to identify the mass (or more specifically the mass/charge ratio) of the ions in order to determine the relative abundance of different isotopes of the same element initially in the target.

2.6.1 Time-of-Flight Mass Spectrometry

The principles of time-of-flight mass spectrometry (TOF-MS) are relatively simple. An ion experiences a force due to an electric potential that can be described by $F = qV$, where q is the integral number of electric charges and V is the potential, and which accelerates ions to a velocity given by $\mathrm{v} = (2qV/m)^{1/2}$, where m is mass. It is immediately obvious that two ions with equal charge but $m_1 \neq m_2$, will attain different velocities when accelerated through the same potential. If these ions are allowed to drift through field-free space they will become separated

in space and could be distinguished by the time at which they arrive at some distance L from the initial position. In fact, with well-defined potentials and a well-known distance L the mass-to-charge ratio can be determined quite precisely given sufficient time resolution ($\frac{m}{q} = \frac{2V}{L^2}t^2$). The advantages of TOF-MS for our application include the experimental simplicity of the technique and the ability to collect a large mass range of ions simultaneously. The disadvantages of TOF include relatively poor mass resolution compared to modern magnetic sector instruments as will be further discussed later in the context of ideal instrumental design. A specific challenge for TOF-MS in RIMS applications is the fact that ions will not only have some initial spread in velocity due to the atomization process but also because the atoms are ionized from within a volume in space. Ions created at different locations will experience different accelerating potentials. Both effects combine to produce a significant spread in ion arrival time at the location of the detector surface.

2.6.2 Ion Sputtering

Ion sputtering covers a wide range of studies of the interactions of charged particles with solid surfaces. We will be brief and qualitative in our description of the complexities involved in this phenomena. Ion sputtering involves bombarding a target surface with ions accelerated to a desired kinetic energy. When an energetic ion (25 keV Ga^+ for our experiments) strikes a surface, collisions with the atoms of the solid begins with several primary collisions of the incident ion with atoms near the surface of the material. The majority of these primary collisions produce atoms with kinetic energies large compared to their binding energies, and are either ejected from the surface or undergo further collisions with neighboring atoms. The latter lead to a cascade of collisions that produce energized atoms and result in the ejection of several secondary particles from the solid, including atoms, ions, molecules, and electrons usually from the top few atomic layers (depending on the momentum of the primary ion). As a general rule the majority of the secondary species are neutral although the relative yields of ions and neutrals are a function of the bulk solid, the bombarding species, the oxidation state of the solid, and the secondary element or molecule considered. Characterizing the exact secondary neutral yield is of course challenging because the atoms cannot be directly manipulated via electromagnetic fields and must be ionized post-sputtering. Often ion yields are less than 1 % of total material removed, except for the alkali elements for which ion yields can exceed 10 %. This means that the remaining fraction of ejected particles is largely neutral, although this group may contain molecules and excited atoms unfit for resonance ionization.

This collision-cascade model for ion sputtering has been verified experimentally and results in distributions of secondary particle energies which are not well-described by a Maxwell-Boltzmann distribution. In fact, the velocity distribution of sputtered material is best characterized by a large almost Gaussian peak at low energy with a very long high-energy tail. The most probable energy for sputtered species is between 2−4 eV, but the distribution is usually best fit with a function $E/(E+E_S)^3$ where E_S is the surface binding energy [59]. Related to our experimental conditions, Lama, *et al.* [60] explored the sputtering of UO_2 using 5−20 keV Ar^+ ions. They show that the angular distribution of uranium atoms ejected from the target is

well-described by a cosine distribution, and that the velocity distribution of uranium from the target is best described by a function that includes two types of binding energy for the atoms, surface (E_S) and bulk (E_B) binding energies. They found that the distribution was best described by a function of the form

$$f(E) = \frac{E}{(E + E_B + E_S)(E + E_S)^2} \tag{2.66}$$

where E_S was around 1.25 eV for all incident ion energies and the bulk binding energy was strongly a function of incident ion energy and varied between 3 and 30 eV. This distribution means that our prediction of a simple Gaussian form of the Doppler broadening will not accurately match the distribution of velocities in the sputtered flux. However, because the majority of species are centered around the low energy peak and the Doppler broadening is proportional to $\sqrt{T}$, we can get an estimate of the Doppler spectral broadening of the resonances corresponding to a temperature of approximately three times the boiling temperature of the solid, which is consistent with empirical observations.

Sputtering has the possibility of causing small isotopic fractionation in the measured isotope ratios [61, 62], but is always associated with the relative mass difference of the measured species or to a smaller extent the specifics of the interaction between the primary beam and the solid (ion energy, matrix effects). Within a set of given experimental conditions, and apart from matrix differences between a standard and unknown samples, the fractionation will be systematic and constant. Thus when comparing measured U isotope ratios to a known standard, correction for these fractionation effects would be included.

Previous studies of multiphoton ionization of uranium oxide species by thermal vaporization [29]and ion sputtering [31] caused concern about the yield of U neutral atoms useful for RIMS from UO_X matrices. Goeringer, *et al.* studied the relative yields of U^+ secondary and resonance ions using Ar^+ ion sputtering (14.5 keV) of uranium metal and oxides and observed that the sputtered neutral atom yield depended strongly on the sample matrix composition. They found that the sputter yield of U atoms ejected from U metal for Ar^+, O_2^+, N_2^+ beams were 5.3, 0.50, and 0.67 U atoms per incident primary ion respectively. The relatively high sputter yield from argon is as expected considering the relative masses of the incident species [31]. They report a sputter yield of 2 ± 0.5 U atoms/primary ion for Ar^+ on UO_2. Compared with sputtering from the metal this is within experimental error of the difference expected from the stoichiometries of the targets. They report the fraction of material removed as neutral U atoms and neutral UO molecules from U metal and UO_2 targets. When U metal was the target, the ratio of neutral-atoms-to-neutral-molecules was 81 ± 23. When the target was UO_2 the ratio was 0.062 ± 0.018. Comparing the results from the two substrates shows that the yield of neutral U is reduced by a factor of 44 ± 20 when going from metal to UO_2. They estimate that the relative fraction of neutral U atoms sputtered from U metal is 84 % of the total material ejected. The estimated secondary U^+ yield for these conditions is 2.8×10^{-2} %. They did not, however, observe any U photoions above background levels on a U_3O_8 target. This finding is inconsistent with experimental measurements reported in the present work (see Sec. 4.12). It is important to note that they were performing this measurement using an inefficient single-wavelength three-photon ionization scheme and although they acknowledge the presence of non-resonant background,

they do not state how they discriminated against the background from the photoion signal in their analog detection scheme. This might explain their negative result on U_3O_8.

2.6.3 Laser Physics

We have already addressed some aspects of the nature of laser light and we will examine in the next chapter how we generate our laser pulses, but first we will draw out a few basic principles involved in laser beam generation. This will be a greatly simplified discussion of the complicated and complex interplay of geometric, atomic, and quantum processes that determine the behavior and character of lasers cavities and interested readers should refer to other references [34, 63, 64]for more substantive descriptions.

If we consider an optical cavity consisting of two highly reflective mirrors with cross sectional area A, open to air, and separated by some length d, as depicted in Fig. 2.10, then picture the introduction of a bright flash of light from a point source in the center of the cavity. The light would reflect from both mirrors in the cavity, and most of the light intensity would be lost after only a few reflections. However, some of the light could establish standing waves in the cavity. These standing waves or modes of oscillation of the cavity would by definition have very low loss of light during the transit across the cavity. The standing waves are called Longitudinal modes are defined by the dimensions of the cavity. They have a frequency given by $\nu_n = \frac{n \cdot c}{2d}$, where n is the number of nodes in the cavity at frequency ν and a wavelength $\lambda_n = \frac{2d}{n}$. A cavity of this sort will have a number of modes in the frequency integral ν to $\nu + \mathrm{d}\nu$ of $8\pi\nu^2 \cdot Ad \cdot \frac{\delta}{c^3}$ [34]. Transverse modes of the cavity are composed of different field configurations across the cavity mirror surface. For a given transverse mode there exist several longitudinal modes which are all equally spaced in frequency, with their spacing being inversely proportional to the separation of the mirrors. For a given longitudinal mode, the different transverse modes will have different frequencies and losses. In addition to this simple geometric consideration of wave formation, one must consider loss of light due to diffraction which can be understood by considering the Fresnel number of the cavity, $N = (A/\lambda d)$, which is a measure of the energy visible at the opposing mirror due to the diffraction pattern of light from the reflecting mirror. The larger the Fresnel number the smaller the losses from diffraction. A linewidth of this "passive" optical cavity can be defined $\triangle\nu_C = \frac{fc}{2\pi d}$, where f is the round-trip loss of power in the cavity, and the coherence time of such a cavity is just the inverse linewidth $\tau_c = 2\pi d/fc$ [34]. Now if we introduce into this cavity an "active" medium as an energy source for the light field, then we've already explored the processes which can contribute to the building up of power in the cavity in our discussion of the Einstein coefficients. We can quickly define a net gain in intensity in a given mode ν by traveling a distance z through an active medium as

$$\frac{\delta I_\nu}{\delta z} = (B_{21}N_2 - B_{12}N_1) \cdot g(\nu) \cdot \frac{I_\nu}{c} \cdot h\nu \tag{2.67}$$

where we have again used our two-states $|1\rangle$ and $|2\rangle$. In order for the medium to actually gain energy it is necessary that $N_2 > \frac{g_2}{g_1}N_1$. But it is well known that for materials in thermal

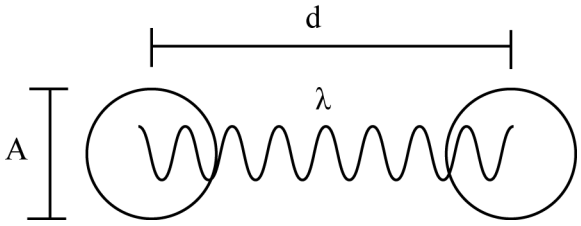

Figure 2.10: Passive Laser Cavity. The cavity is composed of two highly reflective mirrors with cross sectional area A separated by a distance d, will create standing waves of wavelength $\lambda = 2d/n$ where n is the number of nodes in the wave.

equilibrium this is never the case. This requires that energy be pumped into the active medium that preferentially builds up a population inversion (where the medium is mostly in the upper excited state $|2\rangle$) and results in a threshold condition for the oscillation of a particular transverse mode in the active cavity:

$$\frac{A_{mn}c^2}{8\pi\nu^2}\left[N_m - \frac{g_m}{g_n}N_n\right]g(\nu) \geq \frac{f}{d}\,\text{or}\,\frac{2\pi\nu_q}{Q} \tag{2.68}$$

where Q is the quality factor of the cavity ($Q = 2\pi d\frac{\nu}{fc}$). We can summarize the system of interaction of a passive cavity containing some volume of active medium in a few simple steps:

(1) The passive cavity behaves as a filter by propagating and reflecting the light between two end mirrors, this imparts spatial coherence to the light.

(2) Repeated reflection between the mirrors means that only very low loss modes will retain energy in the active medium volume, which supports the stimulated emission of these few modes.

(3) After a population inversion is created, then stimulated emission exceeds absorption and preferentially feeds energy coherently into cavity modes.

(4) The population inversion must be large enough for the gain to overcome cavity losses so that radiation energy will build in that mode. The threshold condition is defined as the point where energy gain and loss in the cavity are identical.

We must also include the fact that spontaneous decay will add energy to the modes of the cavity. This spontaneous emission is what helps define the bandwidth of the laser cavity because it introduces radiation that is random with respect to the phase and amplitude of the modes. Therefore the balance of power must be modified to read,

$$\{Gain\,of\,Active\,Medium - Spontaneous\,Decay\} = Cavity\,Loss$$

Then,

$$Gain - Loss \propto \frac{1}{Q}$$

From this view of the cavity quality factor Q, Schawlow and Townes [65] were able to build an

estimate of the spectral width (bandwidth) of an active cavity from

$$\triangle \nu_L = \frac{8\pi(\triangle \nu_c)^2 \cdot h\nu}{P} \tag{2.69}$$

where $\triangle \nu_c$ is the linewidth of the passive cavity and P is the coherent power out of the cavity. This defines two parameters that influence the bandwidth of the light emanating from a laser, which will be essential in our experiments for stably increasing the laser bandwidth used for the resonance ionization of uranium. Although, the bandwidth of the laser beams produced by the active cavities used in this work are primarily determined by other factors, which will be described in the next chapter.

One additional consideration, is important to understanding the bandwidth of one of the laser beams used in the ionization scheme used in this work. At least one laser must be frequency-doubled using second harmonic generation with an LBO crystal (see Chapter 3). Using perturbation theory to examine the non-linear polarization of an anisotropic dielectric material to generate second-harmonic frequencies, it can be shown that the electric field of the second-harmonic beam is proportional to the square of the electric field of the fundamental beam [64]. Therefore the bandwidth of the second-harmonic beam ($\triangle \nu_2$), when expressed in units of frequency, will be twice the frequency of the fundamental beam ($\triangle \nu_1$) divided by the square root of two[5].

$$\triangle \nu_2 = 2 \triangle \nu_1 / \sqrt{2} \tag{2.70}$$

The square root of two comes from the dependence on the squared electric field intensity and the factor of two comes from changing frequency scales.

[5]This can be proved using a normalized Gaussian centered around $x = 10$ with a FWHM of 4 ($\triangle \nu_1$, maximum value 1 for the function at $x = 10$ and value $y = 0.5$ at $x = 8$ and 12). The values are doubled in frequency, the result is a Gaussian centered on $x = 20$ with the y values of the function obtained by squaring the amplitude (*e.g.* $y = 0.25$ when $x = 16$ and 24). Then $y = 1/2$ is right around $x = 17.2$ and 22.8 yielding a FWHM of 5.6 ($\triangle \nu_2$).

Chapter 3

Experimental Setup and Methods

Our experiments utilized facilities in the Materials Science Division at Argonne National Laboratory including an instrument known as CHARISMA (CHicago-Argonne Resonant Ionization Spectrometry for Micro-Analysis)[24, 13] that will be described below. The instrumental setup is outlined, including the details of the laser cavities used for the excitation and ionization[1] of the isotopes of interest here. We then describe the resonance ionization schemes explored in this work, the details of data collection and analysis, and the standard materials used as uranium isotope references.

3.1 CHARISMA

CHARISMA is a Time-of-Flight (TOF) Laser Post-Ionization mass spectrometer designed for surface analysis of solid samples. It is equipped with both primary ion sputtering and laser desorption capabilities for sample atomization. It can detect either laser-ionized secondary neutral atoms or secondary ions desorbed from a material. Ions are mass separated using a 4-m flight-path reflectron-type TOF mass spectrometer and are detected by time-of-arrival using micro-channel plates.

3.1.1 Design Overview

All mass spectrometers consist of four basic system components, an atomizer, an ionizer, a mass filter, and a data collection system. Many implementations of mass spectrometry combine the functions of atomization and ionization into a single component, but RIMS requires a separate component for the photo-ionization of neutral species post-atomization. A simple schematic of the system components in CHARISMA and their functional relationships are shown in Figure 3.1, which includes a target chamber for sample atomization, a laser system for the ionization of neutrals generated in the target chamber, a mass spectrometer for mass filtering of the ions, and instrument control and data acquisition. The basic sequence of events for a measurement in our system begins with atomizing a portion of a solid sample in the target chamber. The laser system produces photons for ionizing specific desorbed atoms within the target chamber. The ions are then extracted into the mass spectrometer and detected as a function of flight time. The signals generated by the interaction of ions with the detector are sorted by flight time and stored as ion counts in the data acquisition computer. The computer also regulates the relative timing of system components and voltages within the instrument. This sequence of events is considered one cycle of the system. Normal operational conditions for CHARISMA are for each component of the instrument to operate together to perform 1000 cycles per second. We will begin describing each major component of Fig. 3.1 with the laser

[1] We commonly use the term "ionization lasers" to refer to all three lasers used for resonance ionization (typically two for excitation to bound states and a third for the excitation of an autoionizing resonance). If we use the term "ionizing laser" we mean the specific laser in our scheme responsible for the final step of exciting the energized atoms into ions.

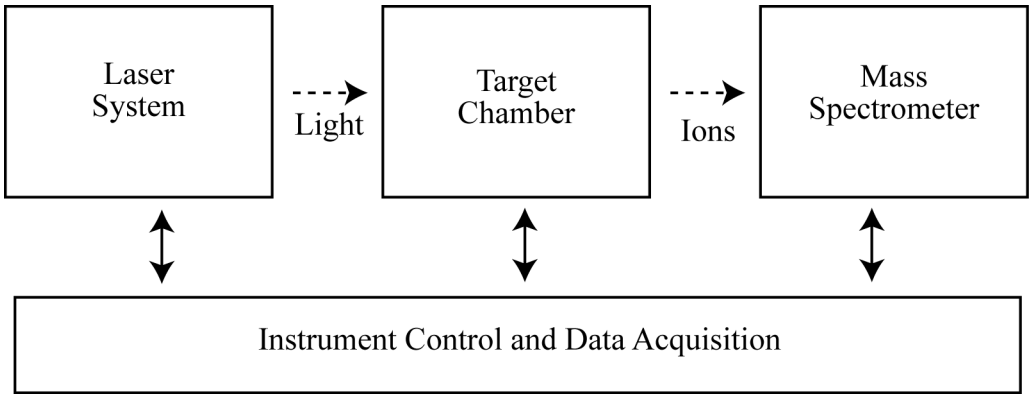

Figure 3.1: Instrument Overview. The four major components of our instrument. The laser system produces photons for ionizing specific atoms desorbed from a target within the target chamber. These ions are then accelerated into the mass spectrometer for detection and the time-of-flight of individual ions is converted into a digital signal recorded by a computer that also regulates instrument voltages and timing.

system because it is the most significant component related to our present work and then proceed to describe the form and function of the other three system components. We will finish the description of CHARISMA with a discussion of the relative timing of the system components (see Sec. 3.1.5.1).

3.1.2 Laser System

The body of the laser system is composed of three nearly identical sets of laser pairs. Each pair consists of a commercial neodymium-doped yttrium lithium fluoride laser (Nd:YLF, $LiYF_4$ crystal doped with Nd) used to pump a tunable titanium-doped sapphire laser cavity (Ti:Sapph, Al_2O_3 crystal doped with Ti). A schematic of the laser system is given in Figure 3.2. The figure shows the three pairs of lasers in the center of the diagram, with a personal computer to the left. The computer receives wavelength measurements from a multichannel wavelength meter (shown at bottom) and can automatically adjust the Ti:Sapph cavities to maintain a specified wavelength. Pickup lenses (squares) focus a small portion of the laser beam onto the end of fiber optic cables connected to the wavelength meter. The LabSmith controller at the top of the diagram is responsible for maintaining the laser pulse times relative to the rest of the instrument ("system clock") by observing the pulses on photodiodes (circles) near the laser beam paths and adjusting the start time of the pump laser flash lamps to ensure the laser pulses arrive at the target chamber synchronized in time (see Sec. 3.1.5.3). The laser beams propagate through air to the target chamber using several steering mirrors. Laser beam power is measured by inserting a power meter (GenTec SOLO 2 meter with a UP19K-110F-H9 head) into the beam path just outside the target chamber after all of the steering optics. Laser beam position and shape can be measured by temporarily inserting a prism (triangle) into the beam path to divert the light

to a beam analyzer at a distance equal to the center of the ionization volume. Measuring the beam shape at a position equidistant to the ionization volume ensures that we know the beam shape in the ionization volume. Together, this system provides the photons for ionization and the capability to monitor all of the essential parameters of laser performance: mean wavelength, bandwidth, power, position, spatial distribution, and time distribution. It is important to note here, that the success of RIMS for measuring isotope ratios depends critically on the reproducibility of these parameters over the course of measurements, which is precisely what we have explored in this work.

3.1.2.1 Tunable Laser Pairs

During these experiments, CHARISMA was equipped with access to a total of four laser pairs to produce our tunable laser light. Although we never used more than three pairs simultaneously, all of these systems were utilized at different times in our investigation. The concept of the tunable laser pairs is to use the frequency-doubled output of a commercial Nd:YLF cavity to pump energy into the tunable Ti:Sapph cavities. Three of the "pump" lasers are identical Photonics Industries model GM30-527 P/S lasers. Although the design and specifications for these pump lasers are identical, in practice they have slightly different performance characteristics, such as pulse energy, pulse length, and transverse mode structure. These differences are due to physical differences in the components and cavity alignments, which in turn are evidenced in some of the performance parameters of the Ti:Sapph cavities. The fourth commercial Nd:YLF is a Quantronix Model 527DP-H. Each of these pump lasers operates at a repetition rate of 1 kHz to produce approximately 20 mJ of second-harmonic light at 527 nm (1054 nm fundamental) with nominal pulse lengths of 200 - 250 ns.

3.1.2.2 Ti:Sapph Cavities

The tunable laser cavities are custom-built Ti:Sapphire systems, an example of which is shown schematically in Figure 3.3. Two of the four are Photonics Industries model TU-TR-S1/UV-S2 cavities, the other two were built in-house. Each Ti:Sapph cavity is independently tunable over the wavelength range from 700 to 1000 nm via a gold-coated grating that functions as the end mirror. The cavities use a simple box design with two turning mirrors (used as entrance and exit for pump light), a Ti:Sapph crystal (the lasing medium), a partially reflective output coupler that allows coherent light to leak out of the cavity in the desired direction, a beam expander, and a reflective diffraction grating. Each cavity is arranged in a configuration to prevent the Nd:YLF pump energy from heating the grating, which would broaden the output linewidth and cause wavelength instabilities. This configuration also allows for reflection and refocusing of the Nd:YLF pump beam back into the Ti:Sapph crystal via the return mirror to boost the power output. Nominally, a four-prism beam expander with a magnification of 40 is used to illuminate a large number of lines on the grating, thereby narrowing the output linewidth. The grating is secured on a rotational mount that turns in the horizontal plane of the cavity. The wavelength of the cavity is selected based on the angle of the diffraction grating relative to the

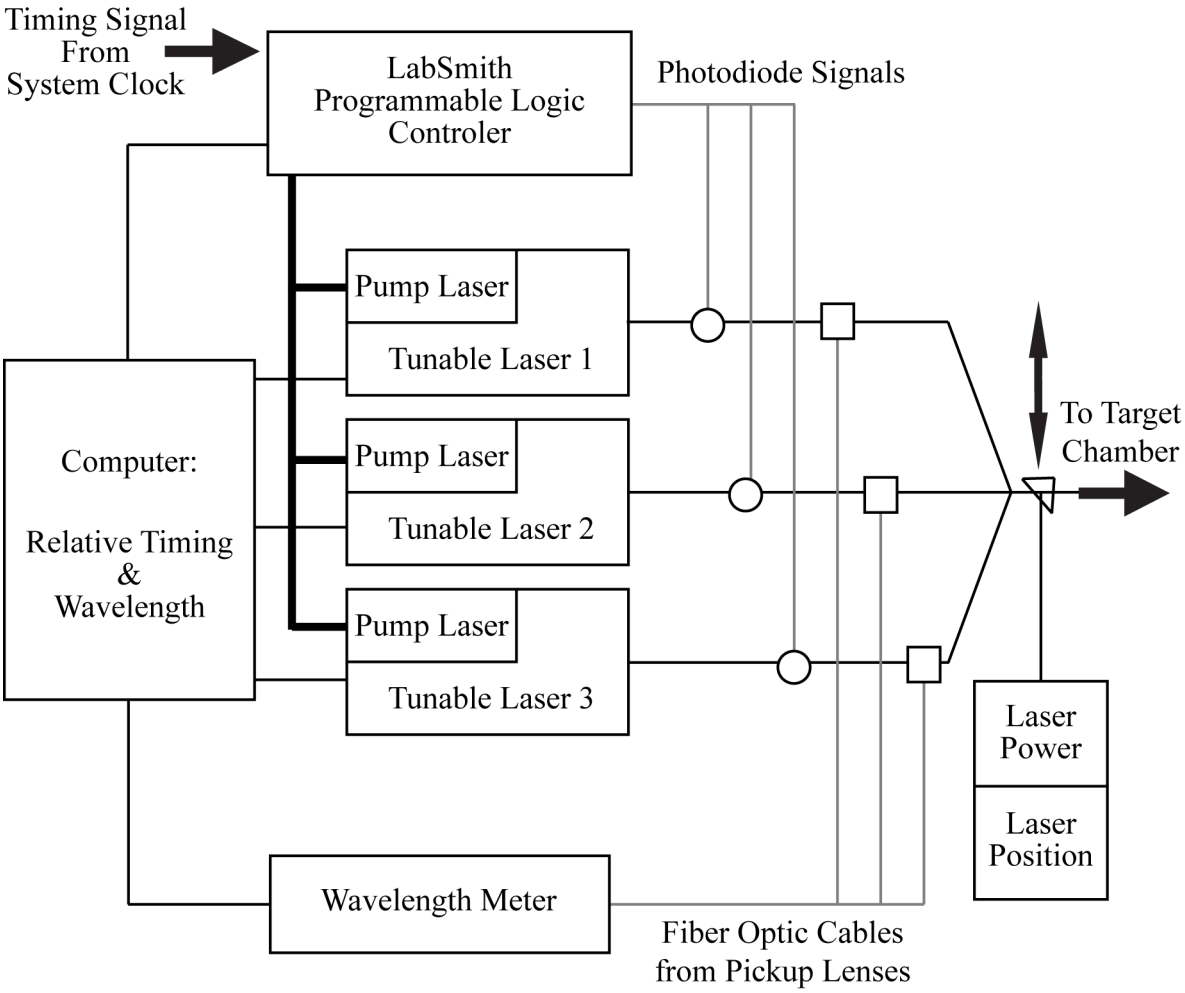

Figure 3.2: Laser system overview. The three laser pairs are shown in the center, a computer (left) controls wavelength with input from the wavelength meter (bottom), timing is set relative to the instrument system clock and monitored by the logic controller (top) which observes laser pulses on photodiodes (○), and adjusts the relative timing of the pump laser pulses according to settings from the computer. Pickup lenses (□) focus a portion of the laser beam onto fiber optic cables connected to the wavelength meter. Laser beam power and position are measured independently just prior to entering the target chamber.

incident light output from the beam expander. The wavelength of the cavity is determined by the positive interference of the first-order reflection from the grating, $\lambda = d[\sin(\theta_m - \theta_i)]$, where λ is the wavelength, d is the spacing between lines on the grating (1800 lines/mm for our grating), θ_m and θ_i are the angles of maximum interference and the incident light relative to the grating surface, respectively. At a pump energy of 20 mJ, each cavity produces 1 mJ of infrared light in a 20 ns pulse with a $\sim$1.5 GHz linewidth.

The second-harmonic (2ω) of the Ti:Sapph fundamental beam is produced in a nonlinear optical crystal as shown schematically in Figure 3.3. The fundamental beam is incident on a 20 mm-thick lithium triborate (LBO) crystal located just outside of the cavity. The laser beam contains both the second-harmonic and the residual fundamental wavelengths on exit from the LBO crystal, which propagate along slightly different optical paths. If only the second-harmonic beam is required, it is separated from the fundamental beam using a dichroic mirror in the position of the first mirror that steers the laser beam towards the target chamber. The plane of polarization of the second-harmonic beam is rotated 90° with respect to the fundamental on exit from the LBO crystal, so a half-wave plate can be used to correct the polarization. The overall conversion efficiency from the fundamental is on the order of 30 % for the second-harmonic, resulting in a typical maximum energy per pulse of $\simeq 0.3$ mJ of second-harmonic light. Each laser beam is then collimated and shaped separately before entering the target chamber using cylindrical lenses. If it is necessary to control the power of a particular beam, a gradated neutral density filter is inserted in the beam line which allows essentially continuous *laser beam* power selection while continuing to operate the *laser cavity* at full power. This helps minimize pulse-to-pulse fluctuations in energy and mean wavelength.

Figure 3.4 is a photograph of one of the Ti:Sapph cavities that helps visualize the physical layout. The green light is the second harmonic light from the pump laser incident on the Ti:Sapph crystal from the left, the four mirrors of the cavity (unlabeled) are held in the black mounts with circular holes surrounding the Ti:Sapph crystal. Fluorescence is emitted from the crystal and reflects from the cavity mirrors. The only light retained in the cavity is in low-loss standing waves. These modes are preferentially supported by the stimulated emission of the crystal. The wavelength of these modes is determined by the angle of the diffraction grating relative to the light output from the beam expander and the bandwidth of the laser cavity is dominantly determined by the number of lines illuminated on the grating by the beam expander. The grating motor is used to change the angle of the grating by driving the rotational stage on which the grating is mounted (see Sec. 3.1.5.2). A photodiode is used to monitor the time distribution of laser light in the cavity (Sec. 3.1.5.1).

Cavity Bandwidth As discussed above the tunable cavities using the four-prism beam expander nominally produce laser beams with bandwidths in the fundamental range of 1.3 GHz[2]. These beam expanders (made by Photonics, Inc.) produce a magnification of a factor of 40 in the horizontal direction. For our cavities a $\sim$0.5 mm beam spreads out to $\sim$2 cm on the grating.

[2] 1.3 GHz is 3 pm at 830 nm and 2.2 pm at 722 nm. When a beam from this arrangement is frequency-doubled into the 415 nm range the result is a bandwidth of 1.8 GHz or about 1 pm.

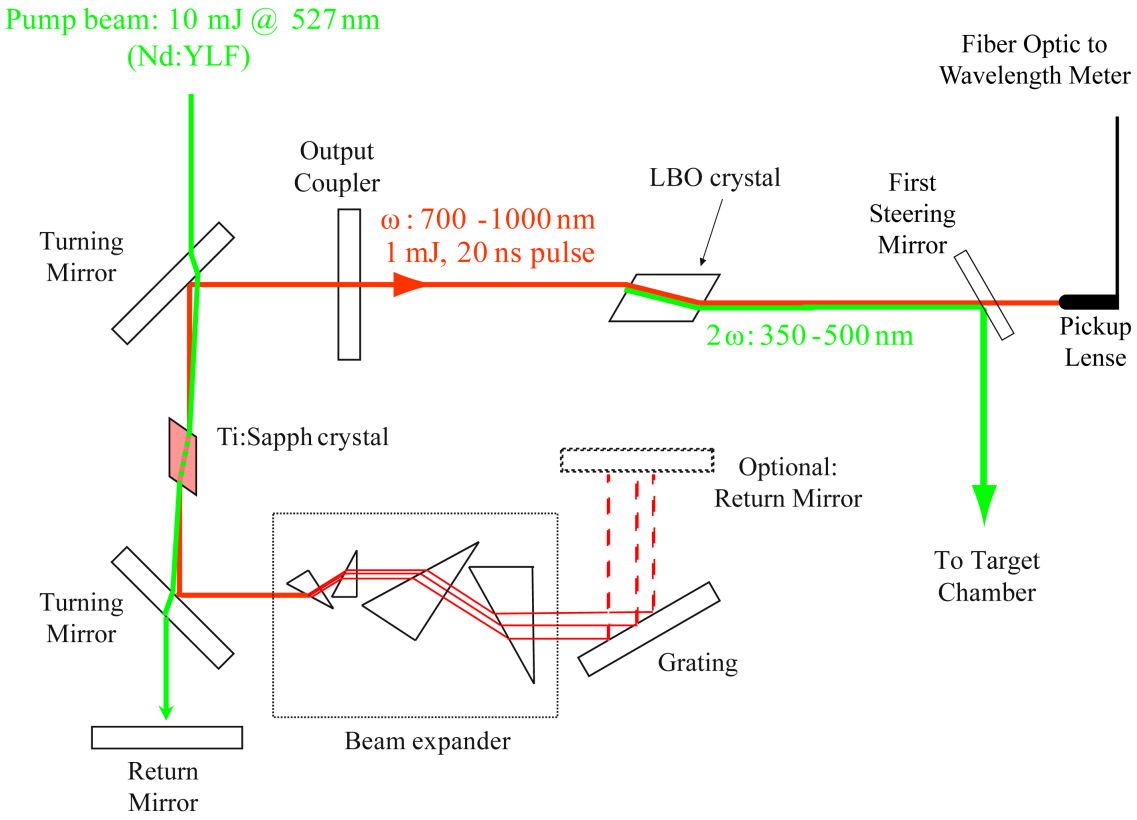

Figure 3.3: Tunable Ti:Sapphire cavity diagram. The cavity is made up of two turning mirrors, a Ti:Sapph crystal, an output coupler, a beam expander, and a diffraction grating. The pump laser beam (527 nm), incident from the top, is directed through the center of the Ti:Sapph crystal and is transmitted through the turning mirrors. The pump beam passes through the Ti:Sapph crystal a second time after reflecting from the return mirror placed just past the second turning mirror. The Ti:Sapph crystal fluoresces and light emitted into the standing-wave modes of the cavity is reflected back into the crystal to generate stimulated emission into that mode. The light is filtered by the cavity, and the mean wavelength is determined by the angle of the grating with a bandwidth defined by the number of lines illuminated on the grating. The bandwidth can be changed by adjusting the magnifying power of the beam expander prisms. To increase wavelength stability and decrease bandwidth, an optional mirror to return the zeroth-order reflection from the grating can be inserted. Coherent laser power is lost through the output coupler (partially-reflective mirror) and can be passed into a LBO crystal for frequency doubling (2ω). The first steering mirror turns the second-harmonic light towards the target chamber while allowing the fundamental beam to pass through for wavelength measurement. A pickup lens focuses the laser light passed through the first steering mirror onto a fiber optic cable connected to the wavelength meter.

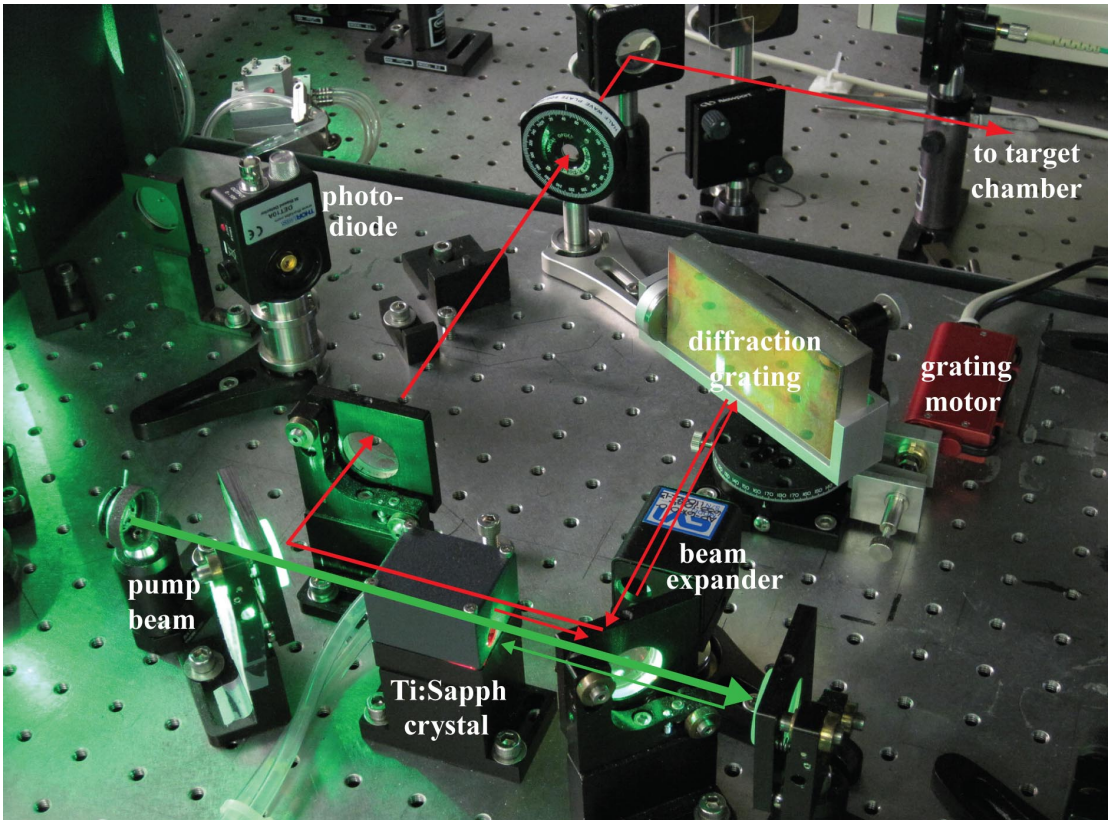

Figure 3.4: A photograph of a tunable Ti:Sapph cavity. The pump beam (green) is incident from the left and passes through the Ti:Sapph crystal before being reflected from the return mirror (bottom right) to pass through a second time. The fluorescence of the crystal is emitted into the modes of the cavity and power is preferentially built up in the lowest loss mode (red), which is determined by the angle of the diffraction grating. The beam expander spreads the cavity light onto the diffraction grating, and the grating motor is used to drive the rotational mount of the grating for angle tuning. For scale, the threaded holes on the laser table are separated by 1 inch.

The wavelength of the cavity is determined by what can be thought of as the interference of a number of point sources in the plane of the diffraction grating. The more lines of the grating illuminated by the light (the more point sources) the better defined the wavelength becomes (*i.e.,* the bandwidth is reduced). We studied the effect of altering the bandwidth of the ionization lasers. We employed beam expanders with different magnification factors to create laser beams with broader bandwidths than produced by using the 40X expander. We used 2X, 4X, and 6X expanders (made by CVI) in several different combinations of total magnification. With a 2X beam expander the pulses were often very asymmetric, one mode of the laser cavity would tend to contain most of the intensity in a pulse but a few neighboring modes would have non-negligible intensity and the mean wavelength could vary widely from pulse to pulse. The 4X expander produced the smallest magnification with which we were able to generate a "stable" laser oscillation in the cavities, meaning that the pulse energy and wavelength were reproducible over a large number of laser pulses. With only a single 4X beam expander in the laser cavity we generated a laser bandwidth of 6 – 10 GHz, or 14 pm for wavelengths near 830 nm. When frequency doubled, the bandwidth of this arrangement was in the range 9 – 13 GHz or about 5 pm.

Next, we will more closely describe the laser spectral distribution we were able to generate using the 40X, 6X, and 4X beam expanders and the reproducibility of wavelength from pulse-to-pulse. We will use the terms "narrow" bandwidth to describe pulses generated with the 40X magnification and "broad" bandwidth for the 6X and 4X.

3.1.2.3 Wavelength Determination and Spectral Distribution

Laser wavelengths were measured using a wavelength meter based on Fizeau interferometers (either a HighFinesse-Ångstrom model WS-7 or WS-6 wavelength meter). The wavemeters are capable of measurements to a relative accuracy of one part in 10^7 (*i.e.,* < 0.0005 nm at the wavelengths used in this study). Wavelengths were recorded as single-pulse snapshots of mean wavelength with multi-pulse averaging possible. The wave-meters provide two modes of reported wavelength precision, "fine" or "wide". The "wide" mode reduces by one (from 7 to 6 for the WS-7) the number of interferometers used in defining the laser distribution. The accuracy of the wavelength meter is determined by the length of the longest interferometer inside the unit. The longer the interferometer, the smaller the allowed spectral width of the laser. If the laser is broader than the "free spectral range" of the interferometer, the interferences vanish and no signal is analyzed. The free spectral range is defined as the distance in frequency between the maxima of two neighboring modes of the interferometer. For simple cavities, the free spectral range is expressed as $\triangle \nu_{FSR} = c/2L$, where c is the speed of light and L is the length of the interferometer. In the "wide" measurement mode, the longest interferometer is ignored for the calculation. The WS-7 in wide mode is able to measure beams with a maximum spectral width of 15 GHz (34 pm at 830 nm). In fine mode, lasers with a spectral width of < 4 GHz may be measured (9.2 pm at 830 nm). The accuracy of the mean wavelength measurement can be a factor of only 3 – 5 better than the laser beam spectral width. If the width of the laser beam is 10 GHz broad (22 pm at 830 nm), the accuracy in mean wavelength is roughly 2 GHz (4.5 pm at

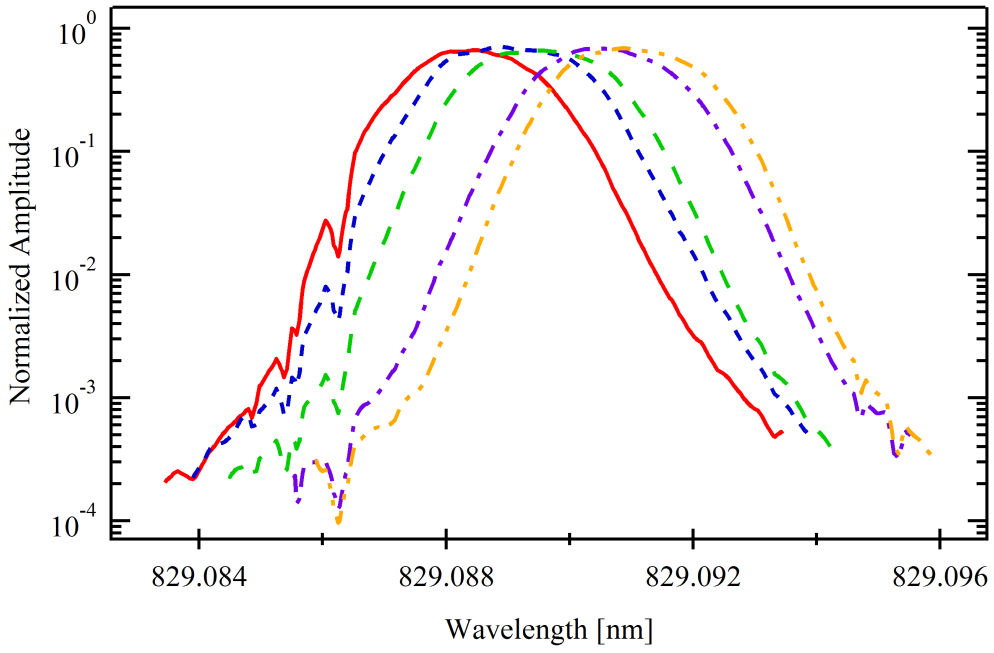

Figure 3.5: Distribution in wavelength of 5 laser pulses from narrow bandwidth cavity (40X) as measured by the WS-7 in fine mode. Note that the deviations from a smooth distribution appear at the same wavelength.

830 nm).

The wavemeters report the central wavelength and bandwidth determined from a Gaussian fit to the measured laser pulse. They can also display and record a spectral distribution as a function of wavelength for one laser at a time. The wavelengths and bandwidths for each laser may be continuously monitored and later output as a file containing measurement time, wavelength, and linewidth. The meters may be paused to collect, observe, and save individual laser pulses. Figure 3.5 shows the wavelength distribution of five laser pulses captured individually with the WS-7 in fine mode produced by the narrow bandwidth laser configuration (40X magnification). The WS-7 records the normalized amplitude of the laser pulse over a 10 pm (0.010 nm) window. In general, the pulses appear to be smoothly varying functions of wavelength with half-widths of about 3 pm. Notice the presence of "notches" in the distributions especially near 829.086 nm. Because these occur at the same wavelength for several different laser pulses of different mean wavelength, it is assumed that they are the result of a artifacts in the wavemeter at that wavelength and not a result of actual wavelength dependence of the laser pulse.

Figure 3.6 displays the wavelength distribution of 20 laser pulses relative to the start of the 10 pm-wide window. It includes the same 5 narrow bandwidth laser pulses in Fig. 3.5 and adds 15 laser pulses from a cavity using a 6X beam expander. The shapes of the pulses are very similar within a given bandwidth despite having different mean wavelengths and power. It is

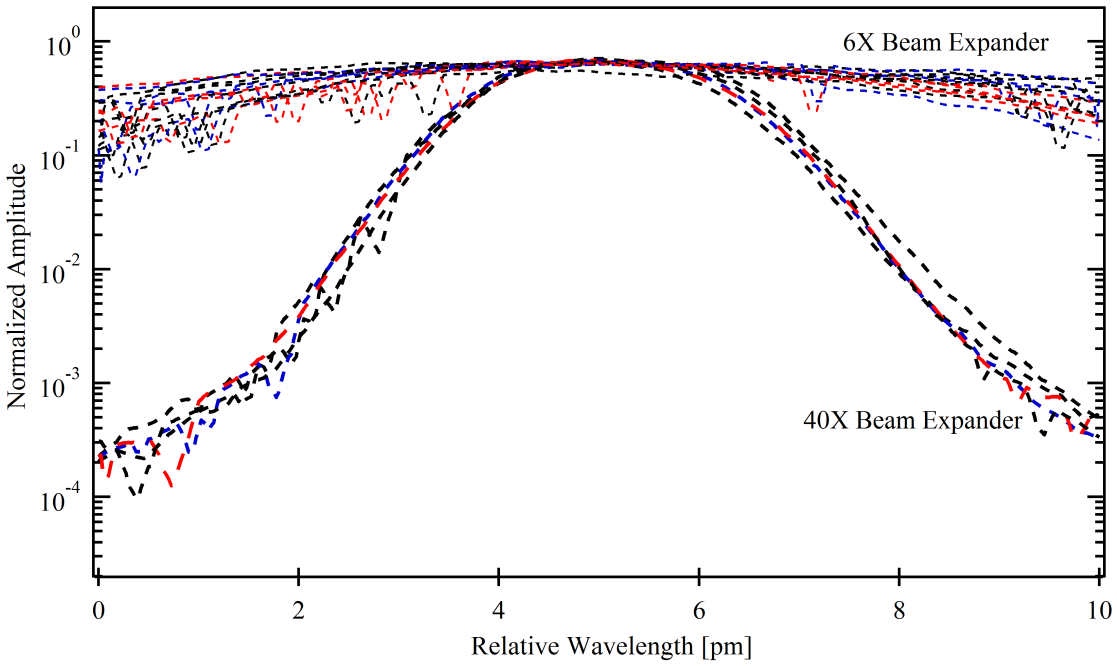

Figure 3.6: Spectral distribution for 5 narrowband (40X) and 15 broadband (6X) laser pulses relative to the peak amplitude of a pulse. Individual pulses are very similar in shape, but the 10 pm window limit of the wavemeter makes it difficult to analyze the shape of the wings of the broad bandwidth laser pulses. All pulses were measured by the WS-7 in fine mode.

clear however that the 10 pm-wide wavelength window of the WS-7 is narrower than would be desired for characterizing the shape of the broad bandwidth pulses well, because the wavemeter does not record the intensity of the distribution outside this window. The average FWHM of 40X pulses is 3 ± 0.1 pm and the average FWHM of the 6X pulses is 9.5 ± 1.5 pm. In order to highlight the average shape of the wavelength distribution from the laser cavities with different beam expanders, Figure 3.7 shows the average lineshape for the laser pulses in Fig. 3.6. Fig 3.7 includes a Gaussian fit to the narrow pulse average, but note that the fit is very poor in the wings. A Gaussian fit represented the lineshape better than that of a Lorentzian lineshape. Attempts to fit the average wavelength distribution from the laser cavity with the 6X beam expander were inconclusive for distinguishing the best type of lineshape for describing the distribution.

From the shapes of the broad bandwidth laser pulses in Fig. 3.6 it can be understood that defining a mean wavelength for these pulses is difficult for our wavelength meter. This introduces significant error into the accuracy and precision of the laser wavelength for broad bandwidth laser pulses. When arranged for generating broad bandwidth pulses our laser spectrum is composed of multiple longitudinal modes, with comparable amplitude. The superposition of multiple modes in a given laser pulse allows multiple maxima and prevents the wavelength meter from providing an accurate reported wavelength. Because the summing of multiple modes

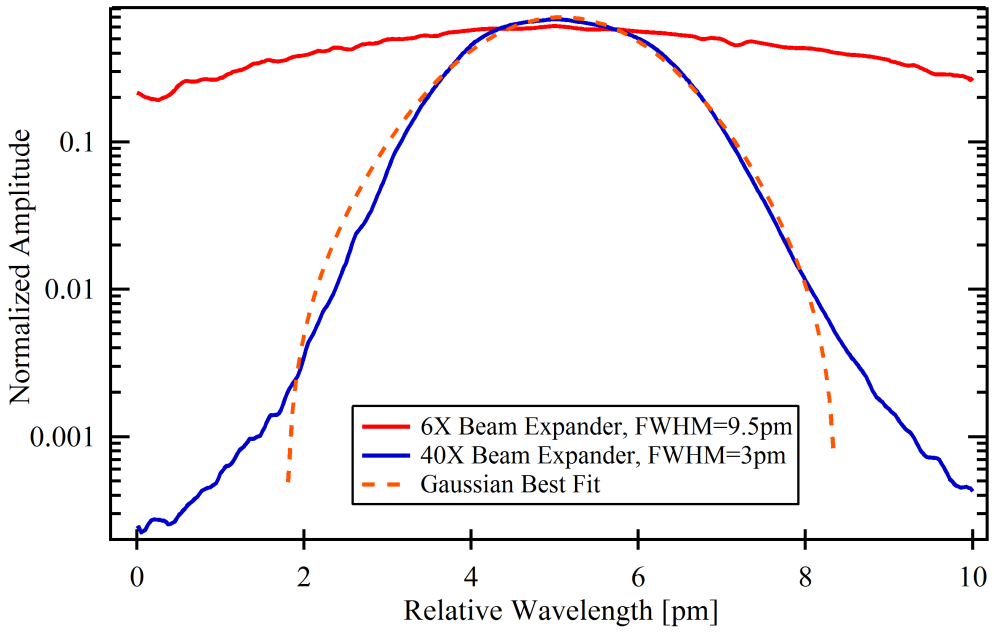

Figure 3.7: Average lineshape of laser pulses for 5 narrow (40X) and 15 broad (6X) bandwidth. Including a least-squares Gaussian fit to the average for the narrow distribution.

creates a distribution that is not well approximated by a Gaussian fit, the reported central wavelength is incorrect. The wavemeter reported a more reproducible wavelength estimate of the broad bandwidth pulses while in "wide" precision mode, but unfortunately resulted in a shift of the reported wavelength from the actual value. This shift could be easily observed for the narrow bandwidth lasers; when the wavemeter was switched between "wide" and "fine" precision mode the reported mean wavelength of a narrow bandwidth laser beam would change by as much as 8 pm, which is much larger than any possible change in the actual wavelength since the laser cavities remained untouched. This wavelength shift varied from day to day and was laser specific. Observing the spectral distribution of wavelength displayed by the wave meter and averaging over a large number of laser pulses ($N \approx 50$) provided a more reliable estimate of the central wavelength, which was different from the reported wavelength. On average, the difference was found to be around 6 ± 2 pm. As a result, we employed a manual calibration of the wavelength meter by correcting for the difference between the reported wavelength and the mean wavelength observed in the spectral distribution. This was performed each day for each laser. The accuracy in mean wavelength found in this manner was $\pm(1 - 2)$ pm during broad bandwidth experiments, but did reproducibly maintain a given mean wavelength. The reproducibility of the mean wavelength as determined by this method was confirmed by observing the resonant response of a target isotope. In an experiment using a narrow bandwidth beam and with the wavemeter inadvertently set in "wide mode, the actual wavelength of the laser for the

first transition was -7 pm different from the "reported" wavelength. Because the isotope shift in the first transition is -7 pm, we observed the resonant ionization response of ^{235}U while all three lasers were "tuned" to ^{238}U. The lesson was that the isotope response to laser wavelength was the best wavelength meter in our laboratory due to the sensitive wavelength response of the atomic resonances.

3.1.2.4 Spatial Distribution of Laser Beams

The laser beams are reflected using steering mirrors on their way to the target chamber and are shaped using spherical lenses to be focused to approximately 1 mm in width by 1.5 mm in height in the center of the ionization volume. The specific size and position of each laser can be recorded before and after experiments when a prism is inserted into the beam path to divert photons onto the camera of the beam analyzer. Our beam analyzer was a USBeamPro with a CMOS detector head (Photon, Inc.) that is placed outside of the target chamber at the same distance as the center of the target holder so the beams will be focused to the appropriate spot size. This beam analyzer enables the observation and recording of relative laser position and 2-D spatial distributions of intensity in the laser beams. Typically, we quantify the beam shape using the elliptical diameters in the horizontal and vertical directions by the $1/e^2$ widths, or the width that the intensity falls to roughly 13.5 % of the peak intensity. The $1/e^2$ width is equivalent to the full-width of four standard deviations for a normal Gaussian distribution. Figure 3.8 is a picture of the output screen from the beam analyzer for a laser beam generated by the Photonics 1 laser pair. The beam size (1.6×1.2 mm) is not in agreement with the typical size of beams used experimentally (1×1.5 mm) but the picture gives a good understanding of the data acquired from the beam analyzer. The main body of the picture is a window with the 2-D spatial distribution of the laser beam intensity represented by the color change above the purple background. A beam statistics window is visible in the upper right which reports both the instantaneous and mean values for the horizontal and vertical diameters across the beam (the $1/e^2$ values) along with the location of the centroid of the laser beam relative to the camera center (3.7 mm in both directions here). The bottom right window contains two figures, each of which shows a 1-D cross section of laser amplitude along the horizontal and vertical axes (the lines in the 2-D plot). The laser beam must be attenuated before illuminating the camera to avoid over-saturation of the camera detector. During our experiment this was accomplished using absorptive filter elements, but due to the risk of thermal lensing in the filters that can cause errors in the estimate of spot size at high laser powers, the attenuation has since been achieved with reflective attenuation. Thermal lensing is not believed to have contributed a significant effect to spot size at the power densities of laser light used in our experiment.

3.1.2.5 Laser Path Nd:YAG

CHARISMA is also equipped with a fixed-frequency Nd:YAG laser (neodymium-doped yttrium aluminum garnet, $Y_3Al_5O_{12}$ with 1% Nd) a custom UL-355 from LaserPath Technologies, Inc., which is available as a high-power, fixed-wavelength source. The LaserPath is often

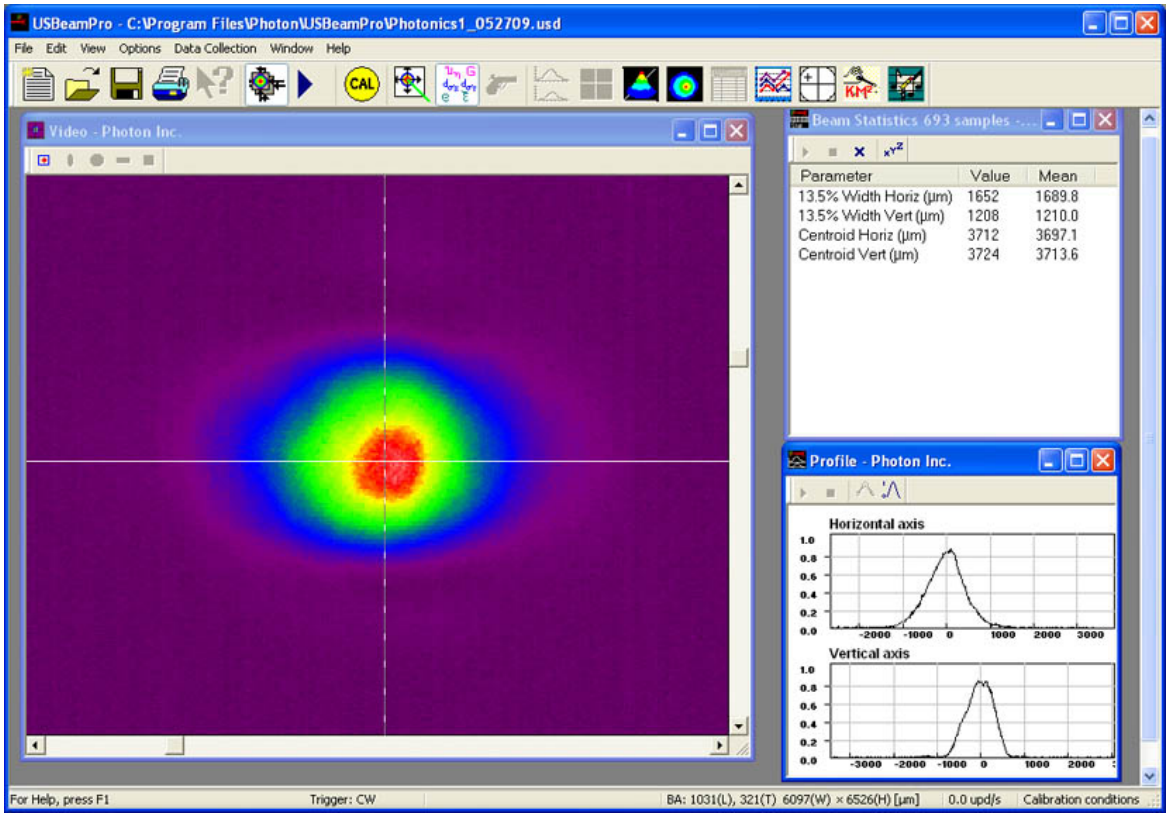

Figure 3.8: Laser beam spatial diagnostics from the beam analyzer. Three main windows are shown: (1) The 2-D representation of the beam spot on the camera as an intensity map, cool colors represent low intensity, hot colors high intensity. (2) In the upper right a window giving the instantaneous and mean statistics for laser spot dimensions and location on the camera in μm. (3) The 1-D profile of the laser amplitude along the two axes shown as lines in the 2-D window.

used to provide photons for the ionization step of resonance excitation schemes that utilize ionization into the continuum and therefore the transitions are not wavelength sensitive but require high irradiance. We used the 532 nm frequency-doubled beam of the LaserPath in a single set of experiments to explore the ionization of uranium into the continuum compared to the use of an autoionizing resonance after two excitation steps as in our 3-photon scheme described below. The maximum energy per pulse of the LaserPath is around 3 mJ in the frequency-doubled beam. The Nd:YAG laser has a typical pulse duration of 15 ns.

3.1.3 Target Chamber

The target chamber is a 0.5-meter diameter stainless steel sphere with a large port connected to a turbo-molecular pump positioned directly below to maintain ultra-high vacuum ($\sim 10^{-9}$ Torr). The chamber contains a rotating sample holder and electrodes for shaping the electric field in the ionization volume for the suppression and extraction of ions. There are several other ports on the target chamber, one containing a sample exchanger, one for the primary ion source, one used for laser desorption away from the normal of the target surface, two ports for input and output of the resonance lasers, and multiple smaller optical windows for observation of the interior of the chamber. Some of these smaller ports house diagnostic devices such as heating elements, thermocouples, vacuum gauges, and a secondary electron detector. Finally, there is a port that houses the Schwarzschild-type microscope and the electrodes used to extract ions into the TOF tube. The Schwarschild microscope is both an optical microscope for observing the target and an input for laser desorption pulses normal to the target surface[24].

A view into the target chamber through the optical port used to introduce the ionization lasers is shown in Fig. 3.9. This picture gives a good view of some of the important components inside the target chamber: (1) a target holder on the rotating sample stage, (2) the tip of the liquid-metal ion (Ga^+) sputtering gun, (3) the conical extraction electrodes covering the Schwarzschild microscope, and (4) the ionization volume between the target and the extraction optics where the lasers interact with the cloud of desorbed material. We will discuss the extraction optics and the details of the Schwarschild microscope in Sec. 3.1.3.4. The target holder is mounted on a rotational stage which can hold up to 3 targets and can be moved in x, y, and z-directions via 3 motors. Originally, the stage was driven by a 3-axis Burleigh 6000 Inchworm piezoelectric positioning system. This system was replaced by 3 "Squiggler" motors from Newscale Technologies. The new motors did not work as intended and increased labor time for changing targets or focusing on different areas of the same target. Despite the inefficiency of the new motor system, the quality of the resulting measurements was not affected by the change.

3.1.3.1 Atomization

As we discussed in the last chapter the process of RIMS requires atoms to be removed from a solid (or liquid) into the gas phase. Our approach for measuring isotope ratios requires the target be desorbed into neutral ground-state atoms. This is because atoms in excited states will

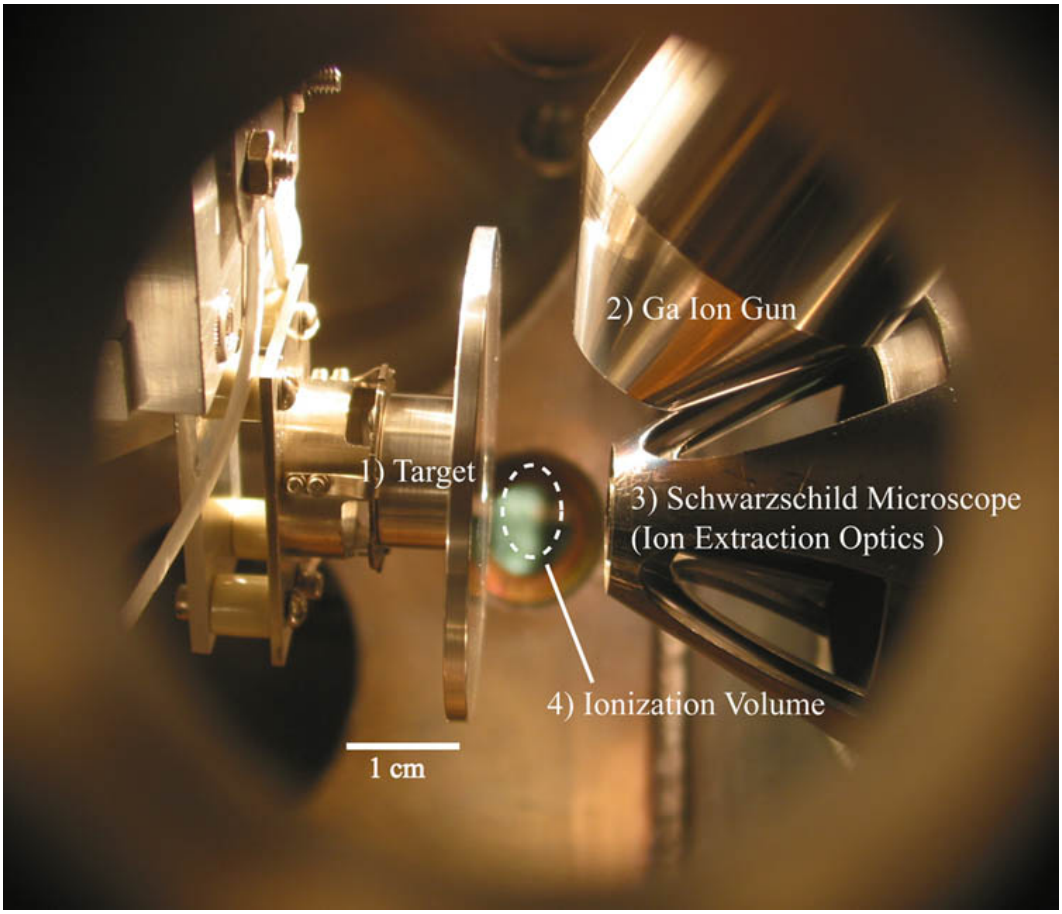

Figure 3.9: The target chamber interior viewed from the optical port used to introduce the ionization lasers. A target (1) is seen on the left being suspended by the rotating target holder. The Ga^+ ion gun (2) is seen in the upper right pointed onto the target surface. The cones of the extraction electrodes are covering the mirrors of the Schwarzschild microscope (3), and the ionization volume occupies part of the space between the target and extraction optics which are separated by 1 cm.

not respond to our specific resonance ionization scheme, and the widths and distributions of the transitions of molecular species are not specific enough to ionize selectively. In addition, molecules cannot always be definitively identified by mass (*e.g.,* $^{234}U^{18}O$ and $^{236}U^{16}O$ both have a mass of 252 amu). As mentioned above, CHARISMA is equipped with two methods of target atomization, ion sputtering and laser desorption. The experiments described in the next chapter focus on the use of ion sputtering for atomizing uranium-rich materials. We focused on ion sputtering because of the reliability of the instrumentation and stability of the sputtering process. We made limited use of laser desorption because laser desorption rates are highly dependent on laser power that can fluctuate from pulse-to-pulse by more than 10 %. This should not however detract from exploring laser desorption as a method for sample atomization in future studies intended to maximize neutral-atomic desorption yield from atom limited samples or complex matrices.

Ion Sputtering

For atomization by ion sputtering, we used an Ionoptika liquid metal ion gun that produces 25-keV $^{69}Ga^{+}$ ions directed onto a target surface at an incident angle of 60° from the surface normal. The ions can be focused onto a spot as small as 50 nm but our analyses typically used a spot size of a 1-2 micron in diameter. The beam spot can be directed to a single location on the target or rastered over an area (horizontally across a row, then down to the next row, etc., similar to the means by which a CRT TV image is projected) that can be up to several hundred square microns. We typically used a raster pattern of $20 \times 20\,\mu$m. The liquid metal tip generates Ga ion currents on the order of a few μA that are then reduced to a desired current on the target by placing apertures of different size in the beam line, typically on the order of nA. The gun can be operated in either a continuous wave (CW) or pulsed mode. The CW mode allows for faster removal of material from a target and so was used to remove surface contamination or to help establish equilibrium of the sputtering process on a target surface, because sputter rates at a fresh spot on a target decrease rapidly within a few seconds of CW sputtering to a more stable rate (see Sec. 4.1.6). Operating the ion gun in pulsed mode allows us to synchronize the desorption event with the ionization lasers and the mass filtering, which increases the efficiency of target consumption by removing material from the target only when measurements are actually performed. The duration of the ion pulse can be varied from tens of ns to a continuous beam. We found that pulse widths in the range 300-500 ns resulted in the steadiest ion signals for two reasons: (1) longer pulse lengths help in achieving equilibrium in the sputtering process within a given pulse (for a 500 ns pulse at a rate of 1 kHz, the ions are incident on the target only 0.05 % of the total time elapsed during an experiment), and (2) longer pulses help to minimize mass fractionation in the ionization volume. By this, we mean that considering the free expansion of two atomic species of different mass after sputtering, their difference in momenta will result in a different number of atoms in the ionization volume at a given time. This difference will produce a bias in the measured isotope ratio proportional to the mass difference of the two species. On average, however, the distributions of those two species in space will be stable for times in the middle of the sputtering pulse. Considering the limit

of continuous sputtering, only the leading edge of the desorbed cloud will show a population difference. Therefore, using a relatively long sputtering pulse of 300 ns relative to the 20 ns pulse of the ionization lasers means that there is a sufficiently long time for ionization in which the population of atomic species in the ionization volume will be equilibrated.

Laser Desorption

The desorption laser is an intracavity frequency-tripled diode-pumped Nd:YAG (IB Laser model DiNY pQ) that is capable of delivering 600 J of 355 nm light in 8 ns pulses at a 1 kHz repetition rate. The system has very high beam quality, which allows for tight focusing at the target. Initially, while relatively new, the desorption laser had excellent pulse-to-pulse stability with power fluctuations as small as 3% that resulted in steady desorbed neutral yields. However, during the time period of our investigation pulse-to-pulse power fluctuations were around 8-10 %. Because the desorption process is nonlinear in laser pulse energy, even moderate pulse-to-pulse fluctuations give rise to large variations in the desorbed neutral flux. This can lead to systematic errors in ion counting, because the recorded counts will not obey a statistical distribution described by the Poisson distribution. Furthermore, the larger the pulse-to-pulse fluctuations, the more likely the laser is to occasionally produce relatively powerful pulses that give a great many ions per time channel, and cause serious under-counting of the major isotopes due to dead-time effects (see Sec. 3.1.4.1). To achieve its maximum stability the laser must be operated at full power, but because 600 J is much higher than the 10 nJ found to be optimal for atomization of SiC [24] the power is attenuated in two steps: first with a half-wave plate and a polarizer, and second with a variable neutral density filter.

Figure 3.10 shows the desorption laser beam path, including the Schwarzschild microscope. The microscope has been described in detail elsewhere [24, 13]. It consists of two spherical mirrors, one large concave mirror and a smaller convex mirror. The smaller mirror is 3.81 cm in diameter and has a 5.08 cm radius of curvature and the larger mirror is 17.8 cm in diameter with a 14.7 cm radius of curvature. A third planar mirror is placed between these mirrors to move the mirror image outside of the target chamber and away from the axis of ion transmission of the mass spectrometer. Because the Schwarzschild microscope is an obstructed-pupil optical element, the optical axis is blind everywhere except at the image and object planes. Therefore, there are holes drilled through the center of all three mirrors along the optical axis that allows ions to pass through into the mass analyzer. The individual mirrors are held in place by Al tubes that form the first set of ion focusing lenses of the mass spectrometer. The mirror system has a numerical aperture of 0.47, giving a magnification factor of 19 and a working distance of 8.1 cm from the sample. This design allows for normal-incidence focusing of the desorption laser to achieve a circular, rather than elliptical, beam spot. In addition to focusing the desorption laser beam with a reduction of laser spot area by up to a factor of 360, the microscope also provides an optical image of the sample with a lateral resolution of 1 μm. This optical image can be directed to a CCD camera with a viewing area of 0.23×0.31 mm.

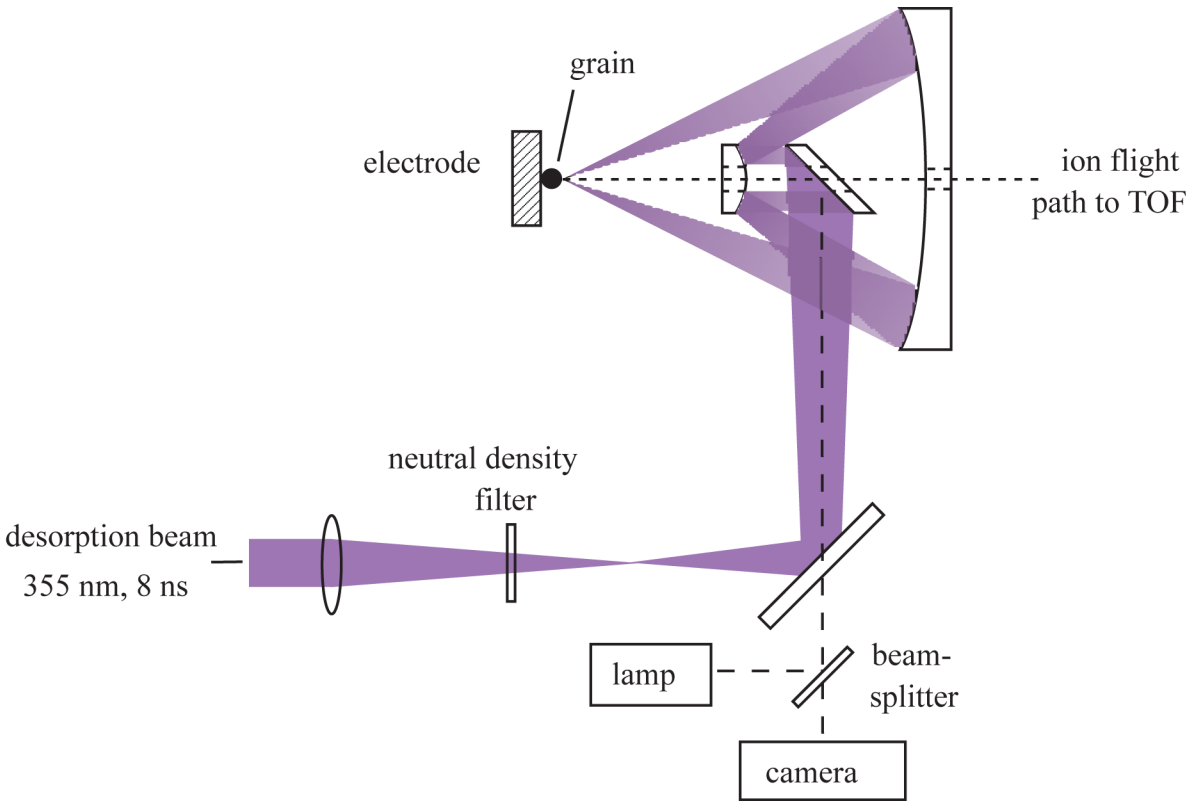

Figure 3.10: The beam path of the Nd:YAG desorption laser including the optics of the Schwarzschild microscope. The beam is attenuated via a neutral density filter before entering the microscope optics and is focused by the spherical mirrors onto the target electrode with a reduction in area of 360. The center of the optical elements in the microscope are drilled out to allow ions to enter the TOF. Visible light from the lamp is also transmitted through the microscope and reflected off the surface of the target back to a CCD camera for observing the target sample.

3.1.3.2 Secondary Ion Suppression

As mentioned earlier, the processes of desorption and sputtering creates a cloud of debris that contains both neutral particles and charged particles. Our aim is to record ions generated through photon-induced ionization of atoms only and thus we wish to remove all charged species that may have been generated in the desorption and sputtering processes prior to introduction of the ionization laser beams into the ionization volume. Although the charged species can be useful for determining the mass/charge ratio of constituents of a target (known as secondary ion mass spectrometry or SIMS), the atomic ions in the cloud have been formed through a non-selective ionization method. Therefore, unless it has already been determined by chemical or physical means (*i.e.*, chemical purification), there is no knowledge of the element number of the ionized species. The suppression of charged particles is accomplished by applying a large voltage pulse to the target holder (nominally +4 kV) for around 300 ns while maintaining the extraction electrodes at ground potential after the desorption pulse and prior to the ionization lasers pulse. The precise timing scheme will be discussed in Sec. 3.1.5.1. This voltage pulse repels any positively charge particles, such as atomic and molecular secondary ions, towards the entrance to the mass spectrometer and the walls of the target chamber. Any charged particles which enter the mass spectrometer will have sufficient energy to travel to the back wall of the flight tube and will not be turned towards the detector by the reflectron, which has a a maximum voltage of +2.1 kV (see Sec. 3.1.4). Any negatively charged particles, which include electrons, atomic and molecular secondary ions, will be drawn back towards the target surface. We refer to this voltage pulse as the SIMS suppression pulse.

3.1.3.3 Laser Ionization

We perform the post-ionization of neutral species by laser irradiation using the laser beams described above. Our lasers produce 15-20 ns pulses (FWHM) that enter the target chamber after the secondary ion suppression voltage has removed any charged secondary species. This delay before laser irradiation also allows time for the neutral particles to propagate from the target surface to the ionization volume. The target potential is lowered to ground $\sim$100 ns before the ionization laser beams encounter the secondary cloud, so that photoionization of secondary neutrals takes place in the absence of strong electric fields. The laser beams are aimed parallel to the target surface, immediately above sample (typically less than 0.5 mm). The highest photo-ion signals are achieved when the ionization laser beams are as close as possible to the target surface. However, there is a risk that if our ionization beams are aimed too close to the target, photons can interact with the sample surface directly. This can desorb species from the target after the SIMS suppression pulse, and result in the creation of ions that can then be extracted into the mass spectrometer in addition to the desired resonant photoions.

3.1.3.4 Ion Extraction

Once ions have been created by the ionization lasers, voltages are applied to the target holder and the extraction electrodes to accelerate and focus the photo-ions into the mass spectrometer

for mass separation. A significant challenge for RIMS compared to other implementations of mass spectrometry is that the ions must be extracted into the mass spectrometer from a relatively large volume ($\sim mm^3$) above the target (see Fig. 3.9). This challenge requires a robust ion extraction method in order to maintain reasonable instrumental efficiencies. The extraction of ions from a volume using a linear electric field gradient typically results in a significant residual spread of ion energy after acceleration due to the linear variation of the electric field across the ionization volume, because an individual ion's energy is dependent on linear distance to the high-voltage electrode when the ion is created. This is why CHARISMA uses a two-potential extraction method. Ions are first created in a field that has a relatively small gradient and then, after the ions are drawn out of the ionization volume, the gradient increases strongly to accelerate the ions to full energy.

Figure 3.11 is a cross section of the ion extraction system in CHARISMA[13]. It shows the target holder, two conical electrodes designed not to obstruct light transmission through the Schwarzschild microscope, and the final electrode on the right that also holds the Schwarzschild microscope (not pictured here). The voltages shown on the target (+2 kV) and extraction electrodes (+1.7 kV, and ground) are the typical values used during ion extraction. About 20 ns after the ionization lasers are fired, the target potential is pulsed to 2 kV, and the newly generated photoions are accelerated into the time-of-flight mass spectrometer. The photoions are focused in time and space by pulsing the second conical extractor electrode to 1.7 kV simultaneously with the target pulse; the first cone is held at ground potential. Effective focusing of the photoions requires that the electric potential vary only slightly over the laser–atom interaction region, with a weak electric field (30 V/mm) directing positive ions into the time-of-flight mass spectrometer. The shapes and sizes of the sample and extractor electrodes are carefully chosen to shape the electric field for optimal ion transmission and focusing. Further details of the extraction optics along with an improved design outfitted on another instrument can be found in [66].

The final energy of the ions is about 2 keV per unit electric charge, plus the energy due to the sputtering process (the majority of sputtered species acquire kinetic energies of only a few eV). Because the electric field gradient across the volume between the target electrode and the second cone electrode is 30 V/mm and the ionization volume is defined by the size of the ionization laser beams ($\sim$1 mm), ions born in this volume can experience a potential difference of only 30 V. If we include a few eV spread ($\pm$5) in energy due to sputtering, this results in a difference in final velocity of 40/2000 V or a spread in energy of 2% between two identical ions born on opposite sides of the ionization volume with large differences in initial velocities. The energy spread is partially compensated for in the reflectron of the TOF mass analyzer as we will see below. Recall for the SIMS suppression pulse, that the target electrode is pulsed to +4 kV but that all the extraction electrodes remain at ground potential so that although some secondary ions may enter the mass spectrometer, they are not focused along the ion optical axis.

3.1.4 TOF Mass Spectrometer

The mass analyzer on CHARISMA is a time-of-flight type mass filter. Two ions of different mass to charge ratio will have different times-of-arrival at the plane of the detector allowing

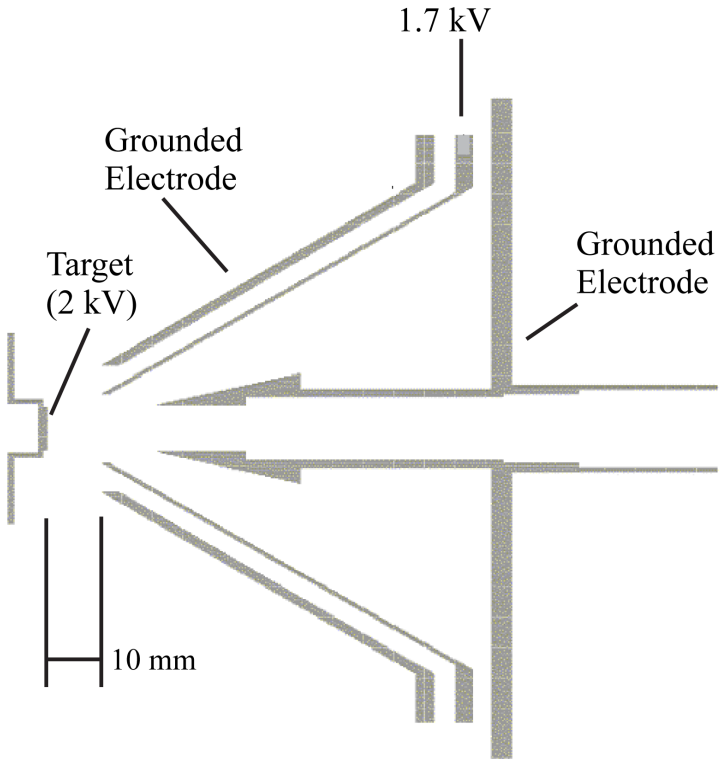

Figure 3.11: Cross sectional view of ion extraction electrodes showing the target, and three extraction electrodes shown with the voltages typically used during the extraction of ions from the ionization volume into the mass analyzer[13].

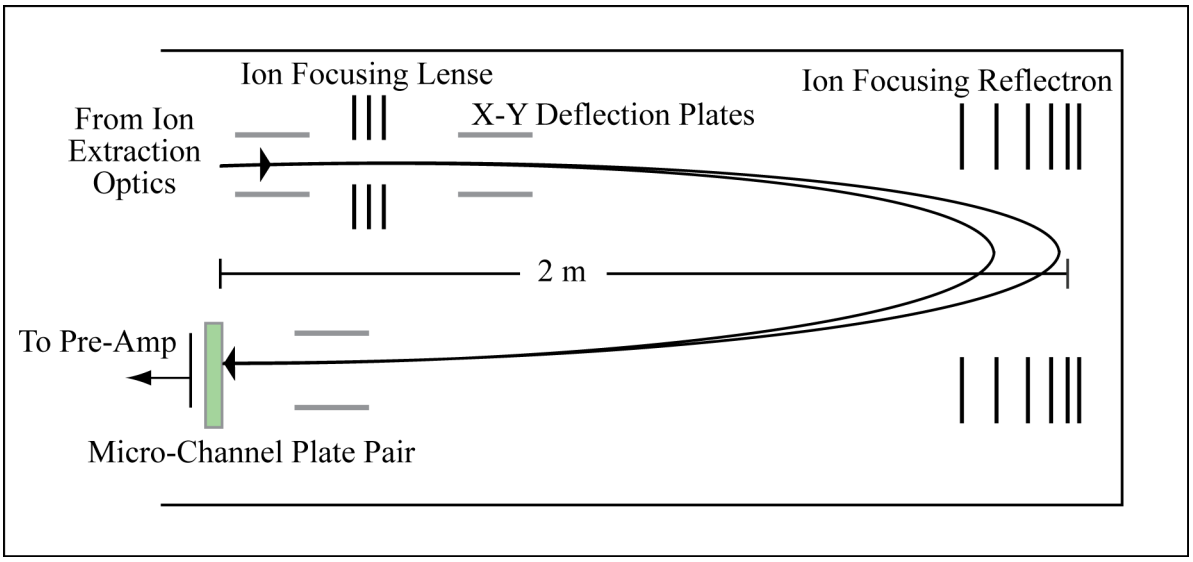

Figure 3.12: The TOF mass analyzer on CHARISMA. Ions are received from the extraction optics at 2 keV, they are focused using Einzel lenses and directed (X-Y deflection plates) towards the center of the reflectron where they are turned around in a multi-potential electric field that focuses ions of different velocities. The reflected ions finish their 4 meter flight path by impacting the surface of the multi-channel plate detector. The two flight paths shown demonstrate the different distances into the reflectron traveled by ions with equal mass of different velocity. The inside parabolic track would be followed by an ion with less energy than an ion following the outer track.

for mass analysis of the ions. The energetic ions drawn into the mass spectrometer by the ion extraction optics are further focused by a set of Einzel lenses and steered onto the axis of highest transmission using charged plate pairs (X−Y deflection plates) that are held at a fixed potential. Figure 3.12 is a schematic of the TOF tube of CHARISMA and shows the incident ions in the upper left corner and two possible flight paths through the mass spectrometer for ions of equal mass but different velocity. The ions are directed towards the center of the high-transmission (>90%) double-focusing (energy and position) ion reflectron to help overcome initial ion spread in energy and trajectory. The ions are turned around by the reflectron and directed onto the micro-channel plate detector by a final set of deflection plates. The maximum potential in the reflectron is 2.1 kV, so that the 2-keV photoions are reflected, but the ions accelerated into the TOF earlier by the SIMS suppression pulse at 4 keV are not and impact the end of the TOF tube.

The reflectron is located at the end of the drift tube and acts as an ion mirror. Because the ion cloud has finite volume, ions in different locations experience different accelerating potentials. For example, ions near the target experience higher potential than ions far from the target and will therefore have higher kinetic energy. The reflectron compensates for the spread in kinetic energies of the ions as they enter the drift region of the mass spectrometer by allowing ions with

higher kinetic energy to spend more time in the reflectron (penetrate further). This correction helps improve the mass resolution of the instrument, which is proportional to the inverse of the minimum distinguishable mass difference. In addition, the reflectron enables doubling the full drifting length of ions in the flight tube. Our reflectron uses four different potential ramps of decreasing slope to gently reflect the ions, but the principle for time-of-arrival focusing of the reflectron can be understood more simply by considering a single linear potential for turning the ions around. For a single linear potential ramp in the reflectron the electrostatic force that acts on the ions is, $F = q\mathrm{E} = ma$, where q is the charge, E is the potential of the electric-field in the reflectron, m is the mass of the ion, and a is acceleration. The distance an ion with mass m penetrates into the reflectron is $d = \frac{1}{2}\frac{q\mathrm{E}}{m}t^2$. Therefore the time an ion spends in the reflectron is, $t_R = \sqrt{\frac{2md}{q\mathrm{E}}}$. The total time it takes for an ion to traverse from the ionization volume to the detector is,

$$t = t_R + 2t_d = \sqrt{\frac{2dm}{\mathrm{E}q}} + 2L\sqrt{\frac{m}{2Vq}} = \left(\sqrt{\frac{2d}{\mathrm{E}}} + 2L\sqrt{\frac{1}{2V}}\right)\sqrt{\frac{m}{q}} \tag{3.1}$$

where t_d is the potential-free drift time in the TOF, L is the one-direction drift length (2 m), and V is the accelerating potential experienced by the ion during extraction from the ionization volume. The total flight times through the instrument for U atoms were $\sim$117 μs for our experiments.

3.1.4.1 Detector

The ion detector used in CHARISMA is actually a pair of Galileo Electro-Optics microchannel plate (MCP) detectors used without spatial imaging for single ion detection with very good time resolution [67]. Each MCP is a lead glass plate perforated by an array of semiconducting capillaries of 6 μm inner diameter such that each channel can be considered an individual continuous dynode structure. The capillaries have been fabricated to optimize secondary electron emission. When a high-energy ion strikes a channel wall, there is a very high probability that several electrons will be emitted. These are then accelerated and multiplied by further collisions with the walls of the MCP as they propagate through the detector channel. The channels are created at an angle of $\sim 8^\circ$ with respect to the surface normal of the MCP so that ions normally incident on the detector will not have a line of sight through the MCP. When two MCPs are placed in a "chevron" configuration as in CHARISMA, the bias angles of the channels are arranged to be oppositely aligned so that even ions that are incident at angles not normal with respect to the surface will not have a line-of-sight path through the detector. The front and back of the MCPs are coated with conductive materials that allow the channels to be biased at high voltage ($\sim$ 2 kV) that accelerates electrons and supplies a recharging current to the walls of the channels as they are depleted by the avalanche of secondary electrons. Each MCP has a nominal gain of $10^3 - 10^4$ so the detector as a unit has a gain of around 10^7. The secondary electrons arrive in a very short pulse of 1-2 ns, which permits good differentiation in ion mass. The flight time difference in our instrument for ions with masses near 235 amu is about

250 ns/amu[3]. Each channel has a deadtime on the order of 10^{-2} s. However, there are roughly 10^6 channels in a MCP and thus the average deadtime of the MCP is closer to $10^{-7} - 10^{-8}$ s so long as no particular channel is used more often than every 10^{-2} s. The dark count rate, or the rate of counts in our detector due to random secondary emission, has been measured at less than 10 ion counts per second (see Sec. 4.1.2). The efficiency of MCPs for ion detection is usually dependent on the fraction of area composed of channels versus the surrounding interstitial glass (often 50 %), although there is some probability that ions striking the front surface of the MCP could release secondary electrons into nearby channels. The detection efficiency of our detector is around 40 %. Individual ions result in electron currents measured on an anode located behind the MCPs. The maximum voltage on the anode as a result of a single ion strike varies between zero and 200 mV. The current signal from the anode is sent to the data acquisition hardware as will be described in the next section.

3.1.5 Instrument Control and Data Acquisition

3.1.5.1 Data Acquisition

The data acquisition system of CHARISMA was upgraded (compared to Ma, *et al.* [24]) with the installation of the current ionization lasers to enable operation of the instrument at repetition rate of 1 kHz as described in Savina, *et al.* [13]. The anode signals from the MCP detector are preamplified with a gain of ten (Phillips 6950). They are then sent into a discriminator (Phillips 6908) that is set to convert voltage signals that exceed 2 mV into 1.6 V square-wave pulses of 2 ns duration. The discriminator interrogates the voltage on its input every 2 ns. The pulse-pair resolution time of the discriminator is 3.3 ns. If the input voltage on the discriminator is above the threshold for more than a single observation of the input (>4 ns) it will extend the length of the output pulse until the input voltage drops below the threshold (2 mV). An Ortec FastFlight digitizer is used to acquire and accumulate the ion signal from the discriminator within a user-defined time window relative to the system clock. The digitizer builds a time-of-flight spectrum by summing the discriminator output into 2 ns bins in a buffer that accumulates 2000 time-spectra (cycles of the system or "shots") before uploading to a computer. Pulses from the discriminator of duration greater than 2 ns are interpreted by the digitizer as multiple ion counts. Each uploaded summation spectrum is recorded as a "loop" on the computer, which converts the spectrum from voltage in a given time bin to ion counts (1.6 V/ion) and sums a user-determined number of loops into a final spectrum. A typical acquisition in our experiments is composed of 50 loops for a total of 100,000 instrument cycles per spectrum. We then compare these individual spectra over time to study the effect of various system parameters on measured ion counts. Operating at 1 kHz, a 50-loop spectrum takes about 2.5 min to acquire, which is due to both duty cycle and upload time from the digitizer to the computer.

Figure 3.13 is a schematic of the instrument control and data acquisition hardware. It is centered around a personal computer running custom software built in-house (known as "Image")

[3]In other words, the mass resolution in CHARISMA is limited by the spread in the flight time for two ions of equal mass, not by the time resolution of pulses on the detector.

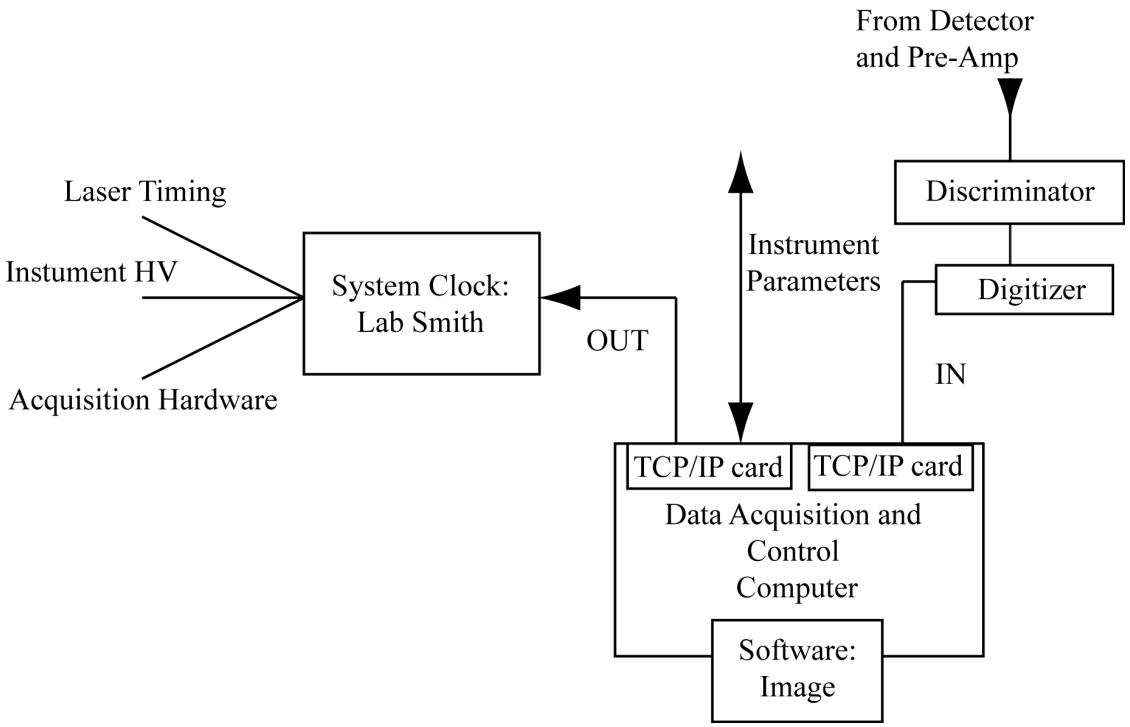

Figure 3.13: Diagram of instrument control and data acquisition scheme. Signals from the detector pre-amplifier are sent through a discriminator before being sent to the digitizer for collection of a time-of arrival spectrum. The digitizer uploads sets of mass spectra to a computer running custom software ("Image") that is used for analysis of the data. The computer also is responsible for setting and monitoring instrument voltages and defining the relative timing of system components. A LabSmith logic controller is used as the system clock for high-resolution time coordination of system components for the laser pulses, the instrument voltages, and the digitizer for acquisition.

and handles all of the tasks involved in receiving signals from the digitizer, setting instrument voltages, and acting as the start/stop for system timing. The master clock of the system is a LabSmith logic controller, capable of time resolutions better than 10 ns. The logic controller receives a "start" signal from the computer that initiates the precise timing logic signals sent to the other instrument components: the laser system, the instrument high-voltages (HV) such as the desorption pulse and the extraction optics, and the acquisition hardware (mainly the digitizer).

The data acquisition system can also be run in an "analog detection mode". In analog mode the discriminator is removed from the system and the digitizer records the voltage amplitude on its input from the pre-amplifier as a function of time instead of converting a voltage into a single ion count as in the "digital detection mode". The recorded data in analog mode are in units of digital bits with 256 bits per volt. The ions striking the detector will create a variable voltage ($0-200$ mV) on the pre-amplifier line as discussed above but for large ion count rates the voltage will be, on the average, linearly proportional to the number of ions detected. Analog mode enables the acquisition of signals with high ion incident rates, but is less accurate than measuring individual ion counts. We mainly used this mode for understanding the variation of uranium ion signal as a function of laser wavelength, where we desired a large signal even when the probability for ionization decreased and where we required information only about the ion signal relative to the ion signals at other wavelengths. Unless otherwise stated, we performed our experiments in the digital detection mode.

Now that we have introduced each system component we can discuss the details of the time sequence of events in our instrument. Figure 3.14 shows the time of operation for different system components in a single cycle or "shot" of CHARISMA (low is off, high is on). A cycle begins with the desorption event, here shown as a pulse of the ion sputtering gun with pulse length of 300 ns. This is followed immediately by the SIMS suppression pulse that is responsible for removing any charged particles generated in the desorption process, typically 500 ns in duration. This permits neutral species to propagate from the target into the ionization volume free of charged particles. The ionization laser beams arrive 100 ns after the end of the SIMS suppression pulse so ionization can occur in field-free space. The laser pulses are approximately 20 ns long and immediately afterward, the target and extraction electrodes are pulsed to their ion extraction voltages in order to accelerate and focus the photoions into the mass spectrometer. The digitizer is turned on at a time defined by the mass of the species specified for counting. For the experiments considered in this work it is turned on at 114 μs for 16 μs to collect the desired ions. Here the singly-charged ions detected would have masses between 225 and 285 amu. The cycle is repeated 1,000 times per second.

Stabilization of Laser Performance

The experiments utilized the improvements in wavelength stabilization, relative laser pulse timing, and laser beam pointing stability described by Levine, *et al*. [14]. Taken together, these enhancements have drastically reduced long-term ($\sim$ hours) fluctuations in measured isotope ratios, enabling longer periods of stable analytical conditions with improved reproducibility.

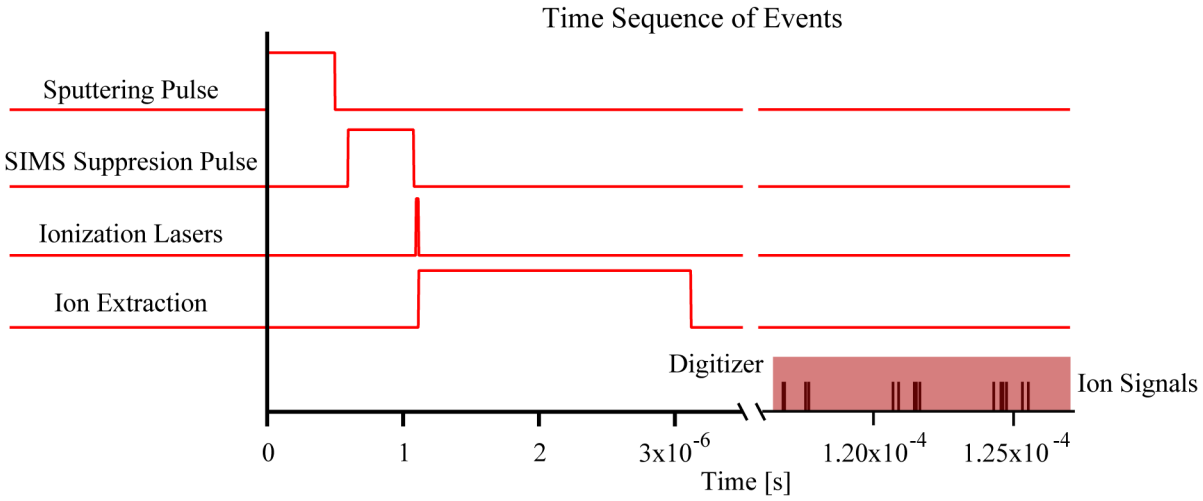

Figure 3.14: Timing sequence of events in our instrument. The operation time of system components for a single cycle of CHARISMA are shown (low is off, high is on). A cycle of the instrument begins with the desorption event, here shown as a pulse of the ion sputtering gun with pulse length of 300 ns, this is followed by the SIMS suppression pulse that is responsible for removing any charged particles generated in the desorption process typically 500 ns long that also allows neutral species to propagate from the target into the ionization volume. The ionization lasers fire 100 ns after the end of the SIMS suppression pulse so ionization can occur in field-free space. The laser pulses are $\sim$20 ns long and immediately afterward, the target and extraction electrodes are pulsed to their ion extraction voltages in order to accelerate and focus the photoions into the mass spectrometer. The digitizer is turned on at a later time defined by the mass of the species specified for counting, here it is turned on at 114 μs for 16 μs to collect the desired ions. Ions arrive at different times as a function of mass and velocity, here the ions detected would have masses between 225 and 290 amu.

3.1.5.2 Laser Wavelength Stabilization

To ensure that the wavelengths of the lasers remain centered around a designated wavelength over an indefinite period, we have implemented a wavelength feedback system [14]. This system operates by comparing the wavelength reported by the wavemeter to a user-specified wavelength. When significant differences between the reported value and the desired value exist the system pivots the diffraction grating of the laser cavity using an actuator. If left unattended, the tunable laser cavities of our system will tend to drift freely in wavelength due to thermal effects in the cavity optics. This feedback system has been demonstrated to reduce the long-term drift in mean wavelength to ± 1 pm in the fundamental range and ± 0.5 pm in the second-harmonic range, indefinitely for a narrow bandwidth laser. These magnitudes are comparable to the ∼1.5 pm pulse-to-pulse variations common with these lasers and are markedly reduced from the 2 pm hr^{-1} variation observed without feedback control.

A brief description of the details of the feedback system are as follows. The wavelength meter used to monitor our system is connected to an 8-channel optical switcher (by HighFinesse-Ångstrom). One channel can be measured every ∼30 ms, so while monitoring 3 lasers each laser is measured every ∼100 ms. The output of the wavemeter is input into custom-built "feedback software" running on the laser control computer (Fig. 3.2). The software calculates a running average of the laser wavelength using a user-specified number of measurements (typically the previous 100 measurements). The software takes the difference between this average and the user-specified wavelength for each laser cavity. The feedback software is connected to the controller for a piezoelectric actuator that are attached to the base of the rotational mount that holds the diffraction grating. Labeled as the "grating motor" in Fig. 3.4. The actuators (New Focus model 8310 closed loop "Picomotors") have 63 nm linear resolution, enabling the software to rotate the gratings in steps of ∼1 μrad. The actuators are calibrated near the desired wavelength by the software to define a change in wavelength per step of the actuator. By rotating the reflection gratings in the corresponding laser cavity via the calibrated actuators we can change the wavelengths of the laser beams to within about 1 pm of the specified wavelength. Second-harmonic beams are tunable in steps of 0.5 pm.

Figures 3.15-3.17 presents distributions of mean laser wavelength over 10^5 laser pulses as recorded by the WS-7 while using the wavelength feedback system. Figure 3.15 shows a distribution for a broad bandwidth laser (4X beam expander) tuned near 831 nm with a FWHM of 4 pm. Figure 3.16 shows a distribution for a narrow bandwidth laser (40X beam expander) tuned near 829 nm with a FWHM of 2 pm. This difference in relative wavelength reproducibility between the narrow and broad bandwidth lasers is consistent with the increase in uncertainty of the wavelength measurement with increasing bandwidth laser.

Figure 3.17 shows the distribution for a laser tuned near 722 nm, which used a 40X beam expander, and shows a bi-modal distribution. This is most likely due to the user-specified wavelength lying somewhere near the center of two laser cavity modes. In such a case, the feedback system attempts to correct the wavelength by moving the actuator by the minimum step size, which may have been sufficient to overshoot the specified wavelength by moving the cavity into the neighboring mode. Note, that the feedback system did, on the average, maintain the user-

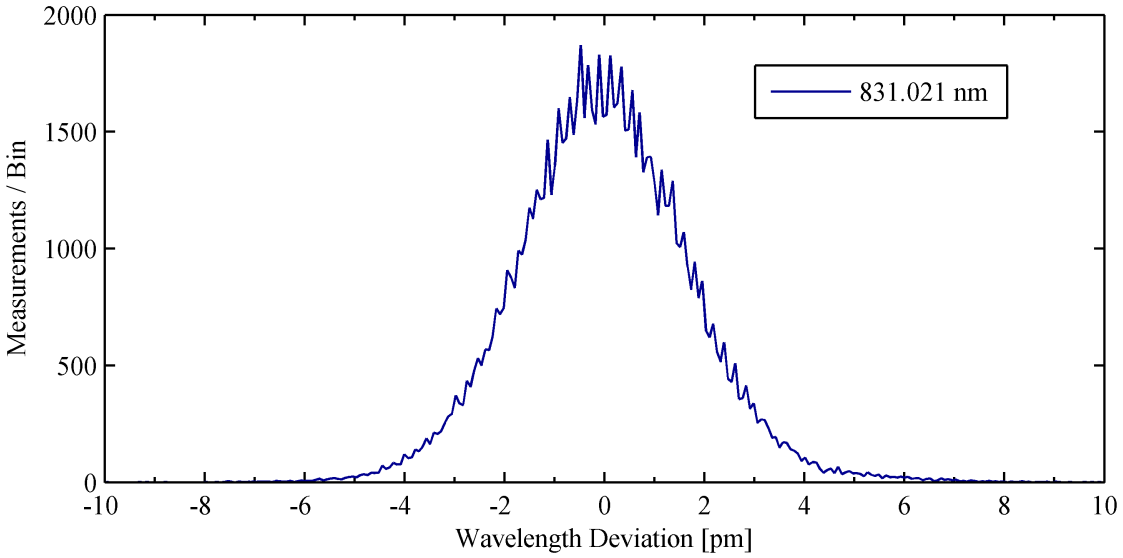

Figure 3.15: The mean wavelength distribution over time for a broad bandwidth (4X beam expander) laser tuned near 831.02 nm.

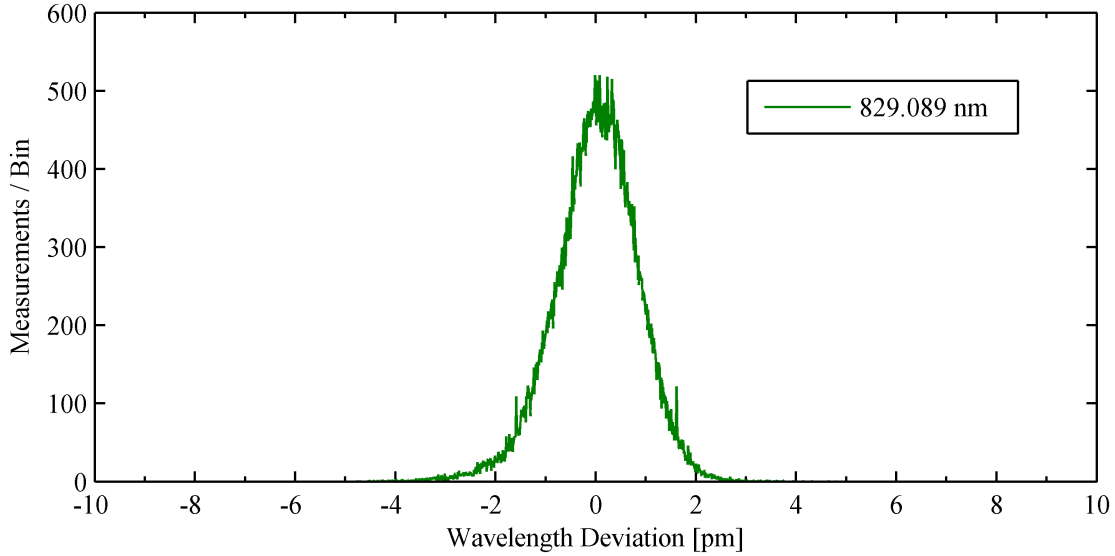

Figure 3.16: The mean wavelength distribution over time for a narrow bandwidth laser (40X) tuned near 829.09 nm.

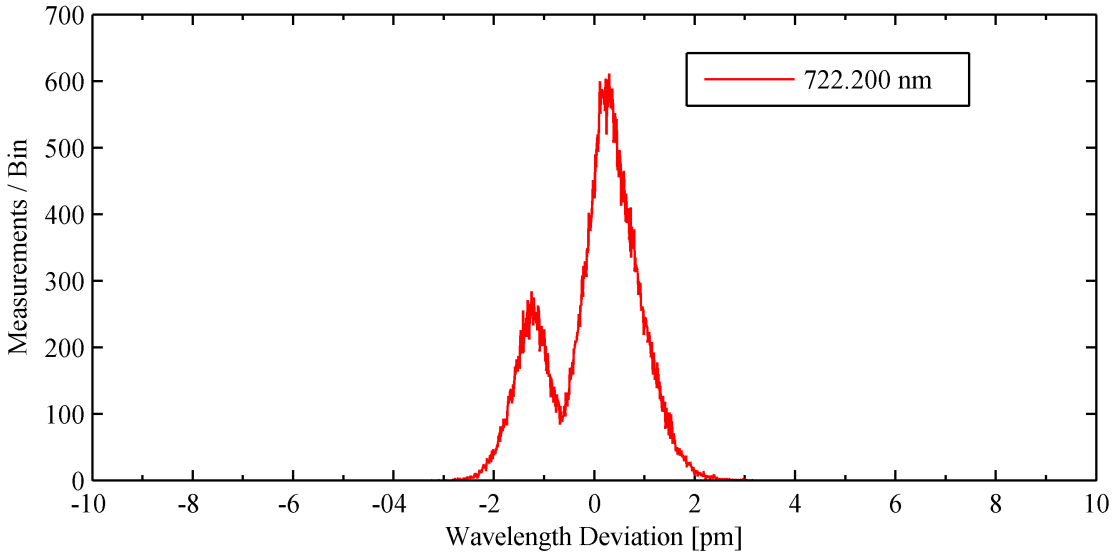

Figure 3.17: The mean wavelength distribution over time for a narrow bandwidth laser (40X) tuned near 722.2 nm that displays a bi-modal distribution.

specified wavelength over the duration of the measurements. This bi-modal distribution could possibly be prevented by either re-calibrating the actuator system or changing the user-specified wavelength by a small amount ($\sim$0.5 pm) to help pick a single mode.

Figure 3.18 shows the two distributions from the Fig. 3.15 for the narrow bandwidth laser near 829 nm and the broad bandwidth laser near 831 nm, along with two Gaussian to the distributions. The fits appear to describe the peak shapes quite well except for the very far wings of the distributions.

3.1.5.3 Relative Laser Timing

Each tunable laser pair (pump and Ti:Sapph lasers) has a unique time-dependence as a result of differences in pump laser power, wavelength-dependence, and transverse mode structure. The pump lasers are optically Q-switched to initiate light output from the cavities with time-resolution on the order of a few ns. Typical time durations of the pulses from the pump lasers are about 250 ns. These pulses enter the Ti:Sapph cavities and begin to cause stimulated emission. The tunable cavities are not controlled via Q-switches and so the timing of the laser output pulse is determined by the build-up of energy in the standing modes of the laser cavity that can vary significantly from pulse to pulse. Thus, in general, the time that laser pulses arrive at the target chamber vary if they are triggered simultaneously. The time-dependence of the laser pulses was measured with photo-diodes (Thorlabs DET10a, rise times <1 ns) connected to a 500-MHz oscilloscope. Figure 3.19 shows the amplitude of a representative laser pulse at 855 nm as a function of time. The pulse is centered near 44 ns and has a FWHM of about 20 ns.

In order to ensure that the laser pulses arrive in the target chamber synchronized in time, we

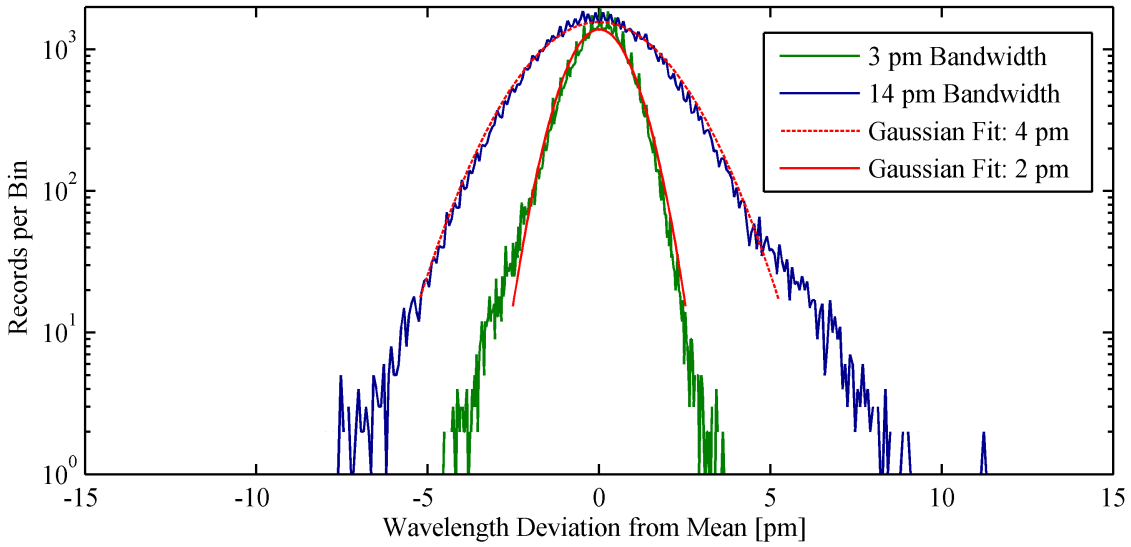

Figure 3.18: Two semi-logarithmic histograms of the mean wavelength reported for 10^5 laser pulses. The distributions are the same broad bandwidth laser (14 pm) and a narrow bandwidth laser (3 pm) shown in Fig. 3.15a and b. Also shown are Gaussian fits for each distribution, the fits estimate FWHM of 2.0(1) pm for the narrow bandwidth laser and 4.0(2) pm for the broad bandwidth laser.

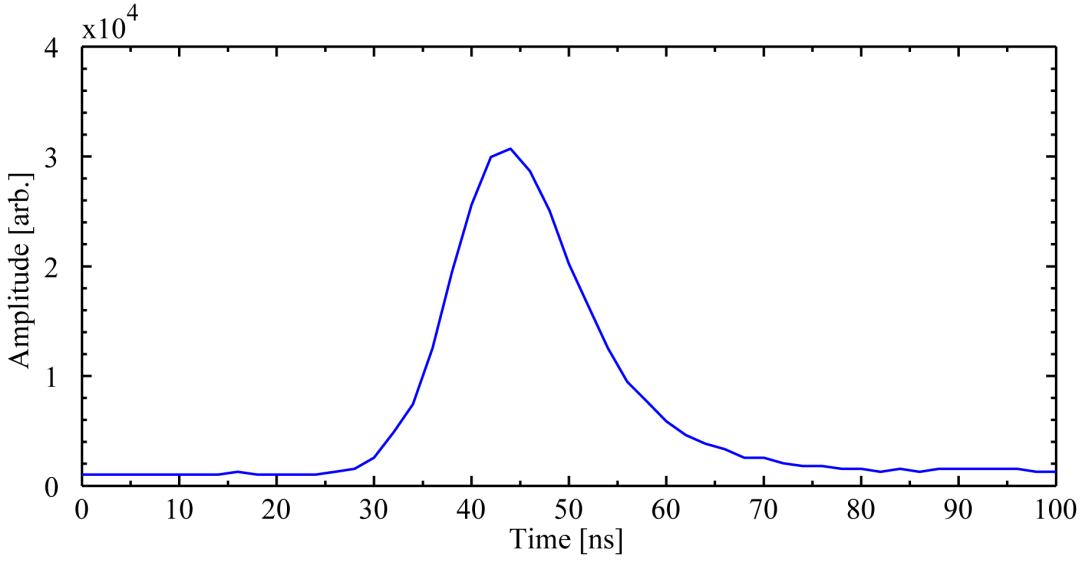

Figure 3.19: Time-dependence of a laser pulse from the tunable cavity of the Photonics 1 laser pair. The peak is centered at 44 ns with a FWHM of 20 ns.

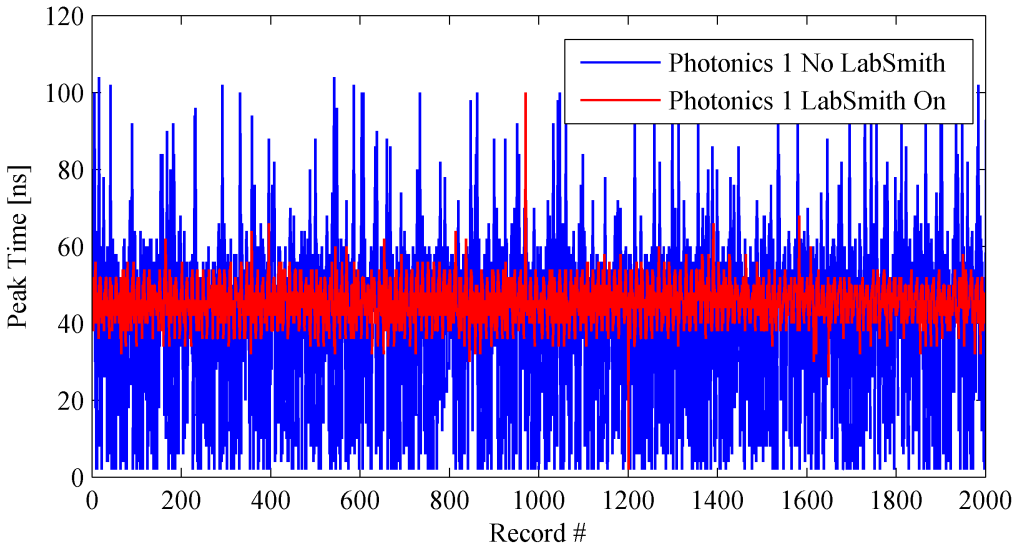

Figure 3.20: The time of the laser pulse peak for 2,000 consecutive laser pulses relative to $t = 0$. The desired time for the pulses was 44 ns. The blue distribution is for pulses not controlled by the feedback system. The red distribution was obtained with the timing-feedback system.

have employed a feedback system. The relative timing of each Ti:Sapph cavity is monitored by a photo-diode connected to one of two LabSmith programmable logic controllers (model LC880). The controllers monitor laser timing using the photo-diode signals as inputs and adjust the timing of the firing signal for the Nd:YLF lasers so that successive laser pulses are synchronized with the system clock. Finally, because each Ti:Sapph cavity produces a pulse at slightly different times relative to its pump laser, adjustments to the timing of the lasers can be made via the laser control computer. Figure 3.20 shows 2,000 consecutive measurements of the time of the laser pulse peak relative to $t = 0$ with and without the use of the LabSmith timing-feedback. $t = 0$ for this measurement represents the end of the SIMS suppression pulse. The desired timing of the pulse peak was at 44 ns. It is clear that the reproducibility of the laser pulse timing is greatly improved with the feedback system. Figure 3.21 shows histograms of the data in Fig. 3.20. The distribution without feedback control (a) has a peak near the desired time of 44 ns but also contains a significant number of pulses with widely varying times. The pulse pile-up seen at short times is likely due to pulses with peaks before $t = 0$. The distribution (b) obtained while the feedback system controlled the laser timing is tightly grouped around the mean of the distribution. It is well described as a Gaussian with a FWHM of about 14 ns. Additionally, there is a statistically significant preference for the laser pulse to arrive ~ 8 ns after the desired time that is not well understood. For this laser cavity design, the time spread (14 ns) is comparable to the pulse length of the lasers (20 ns) and will reduce the efficiency of the laser ionization. This has prompted the move to build new laser cavities for use in future work that reduces pulse-to-pulse timing fluctuations to $\sim$4 ns (see Sec. 6.2).

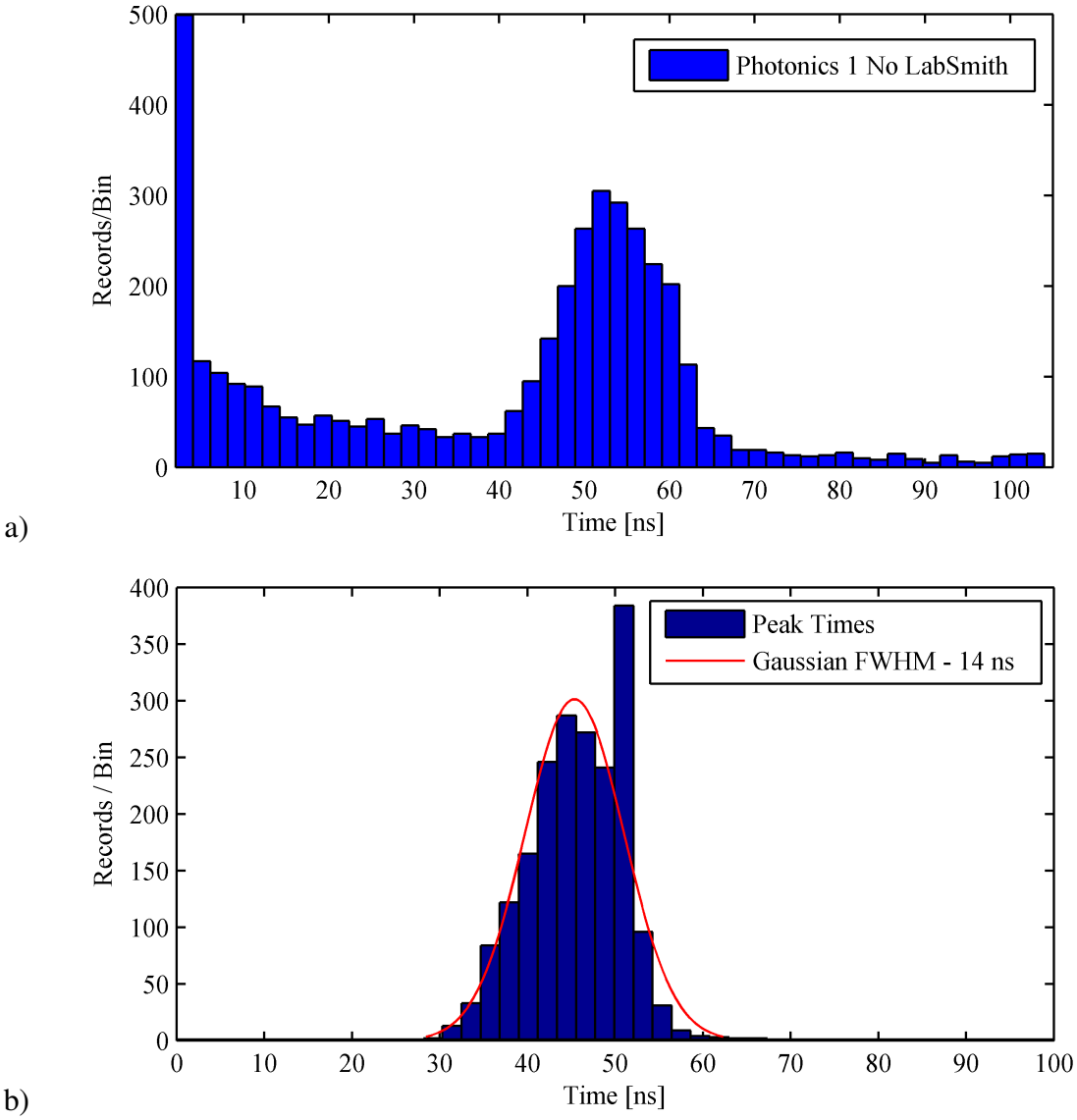

Figure 3.21: Distribution of laser pulse peak time for Photonics 1: a) without timing-feedback, b) with the timing-feedback system.

3.1.5.4 Laser Pointing Stability

Finally, the stability of the position of the laser beams was recently improved [14] by controlling the ambient temperature of the laser cavities and the optics responsible for steering the laser light to the sample chamber. We stabilized the temperature with regulated infrared heaters (Kalglo model MR-1215) that maintain a constant temperature (0.3° C tolerance). The drift in laser beam pointing in the Ti:Sapph cavities is now less than $30\,\mu$rad to ensure that the position of the laser beams directly above the target surface is stable to about 0.1 mm.

3.2 Ionization Schemes

Uranium has one of the most complex atomic structures of the naturally occurring elements. In its ground state it has six optically active electrons outside of a radon shell ([Ra]$5f_3 6d 7s_2$) that result in complicated atomic spectra. The ground state has even parity, an electron orbital angular momentum of $J = 6$, and a Russell-Saunders term structure of $^5L_0$. The ionization potential is 49,958.4 cm^{-1}, which is equivalent to about 6.19 eV[26]. Recall from Sec. 2.3.2 that the only odd isotope we investigate is ^{235}U, which has a nuclear spin of $I = 7/2$.

The main focus of our work employed the scheme from Schumann, *et al.* [51] that uses three resonant steps (3-photons) where each transition utilizes a different wavelength (3-colors of light). We also examined a 2-color, 2-photon scheme outlined in the work of Ray, *et al.* [68].

3.2.1 3-color, 3-photon U Scheme

Figure 3.22 shows a partial energy level diagram of uranium showing the 3-color, 3-photon ionization scheme for ^{235}U and ^{238}U. It includes the energy and angular momentum of the levels involved and the wavelengths of the lasers used to excite each transition. The scheme excites uranium atoms from their ground level ($E = 0\,cm^{-1}, J = 6$) to the first excited level[4], which has odd parity, a total angular momentum of $J = 7$, and an energy of 24066 cm^{-1}. The second transition excites the atoms from the first excited level to a level near 36127 $cm^{-1}$with $J = 8$. Finally the excited atoms are ionized by excitation to one of the two autoionizing states we explored near 49974 cm^{-1} with $J = 9$ or 8. The two autoionizing states were already introduced in Fig. 2.7 and are identified by the arrows in that figure. Schumann, *et al.* preferred the first state at 49,971.785 cm^{-1} with $J = 9$ because it is reached via a $\triangle J = +1$ transition and was the strongest autoionizing state they identified. During our experimental confirmation of the uranium spectroscopy discussed in the next chapter (Fig. 4.20), we found that we could produce more uranium photoions using the very broad resonance (30 GHz) at 49,974.544 cm^{-1} with $J = 8$. The characteristics of the ^{238}U levels and the known isotope shift values for ^{234}U, ^{235}U, and ^{236}U in this ionization scheme are summarized in Table 3.1.

[4]The electron configuration for this level is $5f_3 6d 7s_2 7p$, with a level term assignment of ^{5}L. The other excited states do not have known electron configurations or term level assignments, only angular momentum and parity are known.

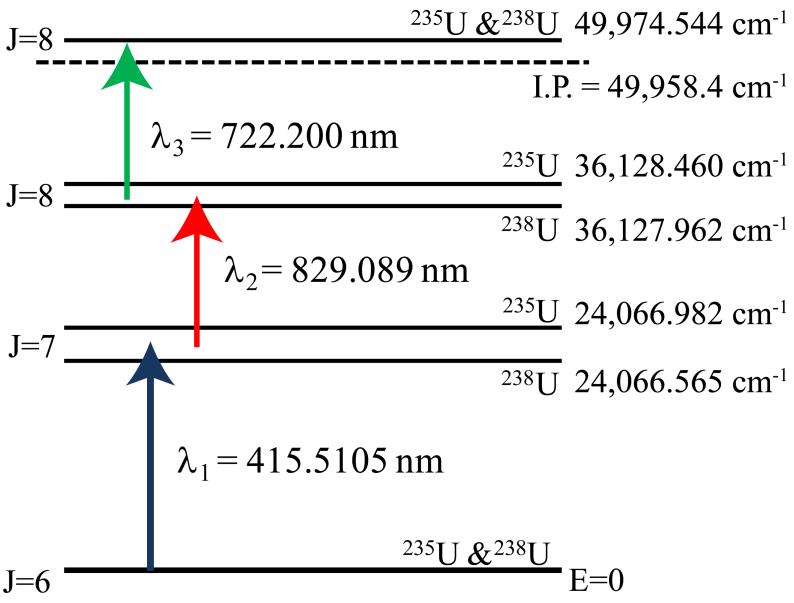

Figure 3.22: A 3-color, 3-photon U ionization scheme. This partial energy diagram shows the isotope shift between the levels of ^{235}U and ^{238}U used in this scheme and the wavelengths of the lasers used to excited these transitions between the levels. On the left are the total electron angular momenta of the levels.

Level	^{238}U [cm^{-1}]	^{238}U [nm]	J	τ [ns] or Γ	^{234}U [MHz]	^{235}U [MHz]	^{236}U [MHz]
Ground	0	0	6	-	-	-	-
1	24066.565	415.514	7	57(5)	14,912.46(95)	12,511.97(58)	7,482.6(28)
2	36127.962	829.091	8	215(21)	17,765.99(34)	14,913.80(44)	unk.
Autoionizing I	49974.544	722.202	8	30(2) GHZ	unk.	unk.	unk.
Autoionizing II	49971.785	722.344	9	65(3) MHz	15,294.47(60)	12,889.90(21)	unk.

Table 3.1: Energy, angular momentum assignments, and average lifetimes of ^{238}U levels used in this scheme and the known isotope shifts of ^{234}U, ^{235}U, and ^{236}U. Unknown values are indicated by unk. [51, 42, 69, 70, 32, 71]

Energy of ^{238}U level [cm^{-1}]	^{235}U Isotope Shift [MHz]	A [MHz]	B [MHz]
0	0	-60.559(3)	4,104.15(20)
24066.565	12,511.97(58)	-108.172(35)	2,074.44(28)
36127.962	14,913.80(44)	-105.639(24)	3,269.7(23)
49974.544	unk.	unk.	unk.
49971.785	12,889.90(21)	59.87(13)	4,382.5(96)

Table 3.2: Hyperfine Splitting in ^{235}U. The isotope shift in ^{235}U is reported as the mean energy of the hyperfine states relative to ^{238}U. The measured constants A and B reported in Schumann, *et al.* and Childs, *et al.*[51, 52] can be used in Eq. 2.56 to find the energies of individual hyperfine states of ^{235}U.

Because ^{235}U is an odd isotope, the spectroscopy is particularly complicated relative to the even isotopes of uranium. Schumann, *et al.* [51] paid particular attention to measuring the hyperfine structure of ^{235}U, which allows us to calculate the energy of individual transitions using their empirically determined constants and the Casmir formula (Eq. 2.56). Table 3.2 lists the values of the mean ^{235}U isotope shift relative to each level of ^{238}U and the measured constants A and B reported in Schumann, *et al.* and Childs, *et al.*[51, 52]. The A and B constants have not been measured for the very broad autoionizing resonance near 49974.544 MHz used in our scheme.

Compared to the isotopically selective application of the ionization scheme by Schumann, *et al.*[51], we were interested in isotopically equivalent ionization probabilities and so use laser wavelengths centered between the wavelengths of ^{235}U and ^{238}U for each transition. Therefore, the wavelengths used to excite the above transitions are $\lambda_1 = 415.5105$ nm, $\lambda_2 = 829.900$ nm, and $\lambda_3 = 722.200$ nm (or 722.344 nm for the very narrow autoionizing state). We also explored the use of the second-harmonic (532 nm) from the LaserPath Nd:YAG as the third laser in order to ionize atoms from the second excited state into the continuum (near 54,923 cm^{-1}).

Other ionization pathways exist in uranium for the laser beams used in this scheme. The most probable pathway is a 2-color, 3-photon process. In this process the atom is excited to the second excited state (36,127 cm^{-1}) by absorption of one photon each from the first and second lasers, but then ionized by an additional photon from the first laser (415 nm, nearly 3 eV) instead of by a photon from the ionizing laser (722 nm). This pathway will be a significant component of the ionization probability only when the ionizing laser (722 nm) is very low in power or not present. More complicated ionization pathways also exist, but require near-simultaneous absorption of at least two photons through virtual excited states. The probabilities for ionization via these pathways will be orders of magnitude smaller than the 3-color, 3-photon pathway. We will explore the influence of these pathways on the ionization probabilities of uranium atoms in Sec. 4.1.5 and Sec. 4.3.4.

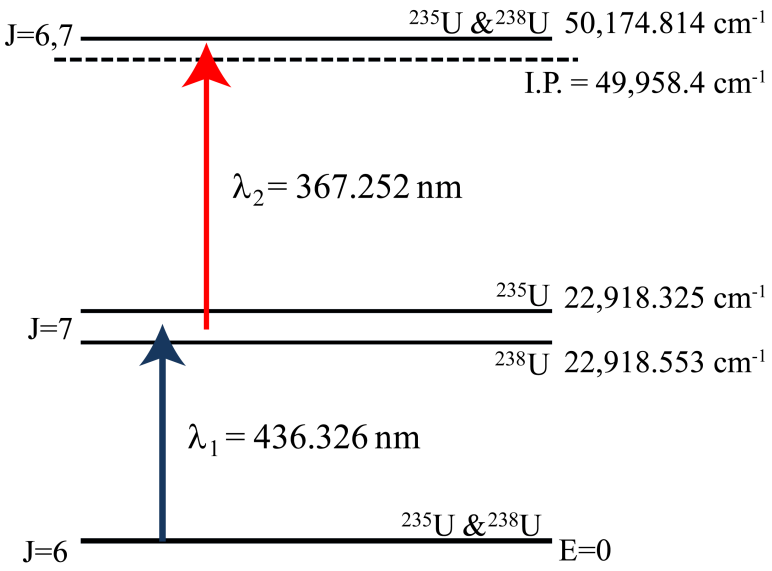

Figure 3.23: 2-photon ionization scheme showing the bound excited states of ^{235}U and ^{238}U and the energy of the autoionizing state along with the laser wavelengths use to induce the transitions between levels.

3.2.2 2-color, 2-photon U Scheme

We also explored the use of a 2-photon ionization scheme described by Ray, *et al.*[68]. Less is known about the hyperfine structure of ^{235}U and the isotope shifts of the minor uranium isotopes for the atomic levels in this scheme. The scheme first excites a bound level near 22,918 cm^{-1} [27] and then ionizes the U atoms using a transition to an autoionizing state near 50,147$\pm$0.5 cm^{-1}. The bound excited state has an electronic configuration of $5f_3 6d 7s_2 7p$, with a level term assignment of ^{5}L, and total angular momentum of $J = 7$. The isotope shift of ^{235}U for the first excited state is -0.228$\pm$65 cm^{-1} (-4.3$\pm$1.2 pm)[27]. The autoionizing state at 6.22 eV is 27,229.25$\pm$50 cm^{-1} (367.252 nm) above the first excited state of ^{238}U. It likely has total angular momentum of $J = 6$ or 7 because it is accessible by transitions from excited states with either $J = 6$ or 7[68]. The partial energy level diagram and the wavelengths of the two lasers used in this scheme are shown in Figure 3.23.

3.3 Data Analysis and Investigated Materials

This section explains the methods used for the analysis of experimental data presented in the proceeding chapter. We begin by exploring how to interpret the time-of-arrival signal to identify the mass of ions detected and then discuss the propagation of uncertainty through our

data analysis. We conclude this chapter with a description of the uranium standard materials that were examined.

3.3.1 Data Analysis

3.3.1.1 Mass Calibration

As we have already discussed, ions of different mass have different times of arrival at the plane of the detector. This time-of-arrival can be converted into a mass-to-charge ratio of ions transmitted through the mass spectrometer to provide a mass calibrated spectrum. This calibration depends on material standards with well-characterized composition. Based on the standard's composition we can predict a pattern of expected ion peaks of known mass. The time-location of the expected ion peaks are assigned mass values by the user and these time-mass value pairs are used to create a mass scale. This is done using the relation, $m = [(t - t_0)/B]^2$, where $t_0$is a time offset and B is a variable that scales the mass peaks to correspond to their time of arrival. Because there are two unknown parameters (t_0 and B) in this relation, using the time-mass values of two peaks is sufficient to solve the pair of equations to determine the unknowns. More practically in our system, the instrument's analysis software fits the values of the two parameters to minimize the least-square difference between the user-assigned mass and the calibrated mass of all the user selected peaks. The time-of-arrival information is recorded by the acquisition software alongside the calibrated mass, so that the data can be re-calibrated after acquisition if necessary.

Figure 3.24 shows the result of a typical mass calibration of time-of-flight signals for a uranium oxide standard that has approximately equal abundances of ^{235}U and ^{238}U, and contains ^{234}U at an abundance of 1 % (see the description of CRM U500 below). The figure shows three major peak groupings each of which contains three prominent peaks of at least 10 counts in the peak channel. There are also a few smaller peaks seen throughout the spectrum. The three groupings correspond to the ion signals from U^+ (near 0.116 ms), UO^+ (near 0.121 ms) and UO_2^+ (near 0.125 ms). Each of these groupings has two peaks of essentially equal total counts and a smaller peak just before them. These peaks correspond to ^{234}U, ^{235}U, and ^{238}U in order of increasing time.

3.3.1.2 Mass Peak

The number of ions at a particular mass in an experimental spectrum is defined by the sum of ion counts ($N_{sum} = \sum_{bins} N_{counts}$) in the peak. The mass peak is defined by setting a range in arrival time for ions of a particular mass. The range is a number of digitizer time-bins (2 ns/bin) that define the extent of the mass peak in time. We use a constant window size for all mass peaks within an experiment. Typically, we set the range to be a window approximately 1 amu wide ($\sim$ 200 ns). By using a constant range, we expect that, on the average, random background counts will contribute equally to each mass peak. However, this increases the relative contribution of background to the total ion signal in low abundance peaks.

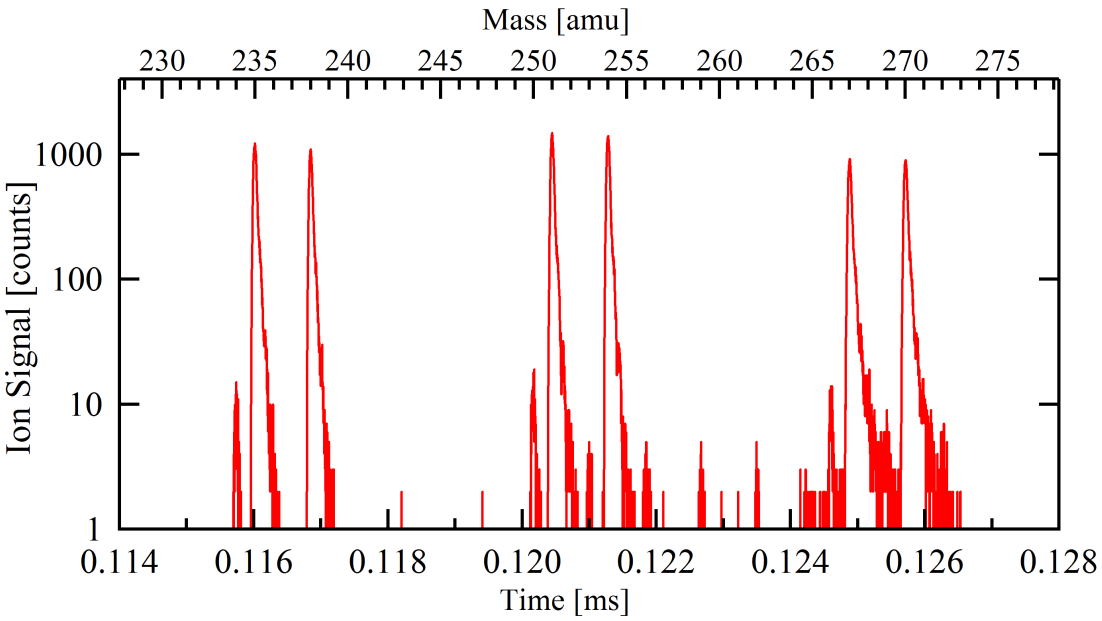

Figure 3.24: Mass calibration of a time-of-arrival signal for U500 standard. There are three prominent groupings of ion peaks in this spectrum, each grouping contains two peaks of nearly equal amplitude and at least one smaller peak on the short time side of the group. These peak groups correspond to the atomic (0.116 ms), monoxide (0.121 ms), and dioxide (0.125 ms) ions of uranium bearing species. The peaks within a grouping correspond to ^{234}U, ^{235}U, and ^{238}U in order of increasing time.

3.3.1.3 Dead-time Considerations

At high count rates in digital detection mode, our system can suffer appreciable dead-time effects that are dominated by the response of the discriminator. Multiple ions that arrive at the detector in a single time bin (2 ns wide) are recorded only as a single ion count. This is by far the largest potential source of missed ion counts in our system. If the count rate is 1 ion in the time bin per 10 laser pulses, then, on average, the probability of two ions arriving simultaneously is approximately 1 %. Thus, to keep the dead-time correction small, we adjust the count rate of ions in the most populated time bin of any peak we wish to quantify to be under 0.2 per laser pulse. The count rate is adjusted by changing the Ga^+ ion current on the target. We can ignore elevated count rates in peaks we do not wish to quantify as long as they arrive in time after the ions of interest or arrive sufficiently early in time as not to prevent the detection of the desired mass peaks by paralyzing the detector. Following these operating guidelines, we expect a maximum of 2×10^4 ion counts per 10^5 laser pulses in the single time bin associated with the peak of a given ion mass peak.

The dead-time correction for the probability of two ions arriving simultaneously in a single time bin is made following the correction outlined in Stephan, Zehnpfenning, and Benninghoven, 1994 [72]. We assume that the probability per unit time that any single ion will arrive at the detector is small. We then assume that the distribution of arrival times is Poisson. As a result of the dead-time effects in the discriminator, the mean number of particles detected, N_{counts}, will be less than the number arriving at the detector, N_{real}, by

$$N_{counts} = 1 - \mathrm{e}^{-N_{real}} \tag{3.2}$$

and,

$$N_{real} = ln\left(\frac{1}{1 - N_{counts}}\right) \tag{3.3}$$

We can approximate that the mean number of counts detected per laser pulse per time bin will be close to N_{counts}/N_{pulses}, where again N_{counts} is the number of counts recorded in a time bin and N_{pulses} is the number of laser pulses for which ions were collected. Therefore, the number of total ions arriving at the detector (N_T) in a given mass peak can be estimated from the sum of the correction for each time bin in that peak,

$$N_T = \sum_{bins}\left[N_{pulses} \cdot ln\left(\frac{1}{(1 - N_{counts}/N_{pulses})}\right)\right] \tag{3.4}$$

Instead of doing the dead-time correction bin-by-bin as above, we instead estimate the number of counts that have been missed due to dead-time effects for the entire mass peak. We assume a typical peak shape for CHARISMA and 10^5 laser pulses. We have developed an empirical estimate of total ion signal as a function of total counts in the mass peak,

$$N_T = N_{sum} + 1.25 \times 10^{-7} \cdot N_{sum}^{2.013} \tag{3.5}$$

where N_T is the total signal and N_{sum} is the total counts in the mass peak. This estimate has been fit to agree with the bin-by-bin dead-time correction in Eq. 3.4 for the peak shapes generated in our experiments. As an example, a ^{235}U mass peak was measured to contain $N_{sum} = 38,971$ counts. Both the bin-by-bin and the empirical dead-time corrections would predict 218 counts were missed over the entire mass peak giving $N_T = 39,189$ total ions. The dead-time correction for this peak is 0.5 % of the ion signal.

In analog detection mode, the acquisition hardware can handle a much larger number of ions in a mass peak before dead-time considerations begin to be appreciable because the discriminator is not used.

3.3.1.4 Background Corrections

The total ion signal (N_T) in a mass peak is a combination of both the desired resonant-photoion signal and ions from all other processes, referred to as background. The sources of background are: dark counts in the detector, incompletely-suppressed secondary ions, ions desorbed by the accidental interaction of the ionization lasers with the target, and non-resonant photoions that may consist of ions generated from neutral atoms or molecules or by the photo-disassociation of molecules. If N_T is the total number of counts and N_B is the total number of background counts, then $N_R = N_T - N_B$ is the number of resonant-photoion counts. N_B can be measured directly by detuning the wavelength of the resonance lasers and measuring the remaining ion signal.

3.3.1.5 Mass Bias from Sputtering and/or Mass Spectrometry

All mass spectrometers are vulnerable to systematic errors in measured isotope ratios resulting from preferential transmission through the instrument. In addition, there is a possibility for the fractionation of isotopes as a result of the sputtering process itself [62]. These biases are corrected by comparing unknown samples with standards of known isotope abundances. This method is only as good as the similarity of chemical and morphological composition of the standard and the unknown sample. The results reported here are only for measurements on uranium standards and thus do not utilize a correction for instrumental mass bias and fractionation in sputtering. However, we can use the isotope ratio of the uranium oxide ion species also collected during our measurements as an internal standard for the instrumental mass bias and sputter induced fractionation. We expect these two sources of isotope ratio bias to be constant as a function of time for a given target material. As we will discuss in Sec. 4.1.1, we find that the measured isotope ratios of UO^+ and UO_2^+ ions agree with the certified isotope ratios to better than 1 %. This indicates that the experimental mass bias expected in the U^+ ion isotope ratios due to instrumental mass bias cannot be greater than 1 %. This estimate does not include the isotope fractionation expected in the resonant ionization process, which as we will soon see dominates the experimental bias in measured isotope ratio.

3.3.1.6 Constructing Measured Isotope Ratios and Error Propagation

To define an experimentally determined isotope ratio (R_{12}) we simply take the total signal for isotope 1 (N_{S1}) and divide by the signal for isotope 2 (N_{S2}), $R_{12} = N_{S1}/N_{S2}$. We typically report isotope ratios relative to the heavy isotope (*i.e.* ^{235}U/^{238}U). We also find it useful to express the measured isotope ratio relative to the certified ratio to emphasize experimental isotopic fractionation. This is expressed using a percent difference from the certified value,

$$\%\,\text{Difference} = \left(\frac{\text{Measured Ratio}}{\text{Certified Ratio}} - 1\right) \cdot 100 \tag{3.6}$$

We express the total uncertainty for the measured value of the isotope ratio by propagating the uncertainties due to the individual steps of determining the photoion signals. We assume that the result of an individual measurement is subject to Poisson statistics and therefore estimate the standard deviation in the sum of counts in a given mass peak, in the absence of any effects from background, dead time, etc., as $\sigma_{sum} = \sqrt{N_{sum}}$. The uncertainty due to a dead-time correction will be proportional to the square-root of the correction $\sqrt{N_{DT}}$, and the combined uncertainty then becomes $\sigma_T = \sqrt{N_{sum} + N_{DT}}$. If a background subtraction is used to estimate the contribution of background sources of ions in the measured mass peak then the uncertainty in the ion signal σ_S will be increased by the uncertainty in the background subtraction $\sigma_B = \sqrt{N_B}$. Finally, the uncertainty of the isotope ratio (σ_R) will be due to the sum in quadrature of the relative uncertainties in the individual isotope signals multiplied by the ratio,

$$\sigma_R = R_{12} \cdot \sqrt{(\frac{\sigma_{S1}}{N_{S1}})^2 + (\frac{\sigma_{S2}}{N_{S2}})^2} \tag{3.7}$$

where N_{Si} is the total photoion signal in the mass peak of isotope i, $N_S = N_{sum} + N_{DT} - N_B$, and σ_{Si} is the uncertainty in the signal for isotope i, $\sigma_{Si} = \sqrt{N_{sum} + N_{DT} + N_B}$.

We define an expectation value for the measurement, $\langle x \rangle = \frac{\sum_i x_i}{n}$, where x_i is the value of the ith measurement and n is the total number of samples of the population. This is used to determine the standard deviation of each measurement about the mean using

$$\sigma_i = \sqrt{\frac{\sum_i (x_i - \langle x \rangle)^2}{n-1}} \tag{3.8}$$

We then define the standard error of the mean from the collection of measurements as

$$\sigma_{\langle x \rangle} = \frac{\sqrt{\sum_i \sigma_i^2}}{n} \tag{3.9}$$

and the relative standard error (RSE) is then defined by the ratio of the uncertainty in the mean to the value of the mean,

$$\text{RSE} = \frac{\sigma_{\langle x \rangle}}{\langle x \rangle} \tag{3.10}$$

that we often express as a percent error ($\%\,error = RSE \cdot 100$) and is a measure of the reproducibility (precision) of the measurement result. That is, the expectation that if we performed another measurement of the investigated quantity, the result of that measurement will fall within the stated percent error of the measured mean about 95 % of the time. This analysis assumes that the sample mean is representative of the population mean.

We can correct the measured isotope ratio of an unknown sample using sample-standard bracketing. This is done by correcting the isotope ratio of the unknown by the difference between the measured and certified values of a standard. When we express the comparison of the measurement of the unknown sample as a percent difference from the measured value of the standard, then the estimated uncertainty in the value of the measurement of a corrected unknown ($\sigma_{Corrected}$) due to the counting statistics is expressed by,

$$\sigma_{Corrected} = (\%\,\text{Difference} + 100) \cdot \sqrt{(\frac{\sigma_{S1}^{unk.}}{N_{S1}^{unk.}})^2 + (\frac{\sigma_{S2}^{unk.}}{N_{S2}^{unk.}})^2 + (\frac{\sigma_{S1}^{std.}}{N_{S1}^{std.}})^2 + (\frac{\sigma_{S2}^{std.}}{N_{S2}^{std.}})^2} \qquad (3.11)$$

where the superscript *unk.* refers to the measurements performed on the unknown sample and the superscript *std.* refers to the measurements of the standard.

3.3.2 Investigated Materials

The uranium composition and the certified isotope abundances (with reported uncertainty) for each uranium isotope standard used in the experiments reported in this work is given at the end of this section in Table 3.3. Together these standards cover a range of ^{235}U abundance from 0.7 to 90 %, over 3 orders of magnitude.

3.3.2.1 SRM 960

The Standard Reference Material (SRM) 960 is a natural U metal isotopic standard with a uranium oxide surface layer from prolonged exposure to air. The SRM 960 initially issued by the National Bureau of Standards in 1972 has been renamed by New Brunswick Lab as CRM 112-A. The standard nominally contains the natural abundances of uranium isotopes. The ratio of ^{235}U /^{238}U is certified to be 0.0072543(40) and the ^{234}U/ ^{238}U is $5.8241(82)\times10^{-5}$. No ^{236}U was detected during certification. Total trace impurities in the material are estimated at 223μg/g. The isotopic homogeneity is not guaranteed on pieces of material less than 1 g. The metal standard was mounted on an aluminum stub 1.27 cm in diameter with conductive epoxy and is shown in two photographs in Figure 3.25 taken at different magnifications with an optical microscope, 3x and 25x. This piece of SRM 960 has dimensions of about $1.5 \times 2 \times 0.3$ mm.

Uranium metal oxidizes rapidly in air. The uranium oxide layer formed on the surface is not single crystal UO_2 but often is composed of a mixture of uranium-oxygen stoichiometries [73]. Generally, the growth rate of the oxide layer in air is dominated by diffusion of oxygen into the substrate and the thickness of the layer is proportional to the square-root of the time of exposure ($\sim$ 10 nm after 15 hr), though at short times (< 1 min) the layer can grow at a faster

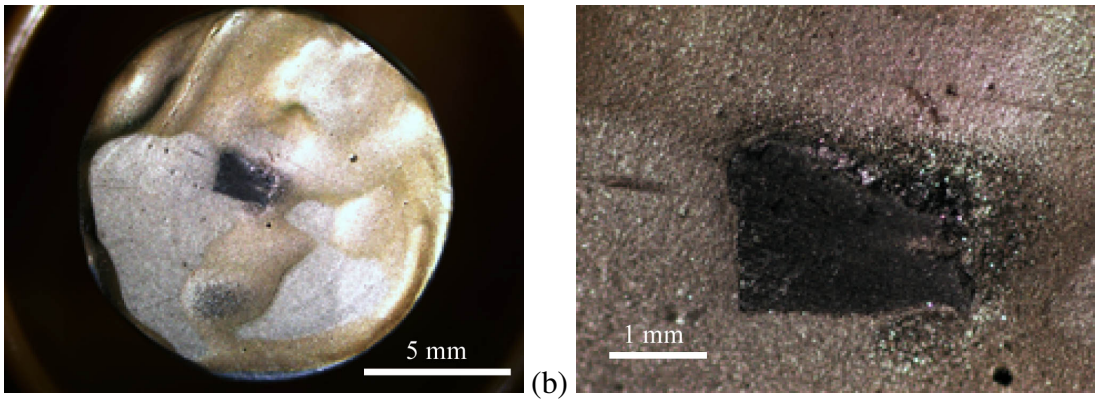

Figure 3.25: Photographs of the SRM 960 mount taken through an optical microscope: (a) at a magnification of 3x, (b) zoomed in on the oxidized U metal standard at 25x.

pace [73]. Because our particular sample of SRM 960 has been exposed to air for several years (if not decades), we can safely assume a thick uranium oxide surface layer. The thickness of this layer has not been measured, but is not particularly relevant to our measurements as we do not require a pure metallic surface and it did not inhibit us from observing atomic uranium photoions produced by sputtering.

3.3.2.2 CRM 125-A

New Brunswick Lab's Certified Reference Material (CRM) 125-A is a standard of highly purified UO_2 enriched to 4 % ^{235}U meant to be utilized as an elemental and isotopic standard for comparison with uranium reactor fuel. In addition to being slightly enriched in ^{235}U, the CRM also has certified values of the trace isotopes ^{234}U and ^{236}U. We used two small pieces of CRM 125-A in our efforts, and transferred these pieces of CRM125-A from their own stub onto the stub that held the U500 (see below) to reduce the need to change samples during experiments. The total mass of the fragments is approximately 3.5×10^{-3} g and the surface area exposed is about 0.5×0.5 mm.

3.3.2.3 CRM UXXX Standards

We also used several standards in the CRM UXXX series that are highly purified U_3O_8. These standards are certified for their isotope abundances of ^{234}U, ^{235}U, ^{236}U, and ^{238}U. The estimated uncertainties in the isotope abundances include estimates of the isotopic inhomogeneity of the materials in addition to the analytical uncertainties. Accurate values for isotopic abundances and their estimated uncertainties are found in Tab. 3.3. All of these standards were mounted by pressing the grains of material into an indium metal foil which in turn was pressed against the aluminum stub. The total mass of each standard mounted on the stubs was 160.1(5) μg, 91.9(5) μg, and 76.1(5) μg for the U010, U500, and U970 mounts, respectively.

(a) 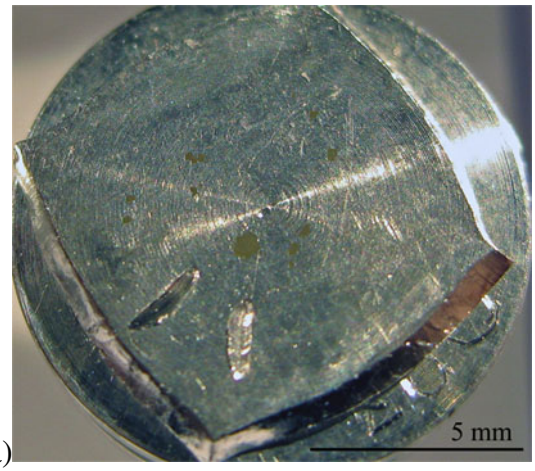

(b) 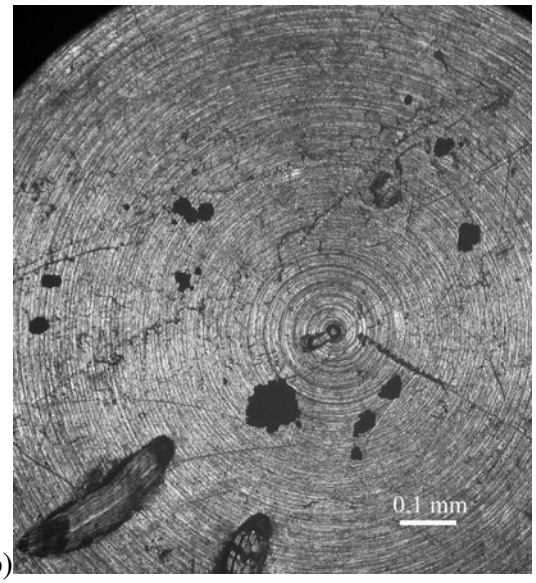

Figure 3.26: U970 standard mount. (a) Photograph of mount taken through an optical microscope at 4x, two scratches for mount orientation are seen near the bottom of the mount. At least one large cluster of U970 grains can be seen just above the two scratches. (b) a photograph of the U970 mount at 20x, the tips of the same scratches are visible in the bottom of the photo and the large grain is also easily identified as the dark dot above the scratches. Several other collections of grains can be identified on the surface of the mount in this picture.

Figures 3.26-3.29 contain optical and secondary electron microscopy (SEM) images of the uranium CRM standard mounts. Fig. 3.26 shows two photographs of the U970 standard mount under different magnifications. Grain clusters of the standard can be seen in both pictures, the largest collection of grains is just above the two tool marks near the bottom of the mount. Fig. 3.27 shows a photograph of the U010 mount at 8x magnification (a) and two SEM images (b and c) of a collection of grains on the mount. The SEM images show that the clusters are composed of a large number of small grains on the order of 1 micron in diameter. These grain sizes are typical across the CRM UXXX standards we investigated. Recall that typical spot sizes for our Ga ion gun are on the order of a few microns in diameter and that during analysis the ion gun beam is rastered over a $20 \times 20\,\mu$m area. Fig. 3.28 shows two photographs of the U500 mount, which has had two pieces of CRM 125-A also embedded in the surface of the In metal. The surface of this mount was also examined closely by SEM to map the position of the grain clusters (Fig. 3.29). Most of the large clusters are bounded by red boxes and a few have been labeled according to the order of investigation. The surfaces of the pieces of CRM 125-A are also clearly visible.

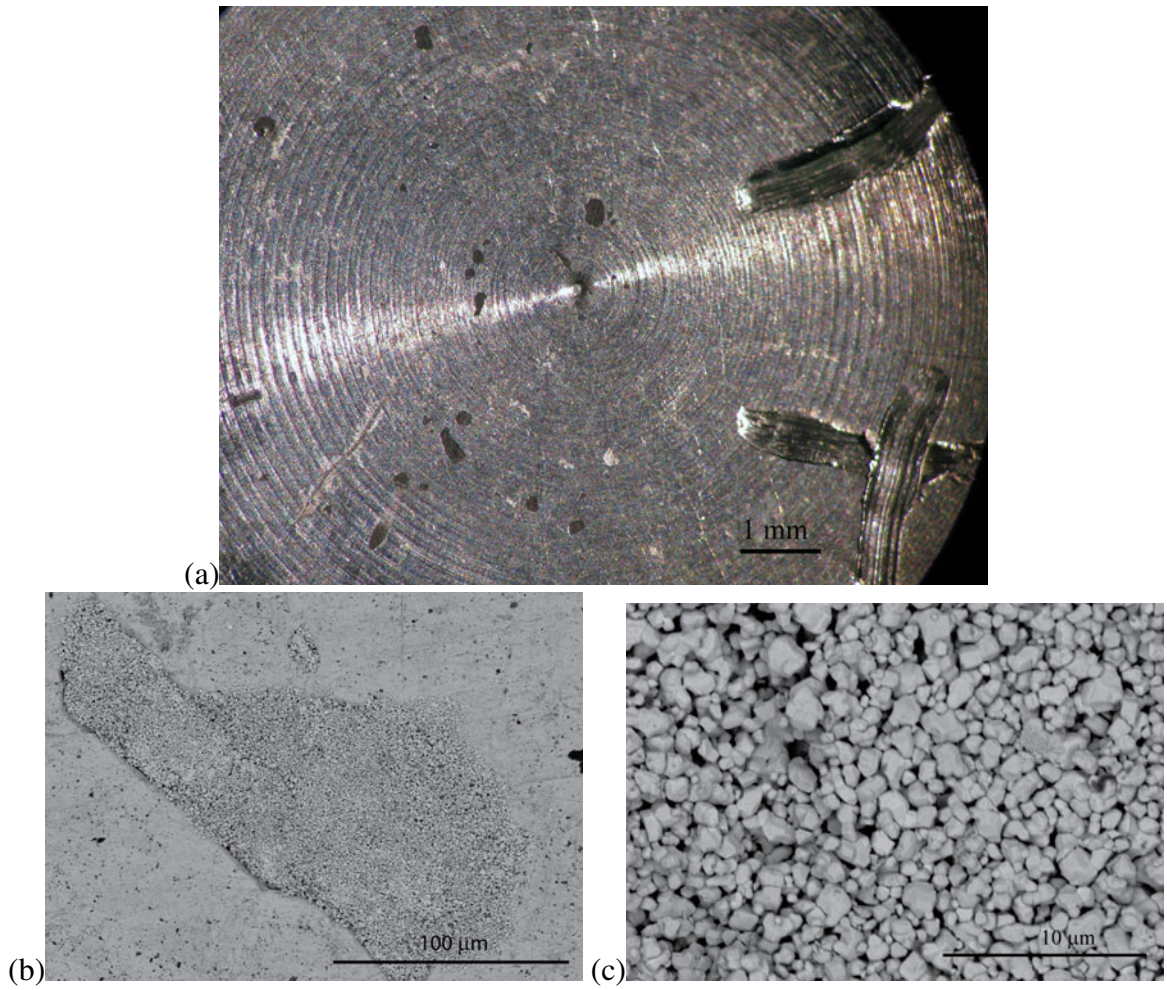

Figure 3.27: (a) Photograph of U010 mount taken through optical microscope at 8x. Secondary electron microscopy of grains of U010 at two different magnifications: (b) Secondary electron image, 5 kV accelerating voltage, scale bar 100 μm, (c) Back-scatter electron image, 5 kV accelerating voltage, scale bar at 10 μm. The size of the individual grains ($\sim 1\mu$m) is typical for all of the CRM UXXX materials.

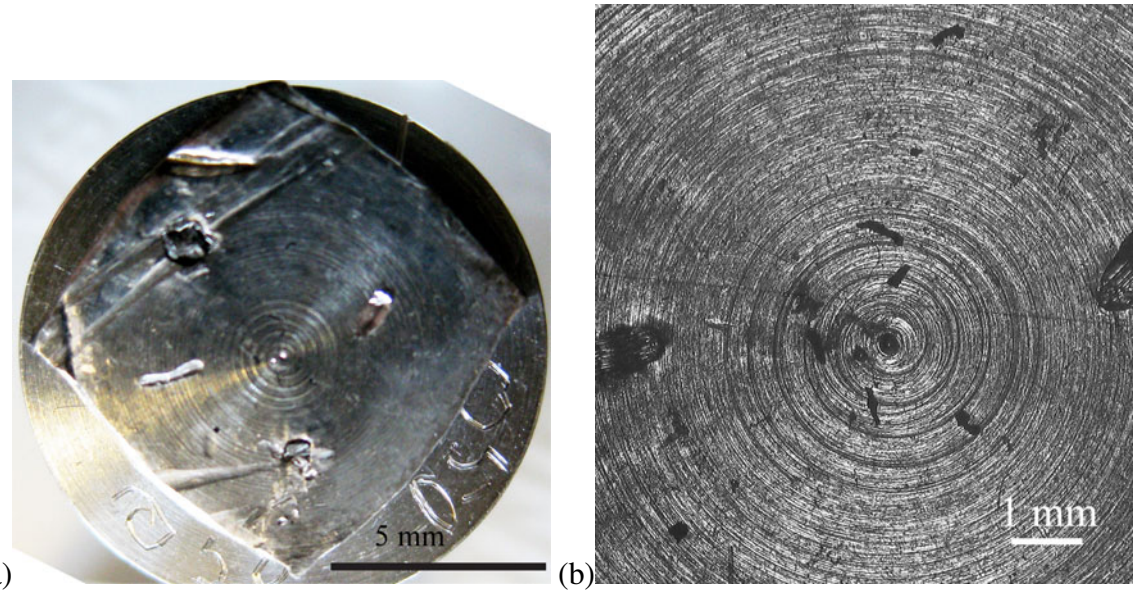

(a) (b)

Figure 3.28: Photographs of the U500 standard mount: (a) A photograph of the mount after two fragments of CRM 125-A have been added to the mount. The CRM 125-A pieces are visible in the upper left and lower middle of the mount near the tool mark impressions left from the embedding process. The U500 grains are concentrated near the center of the mount as is visible in the second image. (b) the U500 mount photographed through an optical microscope at 20x. There are tool mark depressions for orientation purposes visible on the edges of the images and the black spots are grain clusters of the U500 pressed into the In foil.

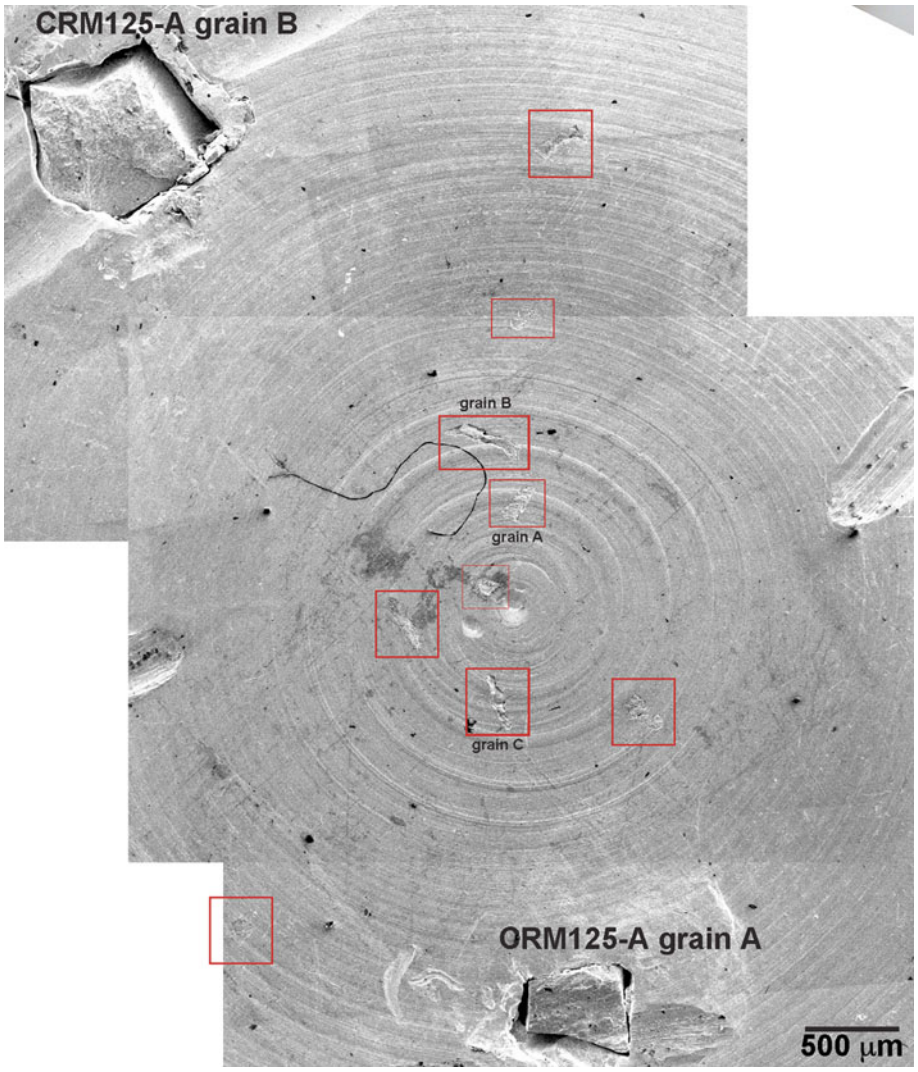

Figure 3.29: Secondary electron image of U500 mount with two CRM 125-A grains. The accelerating voltage was 5 kV. The red boxes identify clusters of uranium grains of U500 observed in back-scatter electron images of this mount. Also labeled, at top and bottom, are the two fragments of CRM 125-A that have been embedded into the indium.

Material	Composition	U Content [wt %]	^{238}U[at %]	^{235}U [at. %]	^{234}U [at. %]	^{236}U [at. %]
SRM 960	U metal	100(5)	99.27458(39)	0.72017(39)	0.0052458(81)	-
CRM 125-A	UO_2	88.129(14)	95.9049(29)	4.0574(28)	0.0374(3)	0.0003(2)
U010	U_3O_8	84.8(1)	98.984(1)	1.0037(10)	0.00541(5)	0.00681(7)
U500	U_3O_8	84.7(1)	49.711(50)	49.696(50)	0.5181(8)	0.0755(3)
U970	U_3O_8	84.6(1)	0.5229(6)	97.663(3)	1.6653(17)	0.1491(5)

Table 3.3: Standard materials and their certified isotope abundances in atomic percent. Errors are reported as 95 % confidence intervals of measured value. The uranium weight content is given in weight percent, the isotopic abundances are given in atomic percent.

Chapter 4

Experimental Results and Discussion

This chapter presents the results of experiments designed to understand the critical laser parameters that effect the measurement of uranium isotope abundances by RIMS. We will begin by exploring the characteristics of various ion signals observed with CHARISMA. Next, we will present the study of the individual resonance transitions involved in the ionization scheme and their dependence on laser performance. Finally, we will demonstrate the measurement of uranium isotope ratios to a reproducibility of better than 1 % on several standards. We will keep track of the different experiments described in a table located in Appendix A, which can be used as a quick reference for the instrument parameters.

4.1 Ion Signals

When the laser system is arranged to provide "on-resonance" ionization conditions, the measured ion signal is a composite of all the ion-forming processes in the instrument (*i.e.*, resonant ionization, non-resonant ionization, unsuppressed secondary ions). The interpretation of the mass spectrum obtained under on-resonance ionization conditions is only practicable when that spectrum is compared to a similar spectrum obtained under "off-resonance" conditions. By on-resonance ionization conditions, we are referring to the laser parameters specific to performing the resonant ionization of the specified atoms. The conditions are considered fulfilled when the wavelength, position, and timing of each laser beam required for the ionization scheme are properly aligned with the atoms and each other. By off-resonance ionization conditions, we are referring to a specific subset of non-resonant ionization conditions where, using the on-resonance ionization conditions as a reference, we change only the wavelength of a single laser (usually the first resonance laser) by a very small fraction of its total energy[1]. This change in wavelength is sufficiently large to reduce the probability of excitation of the resonance transition to be negligible, but is also sufficiently small so that the total energy per pulse is essentially unchanged. Thus, the ion signal from all ion-forming processes other than resonant ionization are negligibly altered from the on-resonance conditions. Off-resonance ionization conditions thus provide a direct measure of the background of the resonant ion signal. We will see clearly how this comparison of on-resonance to off-resonance ion signal works next. Then, we examine the contributions of other ionization conditions to ion formation.

4.1.1 On-Resonance Ion Signal

An "on-resonance" spectrum shown in Figure 4.1 was measured from the U500 target using the 3-photon, 3-color ionization scheme. The instrument conditions for this measurement are summarized in Appendix A as experiment #1, but are also included here for clarity. The wavelengths were adjusted to ionize both ^{235}U and ^{238}U nearly equally, because this target is enriched to 50 % in ^{235}U. The wavelengths, in order of excitation, were 415.5105, 829.089, and 722.200 nm. The laser beam energies were 75, 650, 500 μJ per pulse, respectively. The

[1] We commonly refer to this process as "detuning" the wavelength from the resonance transition wavelength.

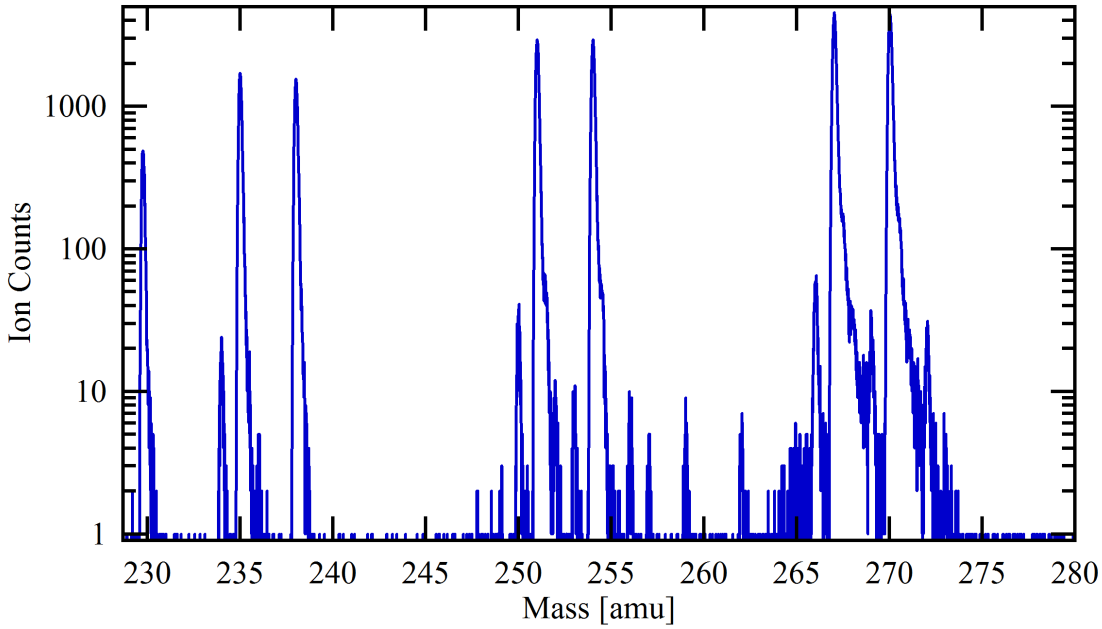

Figure 4.1: On-resonance ion spectrum generated by 10^5 laser pulses on the U500 standard. All three lasers were arranged to ionize ^{235}U and ^{238}U nearly equally. Experiment details are given in the text and in Appendix A under experiment #1.

first laser cavity was operated at an output power of 250 μJ and the beam was attenuated to 75 μJ using a neutral density filter. That laser used a 4x beam expander in its cavity to produce a "broad" bandwidth of $\sim$5 pm in the second-harmonic beam. The second laser cavity used a 6x beam expander to produce a bandwidth of 9(2) pm[2] and the third laser used a 40x beam expander to produce a laser bandwidth of 2.2(1) pm. The spectrum is the sum of 10^5 instrument cycles of CHARISMA (*i.e.,* 10^5 laser pulses).

In Fig. 4.1 there are seven ion peaks with more than 400 counts in the peak channel. The peaks occur at 229.8, 235, 238, 251, 254, 267, and 270 amu. The peaks are clearly asymmetric. Ions arriving early in a mass peak were produced with positions and velocities aligned with the axis of highest transmission of the mass spectrometer. These will be followed by ions that take less direct paths. As we already know the composition of the target and the substrate, we can easily identify the peaks. The peak assignments are summarized in Table 4.1. The peak near mass 230 is likely the dimer of the ^{115}In atoms from the substrate (the atomic mass of ^{115}In is 114.9 amu)[3]. The other six peaks can be assigned to atomic uranium and its oxide ions (UO^+ and $UO_2{}^+$) with approximately equal abundance of ^{235}U and ^{238}U species. After comparing the results of this experiment with an experiment performed under off-resonance conditions, we will examine this mass spectrum in greater detail.

[2]The uncertainties stated in parenthesis are always $\pm 2\sigma$ unless otherwise noted.

[3]Because the In_2 peak is below the mass region of uranium, we frequently neglect that region of the spectrum.

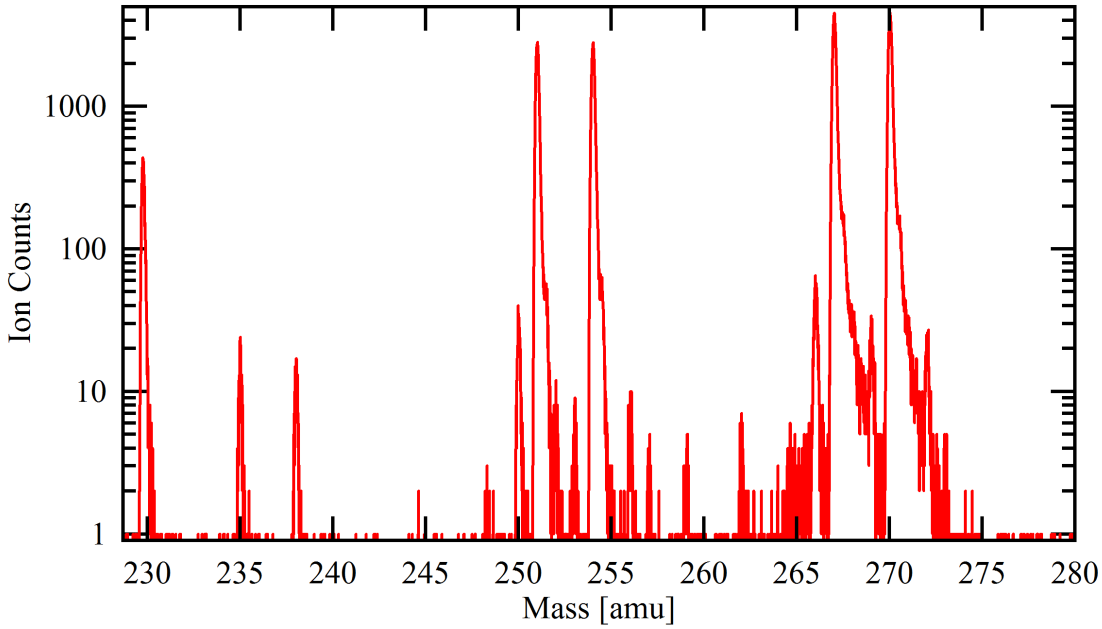

Figure 4.2: Off-resonance mass spectrum when the first resonance laser is detuned from resonance by 50 pm. Note that this spectrum is nearly identical to Fig. 4.1 except for the reduction of the peaks at mass 234, 235 and 238.

During the same experimental session we also measured the ion signal under off-resonance ionization conditions (experiment #2). All instrument parameters were maintained at the values used in the first experiment except for the wavelength used in the first excitation step. The wavelength of this laser beam was changed from 415.5105 to 415.561 nm, a change of only 50 pm. The ion signal resulting from 10^5 laser pulses is shown in Figure 4.2. The off-resonance spectrum in Fig. 4.2 looks identical to the spectrum in Fig. 4.1 apart from the difference in the intensities of the 234, 235 and 238 mass peaks. Because the only observable difference in experimental conditions was a small change in the mean wavelength of the first resonance laser beam, this supports our hypothesis that the peaks that have been reduced by $\sim$ 100-fold in intensity were from the resonant ionization of atomic uranium. The remaining peaks are a result of other ionization processes that do not depend strongly on the wavelength of the first laser, which we generally term "non-resonant" processes[4]. This is consistent with the major peaks in these spectra being identified as In_2^+, UO^+, and $UO_2{}^+$ species, where the oxides are each composed of ^{235}U and ^{238}U species.

Now we will explore two regions in these two spectra more closely: (1) the atomic uranium region, and (2) the uranium oxides region. Figure 4.3 and Figure 4.4 are composed of different mass regions of the on-resonance and off-resonance spectra in Figs 4.1 and 4.2. Fig. 4.3 shows

[4]It may be more appropriate to call these processes "semi-resonant" as the virtual excitation must take place through the tails of nearby resonances, but the essential point is that these processes show negligible dependence on the wavelength of the exciting radiation, but depend strongly on the the total intensity of photons.

Mass [amu]	Ion	Mass [amu]	Ion
229.8	$^{115}In_2^+$	251	$^{235}UO^+$
234	$^{234}U^+$	254	$^{238}UO^+$
235	$^{235}U^+$	266	$^{234}UO_2{}^+$
236	$^{236}U^+$	267	$^{235}UO_2{}^+$
238	$^{238}U^+$	270	$^{238}UO_2{}^+$

Table 4.1: Peak assignments from Figs. 4.1 through 4.4.

the region between 232 and 240 amu. It shows four distinct peaks in the on-resonance trace (blue) and two distinct peaks at 235 and 238 amu in the off-resonance trace (red). The peaks in the on-resonance trace correspond to ^{234}U, ^{235}U,^{236}U, and ^{238}U. There is also a population of single counts scattered randomly throughout the mass region. The peaks for the off-resonance data appear to be two orders of magnitude smaller than the on-resonance peaks, the relative ratio of total counts for the off-resonance/on-resonance peaks at 235 and 238 amu are 0.0098(5) and 0.0091(5), respectively. This result is consistent with other measurements of the atomic uranium signal in the other uranium standards under these laser conditions (wavelength, power, and bandwidth) where we observe that the off-resonance signal is typically less than 1 % of the on-resonance signal. The off-resonance peaks at mass 235 and 238 are likely due to either non-resonant ionization of atomic uranium or the photodissociation of uranium oxide species into uranium ions. We will discuss the probabilities for these processes when we study the dependence of the off-resonance signal on laser power.

The large difference of ion signal in the atomic U mass region stands in contrast to the minimal change in ion signal in the region of the uranium oxide species (250-280 amu) shown in Fig. 4.4. The signals from the two different ionization conditions are essentially indistinguishable. Peaks that do not respond to changes in wavelength cannot be distinguished from isobaric interferences that may be present in the ion signal. Thus, peak assignments in this region are more tentative because all of the ions are generated by non-selective ionization processes and are not used for measuring uranium isotope abundances. Possible isobars at these masses include molecules formed from ions at nearby masses with the addition of hydrogen atoms, or molecules with identical chemical composition but with different isotope combinations (*e.g.*, $^{236}U^{18}O$ and $^{238}U^{16}O$). The uranium monoxide species for the four detectable isotopes of uranium can be seen at masses 250, 251, 252, and 254. Uranium dioxide peaks can be seen at 266, 267, 268, and 270 amu. There are a few additional peaks in the spectrum at 253, 256, 269, and 272 amu that are most likely due to uranium oxide species composed of the minor isotope ^{18}O (0.2 % natural abundance relative to ^{16}O). The peaks at 257, 259, 262, and 273 amu have not been positively identified.

We will explore further the relative isotope abundance and the amounts of atomic uranium

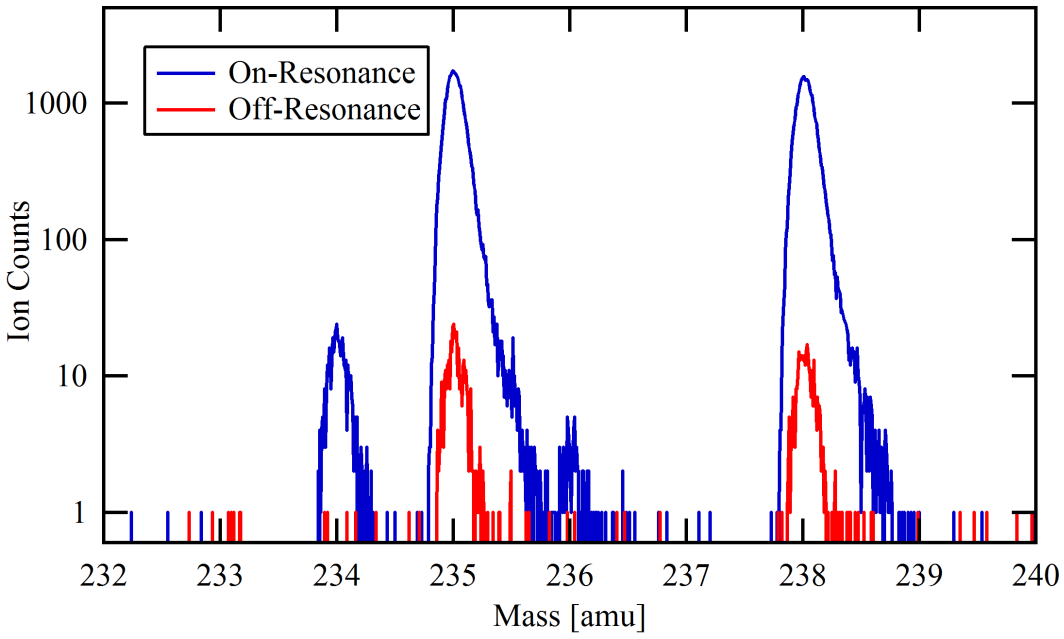

Figure 4.3: Atomic U mass region between 232 and 240 amu for both on-resonance and off-resonance ionization conditions. The ion signal in the off-resonance trace is less that 1 % of the ion signal in the on-resonance case.

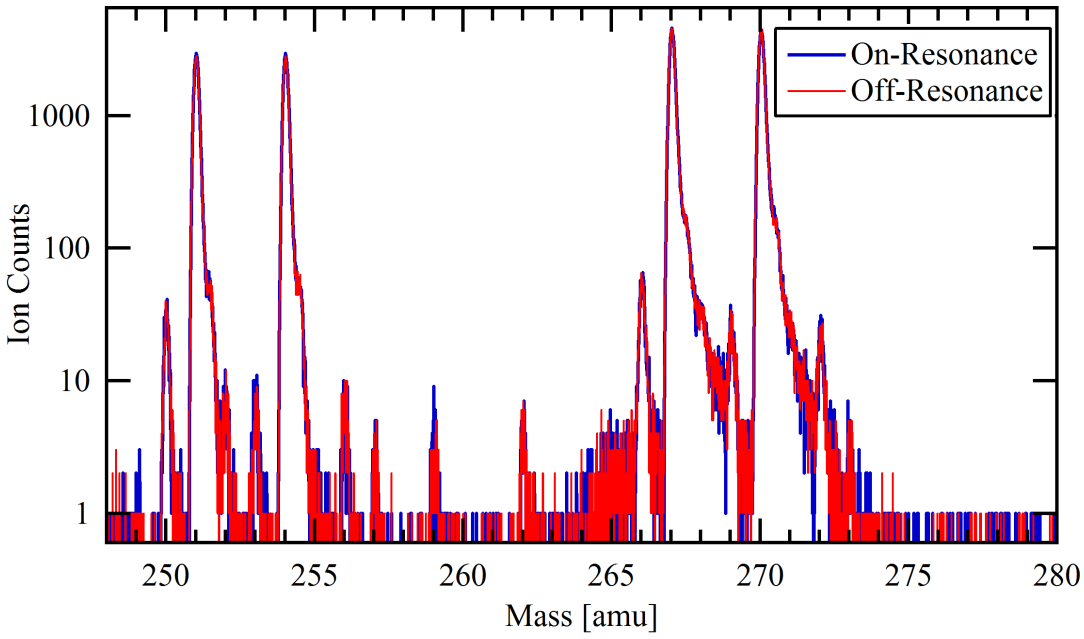

Figure 4.4: U oxide species mass region from 247 to 280 amu. The off-resonance trace has been made thinner than the on-resonance trace to help make both traces visible. The traces look equivalent.

to uranium oxide species in other experiments, but we list these quantities as measured in the present experiments for the interested reader. For the on-resonance experiment, the ratios of $U^+/UO^+/UO_2{}^+$ species are $1/1.74(1)/3.02(2)$. The measured ratio of $^{235}U/^{238}U$ for these three ion species is 1.092(8), 1.002(5), and 1.006(4) while the certified ratio for U500 is 0.9997(1). For the off-resonance experiment, the ratios of $U^+/UO^+/UO_2{}^+$ are $1/172(8)/301(15)$. The measured ratio of $^{235}U/^{238}U$ for these three ion species is 1.18(9), 1.012(5), and 1.007(4) while again, the certified ratio for the U500 is 0.9997(1). Note that non-resonant ionization processes have a chance to occur in all neutral atoms and molecules in the irradiation volume of the laser beam, regardless of initial excitation state, with varying efficiencies. This means that one cannot, from the off-resonance mass spectrum alone, answer the question of the relative population of uranium atoms to UO to UO_2 molecules in the neutral cloud. This would require more detailed experiments that ensured complete ionization of particles in the neutral cloud, although the analysis of experiments of this nature would be complicated by photodissociation.

Now that we have seen the approximate size of the resonant and non-resonant photoion signals we can expect in the analysis of uranium oxide materials, we will discuss the contribution of different sources of counts in the measured signal.

4.1.2 Dark Counts

We measured the count rate in our detector due to random secondary electron emission ("dark counts") by preparing CHARISMA for measurement (*i.e.,* U target in place, ionization lasers and Ga^+ gun on), but did not allow laser photons or sputtering ions into the experimental chamber during the measurement. The ions of the sputtering gun were blocked by turning off the Wien filter[5] of the ion gun, which and reduces ion current on the target to nearly zero (but not exactly zero so some dark counts may, in fact, be secondary ions from sputtering). Laser beams were blocked by placing a beam stop in the beam path prior to the target chamber. All other voltages and signals were left unchanged from a typical on-resonance measurement. A total of 25 counts were detected over the recorded mass range of 226-281 amu for 2×10^5 cycles of the system. The digitizer was on for 13.3 μs each cycle between 115 and 128.3 μs after the zero time of the system clock. This corresponds to a total time of 2.62 s when the digitizer was recording counts during the measurement, and gives a count rate of 9.5(2.0) counts/s. This equates to $1.25(3)\times10^{-3}$ counts per system cycle. In a mass peak ($\sim$100 ns window) acquired over 10^5 laser pulses the dark count rate will contribute 0.18(4) counts/peak, on average. The recorded mass spectrum for this dark count measurement is shown in Figure 4.5.

4.1.3 Secondary Ions

Typically, secondary ions are a potential source of background counts in our measurements. However, CHARISMA can be operated to collect and analyze secondary ion species if desired.

[5] A Wien filter acts as an ion velocity selector, this is accomplished by applying an electric field perpendicular to a magnetic field. When ions are introduced into the fields only those ions with a velocity $v_0 = E/B$ will pass through unperturbed. All other ions will be steered away from their straight line flight path.

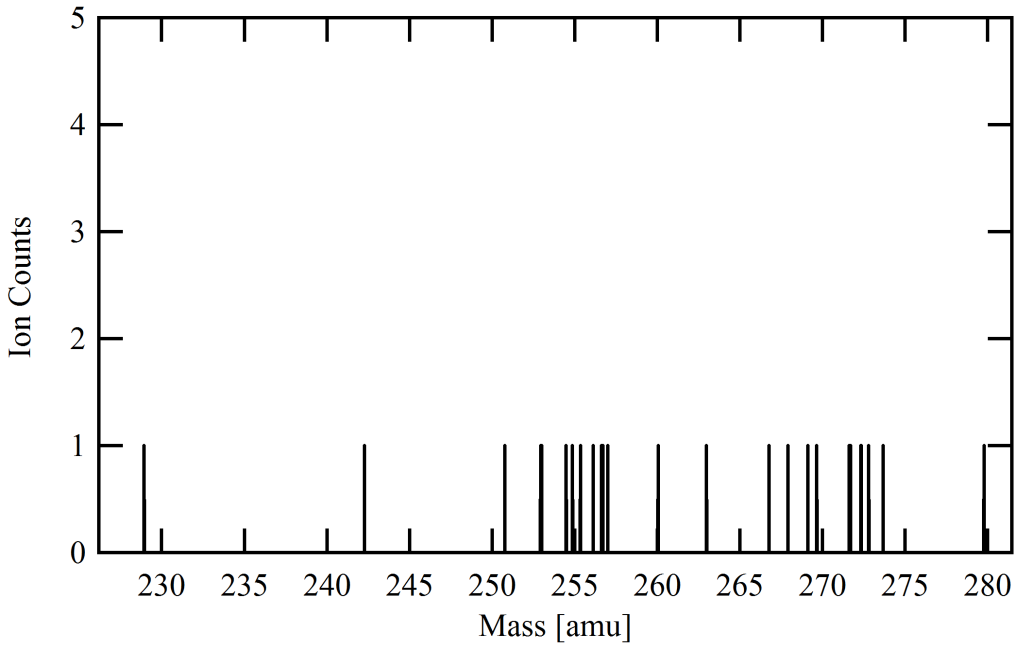

Figure 4.5: Dark count mass spectrum, counts due to random secondary electron emission in the detector. The spectrum was obtained by operating the system under normal operating conditions except for blocking the ionization laser beams and blanking the Ga^+ ion beam.

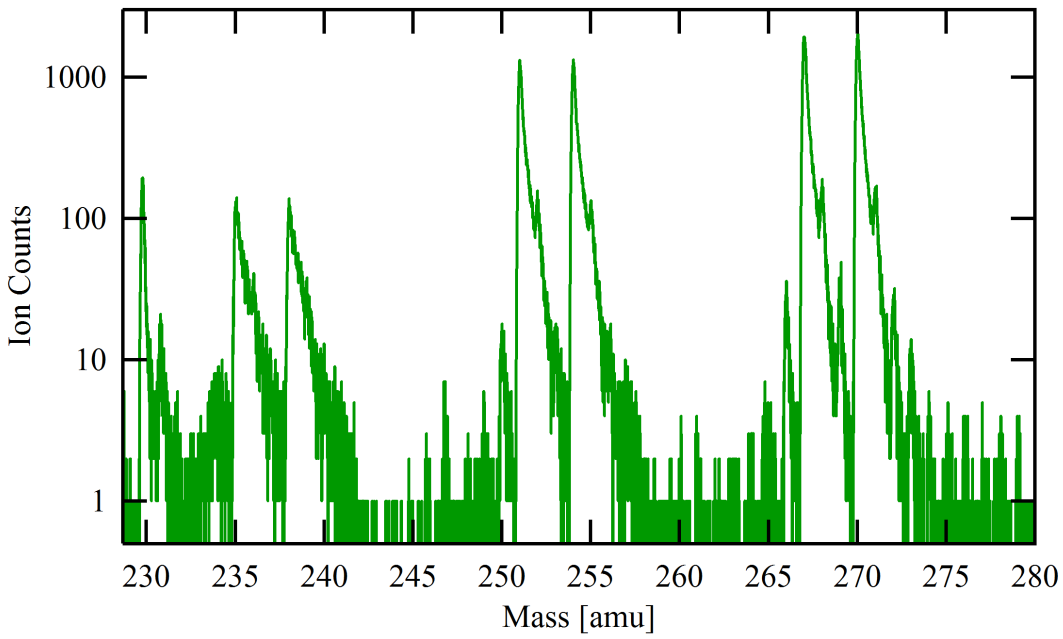

Figure 4.6: Secondary ions collected in "SIMS mode" over 10^5cycles on the U500 standard.

In this "SIMS mode", the SIMS suppression pulse is turned off and the ionization lasers are not used. Therefore, any ions collected will have been created in the sputtering process (or in collisions while leaving the surface of the material) and not by photo-ionization. The ion extraction pulse time is kept constant relative to the sputtering pulse. Figure 4.6 is a mass spectrum acquired from sputtering of the U500 target over 10^5 instrument cycles with CHARISMA operating in this SIMS mode. There are a total of 302,162 total ions detected in this spectrum. Seven ion peaks with more than 100 counts in the peak channel are clearly visible. The peaks in this spectrum are identified as the same ions that form the peaks in Fig. 4.1. They are simply produced by a different ionization process.

In addition to the identified peaks, there are small peaks visible on the trailing edges of the oxide ions for the major isotopes at approximately 1 amu higher in mass. On average, these peaks occur in the time bin 240(5) ns above the peak time bin of the ion mass peak in which they reside, and are 10(2) % of the maximum peak height. They may be the result of UOH ions. Also in the oxide mass regions are even smaller peaks at 2 amu above the peak. The peaks at +2 amu are likely the ion species incorporating ^{18}O as in the photoion signals. The ratio of the corresponding peak counts ($U^{18}O/U^{16}O$) in the experimental data are all less than 0.01, but the tails from the more abundant peaks make it difficult to distinguish the contribution of the ^{18}O peaks accurately. The mean ratios of $U^+/UO^+/UO_2{}^+$are $1/7.2(1)/10.5(1)$. The measured ratio of $^{235}U/^{238}U$ for the three different ion species is 1.025(18), 1.009(7), and 1.000(5) while the certified ratio for the U500 is 0.9997(1).

For comparison, Figure 4.7 shows the atomic uranium mass region of the secondary ion sig-

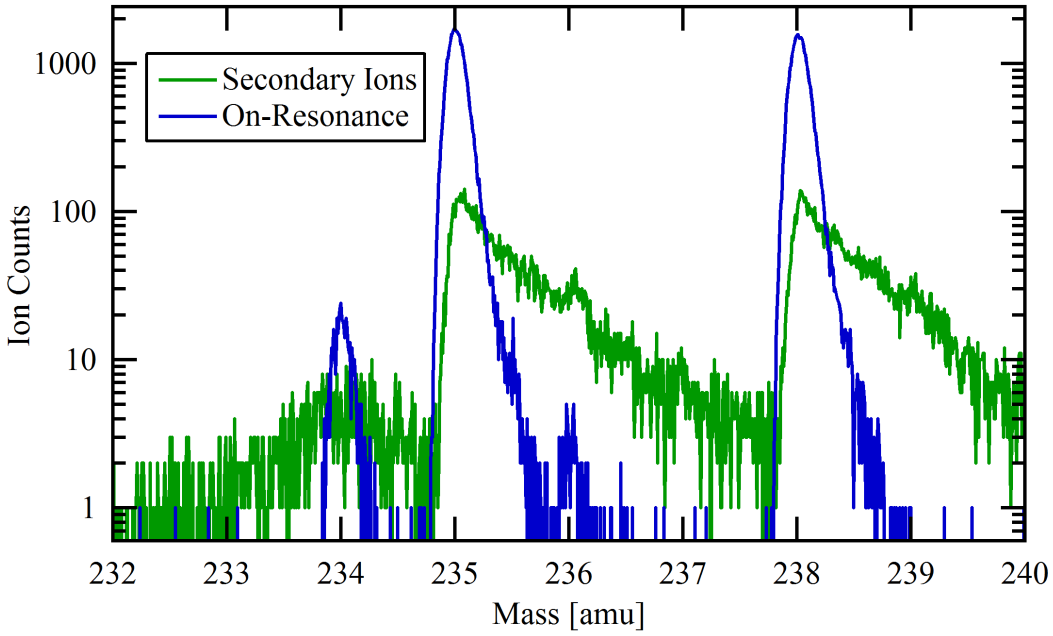

Figure 4.7: Comparison of secondary ion signal with resonant atomic uranium signal.

nal along with the on-resonance data from Exp. #1. The difference in peak width is immediately apparent. The peaks for the secondary ion spectrum (Fig. 4.6) are broader than the peaks in the photoion spectrum (Fig. 4.1), as wide as 1.5 amu. This is a result of the ions freely expanding in the volume above the target with a range of initial velocities for a period of time before the extraction voltage pulse. Thus, the secondary ions will experience an electric potential related to their distance from the target face when the voltages are applied to the extraction electrodes. They will therefore acquire a range of kinetic energies on the order of 300 keV. The peak shapes in the secondary ion experiment could be improved by altering the voltages of the ion optics in the mass spectrometer and extraction pulse timing if desired, but at a cost of the peak shape in the on-resonance experiment.

4.1.4 Suppressed Secondary Ions

During measurements of the uranium isotope abundances by resonance ionization, we wish to suppress any secondary ions created in the sputtering process. Thus, we turn on the SIMS suppression voltage pulse. We collected the ion signal for 10^5 sputter pulses while still blocking the ionization laser beams from the target chamber. All other experimental conditions are identical to the above SIMS mode measurement. The results are shown in Figure 4.8, which shows the drastic reduction of secondary ions recorded in CHARISMA when using the SIMS suppression pulse.

There are a total of 2,000 counts in this spectrum. The majority of counts were detected in

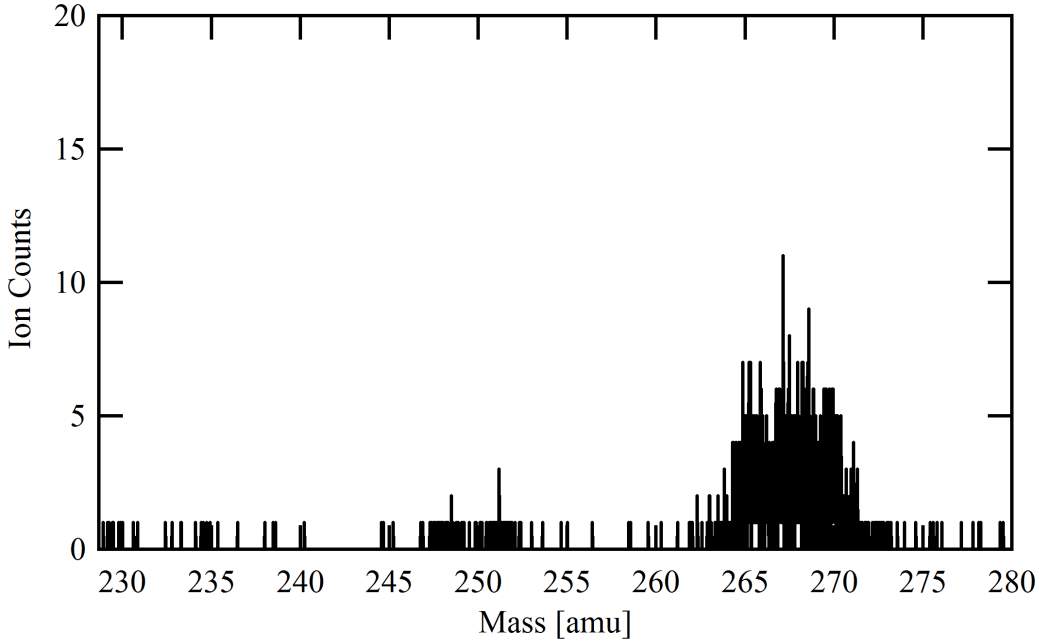

Figure 4.8: The secondary ion signal of 10^5 sputter pulses on U500 with the SIMS suppression pulse on. The ionization laser beams were not allowed into the target chamber. Compared to the when the suppression pulse is off, this is a reduction of a factor of 151(4) in the measured secondary ion signal.

the mass regions near the uranium oxide ions. This is a reduction of the secondary ion signal by a factor of 151(4) when using SIMS suppression. There are a total of 12 counts in the range $233-240$ amu, near the atomic U ion signals. The suppression of the secondary ion signal will be dependent on the composition of the material being sputtered, as well as the specific voltages and timings of the instrument. However, this signal can always be directly measured by blocking the ionization laser beams from the target chamber. The amount of unsuppressed secondary ions in this spectrum is typical for all of the experiments in this work.

4.1.5 Photoions

Now that we have discussed the non-photon induced ion signals in our measurement, we will explore the relative contributions of the ionization laser beams to the ion signals we measure. All three laser beams are necessary for the resonant ionization of the atomic uranium ions via the 3-color, 3-photon ionization process. Thus, we will be most concerned with the relative contribution of each laser to the non-resonant ionization probability of other neutral species in the ionization volume. We will start by looking at the contributions from each laser to the off-resonance ion signal in the atomic U mass region, as this is the signal that can potentially interfere with the measurement of uranium isotopes. We will additionally consider the role of

each laser in the ionization of UO and UO_2.

We performed an experiment (Exp. #5) using the SRM 960 as a target (U metal with oxidized surface layer and natural uranium isotope abundances) to quantify the relative contribution of photons from each laser beam to the non-resonant ion signal. Each acquisition is the sum of 10^5 laser pulses. We used the 3-photon, 3-color ionization scheme with all lasers in the narrow bandwidth arrangement but tuned the wavelength of the first laser away from resonance in order to measure the off-resonance contributions. This detuning is essential because, if the first laser is tuned on-resonance with the first transition then the neutral atoms are excited with very high probability almost half-way to the ionization limit (3 eV out of 6.2 eV) and from this state can be more easily ionized. The other two wavelengths do not have known transitions from the ground state of U directly to an excited state. The wavelengths used were 418.007, 829.091, and 722.202 nm and the energy per pulse for each laser was 210, 710, 610 μJ, respectively. Figure 4.9 shows the ion signal in the range from 234 to 240 amu produced by three ionization conditions. The first condition was the total off-resonance signal (top trace) that used all three laser beams to ionize the neutral species. This condition is equivalent to the measurement in Fig. 4.2 but from the SRM 960 target. For the second ionization condition, the second and third laser beams were blocked and only the first laser beam was allowed into the target chamber. This arrangement is labeled "Laser 1 Only"[6]. Finally, the first laser beam was blocked and the second and third laser beams were allowed to enter the ionization volume. This is displayed as "Lasers 2 and 3". Comparing the three ionization conditions reveals that the first laser is the major source of non-resonant ions in the mass peaks near 235 and 238 amu. By comparing the total counts of the mass peak at 238 amu under each ionization condition, the first laser beam alone produces 54(1) % of the total off-resonance signal. The second and third beams together produce only 4.2(2) % of the signal. The remainder of the signal must be due to the combination of all three beams interacting to produce the total off-resonance trace.

Figure 4.10 shows the uranium oxide mass regions in two plots for the same acquisitions as Fig. 4.9. In the left plot, showing the range near uranium monoxide (250−258 amu), there are several peaks present. The most dominant is the $^{238}U^{16}O$ peak at 254 amu. In that peak, the off-resonance trace is broadened by the effects of dead-time. The trace when only the first laser beam was allowed in the chamber accounts for 70(1) % of the total counts of that peak. In the plot on the right-hand side, the most prominent peak is at 270 amu and corresponds to $^{238}U^{16}O_2^+$. In this case, the first laser alone accounts for 12(1) % of the ions in the off-resonance peak. The trace collected when only the second and third laser beams were allowed into the chamber accounts for nearly 100 % of the peak. This provides information about the non-resonant processes producing the ions in these peaks. The ions in the uranium monoxide region are mainly produced by absorption of photons from the first laser in our excitation scheme, while the ions in the uranium dioxide ion mass region are produced by absorption of photons from the second and third lasers. In an additional experiment to further explore these processes, we

[6]We occasionally refer to the lasers as 1, 2 and 3, which is a description of the order of excitation in which they are used in the 3-color, 3-photon ionization scheme. Meaning, the first resonance laser beam responsible for exciting the transitions between the ground and first excited state is called Laser 1.

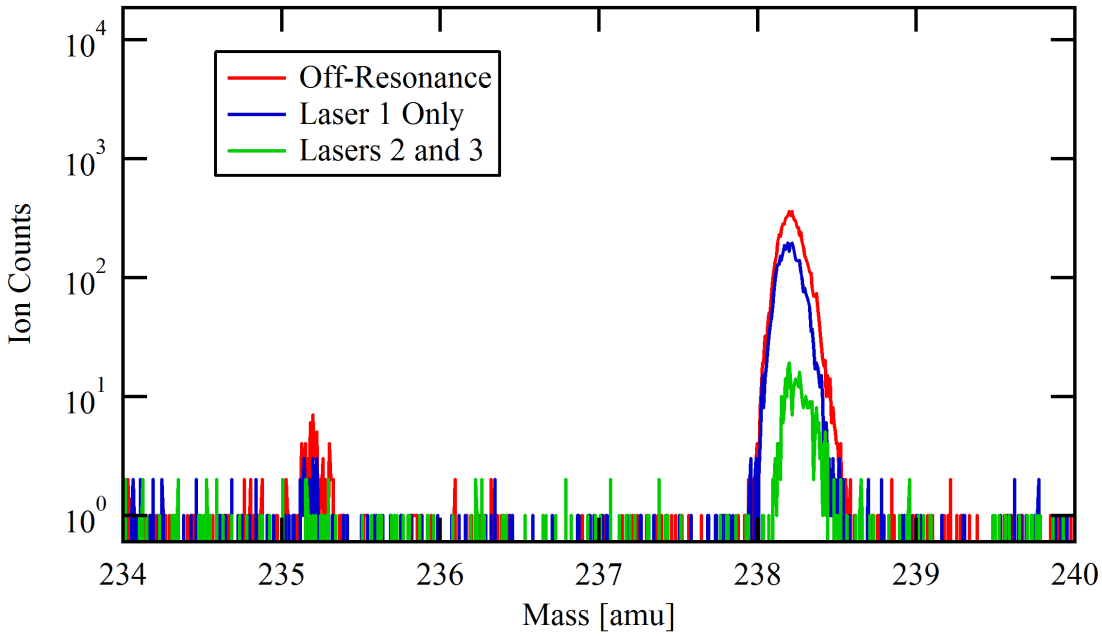

Figure 4.9: Photoion backgrounds from SRM 960 for three ionization conditions when the wavelength of the first laser is tuned to 418.007 nm (off-resonance). When only the first of the three laser beams is allowed in the ionization volume the ion signal at the atomic uranium masses is 54(1) % of the total off-resonance background. When the first beam is blocked and the second and third beams are allowed into the ionization volume together they contribute only 4.2(2) % to the total off-resonance background.

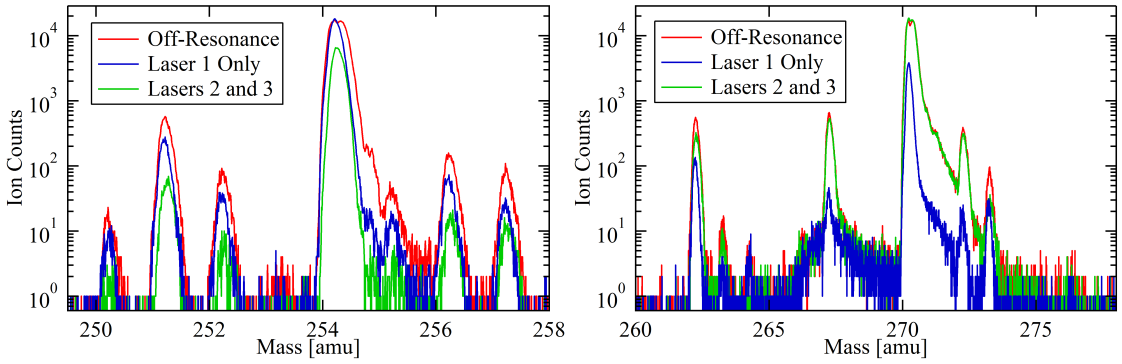

Figure 4.10: The photoion background in the oxide mass regions, measured on SRM 960. (Left) The UO mass region, the first laser accounts for the majority of the non-resonant ions in this region (70(1) %). (Right) The UO_2 mass region, where the first laser accounts for 12(1) % of the non-resonant ions and the second and third laser combined are responsible for almost 100 % of the uranium dioxide ions. Dead-time effects are significant for the 254 and 270 amu mass peak in the off-resonance trace.

found that the contributions to the uranium dioxide peaks due to absorption from just the second and third laser were confirmed to be nearly 100 % of the off-resonance ion signal. When the first and second laser beams were allowed into the chamber together they produced 29.2(3) % of the off-resonance ion signal at 270 amu, and when the first and third laser beams were allowed into the chamber together they produced 33.0(3) % of the off-resonance signal at 270 amu. This means that 30% of the ion signal at 270 amu cannot be accounted for by considering the second or third laser in isolation. This implies that there may be a two-photon resonance in uranium dioxide at the sum of the wavelengths near 829.09 and 722.2 nm.

The ion signal near higher-mass regions is less important when measuring atomic uranium isotopes. However, we have demonstrated that we must consider and control the off-resonance background in the atomic uranium mass region when analyzing uranium oxide materials. We have shown that the generation of off-resonance ions in that mass region is mostly due to contributions from the first resonance laser beam. Thus, we should optimize the intensity used in that laser to limit the background contributions while maintaining a high probability for exciting that transition. This suggests that relying on power broadening alone to saturate the transitions for multiple isotopes of uranium simultaneously can be counterproductive.

4.1.5.1 Power dependence of the 1-Color Off-Resonance Ion Signal

The laser beam used to excite the first resonance transition in the 3-photon, 3-color ionization scheme is the major generator of non-resonant ions in the atomic uranium mass region (234−238 amu). We performed an experiment (#6) to study the dependence of this 1-color ionization process on the intensity of the first laser. This was to understand the dependence of the ion signal on laser intensity relative to the resonance ion signal at these masses. Additionally,

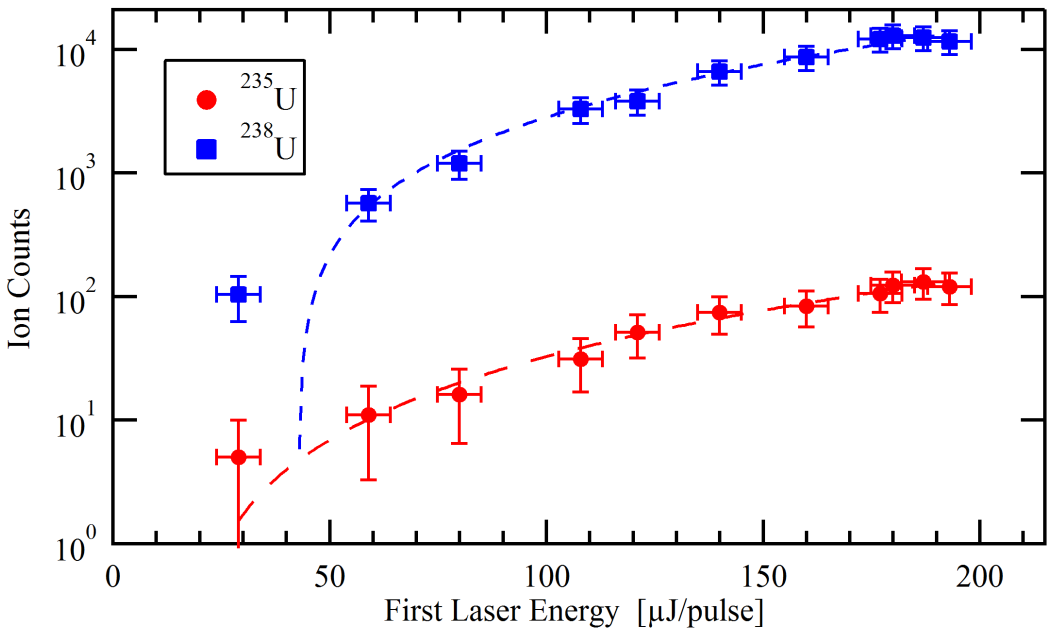

Figure 4.11: Intensity dependence of a 1-color ionization process. Laser 1 was the only laser beam in the target chamber and it was tuned away from the first resonance transition to 417.5 nm. The data are the total counts for the ^{235}U and the ^{238}U mass peaks. The data for each isotope are fit by the function, $y = y_0 + A \cdot x^{pow}$, determined by an unconstrained least-squares fit. For the fits shown $pow_{238} = 2.16(82)$ and $pow_{235} = 2.08(68)$. Measurement performed on SRM 960.

we aimed to determine the number of photons involved in the process (see Eq. 2.63). The first laser beam has a higher photon energy (∼2.98 eV) than the other two laser beams (∼1.5 eV) and therefore requires absorption of fewer photons in order to ionize or photo-dissociate the non-resonant species. We used SRM 960 as the target and tuned the wavelength of the first laser to 417.757 nm (2 nm from resonance). The laser had a narrow bandwidth and we varied the energy per pulse of the beam between 29−187 μJ. The uncertainty in the beam energy is $\pm 5\,\mu$J. The total counts of the ^{235}U and ^{238}U mass peaks at each beam energy are shown in Figure 4.11 along with fits to the data. The fits are the unconstrained least squares fits to the data points, described by the equation $y = y_0 + A \cdot x^{pow}$. For ^{238}U $pow_{238} = 2.16(82)$ and for ^{235}U $pow_{235} = 2.08(68)$, where the uncertainties are 2σ. These fits indicate that there might be an excitation step in the ionization of these non-resonant photoions at masses 235 and 238 that requires the near-simultaneous absorption of at least two photons. Of course, higher-order absorption processes are possible and likely will be non-negligible at high beam intensity. The primary result from this measurement is an empirical description for the non-resonant background at the uranium atomic masses as a function of beam intensity in the first laser. The non-resonant contribution at the atomic uranium mass peaks is highly dependent on the power

of the first laser beam. Changing the power of that beam from the maximum value near 200 μJ to 100 μJ reduces the off-resonance ion signal by 75 %. We'll study the effect that this change in laser power has on the resonant ion signal in Section 4.3.1.

In addition to simply measuring the 1-color, non-resonant ion signal at 235 and 238 amu, we also hoped to identify the neutral species that give rise to these ions, in part, to understand how the signal may vary as a function of the target composition. There are at least three neutral species that may give rise to ions at atomic masses of uranium and that we know are in the ionization volume during irradiation: U, UO, and UO_2. In their electronic ground states, each of these species requires more than 2 photons of 3 eV to form ions at the atomic uranium masses. The ionization potential of neutral U atoms is 6.19 eV, and in order for U to be ionized using only two photons, would require the uranium atoms to be in excited states of greater than 0.25 eV as a result of collisions during sputtering. Uranium is known to populate a low-lying excited state near 620 cm^{-1} during sputtering, but this has an energy of only 0.07 eV[68]. On the other hand, UO and UO_2 may be photodissociated into U^+ and a variety of oxygen species. The dissociation may also produce neutral uranium atoms in a variety of excited states that then interact with an additional photon to become ions. However, the dissociation energies to produce U^+ from UO and UO_2 are relatively high at 13.9(2) and 21.7(3) eV, respectively[74]. This requires the absorption of 5 and 8 photons of 2.98 eV for ionization, respectively, if we ignore the possibility of excited states prior to photo-excitation. There are then at least three factors that may cause the apparent order of the photons required for ionization to be smaller than 3:

1) Statistical effects for low-probability events described by Poisson statisitics.

2) Species in excited states prior to the arrival of the ionizing photons.

3) Other single-photon steps with higher absorption cross sections that do not limit the rate of the ionization probability. According to simple estimates using the rate equations, the rate of ionization would not be significantly affected for any excitation steps that had cross sections on the order of $\sim 10^{-16}$ cm^2 or greater. Typical allowed dipole transitions have cross sections of $10^{-12} - 10^{-14}$ cm^2 while cross sections for absorption in regions far from resonance centroids must be several orders of magnitude smaller ($\sim 10^{-17}$ cm^2). Characteristic cross sections for two-photon transitions are in the range $10^{-48} - 10^{-54}$ cm^4[43].

Other workers ([29, 31]) have observed non-resonant ions at the atomic uranium masses while working with uranium oxides, but in several cases did not observe a *resonant* atomic uranium signals during those measurements. They did observe resonant uranium ions from other uranium-rich targets. This suggests that either the non-resonant ionization probability was close to unity (and thus, all the uranium in the ionization volume was ionized regardless of wavelength), or that ground-state neutral uranium atoms were present only in amounts below the detection limits of their experiments. The former is unlikely given the beam irradiance and the observation of resonant ions from other targets. The later suggests that the species that give rise to the non-resonant ions at 235 and 238 amu are not neutral uranium atoms. Even if the U atoms were in highly-excited states before laser irradiation, there would likely be some measurable population of ground state atoms.

4.1.6 Dependence of the Ion Signals on the Desorption Process

For a given target material, the photoion signal is highly dependent on the sputter yield and the laser beam parameters. We will spend most of the remainder of this chapter focusing on the effect that varying laser beam parameters have on the measured photoion signal but first we will examine the effect that variations in the rate of production of neutral species by ion sputtering can have on our measurements. The term "sputter yield" is defined as the efficiency for creating a specified secondary particle (ion, neutral, atom, molecule) by sputtering. In ion sputtering the amount of material removed is, in general, linearly proportional to the ion current of the bombarding species. However, the efficiency for creating a particular secondary particle is dependent on the condition of the target. Factors that influence the relative sputter yield as a function of time include variation of the sputtering ion current, the effects of implantation of Ga^+ into the surface, and the rate of oxidation of the target surface. Preferential sputtering of oxygen from UO_2 has also been observed by other workers[75], producing a partially-reduced uranium metal surface as sputtering progresses. The sputter yield for the neutral atom species we ionize is quite variable as a function of time and sputtering parameters.

Figures 4.12 and 4.14 show the counts for atomic U, UO, and UO_2 measured from CRM125-A and U500 as a function of sequential acquisitions, each of 10^5 laser pulses. All laser and experimental parameters were kept constant during these acquisitions. Again, each acquisition required approximately 2.5 minutes and thus the entire experiment took about 100 minutes. First, Fig. 4.12 shows the ion signals of three ^{235}U ion species as a function of acquisition number from U500, a U_3O_8 target (Exp. #7). In order to ionize both isotopes nearly equally, the ionization lasers were tuned between the resonances of ^{235}U and ^{238}U and arranged to produce a broad bandwidth in the first and second laser beams. The ion gun was run at an internal current of 3.5 μA, which was reduced using a 300 μm aperture to produce a primary ion current of a few nA. The beam spot was rastered over a 20×20 μm square area that had not been previously sputtered. We chose this raster size and ion gun current because they had been previously shown to provide a relatively-steady atomic uranium ion signal on U500 after some period of sustained sputtering. This appears to be the case after 15 acquisitions or so (about 40 min). At other raster sizes or ion beam currents the count rate would tend not to approach a quasi-steady rate as quickly. The ion signals for the atomic and monoxide uranium ions show a steep decline at the start of the sputtering process and then the monoxide signal begins to increase while the atomic signal appears to become fairly steady.

To first-order, the isotope ratio within an ion species is not dependent on the sputter yield. Figure 4.13 shows the measured $^{235}U/^{238}U$ ratio for the acquisitions shown in Fig. 4.12, along with a dashed line representing the mean of the ratios. The ratios have not been corrected for background and the uncertainties are the 2σ uncertainties expected from counting. The mean of the measured ratios of 1.007(2) is slightly higher than the certified ratio of 0.9997(1). The measured ratio does not show a significant dependence on the time-dependent count rate of atomic uranium shown in Fig. 4.12. The fluctuations in the yield of neutral species useful for resonance ionization has been a main limit to the precision and accuracy achieved in isotope selective approaches to measuring uranium isotope abundances when ion signals of different

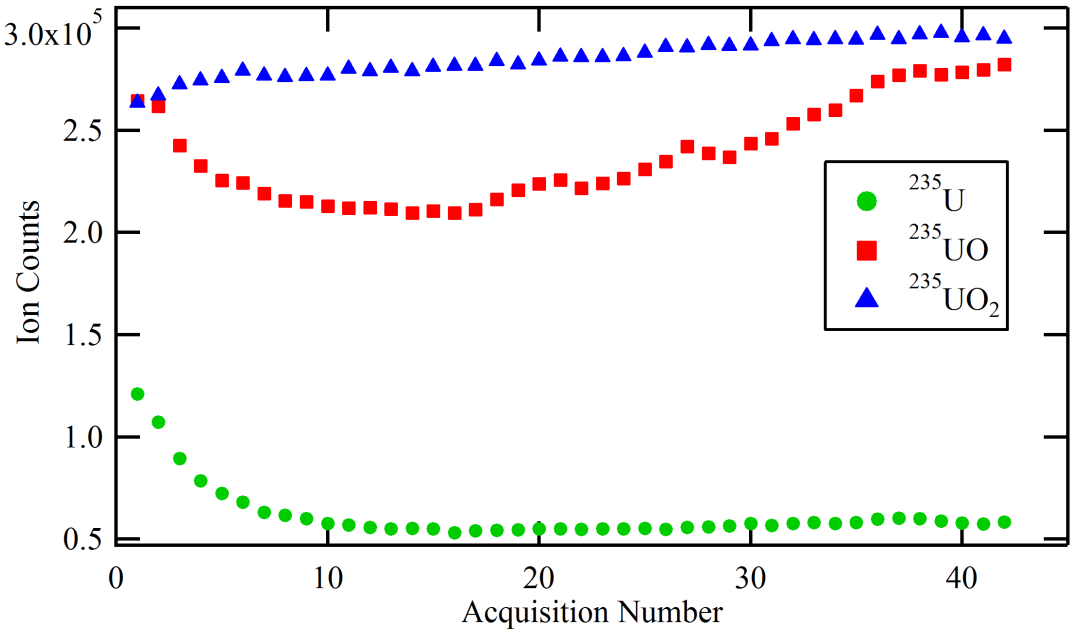

Figure 4.12: Sequential acquisitions of three ^{235}U ion species sputtered from CRM U500. Note the ratio of atomic to monoxide to dioxide species is not constant. Uncertainty from counting statistics is smaller than the data markers.

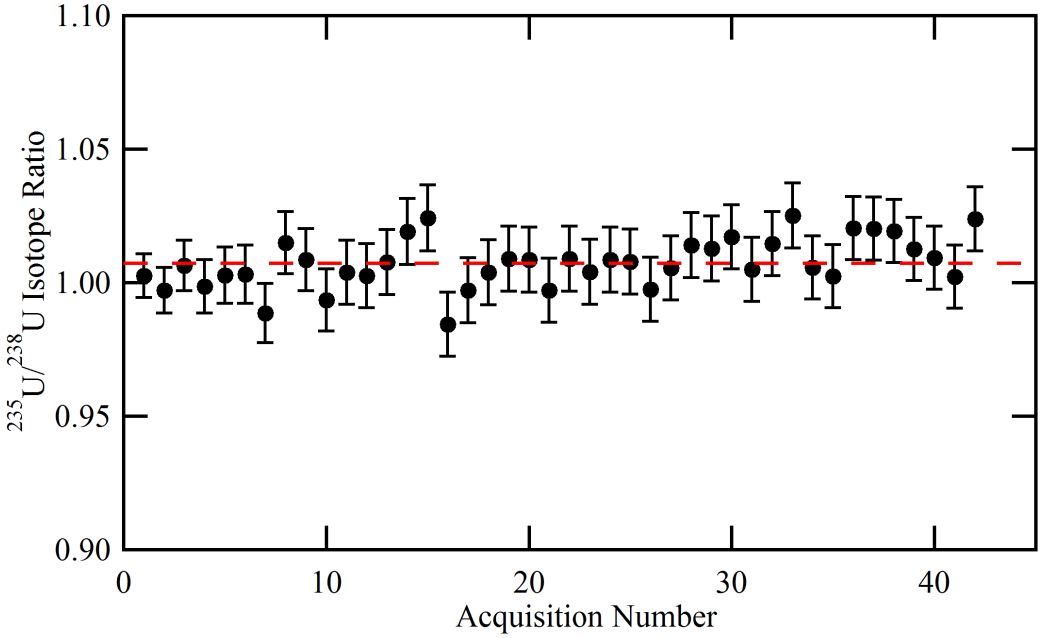

Figure 4.13: The measured $^{235}U/^{238}U$ ratios with a mean of 1.007(2) on U500 with a certified ratio of 0.9997(1). The ratios are from the experiment in Fig. 4.12. The ratio does not display any dependence on the count rate of atomic uranium. The data are not corrected for background. The red line is the mean of the ratios.

isotopes are measured sequentially[10, 32]. The insensitivity of the measured ratio to changes in desorption yield, is one of the main advantages to our approach of measuring several isotopes simultaneously.

In Fig. 4.14 (Exp. #8) the integrated ion signals of $^{238}U^+$, $^{238}UO^+$, $^{238}UO_2^+$ from CRM-125A are shown as a function of acquisition number. The lasers were tuned to ionize both ^{235}U and ^{238}U equally, and the first and second lasers used a broad bandwidth. Each acquisition required about 2.5 min to collect and the collection was paused for about 20 min between acquisitions 13 and 14, which corresponds to the large change in ion signal between these acquisitions[7]. Generally, all three of the count rates increase as a function of time, but the ion signals also change relative to one another. Figure 4.15 shows the ratios of the atomic uranium ion signal to the uranium oxide signals shown in Figures 4.12 and 4.14. For these uranium oxide targets (UO_2 and U_3O_8) the ratio of ionized atom to oxide species decreases sharply at short times (by factors of $\sim$2) and varies from 0.1 to almost 0.5 depending on the sputtering conditions.

We must consider the fluctuations in sputter yield when considering measurements that

[7]The collection between these acquisitions was paused, but the sputtering pulses were not. If the abscissa is changed to represent total elapsed time, rather than acquisition number, the count rates appear to be a smoothly varying function of time (with a 20 min gap).

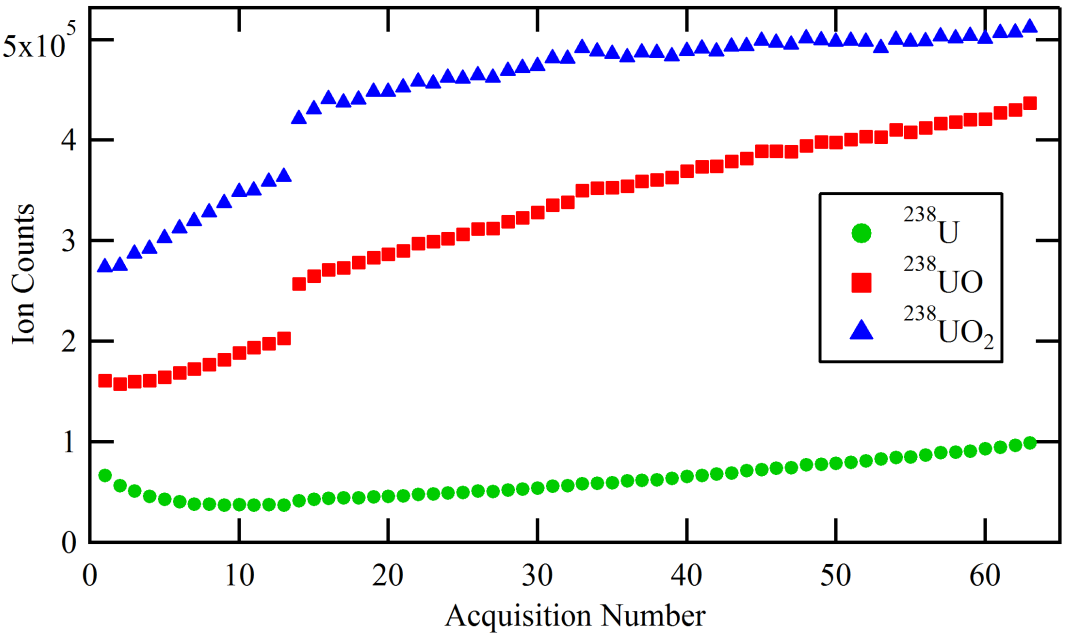

Figure 4.14: Sequential acquisitions of ^{238}U species ion signal sputtered from CRM125-A. Each acquisition took 2.5 min. 20 minutes elapsed between acquisitions 13 and 14. Uncertainties from counting are smaller than the data markers.

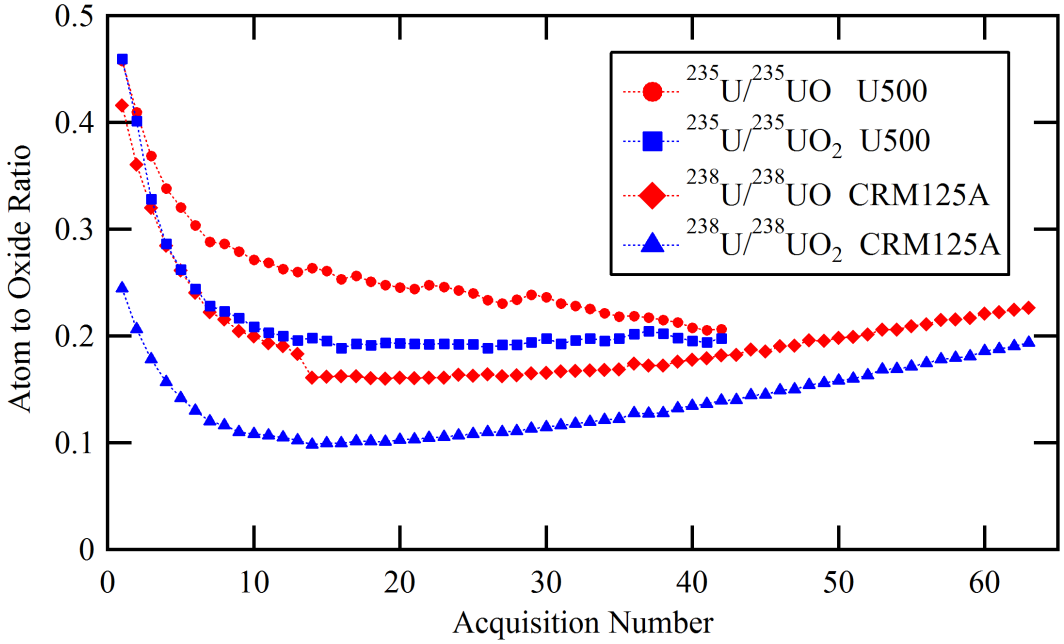

Figure 4.15: U atom to oxide ion ratios for CRM 125-A (UO_2) and U500 (U_3O_8). The ratios are not constant and are not the same between materials.

compare the ion signal of a single species from acquisition to acquisition. The ion count rates appear to be functions of sputtering ion current, ionization probability, and condition of the target surface being probed. We attempt to use conditions where the count rates across acquisitions change very little, but typical variations on the order of 1 % from acquisition to acquisition remain and the total change over many acquisitions can be significant. This means that experiments that rely on the magnitude of a single ion must consider the influence of the change in count rate from acquisition to acquisition. The magnitude of the count rate should also not be directly compared to the rates from other experiments.

4.2 The Dependence of Uranium Ionization on Wavelength

We now describe experiments designed to explore the spectroscopic information relevant to the resonance transitions of the 3-color, 3-photon ionization scheme described in Sec. 3.2.1. This is accomplished by scanning the wavelength and intensity (power per unit area) of each laser independently and observing the photoion signal as a function of the variation in that laser parameter. Our primary interest is to observe the resonance transitions for our experimental arrangement, as the energy and lifetimes of these transitions have been measured by more sophisticated laser arrangements[51]. The experimentally observed width of the resonances in terms of wavelength will be a function of several factors: the natural lifetime of the resonance,

the average Doppler shift in wavelength of the freely-expanding atoms, the bandwidth of the exciting laser radiation, and the energy density of the laser beam. The combination of these factors in addition to the acquisition-to-acquisition fluctuations in ion signal caused by changing sputter yields prevent the quantitative description of these individual factors directly from the experimental data. The measurements mainly provide an estimate of the total combination of these factors for our experiments.

We are interested in the relative variation of the ion signal as a function of the given laser parameter and not in the absolute magnitude of the signal. Therefore, we often report the experiment results relative to the acquisition with the highest number of counts. For the following experiments, the stated uncertainties include not only those expected from counting statistics but also the uncertainty in ion signal due to changes in sputter yield during the experiment. The later uncertainty is estimated from duplicate acquisitions at a given laser parameter value.

For all experiments, we have attempted to report data only after we observe that the count rate is fairly steady from acquisition to acquisition. In addition, to minimize systematic errors, we vary the investigated laser parameter randomly (*i.e.*, when changing the energy per pulse over the range 1 to 5 μJ we choose energies in the order 4,1,3,5,2 μJ, etc.).

4.2.1 Wavelength Dependence of the First Resonance Transition

We measured the $^{235}U/^{238}U$ ratio of the SRM 960 target using the 3-color, 3-photon ionization scheme as a function of the wavelength of the first excitation laser with a bandwidth of 1 pm (Exp. #9). The wavelengths of the second and third resonance lasers were held fixed at 829.089 and 722.344 nm, respectively. The energy per pulse of the first laser was 150 μJ. The second and third laser had energies of 900 and 540 μJ/pulse, respectively. Figure 4.16 shows the normalized counts for ^{235}U and ^{238}U as a function of the wavelength of the first resonance laser. For the normalization of ^{235}U, we have divided the total counts from each acquisition by the mean of the two acquisitions made at the resonance wavelength (415.507 nm). The ^{238}U signals have been normalized by the acquisition at 415.515 nm, which had the largest number of counts. The average FWHM of a Gaussian least squares fit (not shown) to the resonances is 4.6(5) pm. The isotope ionization probability clearly displays a strong dependence on the wavelength of the laser. The difference in resonance wavelength for the two isotopes demonstrates immediately the challenge of measuring the ratio of these isotopes with reasonable precision and accuracy. For wavelengths near the peak of the resonance of either isotope, the probability of ionizing the other isotope is quite small. For wavelengths between the two resonances the measured isotope ratio will be highly sensitive to changes in wavelength.

We also measured the $^{235}U/^{238}U$ ratio on the same target (SRM 960) a function of the wavelength of the first laser when the laser cavity was arranged to produce a beam with a bandwidth of $\sim$5 pm (Exp. #10). The energy of the laser beams in excitation order were 75, 900 and 600 μJ/pulse. Note that the energy per pulse of the first laser is a factor of two lower than for the previous experiment. The second and third laser beams were both narrow in bandwidth and their wavelengths were tuned between the corresponding resonances for these isotopes as in the previous experiment. Figure 4.17 shows the measured isotope ratio from this "broad"

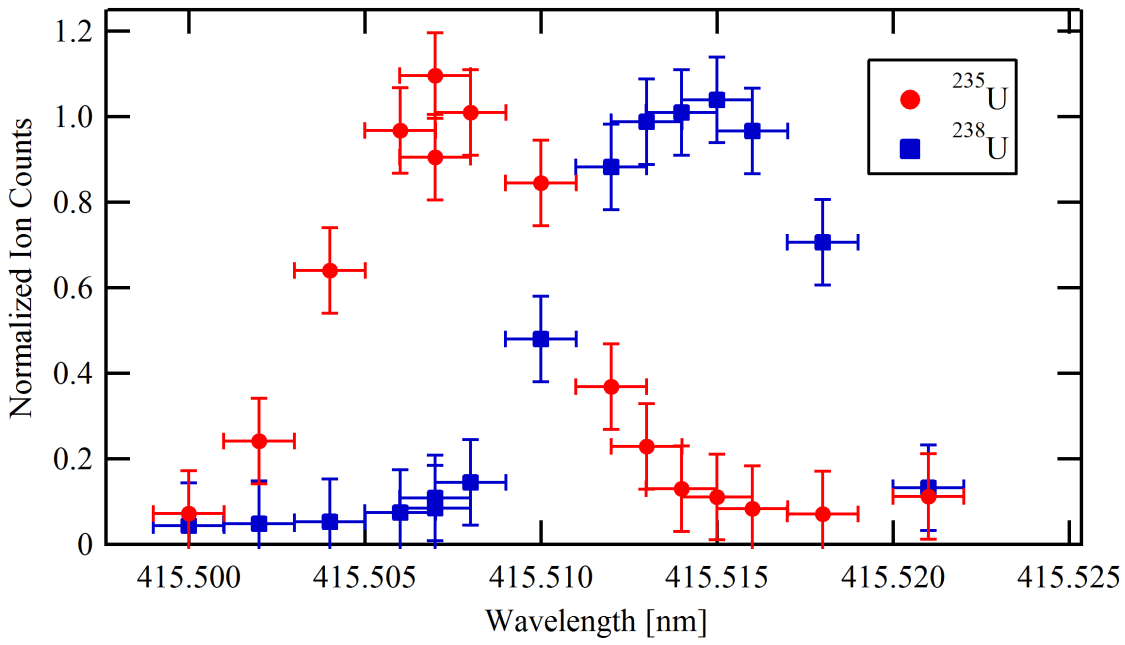

Figure 4.16: Dependence of the ionization probability for ^{235}U and ^{238}U as a function of the wavelength of the first laser of a 3-color, 3-photon ionization scheme. Each point is the sum of ions from 10^5 laser pulses. Measurement performed on SRM 960. (Exp. #9)

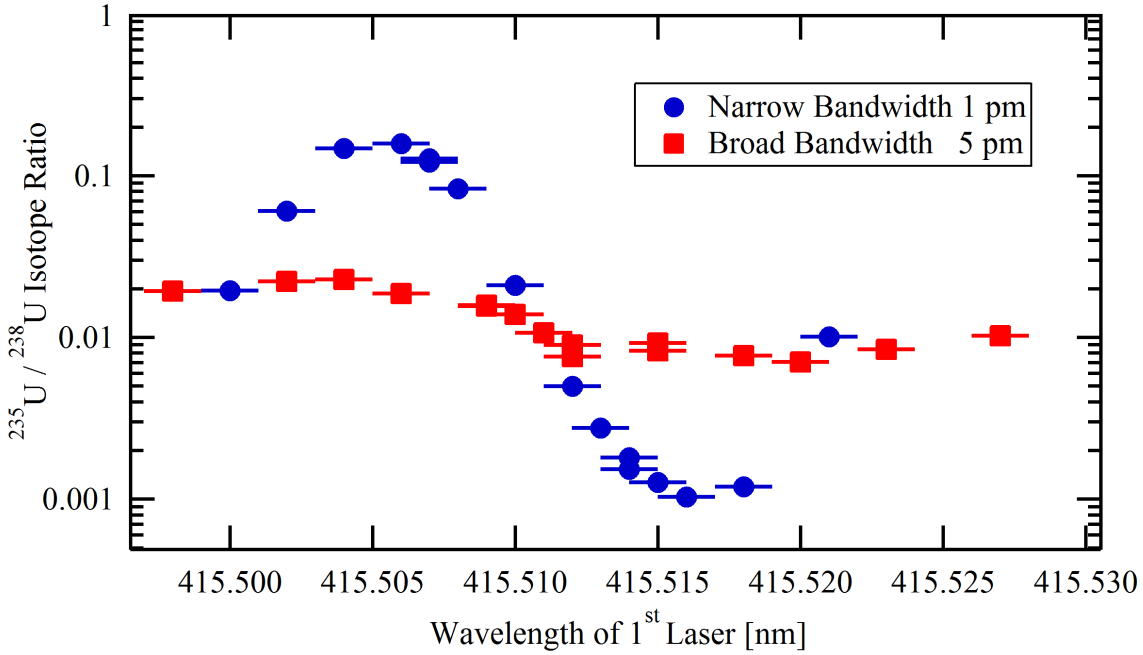

Figure 4.17: $^{235}U/^{238}U$ ratio vs. wavelength of the first resonance laser at two laser bandwidths, measured from a natural uranium metal standard (SRM 960). The wavelength of the second and third resonance lasers were held fixed at 829.089 nm and 722.344 nm respectively. The vertical error bars are not shown, but the uncertainties due to counting statistics are less than 1% relative for all data points.

bandwidth experiment and the "narrow" bandwidth experiment shown in Fig. 4.16. The certified $^{235}U/^{238}U$ ratio of SRM 960 is 0.0073(1). At a bandwidth of 1 pm the $^{235}U/^{238}U$ ratio varies by over 2 orders of magnitude as the wavelength of the first resonance laser is scanned over the resonances of ^{235}U (415.507 nm) and ^{238}U (415.514 nm). When the bandwidth was increased to 5 pm, the variation in isotope ratio over the same wavelength range was reduced to a factor of 3. The dependence of the measured ratio, as function of wavelength, on the bandwidth is obviously quite large. For the 1 pm bandwidth, the rate of change of the ratio near the midpoint of the resonances is -220 ± 30 % per pm, while for 5 pm bandwidth the deviation is 13.5 ± 3 % per pm. Although the sensitivity to wavelength is greatly reduced, it seems clear that a laser bandwidth well in excess of 5 pm is necessary to reduce the sensitivity to wavelength variation to levels of <0.1 % per pm. By increasing the bandwidth of the first resonance laser by a factor of about 5 we have reduced the sensitivity of the measured isotope ratio on wavelength of that laser by over an order of magnitude. This reduction in sensitivity relaxes the requirement of pulse-to-pulse wavelength variations that are acceptable in a laser system intended to make reproducible measurements of the isotope ratio.

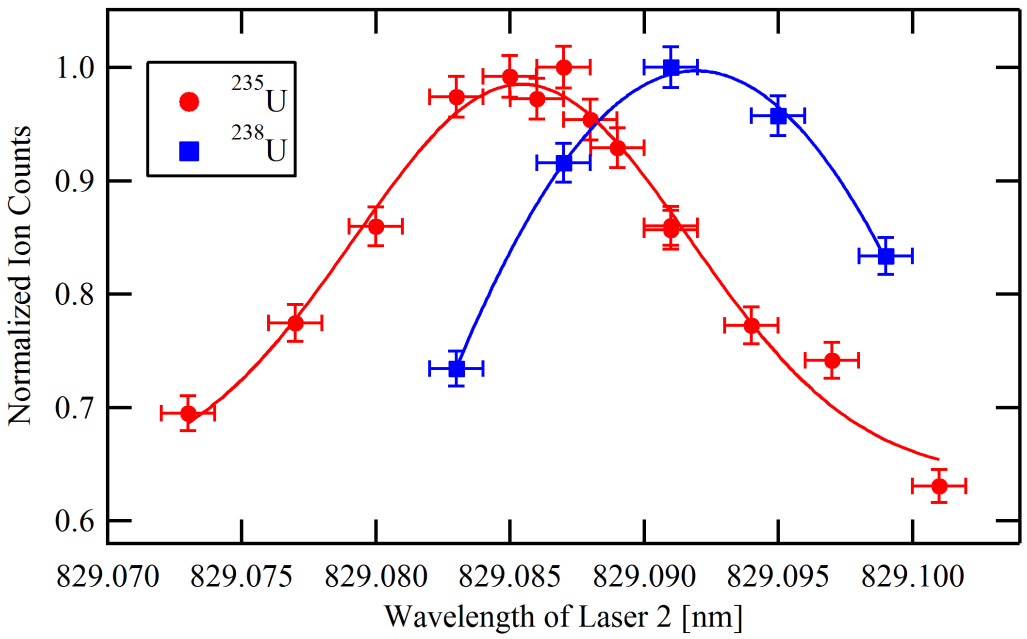

Figure 4.18: Wavelength scans of the second resonance transition for ^{235}U and ^{238}U. Counts reported relative to the acquisition with the maximum number of counts. Both isotope resonances are shown with least squares fit Gaussian lineshapes. Measurement performed on SRM 960.

4.2.2 Wavelength Dependence of the Second Resonance Transition

We also performed a set of experiments to study the wavelength dependence of the second resonance transition on the ionization probabilities of ^{235}U and ^{238}U. Figure 4.18 shows data from two experiments on SRM 960 where the lasers were tuned to the resonance wavelengths for the target isotope and then the wavelength of the second laser was scanned across the resonance region. The data for ^{235}U are from Exp. #11 and the data for ^{238}U are from Exp. #12. All the lasers were arranged to produce narrow bandwidth and the energies per pulse for the lasers were 150, 825, 610 μJ for the ^{235}U data and 200, 900, and 540 μJ for ^{238}U, respectively. The data are plotted as total counts of the mass peaks for ^{235}U and ^{238}U divided by the total counts from the largest acquisition of each isotope. These measurements confirmed the resonance of ^{235}U near 829.087 nm and the resonance for ^{238}U near 829.091 nm.

Figure 4.19 shows the ^{235}U/^{238}U ratio measured from Fig. 4.18 and includes the isotope ratio measured during an experiment (Exp. #13) when the bandwidth of the first and second lasers were broadened to $\sim$5 and $\sim$8 pm, respectively. The wavelength of the second laser was again scanned over the resonance region. The ratios for the narrow laser bandwidth data (3 pm) were constructed from the Gaussian fits to the two isotope distributions averaged over each picometer due to the limited data for ^{238}U from experiment #12 and shown in Fig. 4.18. The data provide a rate of change in the ratio ^{235}U/^{238}U near the isosbestic point of

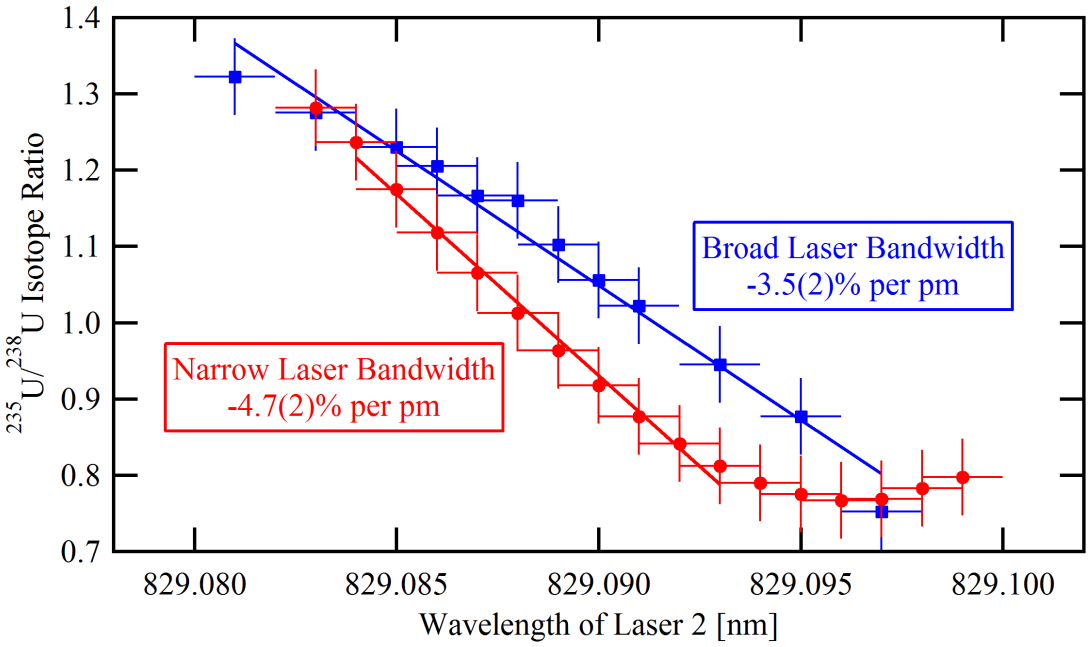

Figure 4.19: Measured $^{235}U/^{238}U$ ratio as a function of wavelength of the second resonance laser beam for two bandwidths. The narrow bandwidth data is from the Gaussian fits of Fig. 4.18 when the bandwidth was 3 pm. The broad bandwidth data was obtained while the bandwidths of the first and second laser beams were 5 and 8 pm, respectively. Linear fits to the isotope ratios near the isosbestic point of the resonances are shown. Broadening the bandwidth of the second laser beam decreases the slope from -4.7(2) %/pm to -3.5(2) %/pm. The systematic increase of isotope ratio in the broad bandwidth data compared to the narrow bandwidth data is likely from bias in the wavelength of the first laser towards the ^{235}U resonance. Measurement performed on SRM 960.

-4.7(2) % per pm. The measured ratio obtained with the broad bandwidth laser displays a rate of change of $-3.5(2)$ % per pm. Contrast the slope of these lines with those measured for the first resonance laser in Fig. 4.17. The difference between the rate of change in this ratio for the first and second resonances is a result of several factors: the second resonance has a smaller isotope shift, the bandwidth of the "narrow" second resonance laser beam is broader than the first resonance laser beam because of frequency-doubling (3 pm versus 1 pm), and the power of the second laser beam is sufficient to broaden this transition significantly compared to the first transition (see Fig. 4.26). These experiments demonstrate that we can expect to observe a bias in the measured isotope ratio as large as 9 % due to uncertainty in the mean wavelength ($\pm$2 pm) of the second laser.

4.2.3 Wavelength Dependence of the Ionization Transition

Figure 4.20 is a wavelength scan over an 800 pm range of the ionizing laser for ^{238}U from measurements on SRM 960 (Exp. #14). The ionizing laser had an energy per pulse of 610 μJ. The other two lasers were set to the resonance wavelengths for ^{238}U (415.514 and 829.091 nm), both using narrow bandwidth with the energies per pulse of 130 and 730 μJ, respectively. The signals from the micro-channel plate were processed in analog mode and signals from 40,000 laser pulses were collected per acquisition. We report the mass peak counts relative to the highest recorded number of counts in an acquisition. The estimated uncertainties include those from the variation in ion signal expected due to fluctuating sputter yields. Our scan in wavelength between 721.8 and 722.6 nm can be compared to the scan in Schumann, *et al.*[51] that has been reproduced in Fig. 2.7. The most significant differences between the measurement reported here and the results from Schumann, *et al.* is the lack of a sharp resonance at 722.344 nm (49,971.785 cm^{-1}). This is likely due to the greater pulse-to-pulse wavelength fluctuation of our lasers ($\pm$2 pm, see Fig. 3.15). The result is that, on average, only a small portion of the total laser photons are actually resonant with the very narrow resonance and we tend to average the cross section over a broader wavelength range. Thus, when we tune our laser to the very broad resonance near 722.202 nm (49,974.544 cm^{-1}) we increase the resonant photoion signal for ^{238}U by a factor of 1.58(2). This is the reason we adapted the 3-color, 3-photon ionization scheme to use the very broad resonance at 722.202 nm.

We performed more detailed wavelength scans of the resonance at 722.202 nm for both ^{235}U and ^{238}U and the results are shown in Figure 4.21. The experiments (#15 & #16) were performed on the SRM 960 target with the other two lasers tuned to the resonance wavelengths for the appropriate isotope. The total counts are shown relative to the maximum total count recorded for a single acquisition. The acquisitions were performed in analog detection mode. The uncertainties shown in Fig. 4.21 incorporate the typical acquisition to acquisition fluctuation in sputter yield and the curves represent least squares fits with Gaussian functions. The energy per pulse of the first laser dropped during the measurement of ^{238}U from an initial value near 190 to 170 μJ and may account for some of the variation in ion signal between repeated acquisitions at a given wavelength. The fluctuations from acquisition to acquisition are too large to provide meaningful information on the isotope shift between ^{235}U and ^{238}U for this transition.

The difference in the relative widths of the transitions for the two isotopes is significantly larger than expected. The least squares fits through the data have FWHM of 167(280) and 98(45) pm for ^{235}U and ^{238}U, respectively. Some differences may be a result of cross section differences between the two isotopes, but the significant broadening of the autoionizing transition in ^{235}U should be tested in an additional experiment with improved instrumental precision.

4.2.4 Wavelength Dependence of UO and UO_2 Ionization Probabilities

We have previously assumed that the ionization of UO and UO_2 is not wavelength dependent. Figure 4.22 displays the normalized counts for $^{235}U^+$, $^{235}UO^+$, and $^{235}UO_2^+$ collected

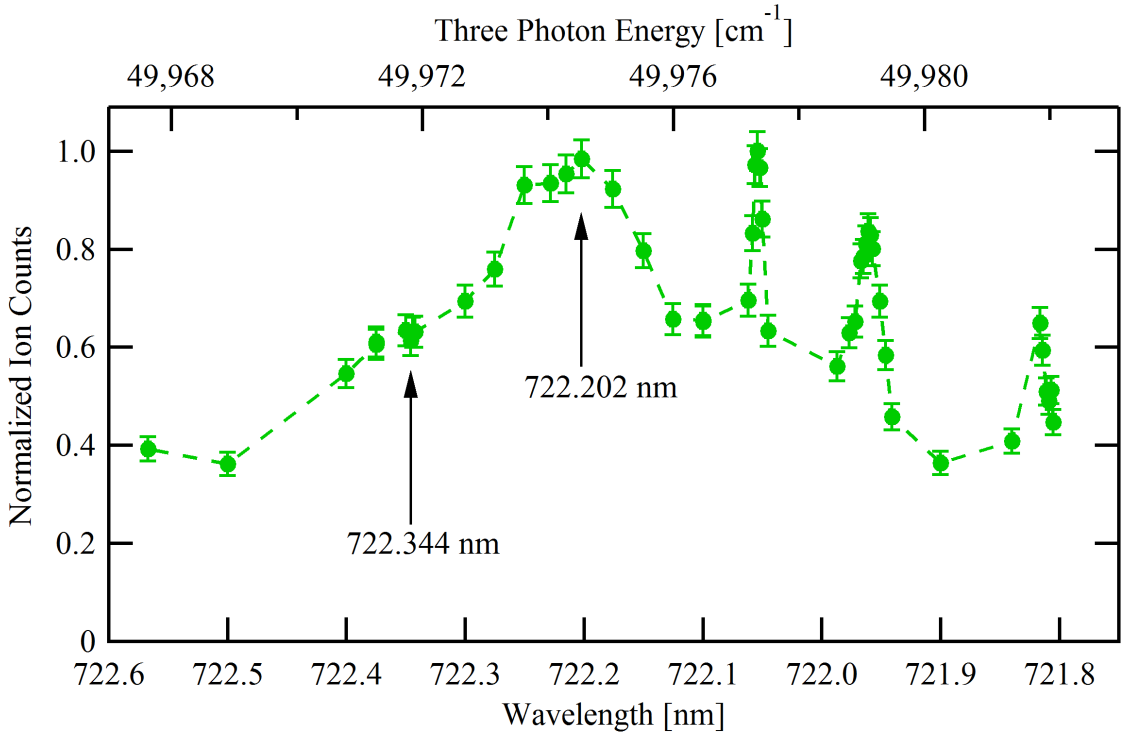

Figure 4.20: Third resonance laser scan of ^{238}U. The other two lasers were tuned to 415.514 and 829.091 nm both with narrow bandwidth. The arrows mark the location of the two autoionizing resonances used in the 3-color, 3-photon ionization scheme (see Sec. 3.2.1). Compare this scan to the right half of Fig. 2.7. Measurement performed on SRM 960.

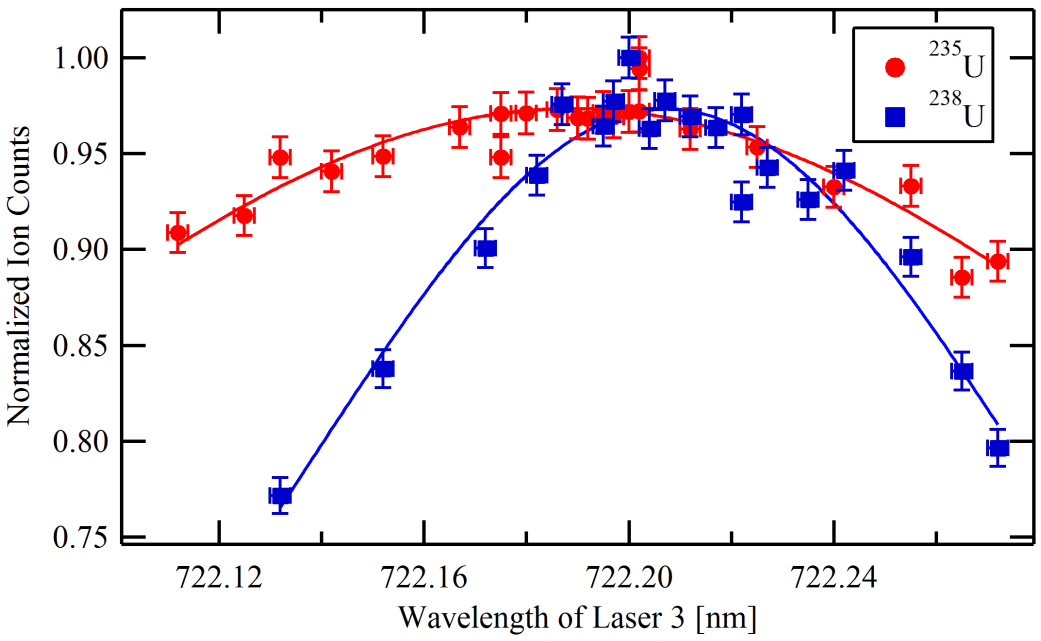

Figure 4.21: Wavelength scan of autoionizing transition near 722.202 nm for ^{235}U and ^{238}U. Note the wavelength scale covers a range of almost 200 pm. Measurement performed on SRM 960.

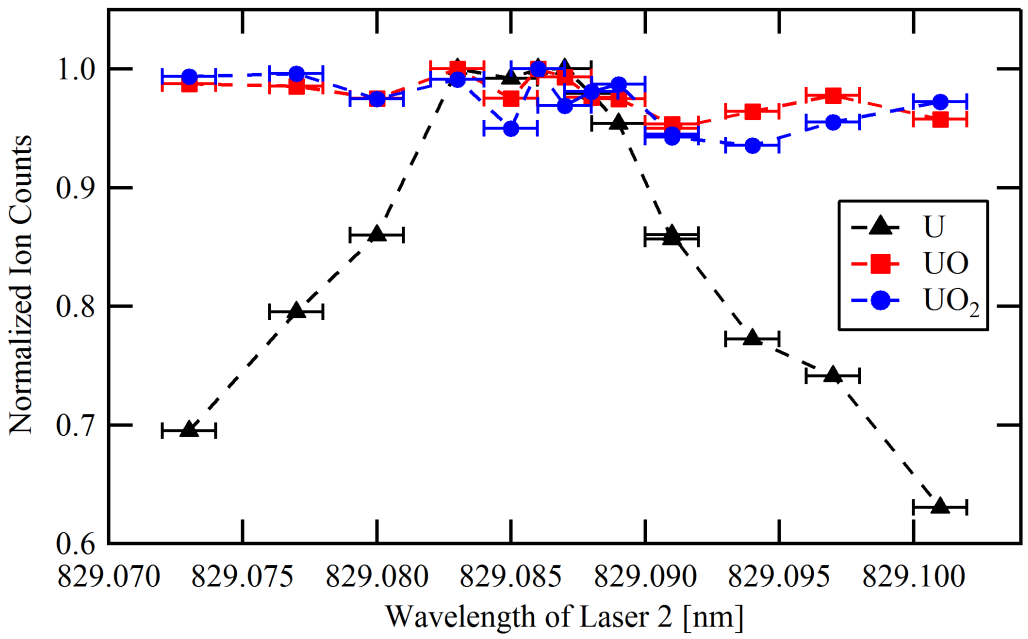

Figure 4.22: Normalized mass peak counts for ^{235}U, UO, and UO_2 from the wavelength scan of the second resonance transition (Exp. #11). Uncertainties from counting statistics (vertical) are smaller than the data markers. As the wavelength of Laser 2 is changed, near the second resonance transition for ^{235}U, the atomic U ion signal displays a large dependence on the wavelength. No wavelength dependence is observed in the ion signals from UO or UO_2.Measurement performed on SRM 960.

during experiment #11 (see Fig. 4.18). The counts are normalized relative to the maximum total counts recorded for a single acquisition of that ion. The uncertainties estimated from the counting statistics alone are below 0.1 %. The atomic uranium ion signal is highly-dependent on wavelength, but the ion signals for UO and UO_2 show no discernible dependence on the wavelength of the second resonance laser. The variation in measured ion signal for the oxide species is assumed to be primarily from a change in sputter yield during the experimental acquisition ($\sim$ 0.5 hr).

4.3 The Dependence of Uranium Ionization on Laser Beam Intensity

We present a study of the dependence of the resonance transitions on the intensity of the laser beams used in our 3-color, 3-photon ionization scheme. The aim is to maximize the probability of ionizing the target isotope while minimizing the ionization of any other species that may be present in the ionization volume. With sufficient laser energy density in the ionization

volume, we should be able to saturate a given transition, that is, equilibrate the rate of stimulated absorption and stimulated emission. We consider a transition effectively saturated when at least 95 % of the ions in the volume of the beam are excited.

The laser beam parameter important for describing the likelihood of resonantly ionizing an atom is the spectral irradiance (Eq. 2.10). Empirically, we discuss the intensity (power/unit area) or energy per pulse of the laser beams, which are both directly proportional to the irradiance. We report the results of all experiments in units of average total energy per laser pulse[8]. Uncertainty in the reported laser pulse energy is $\pm 5\,\mu$J. The other quantity aside from intensity necessary to describe the irradiance of a laser beam is the spatial distribution of the beam energy. The spatial distribution of the beam energy is measured independently from the total beam energy. The experiments presented in this work should be understood in terms of laser pulse energy for the beam used. The beam shape is assumed constant. This assumption neglects the consideration that the cross-sectional area increases with pulse energy. The elliptical areas of the laser beam, as reported in the following experiments, are defined by half of the $1/e^2$ width in the horizontal and vertical directions.

The excitation probability for single-photon absorption is linearly dependent on the number of photons present in a laser beam as long as the probability for excitation of any single atom remains small. When the probability for excitation becomes appreciable, the effects of saturating the transition become significant. The saturation of a transition will cause the excitation probability to asymptotically approach the ratio of the level degeneracies of the states involved. Therefore, we expect the dependence of the excitation and ionization probability to be of the form, $P(LX) = 1 - Ae^{C \cdot LX}$, where A and C are constants, and LX is the intensity of the laser beam involved in stimulating transition X.

4.3.1 Ionization Dependence on the Intensity of the First Laser Beam

Experiment (#17) studied the intensity dependence of the first resonance transition on laser energy when the bandwidth of that laser was narrow. The measurement was performed on the SRM 960 target. We chose to set the wavelength of the lasers at the resonance transitions for ^{235}U, because we were using a narrow bandwidth and could not resonantly excite both ^{235}U and ^{238}U simultaneously. We also observe moderate ionization of ^{238}U, because the wavelength of the laser was only -7 pm from the resonance centroid for the corresponding transition in ^{238}U. The approximate elliptical area for the first resonance laser beam was 1.30(3) mm^2. Figure 4.23 shows the measured isotope signal as a function of laser pulse energy in the first resonance laser beam. The uncertainties shown include an estimate of the change in sputter yield, and for ^{238}U an additional contribution to uncertainty is included from fluctuations in the ion signal expected from wavelength fluctuations. The ^{235}U resonance appears to be saturated with as little as 20 μJ/pulse, with only small increases in ion signal above that energy. The increase in counts after saturation with increased beam intensity is a result of both the off-resonance ion

[8]For our laser cavities operating at a repetition rate of 1 kHz, the laser pulse energy can be easily converted to laser beam power. At this repetition rate, 1 mW = 1 μJ per pulse.

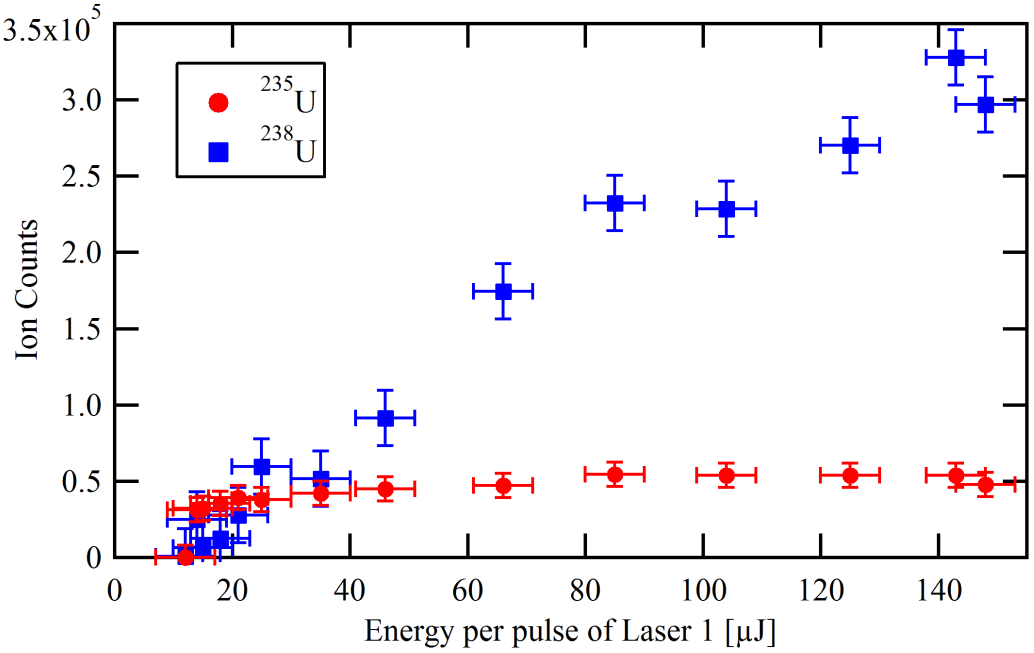

Figure 4.23: Dependence of atomic uranium ion signal on the intensity of the first resonance laser beam. Measured on SRM 960. The wavelength of each laser was tuned to resonantly ionize ^{235}U with narrow bandwidth. The ion signal for ^{235}U is saturated with less than 20μJ, while the ion signal for the off-resonance ^{238}U increases linearly with laser power.

signal (see Fig. 4.11) and the increase in the cross-sectional area of the beam. The slope of a linear fit to the data points above 20 μJ is 134(27) counts/μJ. In contrast to ^{235}U, the ion signal for ^{238}U appears to increase nearly linearly throughout the region of laser intensity explored. The slope for a linear fit to the ^{238}U ion signal is 2,375(175) counts/μJ. We expect that very high irradiance would be required to saturate this transition at this wavelength, because this laser is tuned to a wavelength on the wing of the ^{238}U resonance (3-4 σ from the peak).

Similarly, an experiment (#18) was carried out with the bandwidth of the first and second resonance lasers broadened to $\sim$5 pm and $\sim$6 pm, respectively. The mean wavelengths of all three lasers are tuned to the midpoints of the isotope shifts between ^{235}U and ^{238}U. The results from this measurement of the CRM U500 target are shown in Figure 4.24, each point is the sum of 5×10^4 laser pulses. The transition appears to saturate around 25 μJ/pulse in the first laser beam at this size, approximately 1.06(2) mm^2. This result provides for the excitation of the first resonance transition for both ^{235}U and ^{238}U nearly equally at a single mean wavelength. The increased ionization probability for ^{235}U over ^{238}U will be discussed later.

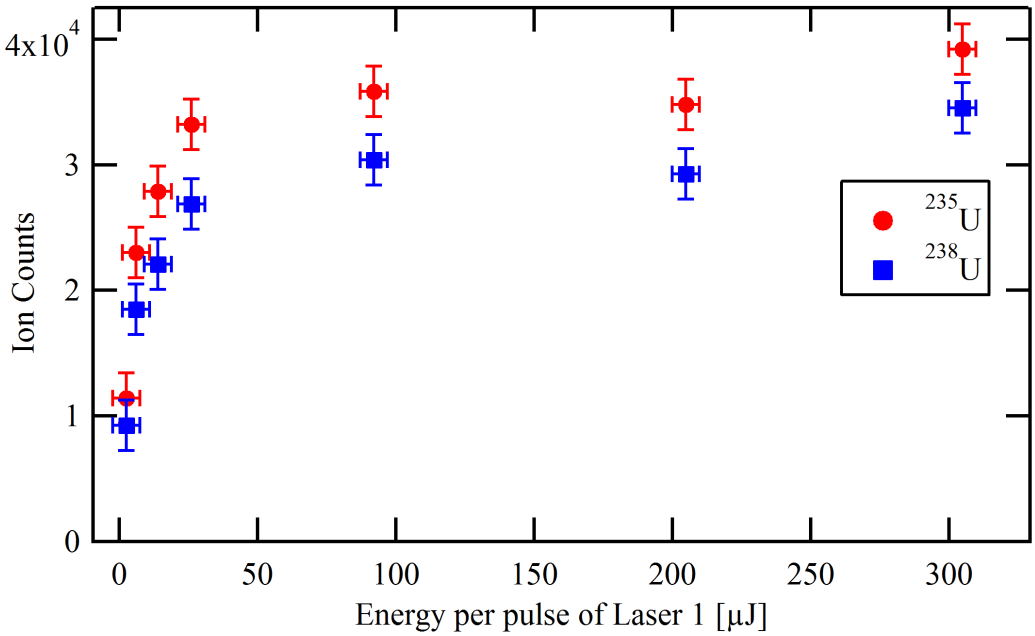

Figure 4.24: Ion signal as a function of the beam energy of the first resonance transition with a broad bandwidth first laser cavity (∼5 pm). The mean wavelengths of all three lasers were set to ionize both isotopes equally. The resonance is saturated above intensities of 25 μJ. Uncertainty estimates include changes in sputter yield during the experiment. Measurement performed on CRM U500.

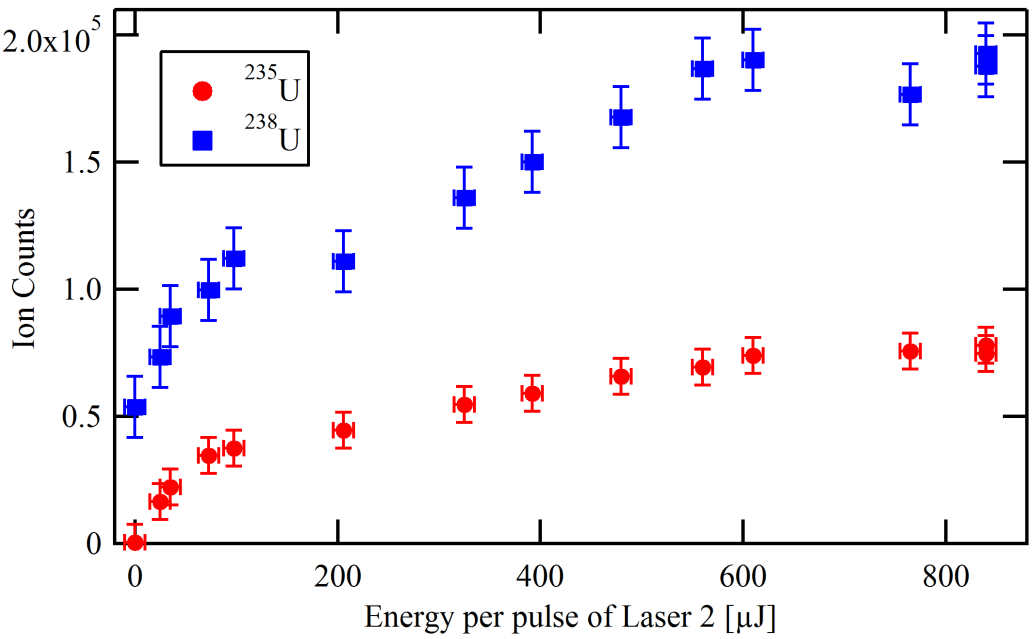

Figure 4.25: Ion signal as a function of total energy per pulse in the laser used to excited the second resonance transition. All three lasers were tuned to the wavelengths of the ^{235}U transitions and were arranged for narrow bandwidth. Measured on the SRM 960 standard with a natural U isotope composition. Measurement performed on SRM 960.

4.3.2 Ionization Dependence on the Intensity of the Second Laser Beam

We explored the energy dependence of the ionization of uranium atoms on the intensity of the second resonance transition for both narrow and broad bandwidth laser conditions. For the narrow bandwidth experiment (#19) using SRM 960, the lasers were tuned in wavelength to the transitions of ^{235}U and we collected ions from 1.5×10^5 laser pulses. The approximate beam area of the second laser beam was 1.76(8) mm^2. The results are shown in Figure 4.25. The second resonance transition of ^{235}U appears to be saturated at laser pulse energies above 200 μJ/pulse. The slope of the least squares linear fit to the ^{235}U data above 200 μJ is 47(5) counts/μJ. This can be compared to the increase of the ^{235}U count rate as a function of energy above saturation for the first resonance laser of nearly 150 counts/μJ. The mean wavelengths of the lasers are on the tails of the ^{238}U resonance for both the first and second transitions, which explains why the measured ^{235}U/^{238}U ratio is closer to 0.5 than the certified ratio of the sample of 0.0073(1). The uncertainties shown include an estimate of the change in sputter yield, and for ^{238}U an additional contribution to the uncertainty is included due to fluctuations in ion signal expected from wavelength variation.

The energy dependence of the second resonance transition was also studied (Exp. #20) using bandwidths for the first and second lasers of $\sim$ 5 pm and $\sim$ 6 pm, respectively. The area of the

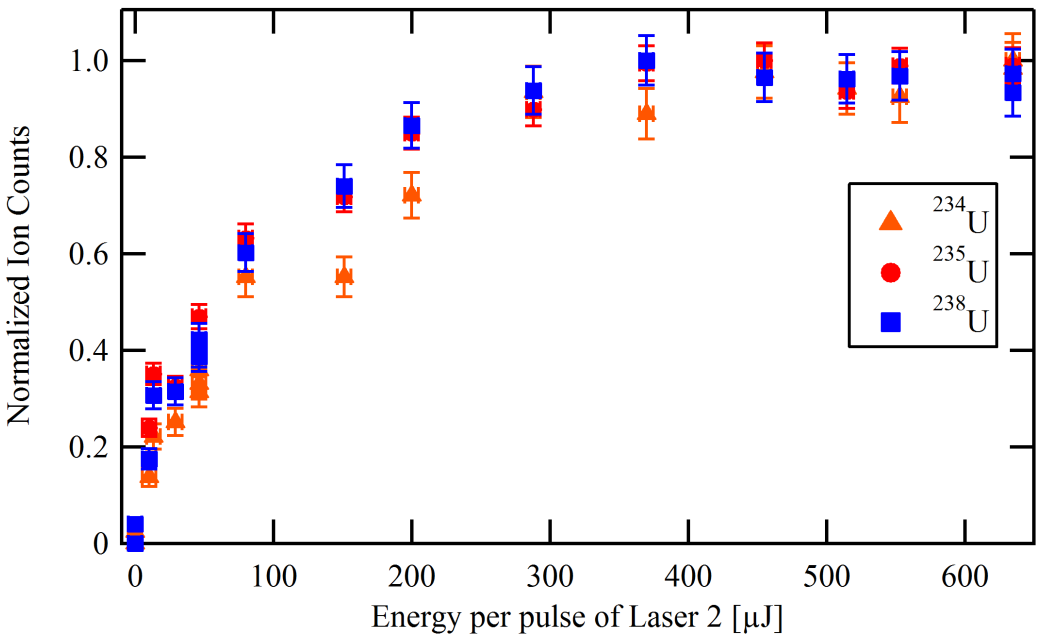

Figure 4.26: The normalized ion signal as a function of energy per pulse of the second resonance laser beam with the bandwidth of the first and second laser cavities broadened to ∼5 pm and ∼6 pm, respectively. The total counts are normalized so that the ^{234}U can be compared with the major isotopes. The transition of all three isotopes appear to be saturated above energies of 400 μJ/pulse in the second laser beam. Uncertainty estimates include changes in sputter yield. Measurement performed on CRM U500.

second laser beam in this experiment was approximately 1.02(2) mm^2. We report in Figure 4.26 the total counts of the ion mass peaks for ^{234}U,^{235}U, and ^{238}U normalized to their maximum total count for 5×10^4 laser pulses measured on the CRM U500 standard. All three wavelengths were tuned to the midpoints of the ^{235}U and ^{238}U resonances. The resonance transition for all three isotopes appears to be saturated at energies above 400 μJ/pulse. With the wavelengths tuned to the isosbestic point for the ^{235}U and ^{238}U, the wavelengths for the ^{234}U resonances will be the furthest from the mean wavelengths. From this we would expect the ion signal of ^{234}U would be the most sensitive to fluctuations in wavelength and intensity, which may explain the increased scatter of ^{234}U in this experiment, particularly at low beam energies.

4.3.3 Ionization Dependence on the Intensity of the Third Laser Beam

We explored the dependence of ion signal on the beam intensity of the ionizing laser in the 3-color, 3-photon scheme for both narrow and broad bandwidth laser arrangements. The narrow bandwidth measurement was made on SRM 960 (Exp. #21) with all three wavelengths tuned to resonantly ionize ^{235}U. This measurement was performed with the third wavelength

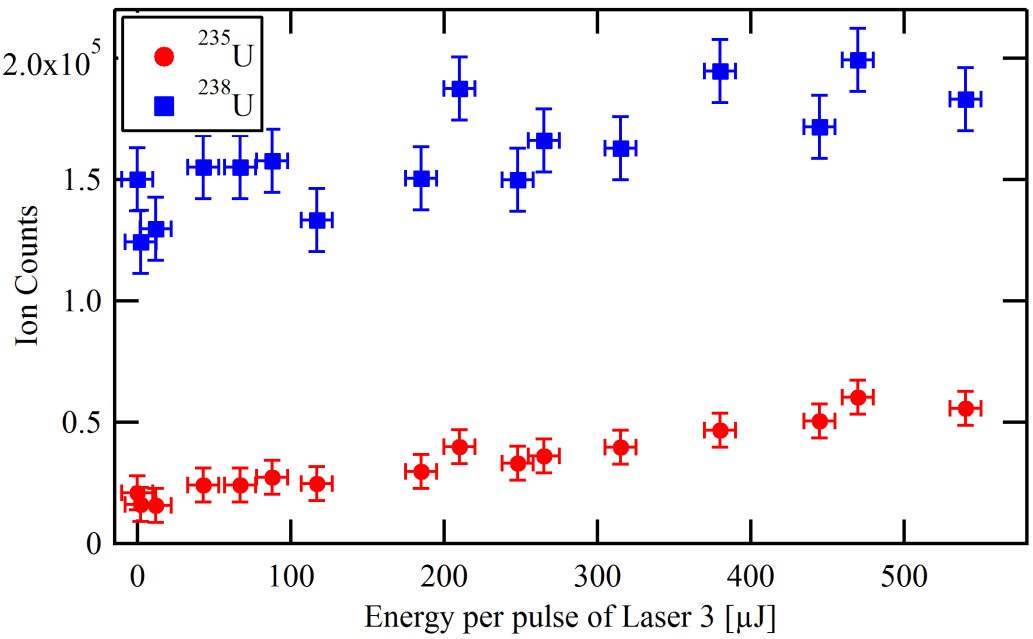

Figure 4.27: Ion signal as a function of energy per pulse in the third laser measured on SRM 960. All three lasers had narrow bandwidth and their wavelengths were tuned to the transitions of ^{235}U.

tuned to 722.344 nm instead of our preferred wavelength of 722.202 nm. The measured ion signals for ^{235}U and ^{238}U as a function of total energy per pulse in the third laser beam are shown in Figure 4.27. The ion signals appear to vary linearly with beam energy across the region explored. The slope of the least squares linear fit to the ^{235}U data is 75(5) counts/μJ, while for the ^{238}U data it is 98(20) counts/μJ. We do not have sufficient intensity, for this beam size (approximately 4.52 mm^2), to saturate the ionization step in this scheme. We know that by changing the wavelength of this laser to near 722.200 nm we can utilize an increase in the ionization cross section of about 60 % (see Fig. 4.20), but it is still unlikely that we can saturate this transition at this beam size with the energy provided by our laser system, as we will see next. The uncertainties shown include an estimate of the change in sputter yield and for ^{238}U an additional contribution to uncertainty from fluctuations in ion signal expected from wavelength fluctuations. We do not expect the ion signals to go to zero as the intensity of the third laser beam goes to zero because of a 2-color, 3-photon ionization process discussed in the next section (see Fig. 4.29).

Experiment #22 measured the ion signals for ^{235}U and ^{238}U from U500 using the 3-color, 3-photon ionization scheme as a function of intensity in the third laser with the bandwidth of the first two lasers broadened. The results are shown in Figure 4.28. The wavelength of the third laser was tuned to 722.200 nm. The ion signals are better fit by an exponential function of the form $y(x) = y_0 + Ae^{C \cdot x}$, than by a linear function over the range of laser pulse energy

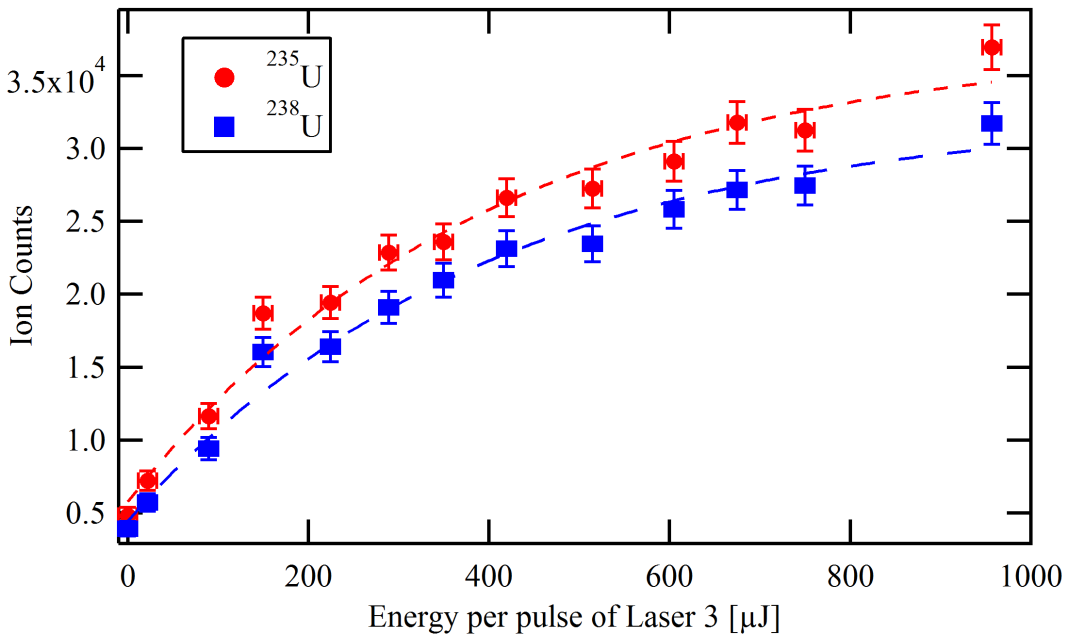

Figure 4.28: Ion signal as a function of laser pulse energy used to excited the ionization step measured on U500. Least squares fits of the form $y(x) = y_0 + Ae^{C \cdot x}$ are shown for each isotope. Both the first and second lasers were broadband and all three lasers were tuned in wavelength to excite both isotopes nearly equally. Uncertainty estimates include changes in sputter yield during the experiment.

studied. This was determined by the examination of the residuals of the least squares fit for both types of functions. The coefficients for the fits of each isotope are given in Table 4.2. The fits predict that 95 % of the ions in the volume of the laser beam would be ionized at an energy of ∼1125(50) μJ/pulse for this beam shape, with an approximate elliptical area of 1.11(2) mm^2. With this beam shape and the limit of pulse energy produced by the laser system at this wavelength we do not have sufficient energy density to saturate the ionization step of the 3-color, 3-photon ionization scheme using the 722.200 nm transition. It is possible to produce a laser beam with a higher energy density at the cost of beam cross-sectional area and consequently a cost of total atoms in the irradiation volume of the beam. We discussed earlier (Sec. 2.3.2.2) the theoretical benefits to measurement reproducibility when using a cross-sectional area for the ionizing laser beam that is larger than the area of the excitation laser beams. This should be remembered when considering changing the area of the ionizing laser beam to increase ionization probability.

Enrichment of the odd isotope compared to ^{238}U in this experiment can be a result of several factors. We cannot exclude the uncertainty in the wavelength of the laser beams as a cause of bias in the relative ion signal. We know that this can be responsible for as much as 20 % enrichment (Fig. 4.17). However, the enrichment in this measurement is similar in nature to other

Isotope	y_o	A	C	$y(x)/y_0 = 0.95$
^{235}U	37423(5600)	-31666(4670)	0.00250(90)	1131(52) μJ
^{238}U	32479(4070)	-28031(3760)	0.00253(87)	1125(47) μJ

Table 4.2: Coefficients of the least squares exponential fits to the data in Fig. 4.28. Uncertainties are 2σ. The final column gives an estimate of the laser pulse energy necessary to ionize 95 % of the ions in the ionization volume for the laser beam used in this experiment (elliptical area of 1.11(2) mm^2).

experiments performed with the wavelengths arranged to ionize both isotopes nearly equally. The tendency is for the measured ratio to be enriched in the odd isotope rather than be normally distributed about the certified value of the isotope ratio. This suggests that either our wavelength determination is consistently biased towards the odd isotope or that another effect is contributing to the ionization bias. Under conditions where the ionization of both isotopes is not saturated, we can anticipate a difference in the ionization rate of odd and even isotopes due to dynamic effects (see Sec. 2.3.2.2). These effects arise from differences the number of angular momentum states[76] and differences in the ionization cross section of even and odd isotopes due to angular momentum factors[36]. Fig. 4.28 shows that we have not experimentally achieved saturation of the ionization step, so we cannot ignore dynamic effects in the measured isotope ratio as a factor in this enrichment. As the ionization probability for both isotopes approaches unity we expect that the measured isotope ratio would approach the certified value. See Sec. 5.1.2 for a discussion of the differences in the average cross sections between ^{235}U and ^{238}U.

4.3.4 Ionization Dependence on the Intensity of the Second Laser Beam Without the Third Laser Beam

In addition to the desired 3-color, 3-photon ionization pathway we intend for the ionization of atomic uranium, it is also possible for ionization to occur through a 2-color, 3-photon ionization pathway. This pathway is diagrammed in Figure 4.29, alongside the 3-color, 3-photon pathway. In the 2-color, 3-photon ionization pathway the atom is excited to the second resonance state near 36,127 cm^{-1} (4.48 eV) using the first two resonance transitions in our scheme. From the second excited state, it is energetically possible to ionize the atom via absorption of an additional photon from the first laser (415.510 nm) instead of using a photon from the third resonance laser (722.200 nm). This is the most probable ionization pathway from the second resonance state in the absence of a third laser beam, because the absorption of a single additional photon from the second resonance laser beam (1.50 eV) is insufficient to reach the ionization limit (6.19 eV).

We studied the 2-color, 3-photon pathway (in experiment #23) by blocking the third resonance laser beam and allowing the first and second laser beams only into the ionization volume. The total counts for ^{235}U and ^{238}U from 5×10^4 laser pulses measured from CRM U500 are

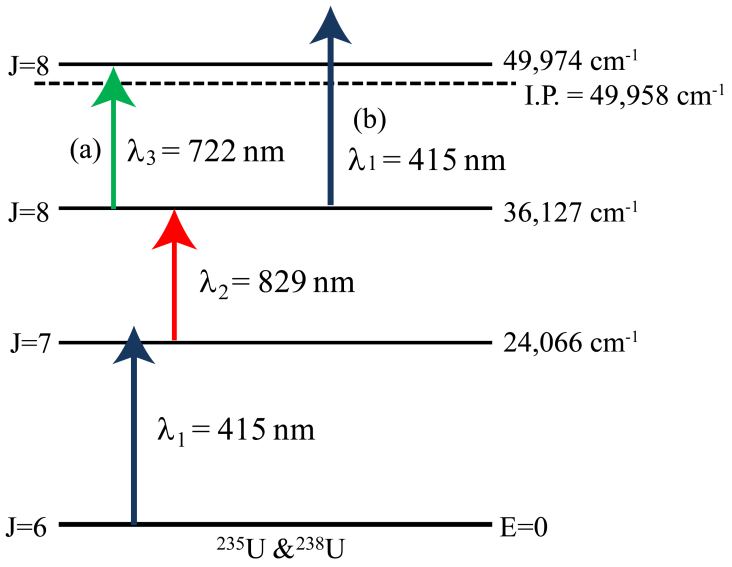

Figure 4.29: A partial energy level diagram of the (a) 3-color, 3-photon and (b) 2-color, 3-photon ionization pathways. The levels and wavelengths are rounded to the nearest integer. Both pathways excite the atom to the second excited state near 36,127 cm^{-1}, but use photons of different wavelength for the ionizing transition.

shown in Figure 4.30. They show an essentially linear dependence on laser pulse energy for the second resonance in the range of energy explored, the least squares fit line through both isotopes gives a slope of 4(1) counts/μJ. This relatively small dependence on beam intensity of the second laser is expected as we know the first transition is saturated at the intensity used, and the second transition is saturated above intensities of 400 μJ. We expect the ionization probability would show a greater dependence on the intensity of the first laser beam, but did not perform that measurement. The dead-time corrected intensities for these acquisitions cover a range between 2,500 and 5,700 counts. These count rates can be compared to acquisitions taken immediately after this experiment (#18) when all three lasers were used under on-resonance ionization conditions and the intensities of the first two lasers were maximized. The total intensity for ^{235}U and ^{238}U in that experiment were roughly 39,000 and 34,500 counts, respectively. Under these conditions, the 2-color, 3-photon ionization pathway provided an ion signal of 10-15 % of the maximum on-resonance ion signal of the 3-color, 3-photon pathway. Therefore, this 2-color pathway is not negligible in the resonance ionization scheme used in this work, but the 3-color, 3-photon pathway will dominate the ionization rate when present at the beam intensities typically used in our experiments.

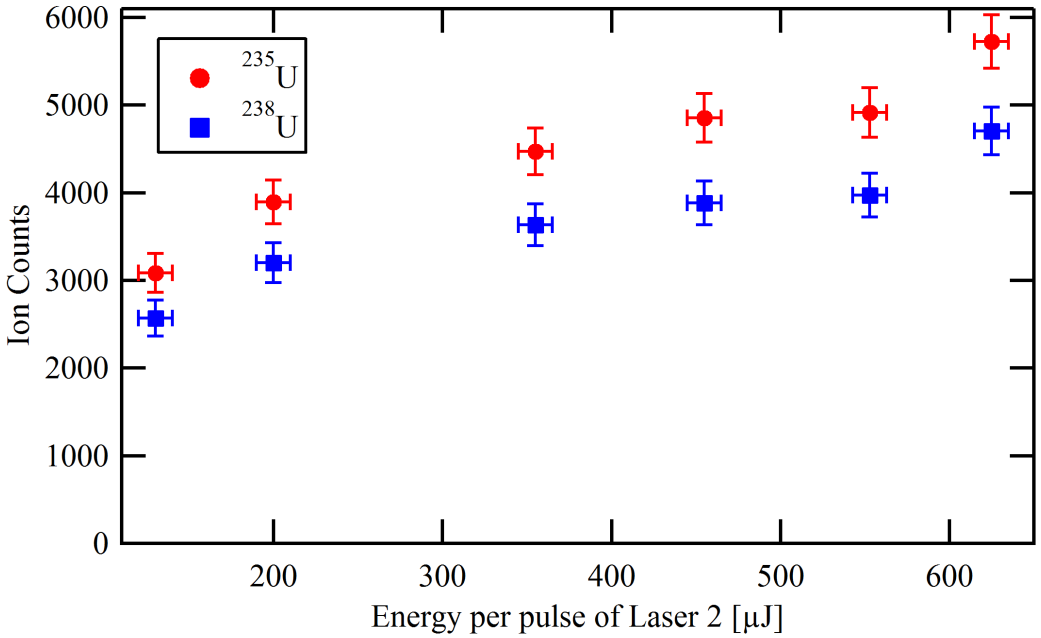

Figure 4.30: Dependence of ion signal on the energy per pulse of the second resonance laser when the third resonance laser beam is not present. The first laser beam is present and tuned to the midpoint between the two isotopes with an energy of 310 μJ/pulse. The ion signal increases linearly with energy in the second laser and the total signal is 10-15 % of the maximum on-resonance ion signal measured with all three laser beams present in the ionization volume. Uncertainty estimates include changes in sputter yield during the experiment. Measurement performed on CRM U500.

4.3.5 Ionization using a 532 nm Laser Beam

We now consider the use of a 532 nm laser beam (Exp. #24) to provide photons for the ionization step of our 3-photon scheme (instead of a 722 nm beam). In total, we explored the use of three wavelengths for the ionization step of our 3-color, 3-photon ionization scheme. These included 722.344, 722.202 nm from the tunable Ti:Sapph cavities and 532 nm from the fixed-wavelength LaserPath. The ionization cross section for a transition of 532 nm from the second resonance state into the continuum is smaller than for a transition that uses an autoionizing state. We can compare the relative cross sections for transitions involving 532 or 722 nm by measuring the atomic uranium ion signal with and without the third laser beam present. This provides a quantification of the enhancement in ion signal of the particular 3-color pathway compared to the 2-color, 3-photon pathway described in the previous section.

Table 4.3 compares the relative ion formation of the 3-color, 3-photon schemes using different ionization wavelengths compared to the 2-color, 3-photon scheme. This is accomplished by dividing the signal obtained when all three laser beams are present by the signal obtained when the beam used for the ionization step is blocked (second column of the table). The measured ion signal is linearly dependent on the laser intensity for these transitions assuming that the ionization probability is not near saturation. Thus, to ensure we are not near saturation for the 722 nm pathway, we have intentionally chosen a measurement in which the intensity of the third laser beam was relatively small compared to the maximum intensity available (from experiment #22, see Fig. 4.28). We can estimate the relative strengths of the absorption cross sections if we consider the influence of the relative laser beam intensities. The 2-color, 3-photon process will be linearly dependent on the intensity of the first resonance laser, assuming that there is sufficient intensity to saturate the first transition but not the ionizing transition. The 3-color, 3-photon processes will be linearly dependent on the intensity of the ionizing laser. Thus, we estimate the cross section for the autoionizing state (722.200 nm) relative to the continuum (532 nm) as

$$\frac{\sigma_{722}}{\sigma_{532}} = \frac{I_{722}}{I_{532}} \cdot \frac{L3_{532}}{L3_{722}} \cdot \frac{L1_{722}}{L1_{532}}$$

where the subscripts specify the scheme by the wavelength used in the ionization step, σ is the cross section, I represents the 3-color ion signal divided by the 2-color ion signal and LX represents the energy of laser beam X in excitation order. By this method, the estimated cross section for the autoionizing state near 722.200 nm is 32 ± 3 times higher than the cross section for ionization into the continuum by a photon from a laser of 532 nm[9]. This estimate is a lower limit of the relative cross sections, assuming that no other ionization or excitation pathways are involved. Multi-photon absorption processes that must be possible but are not considered in this treatment would mainly cause an over-prediction of the 2-color, 3-photon ionization rate.

When the wavelength of the first resonance laser beam was changed for the experiment using the 532 nm ionization step, the ratio of off-resonance/on-resonance atomic ion signals

[9]This result helps confirm our assumption that the ionization probability for the 532 nm process is not near saturation, as the beam intensity is larger than the 722 nm beam by a factor of $\sim$23 but the relative cross section is smaller by a factor of $\sim$32, so that, we expect a smaller fraction of atoms to be ionized compared to the 722 nm scheme with 90μJ/pulse in the ionizing laser.

λ of Ionization Step [nm]	3-color/2-color Ion Signal	Intensity of First Laser [μJ]	Intensity of Third Laser [μJ]	Relative Cross Section
532	3.7(2)	150(5)	2,100(100)	1
722.200	2.4(2)	315(5)	90(5)	32(3)

Table 4.3: Relative cross sections of ionization steps in 3-color, 3-photon schemes. The efficiency of a particular ionizing wavelength is quantified by dividing the 3-color, 3-photon ion signal by the ion signal obtained with the third laser beam blocked (2-color, 3-photon process). The relative cross sections at the two ionization wavelengths can be estimated by considering the laser intensities (see text).

for was 1.3 ± 0.1 %. This is comparable to the off-resonance/on-resonance ratio for the 3-color ionization schemes to autoionizing states with a range of 0.5 to 2.5 %, depending on the intensity of the laser beams. The similarity of the magnitudes of the ratios produced by these schemes was expected because these schemes have the first resonance laser beam in common, which has been measured to be the primary source of off-resonance atomic ions. Therefore, while clearly not as efficient as schemes that access an autoionizing state, the contribution from high-intensity fixed-frequency laser beams to the off-resonance signal does not inhibit their use in a scheme utilizing ionization into the continuum.

4.4 2-color, 2-photon Ionization Scheme

Experiment #25 was performed to quantify the effectiveness of the 2-color, 2-photon ionization scheme described in Sec. 3.2.2[68]. This experiment utilized the Nd:YAG desorption laser instead of ion sputtering for atomization of the SRM 960 target. The aim was to resonantly ionize ^{238}U using narrow bandwidth lasers. The 2-color scheme uses two relatively high-energy photons with 2.84 and 3.39 eV, in order of excitation. The wavelength used for the resonance step was 436.328 nm and the wavelength for the ionization step was 367.252 nm, both of which require frequency-doubling of the Ti:Sapph fundamental beam. The energies per pulse were 18 and 230 μJ, respectively. We also performed a measurement with the wavelength of the laser used to excite the resonance step detuned away from the resonance by 50 pm to 436.378 nm. The mass spectra in the atomic uranium region for the on- and off-resonance ionization conditions are shown in Figure 4.31. We had previously observed that the majority of the off-resonance signal was attributed to photons from the laser for the resonance step, which is why we used an energy per pulse of only 18 μJ in that laser. This reduction in laser intensity resulted in a ratio of the ^{238}U peaks when the lasers were off-resonance/on-resonance of 16.5(7)%, which was the lowest value of this ratio we observed with this scheme. Surprisingly, it is the 2.84 eV photon that contributes most to the off-resonance ion signal in the atomic uranium mass region (we would have expected the higher energy photon to be more effective, except in the case of nearby resonances). We eliminated this scheme as a useful approach for measuring U isotopes on uranium oxide targets, due to the high off-resonance background of the scheme compared

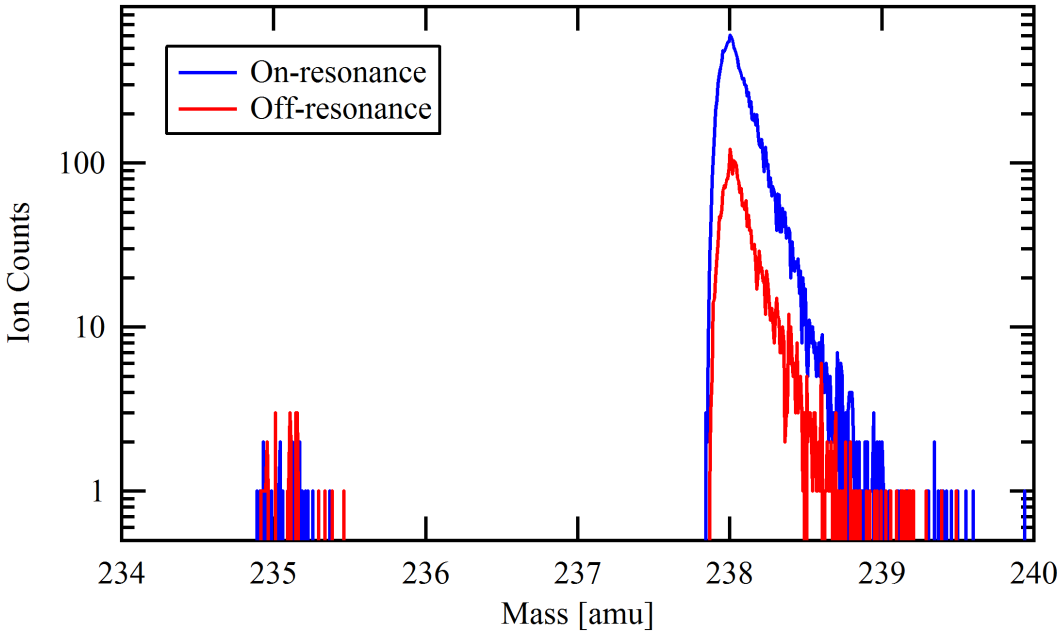

Figure 4.31: The on-resonance and off-resonance mass spectra obtained using a 2-photon, 2-color ionization scheme. The wavelength of the first laser was changed from 436.328 nm (on-resonance) to 436.378 nm (off-resonance) at an energy of 18μJ/pulse. The ionization wavelength was 367.252 nm with an energy of 230 μJ/pulse. Measurement performed on SRM 960.

with the background of the 3-color, 3-photon schemes of about 1 %.

4.5 Uranium Isotope Ratio Measurements

We will now report the results of several measurements of uranium isotope ratios and, eventually, demonstrate measurement to a reproducibility of better than 1 %. In the following section we frequently express the value of measured isotope ratios in terms of the percent difference, see Eq. 3.6. The percent difference between a measured value and the corresponding certified value is a notation useful for highlighting the bias of a measurement from the true value of a quantity. It is particularly useful in comparing measurement results on quantities of different magnitude. Because of the need to correct isotope ratios measured by resonance ionization mass spectrometry using known standards, we are more concerned with how well we can determine a measurement result than with the accuracy of a particular measurement prior to correction.

	$^{235}U/^{238}U$		$^{234}U/^{238}U$	
Material	Certified	Measured	Certified	Measured
SRM 960	0.0073(1)	0.0086(8)	–	–
CRM 125-A	0.041(1)	0.044(8)	0.00039(1)	0.00034(30)
CRM U500	0.9997(10)	1.155(10)	0.0104(1)	0.0118(20)

Table 4.4: Certified uranium isotope ratios from three standards as measured in Fig. 4.32. Estimates of 2σ uncertainties based on counting statistics from single measurements and reported uncertainties of standards.

4.5.1 Isotope Ratios from Sputtered Uranium-Rich Targets.

We have already presented a comparison of the relative sputter yields of U, UO, and UO_2 photoions from the targets used in this section (see Sec. 4.1.6) but we want to briefly compare the ion signal in the atomic uranium ion region for these different uranium-rich materials. RIMS spectra from the three standards collected with the bandwidth of the first excitation laser set to 5 pm are shown in Figure 4.32. The laser energies per pulse were 75, 780, and 620 μJ, respectively. The spectra are normalized to the $m/z = 238$ peak and are offset for clarity. The spectra for CRM 125-A (Exp. #27) and CRM U500 (Exp. #31) represent data from a total of 10^5 laser pulses while that for SRM 960 (Exp. #26) represents data from $4 \cdot 10^5$ pulses. The measured $^{235}U/^{238}U$ ratios are given in Table 4.4. They are seen to be within 20 % of the certified values for each target, which vary by over 2 orders of magnitude. The uncertainties reported are based on counting statistics and can be improved with longer or multiple acquisitions. The differences between the certified and measured ratios are mainly a consequence of the difference between the intended and actual wavelengths and, to a much lesser extent, instrumental mass fractionation. It can be shown from the off-resonance spectrum in Fig 4.2 and from other mass peaks not shown (UO^+ and UO_2^+) that the instrumental mass fractionation for the ratio $^{235}U/^{238}U$ is about 0.3%. The instrumental mass fractionation is negligible compared to the laser-induced isotope variation. In addition to the major isotopes, the detection of ^{234}U from the CRM 125-A target is statistically significant relative to background and CRM U500 shows evidence for the detection of ^{234}U and ^{236}U above background.

This result is contrary to that of Goeringer, Christie, and Valiga[31], who did not observe resonant U^+ photoions from Ar^+ sputtered U_3O_8. In our experiments, the Ga^+ sputtering of uranium oxides exhibits a dominance of UO and UO_2 species in the sputtered flux as observed by other workers[31, 30] and we also confirm the observation of non-resonant photoions in the uranium mass peaks[29]. In contrast with the findings of Goeringer, Christie, and Valiga[31], however, we observe significant resonance ionization of U from U_3O_8 (resonant to non-resonant signal of $>$100). Our enhanced signal to noise is derived from single-ion detection sensitivity and the use of a 3-color resonance ionization scheme in which we optimize the laser power to minimize non-resonance ionization while preserving a high ionization probability for U atoms. There is also evidence that the neutral yield of uranium atoms may be reduced in the presence of nitrate [M.R. Savina, *personal communication*, August 8, 2011]. Goeringer, Christie, and

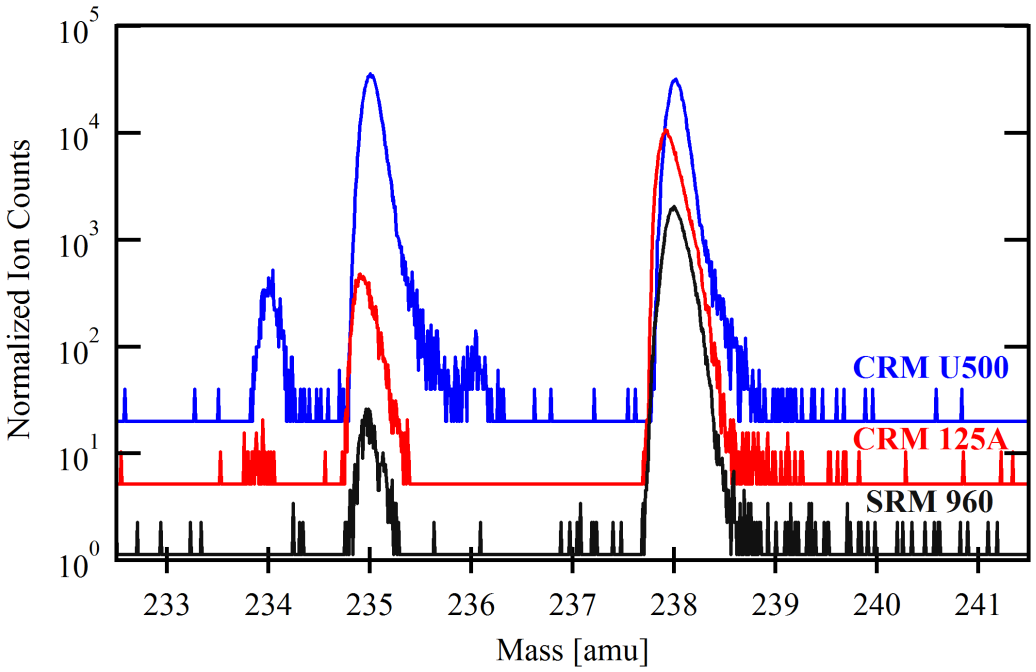

Figure 4.32: Uranium sputtered from three U-rich materials of varying uranium isotopic composition. The spectra are normalized to the total counts in the 238 amu mass peak. One count has been added to each data trace to make the baseline visible on a logarithmic scale. The scale is for the SRM 960 spectrum and the baselines of the other two spectra are offset (by a factor of 4 and 20). The mass spectrometer was tuned for maximum sensitivity instead of mass resolution or abundance sensitivity and the tuning was not identical for each measurement, resulting in different peak shapes.

Valiga's work, however, does underline the reduction in sputter yield for U atoms from uranium oxides compared to uranium metal. Uranium oxides are challenging matrices for RIMS due to the strong tendency for U to desorb or sputter as molecular UO_X, and the efficiency of desorbing or sputtering neutral ground state atoms has not been optimized. Several groups have demonstrated increased efficiency for liberating neutral U and Pu atoms from oxide materials using Ti as a reducing medium[77, 78]. There is also evidence to suggest that laser desorption methods may be more efficient than ion sputtering for creating neutral atoms[79].

4.5.2 Measured Isotope Ratio of Uranium Oxides

By including the mass range of the uranium oxide species during many measurements on a variety of targets, we can consider the isotope ratios of the oxide species (*i.e.*, $^{235}UO/^{238}UO$). For fixed instrument and laser parameters, the measured isotope ratios for UO and UO_2 were always reproducible from acquisition to acquisition. As an example, Figure 4.33 shows the measured ratios for U and UO ions relative to the certified ratio as recorded during experiment #28 (performed on U500). During this experiment, the only recorded change in the instrument or laser parameters was the internal current of the ion gun, which was fluctuating significantly until acquisition 60 when it was stabilized. At this time the total ion beam current and, thus, the count rate was also reduced, which is the reason for the uncreased measurement uncertainty. The non-resonant background signal for the atomic uranium ions was measured at <0.1 % of the atomic uranium ion signal. The UO ions are all technically non-resonant background, so we have neglected a background correction for this experiment. We did perform a deadtime correction on the data and the correction for the UO ion signals was on the order of 2 % of the measured signal. The figure shows the difference between the measured and certified atomic isotope ratios falling over the course of sixty acquisitions from an enrichment of the lighter isotope of almost 40 % until the ratio apparently stabilizes near an enrichment of 15 %. Meanwhile, the measured isotope ratio of the UO ions appears unchanged relative to the certified value within the uncertainties estimated by counting statistics. Regardless of the cause of the variation in atomic isotope ratio difference, the measured ratio difference of the oxide species remains stable.

The mean of the measured $^{235}UO/^{238}UO$ ratio difference is -0.11 ± 0.22 %, thus the measured ratio is indistinguishable from the certified ratio. This result is consistent with all measurements of that ratio for the uranium oxide species. The measured means have all been within 0.25 % of the certified ratio. The ratios for the uranium dioxide species have also been consistently near the certified ratio but the complex nature of the mass spectrum (see Fig. 4.4) in that region makes the statistical analysis of those mass peaks overly complicated for our purposes.

The $^{235}UO/^{238}UO$ ratio provides a measurement of the instrument fractionation induced by sputtering and transport in the mass spectrometer. We conservatively estimate this fractionation at less than 0.3 % of the measured $^{235}U/^{238}U$ ratio (*i.e.*, 0.1 %/amu). Any variation larger than this must be a result of fractionation in the ionization process or in the target composition. Regardless of its magnitude, the instrument fractionation should be mass-dependent and constant, although some variation of isotope fractionation during sputtering could occur[62]. The bias

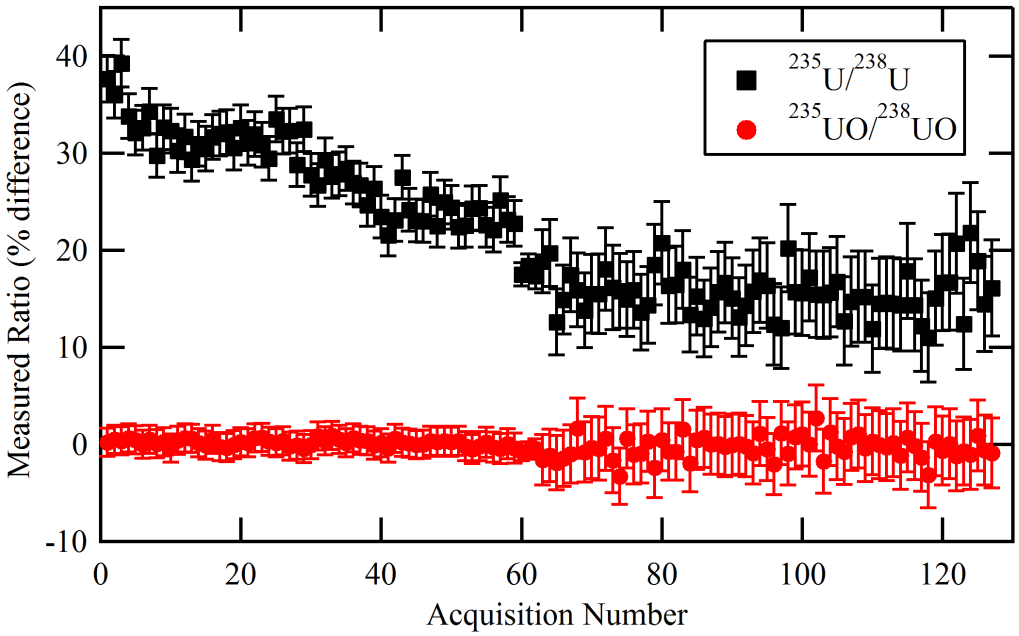

Figure 4.33: Consecutive acquisitions over the course of one day. The data represent the relative measured isotope ratio for the atomic and monoxide ion signals, expressed as the percent difference from the certified ratio. The measured difference for $^{235}UO/^{238}UO$ is -0.11 ± 0.22 %. The data have been corrected for dead-time effects and background signals have been neglected as discussed in the text. The uncertainties shown are from counting statistics alone. Measurement performed on CRM U500.

in a measured isotope ratio can be mitigated, for this cause of isotope fractionation, by using a comparative standard.

The reproducibility of the $^{235}UO/^{238}UO$ ratio also supports the hypothesis that the significant isotope fractionation occurring in the atomic isotope ratios must be due to the ionization process and not sputtering, transport in the mass spectrometer, detection efficiency, count rate, or ionization volume effects. That only leaves factors relating to the resonant ionization of the atoms such as laser beam wavelength, timing, bandwidth, power, and position.

4.5.3 Laser Position Dependence of the Isotope Ratio

We explored the dependence of the measured $^{235}U/^{238}U$ ratio on the relative spatial position of the ionization laser beams using the 3-color, 3-photon ionization scheme (Exp. #29). The experiment was performed on U500 with the first and second laser arranged for broad bandwidth and the wavelengths tuned to resonantly ionize both isotopes nearly equally. Previous to performing this experiment, we observed variation in the measured atomic isotope ratio on the order of 5 % about the mean. This amount is well outside of the uncertainty expected from the counting statistics for the measured signals. We hypothesized that the fluctuation of the laser beam positions relative to each other were inducing a fractionation of the measured isotope ratio. These fluctuations in beam position are measured to be less than 1 % of the width of the beams for sequential acquisitions of the ion signal.

We performed sequential acquisitions of the ion signal as we moved the second of the three laser beams relative to the position of the first beam. The measured isotope ratio relative to the certified ratio was acquired for different positions of Laser 2 relative to Laser 1 is shown in Figure 4.34. The first two acquisitions were made when the beams were both centered. The third acquisition was made with the second beam moved by 3/4 of its width towards the target (left) relative to the beam of the first laser. The fourth and sixth acquisitions were made when the beam of the second laser was moved by greater than its beam width away from the target (to the right), the laser beams were not moved between these acquisitions. There is still some overlap of laser intensity for the two beams because the tails of the Gaussian distributions, which define the spatial distribution of the beams. The ion signal for these two acquisitions was 45(3) % of the ion signal for the first two acquisitions (when both beams were well overlapped). The fifth acquisition was made while the second beam was blocked completely, the ion signal for that acquisition was only 2.0(2) % of the ion signal for acquisition 2. Including the two sigma uncertainty estimates shown, all of the data overlap the mean of the acquisitions performed with all the beams centered. The variations in the measured isotope ratio are all within 5 % of the each other for the acquisitions obtained with three laser beams present. We cannot exclude the possibility that the pointing stability of the laser beams was responsible for this variation in the measured ratio. However, if this were the cause, we would expect to observe a larger fluctuation of the ratio during this experiment due to the relatively large changes in beam position explored.

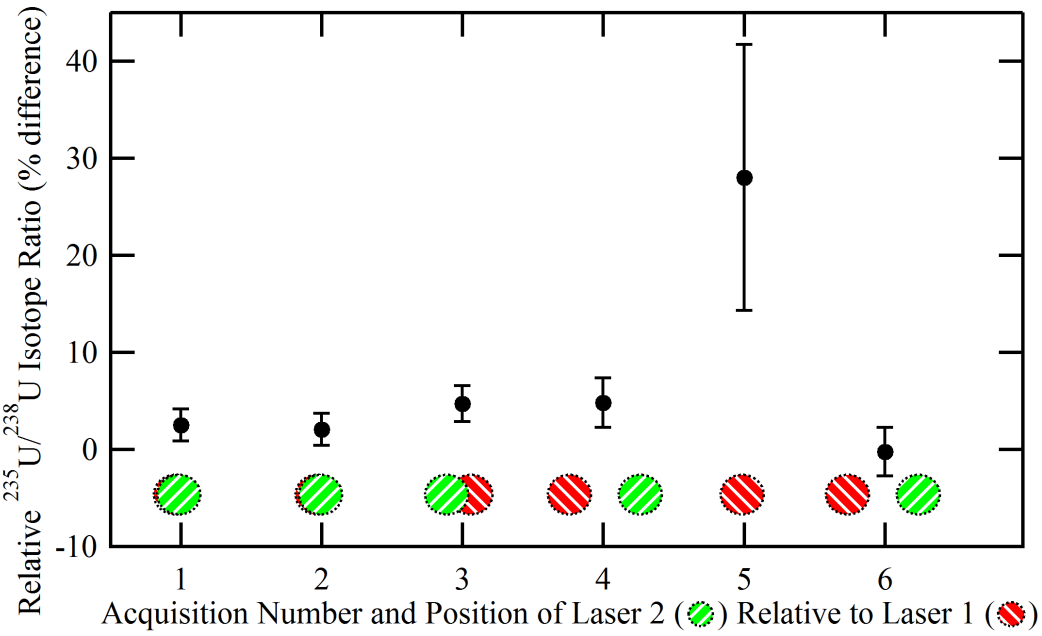

Figure 4.34: Relative isotope ratio expressed as the percent difference between the measured value and the certified value for different beam positions of Laser 2 relative to Laser 1. Laser 3 was present and centered on Laser 1. The first two acquisitions were made when all the beams were centered. The third acquisition was made with the second beam moved by 3/4 of its width towards the target (left) relative to the first beam. The fourth and sixth acquisitions were made when the second beam was moved by greater than its width away from the target (right), the laser beams were not moved between these acquisitions. The fifth acquisition was made while the second laser beam was blocked completely. Including the two sigma uncertainty estimates shown, the data all overlap the mean of the acquisitions made with all the beams present. Measurement performed on CRM U500.

4.5.4 Isotope Ratios Measured Via Isotopically Selective Ionization

Isotopically selective ionization is employed [10, 32] as one method for measuring isotope abundance ratios for elements that have large isotope shifts such as uranium. This is accomplished using narrow bandwidth lasers to resonantly excite only a single isotope within an element and then changing the wavelength of the lasers to selectively ionize each isotope of interest in sequence. An isotope abundance ratio can then be constructed by comparing the ion signal of sequential acquisitions where each isotope is being resonantly ionized in turn.

We performed an isotopically selective measurement of the $^{235}U/^{238}U$ ratio of SRM 960 using the 3-color, 3-photon ionization scheme with all the laser cavities arranged for narrow laser bandwidths (Exp. #30). Figure 4.35 shows acquisitions (of 10^5 laser pulses) of the ^{235}U and ^{238}U ion signal as the first laser was cycled between three wavelengths. For simplicity, only the isotope that was resonantly ionized is shown as a solid marker for each acquisition. The first acquisition used the wavelength of the ^{238}U resonance (415.514 nm). The next acquisition used the ^{235}U resonance (415.507 nm). The third acquisition used a wavelength at the isosbestic point directly between these two resonances (415.5105 nm), no ion signal from these acquisitions are shown in the figure. This sequence was repeated 8 times. Also shown in this figure are calculated values for the ^{238}U counts during the resonant acquisitions for ^{235}U. The calculated values were obtained by assuming a linear change in the ^{238}U count rate as a function of acquisition number. The dashed lines show the linear fit between successive measurements of ^{238}U. Figure 4.36 shows the $^{235}U/^{238}U$ ratio reported as the percent difference from the certified value of the target (SRM 960). The measured ratio was constructed for the 7 acquisitions of ^{235}U bracketed by acquisitions of ^{238}U, using the measured counts of ^{235}U divided by the calculated ^{238}U counts for each acquisition. The mean of the differences is $-1.7 \pm 4.8\,\%$. For comparison, the mean difference when the wavelength of the laser was tuned to the midpoint of the resonances (415.5105 nm) was measured to be $16.1 \pm 6.6\,\%$.

The measured isotope ratio does not appear to be sensitive to the count rate within a factor of about three, in agreement with other measurements we have made (see Fig. 4.13). However, the method of isotopically selective ionization for measuring isotope ratios can introduce additional uncertainty in the result caused by two factors. First, if a target material is heterogeneous with respect to the distribution of the specific element this will directly effect the measured ratio as the individual isotope signals will, by definition, come from different samples of the target material. The second factor that increases the uncertainty of the measured ratio is the potential change of ion signal between acquisitions. This method can not record fluctuations in the relative ion signal that might arise from a change in the atomization rate or ionization rate when a specific isotope is not being acquired. One must assume with isotopically selective ionization methods that the count rate between acquisitions varies only monotonically (*i.e.*, linearly or exponentially).

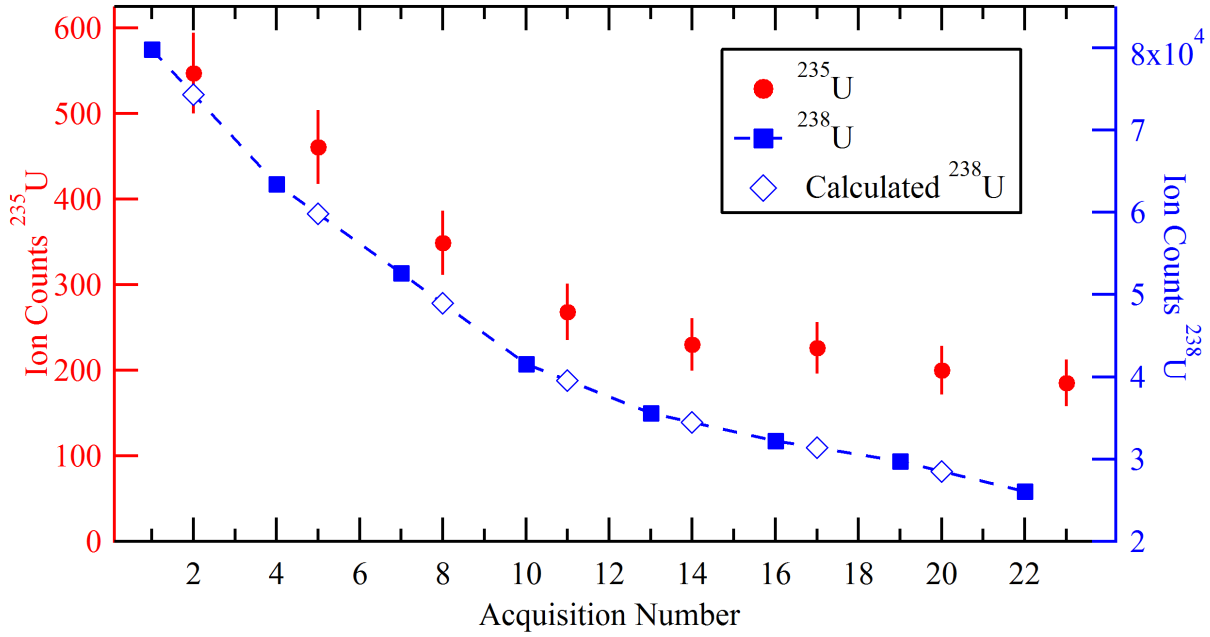

Figure 4.35: The ^{235}U and ^{238}U ion signal as the first laser was cycled between three wavelengths. First, the laser was tuned to the ^{238}U resonance (415.514 nm), for the next acquisition it was tuned to the ^{235}U resonance (415.507 nm), and finally, it was tuned to the wavelength between these two resonances (415.5105 nm). This sequence was repeated 8 times. The figure only shows the resonant ion signal for that acquisition (*e.g.*, the first acquisition shows only the ^{238}U signal) and calculated values of the ^{238}U counts for the resonant acquisitions of ^{235}U. The dashed line shows the assumed linear change of ^{238}U signal between successive acquisitions.

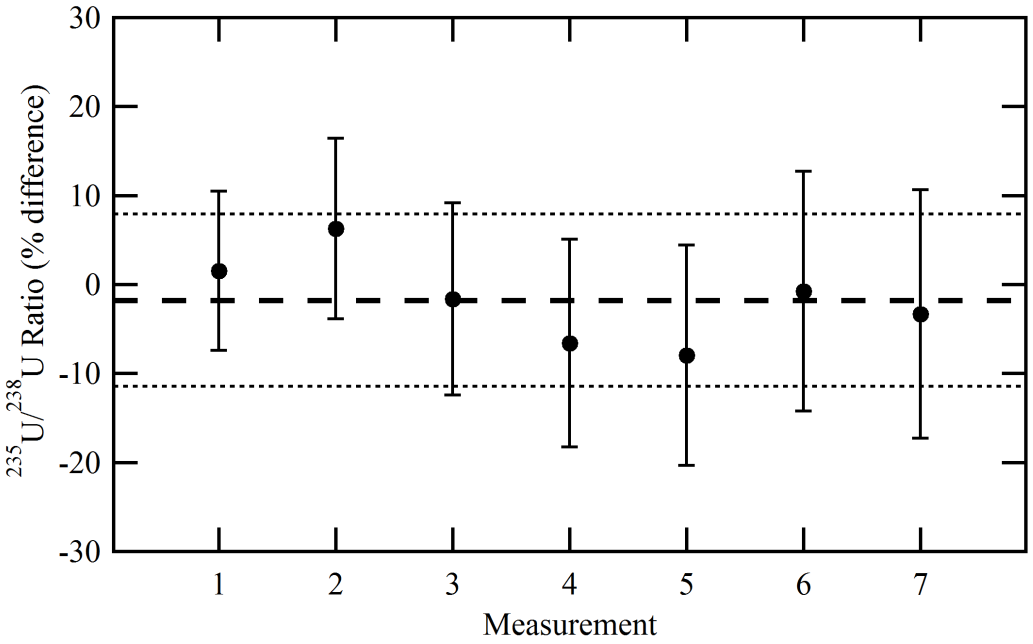

Figure 4.36: The measured $^{235}U/^{238}U$ ratio reported as the percent difference from the certified value of the target (SRM 960), as obtained from isotopically selective resonance ionization. The measurements of the isotope ratio are generated by dividing the resonant ^{235}U counts for each acquisition by the calculated value of ^{238}U from Fig. 4.35. The mean of the differences is $-1.7 \pm 4.8\,\%$ (thick dashed line), the thin lines represent two standard deviations of the mean.

4.5.5 Reproducibility of the Measured Ratio Using Broad Bandwidth

Given the significantly reduced sensitivity to wavelength variations using the broad bandwidth for the first excitation laser and the large signal-to-noise ratio found with the U_3O_8 target, a study was performed to examine the reproducibility of the $^{235}U/^{238}U$ ratio over a large number of sequential acquisitions (Exp. #31). Sixty four consecutive spectra, each consisting of 10^5 laser pulses, were acquired from CRM U500. The bandwidth of the first excitation laser set to $\sim$5 pm. Laser energies per pulse were 75, 725, and 510 μJ, respectively. The total duration of the acquisitions was approximately 2.5 hours. The m/z = 235 and 238 peaks were integrated without background subtraction and 2σ uncertainties assigned from counting statistics alone. The analysis results are shown in Figure 4.37 and values are given in Table 4.5. The measured $^{235}U/^{238}U$ ratio of 1.155 ± 0.005 was 15 % higher than the certified value, likely due to differences in the intended and actual wavelength of the resonance lasers, as we see a similar enhancement of ^{234}U over ^{238}U as shown below. Other possible sources of inaccuracy are the odd-even effect as a result of hyperfine splitting, or mass-dependent bias. Mass-dependent bias can be eliminated as a primary cause by examining the behavior of non-resonant species also detected (but not displayed) in these experiments (UO^+ and UO_2^+). The $^{235}U/^{238}U$ ratio measured on UO^+ and UO_2^+ yield a mass-dependent bias of less than 0.1 %/amu. Finally, non-resonant background could, in principle, contribute to the over abundance of ^{235}U in the measured ratio. However, Fig. 4.2 shows that the background is less than 1 % of the signal, and thus cannot account for the observed enhancement. The $^{234}U/^{238}U$ ratio from the same series yields a value of 0.0118 ± 0.0004 (Table 4.5). This corresponds to a 13.4 % enhancement of ^{234}U over ^{238}U. The low abundance of ^{234}U makes it necessary to consider potential sources of background counts. The average intensity in the m/z = 234 peak is 70 counts per 10^5 laser pulses. The off-resonance spectrum (Fig. 4.2) shows less than 0.7 counts in the m/z = 234 peak per 10^5 laser pulses. Including the background subtraction in the calculation of the $^{234}U/^{238}U$ ratio yields a value of 0.0117 ± 0.0004. Propagating the uncertainty of this background correction increases the relative standard error of the mean by 0.2 %, from 3.0 to 3.2 %. The average $^{234}U/^{235}U$ ratio (note the isotope change in the denominator) differs from the certified value by only 1.5 %, the difference between this ratio and the $^{234}U/^{238}U$ ratio supports the conclusion that the enhancement of the lower mass isotopes is due to spectroscopic factors.

Simultaneous enhancement of ^{234}U and ^{235}U over ^{238}U is expected if the first resonance wavelength is slightly shorter than the wavelength corresponding to the midpoint of the centroids of the ^{235}U and ^{238}U resonances. Assuming that all of the bias observed in these measurements is due to a slight detuning in the first resonance laser, and using the measured wavelength dependence of 13 %/pm (Figure 4.17), we estimate a detuning of -1.1 pm (to 415.509 nm). This is within the estimated precision of our wavelength measurement ($\pm$2 pm) for our broadband laser. In spite of this laser-induced bias and the decrease in wavelength accuracy obtained for the 5 pm bandwidth laser, the RSE of 0.4% and a χ^2 near unity (Table 4.5) indicate that the variation in the mean wavelength is sufficiently small to measure the $^{235}U/^{238}U$ ratio reproducibly over an entire analytical session.

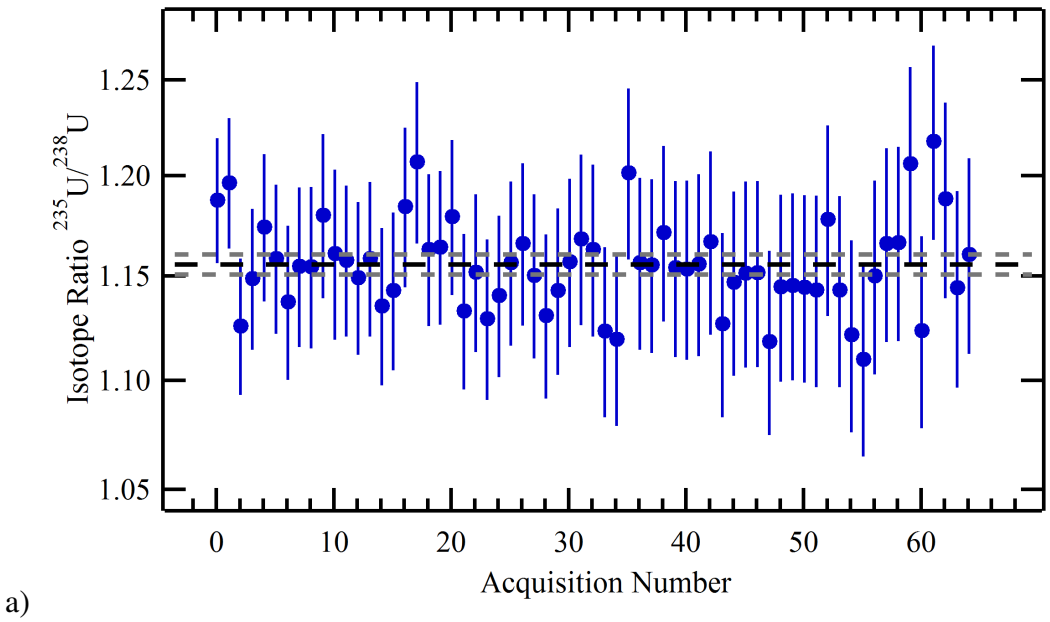

a)

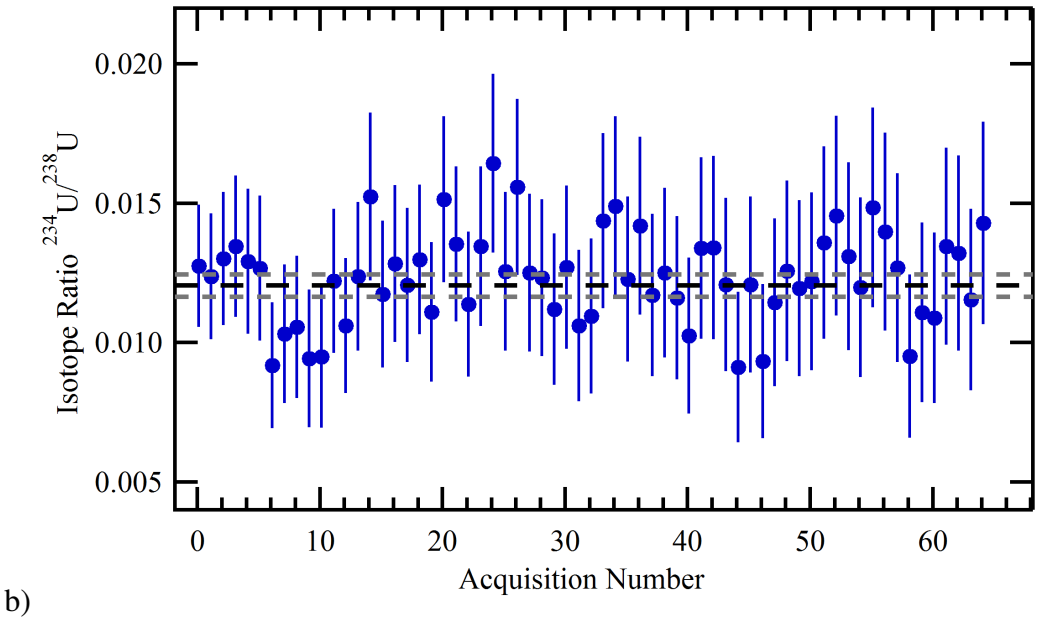

b)

Figure 4.37: A series of 64 analyses performed in succession on the CRM U500 standard using the 3-color, 3-photon ionization scheme with the bandwidth of the first resonance laser set to 5 pm. a) The mean value of the $^{235}U/^{238}U$ acquisitions is 1.155(5). Error bars represent 2σ uncertainties in individual acquisitions. The standard deviation of the mean is 0.4% (gray dashed lines). $\chi^2 = 1.15$, a χ^2 of one indicates that the deviation of the individual acquisitions is consistent with the uncertainty expected from statistical limits alone. b) The mean value of the $^{234}U/^{238}U$ acquisitions is 0.0118(4). The standard deviation of the mean is 3.2 % (gray dashed lines). χ^2 for the set of acquisitions is 1.27.

Isotope Ratio	Measurement Mean	RSE	χ^2	Certified Value	Relative Difference
$^{234}U/^{238}U$	0.0118 ± 0.0004	3.2 %	1.27	0.0104 ± 0.0001	$+13.4 \pm 4.9\%$
$^{235}U/^{238}U$	1.155 ± 0.005	0.4 %	1.15	0.9997 ± 0.0010	$+15.5 \pm 0.6\%$

Table 4.5: Summary of 64 replicate analyses on CRM U500 with the measured mean compared to the certified value. The uncertainties are 2σ, including the relative standard error (RSE).

4.5.6 Measured Isotope Ratios from U_3O_8 Standards of Varying Enrichment

Building on the success of reproducing a measured isotope ratio with uncertainties dominated by counting statistics rather than systematic fluctuations, we measured three U_3O_8 standards with a range of relative isotope abundances. ^{234}U, ^{235}U and ^{238}U were all measured simultaneously on the CRM U010, U500 and U970 targets to form the ratios reported (Exp. #32). The certified ratios cover a range of almost 7 orders of magnitude, from 5×10^{-5} to nearly 200. All three lasers of our 3-color, 3-photon scheme were tuned in wavelength to the isosbestic point for ^{235}U and ^{238}U. At these wavelengths we also expect a high probability for the ionization of ^{234}U. The instrument parameters for the measurement of each target were identical, within the limits of our accuracy.

A summary of the certified and measured values for the $^{234}U/^{238}U$ and $^{235}U/^{238}U$ ratios are displayed in Table 4.6 along with the percent difference between the two values for each ratio. The reported uncertainty for the difference between the measured and certified ratios is an expression of the relative standard error of the mean measured value. The first three rows of the reported measured values are uncorrected for isotope bias. The U500 and U970 were measured in quick succession on the same day but the U010 target was measured two days prior. This makes correcting the measured values of the U010 target by one of the other standards less reliable. We do, however, provide a standard-corrected value for the U970 measurement based on the difference between the measured and certified values of the U500 standard. The corrected value of the measured $^{235}U/^{238}U$ ratio for U970 is 187.04(5.67), which is within 1σ of the certified value for that ratio. For a more accurate and precise measurement of the $^{234}U/^{238}U$ ratio we would prefer to perform a measurement of the target with the lasers tuned to the isosbestic point between those two isotopes, or better yet, would report the $^{234}U/^{235}U$ ratio measured with the lasers tuned to the isosbestic point for that ratio.

Figure 4.38 displays the measured ratios from Table 4.6 as a function of the certified ratio. The measured ratios have not been corrected for isotope bias. Also shown in the figure is a least square linear fit to the measured ratios with a slope of 1.068 ± 0.009. A slope of unity would represent an accurate agreement of the measured and certified values of the ratios over the range studied. These experiments have confirmed that it is possible to measure a range of uranium isotope ratios for ^{234}U, ^{235}U and ^{238}U that can be corrected by comparison with a known standard to a precision of better than 1 % directly from uranium oxide materials.

	$^{234}U/^{238}U$			$^{235}U/^{238}U$		
Target	Certified	Measured	Difference (%)	Certified	Measured	Difference (%)
U010	$5.4(1)\times10^{-5}$	$7.2(7)\times10^{-5}$	30(10)	0.01014(1)	0.0110(1)	8.67(81)
U500	0.01042(5)	0.01045(23)	0.5(2.1)	0.9997(10)	1.067(3)	6.74(30)
U970	3.185(5)	3.351(75)	5.2(2.2)	186.77(21)	200.54(3.91)	7.37(1.95)
U970 (corr.)	3.185(5)	3.33(3.18)	4.7(3.1)	186.77(21)	187.04(5.67)	0.64(1.97)

Table 4.6: Results of measured isotope ratio compared to the certified value as the percent difference between the measured and certified values. The 2σ uncertainties are shown. The measured values are not corrected for bias in the ionization process except the final row (U970 corr.), which has been corrected by the results of the measurements on U500 taken during the same analytical session. The corrected value for the ^{235}U is within 1σ of its certified value.

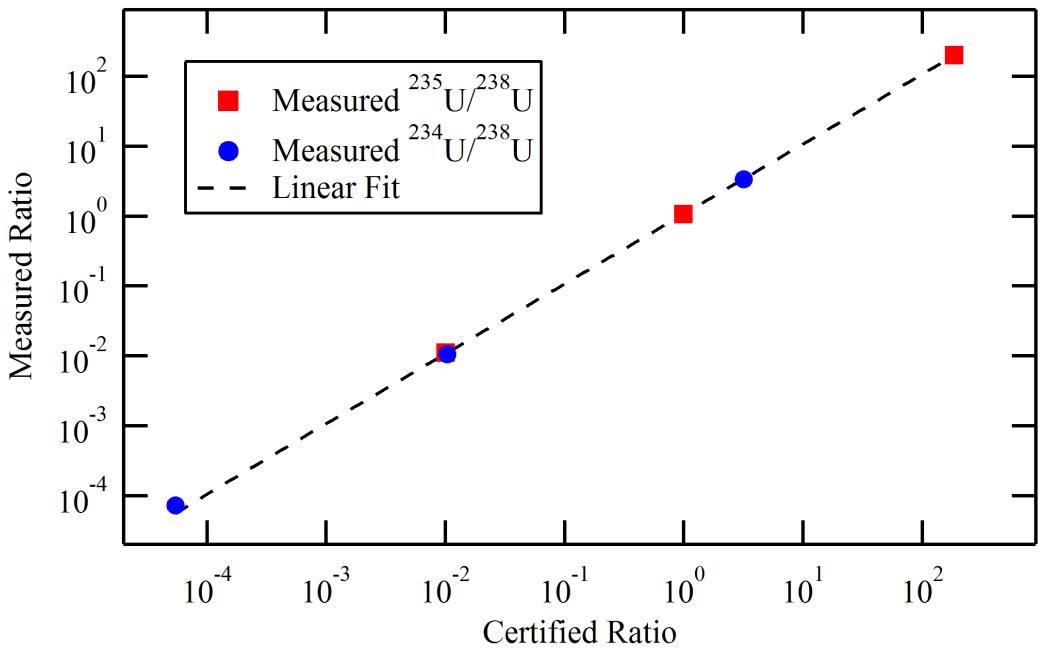

Figure 4.38: Six measured isotope ratios relative to the certified ratio over a range of more than seven orders of magnitude. Also included is a linear least square fit to the measurement results with slope 1.068(9). Estimated statistical uncertainties are smaller than the data points.

Chapter 5

Rate Equation Model of Relative Ionization Probability

This chapter describes the predictions of a rate equation model of the relative ionization probability for free uranium atoms in a volume undergoing irradiation by the 3-color, 3-photon ionization scheme. The goal of the modeling was to confirm the experimental result of reduced sensitivity of measured isotope ratios to variations in laser bandwidth (*i.e.*, Fig. 4.17). This was both to support our conclusion that uranium abundance ratios could be reliably measured using broad bandwidths and to help define laser parameters necessary for success. The model has been fairly successful at describing the distribution of observed isotope ratio as a function of wavelength for the narrow bandwidth experiments. The model agrees with the broad bandwidth data in that the isotope ratio is less sensitive to wavelength in the region between the two resonances. The model disagrees with the broad bandwidth data by predicting large changes in the measured isotope ratio away from the region between the resonances. We have concluded that this is likely a consequence of uncertainty in experimental parameters and their fluctuations during an experiment that are not properly characterized in the model. Recent experiments performed with better characterized laser systems show significantly improved agreement with the model predictions than the data presented in this work [M.R. Savina, *personal communication,* April 12, 2011].

The large number of experimental parameters and their variation across experiments have led to the development not of a single model of ionization probability, but a series of models depending on the experimental conditions. We first present the model using simple assumptions of atomic and laser characteristics. Then we address some of the variations around those simple assumptions that were used in an attempt to more closely approximate the various experimental conditions.

5.1 Model Description

The model calculates the population density of four specific states of a uranium atom as the atoms are irradiated by the excitation lasers in a normalized volume. It predicts the ionization probability for an ensemble of atoms present within the ionization volume for any two uranium isotopes under various model parameters. We assume that the atoms are in the ground state at $t = 0$. The inputs to the model may either be discretely defined or allowed to vary stochastically within a defined probability distribution.

Figure 5.1 is a diagram of the major model components involved in the computation of the ionization probability. Each of these components will be described in detail below, but first we will summarize the process for a specific isotope. The model begins by building the cross section and laser beam spectral irradiances for each of the transitions to be considered. These are combined with the time-dependent laser amplitude to generate a time-dependent transition rate. Each of these transition rates is used to define the parameters of the rate equations that describe the change in population of each atomic level. Once the rate equations parameters are defined, the equations are numerically integrated as a function of time. After the integration, the cumulative fraction of ions produced is recorded. This process is repeated for each isotope and is usually iterated over various parameter values (*e.g.*, laser wavelength).

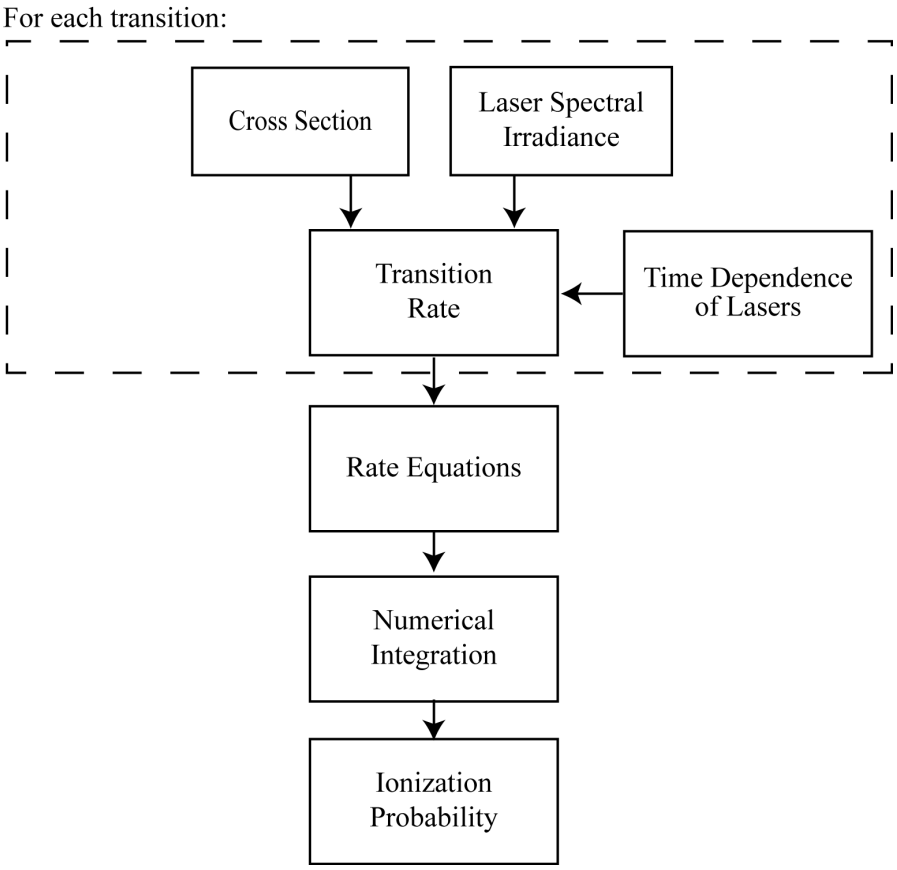

Figure 5.1: Rate equation model diagram showing the major components involved in modeling the ionization probability of a given isotope.

5.1.1 Rate Equations

Our model is built on the rate of change in the population of atomic levels, estimating the fraction of atoms in each level as a function of time in the range from 0 to 100 ns. Our ionization scheme involves four levels: the ground level, two bound excited levels, and an ionizing level. We have four equations, describing the rate of change for the populations of each level. For even-A isotopes, this will be equivalent to describing the change in the states: $|1\rangle$, $|2\rangle$, $|3\rangle$, and $|ion\rangle$[1]:

$$\frac{dN_1}{dt} = W_{12}(N_2 - \frac{g_2}{g_1}N_1) + \frac{N_2}{\tau_2} \tag{5.1}$$

$$\frac{dN_2}{dt} = W_{12}(\frac{g_2}{g_1}N_1 - N_2) + W_{23}(N_3 - \frac{g_3}{g_2}N_2) - \frac{N_2}{\tau_2} + \frac{N_3}{\tau_3} \tag{5.2}$$

$$\frac{dN_3}{dt} = W_{23}(\frac{g_3}{g_2}N_2 - N_3) - \frac{N_3}{\tau_3} - W_{3ion}N_3 \tag{5.3}$$

$$\frac{dN_{ion}}{dt} = W_{3ion}N_3 \tag{5.4}$$

where N_i is the number of atoms in state $|i\rangle$, W_{ij} is the rate of the transition per atom from state $|i\rangle$ to state $|j\rangle$, g_i is the degeneracy factor (number of participating magnetic substates, $g_i = g_j$ for linearly polarized light) for state $|i\rangle$, and τ_i is the average lifetime of state $|i\rangle$. We have assumed that all spontaneous decay occurs to states within the scheme, which simplifies the conservation of atoms in the model. The probabilities for collisional relaxation and radiative decay to states outside the level scheme are small relative to the laser excitation rates and are ignored[2]. In order to consider additional ionization pathways, we can construct terms of the form $\pm W_{nonres}N_i$ to express the rate of ionization into the continuum from state $|i\rangle$, where the negative term is added to the equation for state $|i\rangle$ and the positive term is added to the equation for the $|ion\rangle$ state. Approximate solutions to Eqs. 5.1−5.4 are rather simple to compute through numerical integration as soon as we define the W's.

The transition rates are defined as the spectral overlap of the time-dependent spectral irradiance of the lasers with the cross sections of the atomic states and are given by

$$W_{ij} = \int\int \sigma_{ij}(\lambda) \cdot I_i(\lambda, t)\, d\lambda\, dt \cong \sum_l \sum_k \sigma_{ij}(\bar{\lambda}_k) \cdot I_i(\bar{\lambda}_k, t)\, \Delta\lambda\, \Delta t \tag{5.5}$$

where $\sigma_{ij}(\lambda)$ is the cross section for the transition between state $|i\rangle$ and state $|j\rangle$ expressed as a function of wavelength, and $I_i(\lambda, t)$ is the spectral irradiance of the laser used to excite that transition (the lasers are numbered using the excitation order of our ionization scheme). The integral is for the continuous case. In the model, the integral is replaced by a summation over finite elements of width $\Delta\lambda$ extending over the wavelength range of the irradiance. The bars represent evaluation of the quantity at the average wavelength of each element.

[1] We start our numbering with 1 instead of 0 to match the description of the states in the computer code.

[2] Note that state $|3\rangle$ cannot decay back to the ground state via a single photon emission due to parity conservation.

The rate is a function of the time-varying amplitude of the laser pulses, but because the time dependence is independent of wavelength, we approximate it as a separate function. The time-dependent rate is expressed by

$$W_{ij}(t) = W_{ij} \cdot T_i(t) \tag{5.6}$$

where $T_i(t)$ is the time distribution of a pulse produced by the laser used to excite the transition from $|i\rangle$ to $|j\rangle$. In the model, it is is assumed to be Gaussian in shape and described by

$$T_i(t) = \frac{1}{\sqrt{2\pi\sigma^2}} \mathrm{e}^{-\frac{(t-T_0)^2}{2\sigma^2}}$$

where σ is the standard deviation and T_0 is the time of the peak of the laser pulse. The FWHM of the laser pulses have been measured to be about 20(2) ns. T_0 may be defined by a fixed value or may be randomly sampled from an empirical probability distribution to describe the pulse-to-pulse fluctuation of relative laser timing observed in our experiments (Fig. 3.21). On average, the distribution of T_0 for succesive laser pulses can be approximated as a normal distribution with a FWHM of ~ 14 ns.

5.1.2 Cross Sections and Atom Assumptions

The cross section for absorption expressed in units of angular frequency from a given substate m_1 of state J_1 for a level $|1\rangle$ to a substate m_2 of state J_2 for a level $|2\rangle$ in an atom is given by

$$\sigma_{m_1 m_2}(\omega) = \frac{\lambda_0^2}{4}\Gamma_{21} g(\omega) = \frac{2\pi^2 g(\omega)}{3\varepsilon_0 \hbar \lambda_0}|D_{12}|^2 \tag{5.7}$$

where λ_0 is the mean transition wavelength, Γ_{21} is the partial width of the excited state[3], $g(\omega)$ is the normalized lineshape of the transition, and $|D_{12}|^2$ is the squared magnitude of the dipole matrix element for the transition. Note that the degeneracy factor g_2/g_1 is not included as we are dealing with the specific substates.

The Wigner-Eckart Theorem The Wigner-Eckart theorem states that we can express the transition dipole matrix element between specific magnetic substate as the product of a reduced matrix element and the Clebsch-Gordan coefficient for the transition,

$$\langle J_2, m_2 | D_{even} | J_1, m_1 \rangle = C(J_1, J_2, \triangle J, m_1, m_2, \triangle m) \langle J_2 \| D_{even} \| J_1 \rangle \tag{5.8}$$

where $C(J_1, J_2, \triangle J, m_1, m_2, \triangle m)$ is the Clebsch-Gordan coefficient for the transition. The reduced matrix element, $\langle J_2 \| D_{even} \| J_1 \rangle$, does not depend on the magnetic substates involved. The dipole operator does not change the electron spin angular momentum (S), so that $\langle J_2 \| D_{even} \| J_1 \rangle =$

[3]We are assuming that $\Gamma_{12} = \Gamma_{21}$ and that the width of the initial state does not contribute significantly to the cross section.

$\langle L_2 \| D_{even} \| L_1 \rangle$. Therefore, the reduced matrix element depends only on the radial distribution of the wavefunction, which we assume is the same for each substate within a transition. For even isotopes, the squares of the Clebsch-Gordan coefficients for transitions between each substate will sum to unity and do not need to be calculated. In this case, we define a degeneracy g_i equal to the number of substates with allowed transitions. g_i has a maximum value of $2J_i + 1$, but can be reduced when considering polarized light.

For odd isotopes, the degeneracy of the states within a level is removed and not every transition has equal energy. We must keep track of the probability for excitation to a particular substate within each level. This is done by adapting the Wigner-Eckart theorem to consider the total atomic angular momentum F and the reduced matrix element that depends on J but not on m_J:

$$\langle F_2, m_2 | D_{odd} | F_1, m_1 \rangle = C(F_1, F_2, \triangle F, m_1, m_2, \triangle m) \langle J_2 \| D_{odd} \| J_1 \rangle \tag{5.9}$$

$$\langle J_2 \| D_{odd} \| J_1 \rangle = \langle J_2 \| D_{even} \| J_1 \rangle \tag{5.10}$$

where $\langle J_2 \| D_{odd} \| J_1 \rangle$ is the reduced matrix element for the odd isotope for the transition expressed by $\langle F_1, m_1 | D_{odd} | F_2, m_2 \rangle$.

Calculating Transition Cross Sections for Even and Odd Isotopes The cross section as a function of wavelength is calculated by the model as the product of the peak cross section amplitude and a normalized lineshape

$$\sigma_{12}(\lambda) = \sigma_0 \cdot g(\lambda) \tag{5.11}$$

where $\sigma_0 = \frac{\lambda_0^2}{4}\Gamma_{21}$ is the peak cross section and $g(\lambda)$ is given by the lineshape profile of the transition. The lineshape will be dependent on the natural linewidth of the transition and the velocity distribution of the atoms in the ionization volume. Atoms in the ionization volume will have a velocity distribution related to the desorption process used for atomization. We assume that the velocity distribution of atoms in the gas phase is a Maxwell-Boltzmann distribution, resulting in Doppler broadening of the atomic lineshape. The lineshape required to describe the combination of the Doppler broadening and the width due to spontaneous decay, is a convolution of a Gaussian function with a Lorentzian function (as discussed in Sec. 2.2.5).

The cross section for transitions in even isotopes is of the form

$$\sigma_{even}(\lambda) = \frac{\lambda_0^2}{4}\Gamma_{21} \cdot \frac{g_2}{g_1} \cdot [\mathscr{D}(\lambda) \otimes \mathscr{L}(\lambda)] \tag{5.12}$$

where $\mathscr{D}(\lambda)$ is the Doppler broadened lineshape (see Eq. 2.48) and $\mathscr{L}(\lambda)$ is a Lorentzian function describing the natural linewidth of the resonance (see Eq. 2.5).

The cross sections of odd isotopes require a bit more effort in order to properly distribute the transition probabilities across the individual transitions between magnetic substates. We must also account for the small differences in resonance wavelength of each of the transitions. As the cross section is proportional to the square of the transition dipole matrix element, we

can multiply the peak cross section by the squared Clebsch-Gordan coefficient for a particular transition between substates, $\langle J_2, m_2 | D | J_1, m_1 \rangle$ as,

$$\sigma_{m_1 m_2}(\lambda) = \frac{\lambda_0^2}{4}\Gamma_{21} \cdot C(F_1, m_1, F_2, m_2)^2 \cdot g(\lambda) \tag{5.13}$$

where $C(F_1, m_1, F_2, m_2)^2$ is the squared Clebsch-Gordan coefficient between two magnetic substates. The average cross section for an odd isotope is proportional to the sum of the squared Clebsch-Gordan coefficients for each transition, where we must also consider the difference in transition energy as a result of differences in total angular momentum F,

$$\sigma_{odd} \propto \sum_F D_{odd}^2 = \sum_F \left[\sum_{m_F} [C(F_1, m_{F1}, F_2, m_{F2})^2] \cdot D_{even}^2 \right] = \sum_M C_M(F_1, m_{F1}, F_2, m_{F2})^2 \cdot D_{even}^2 \tag{5.14}$$

where M represents each transition with unique energy, each of which is composed of degenerate transitions between magnetic substates. Remember from Sec. 2.3.2, the states of a given level in the odd isotopes are split in energy defined by the total angular momentum of the state and that each state is $2F+1$ degenerate. There are 21 transitions with unique energies in the excitation of the first resonance of ^{235}U, but a total of 104 transitions allowed by the selection rules for linearly polarized light (see Fig. 2.9).

We generate an average cross section for the allowed transitions between two levels in an odd isotope as the sum of the cross sections for each transition with unique energy convolved with the Doppler-broadened lineshape

$$\sigma_{odd}(\lambda) = \frac{\lambda_0^2}{4}\Gamma_{21} \cdot \frac{1}{(2J+1)(2I+1)} \left[\mathscr{D}(\lambda) \otimes \sum_M \left(C_M(F_1, m_{F1}, F_2, m_{F2})^2 \cdot \mathscr{L}_M(\lambda) \right) \right] \tag{5.15}$$

where M represents the sum of degenerate transitions between substates for a transition of unique energy. $\mathscr{L}_M(\lambda)$ represents the Lorentzian lineshape of each transition M. Unlike for the case of transitions in even-A isotopes, the quantity in square brackets is no longer normalized to unity because of the squared Clebsch-Gordan coefficients. We normalize the lineshape by the total statistical weight of the initial level, $(2J+1)(2I+1)$, to account for the increased number of states[80]. For the first transition in ^{235}U the sum of the squared Clebsch-Gordan coefficients is 164 while the statistical weight of the ground level is 104. This results in the peak cross section for ^{235}U being a factor of approximately 1.58 greater than for ^{238}U.

Figure 5.2 shows the calculated cross sections for the first transition in our scheme as a function of wavelength for ^{235}U and ^{238}U. Both cross sections include an estimated Doppler broadening of 0.002 pm. The cross section for ^{235}U is on the left side of the figure, centered at 415.507 nm and the cross section for ^{238}U is on the right, centered at 415.514 nm.

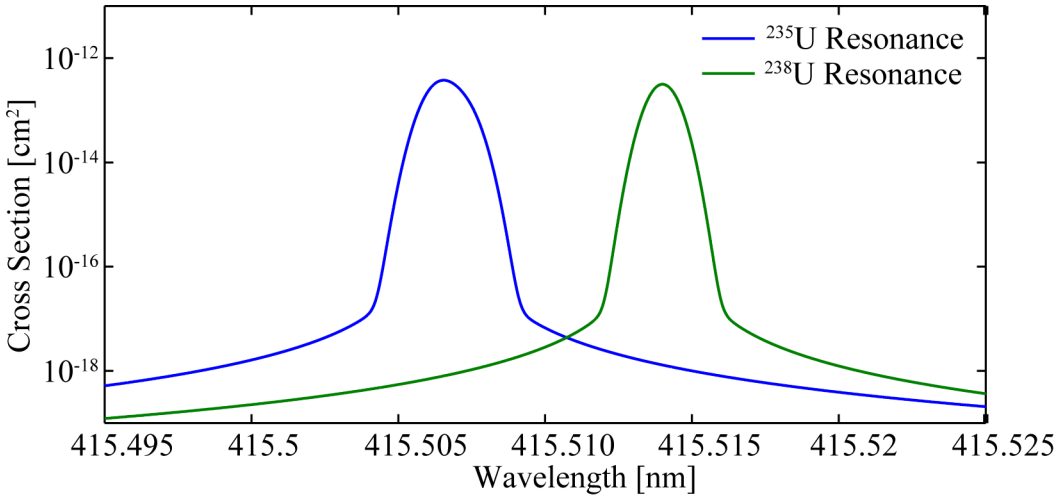

Figure 5.2: Calculated cross sections for ^{235}U and ^{238}U as a function of wavelength for the first resonance transition. The non-zero nuclear angular momentum in ^{235}U results in its cross section being both broader and larger than that of ^{238}U.

5.1.3 Laser Spectral Irradiance

The time-independent spectral irradiance $I_i(\lambda)$ of each laser is the product of the photon flux (ϕ_i) and a normalized spectral distribution we will call the laser lineshape ($l(\lambda)$)

$$I_i(\lambda) = \phi_i \cdot l(\lambda)$$

In our experiments, we have a three-dimensional distribution of photon flux interacting with the cloud of desorbed neutral species, also distributed in three dimensions. A proper attempt to quantify the spatial dependence of the ionization probability must consider the non-linear nature of the photon flux distribution and the complexity of the distribution of neutral atoms in the ionization volume. This would require the calculation of the photon flux at many positions of space within the ionization volume and a weighting of their contribution to the prediction of ionization probability by the atom density in that volume. However, the measured isotope ratios resulting from our experiments must represent some type of average over these spatial distributions and therefore, must be capable of being reproduced using a single point model representing this average. To be clear, the average value of photon flux used in this type of point model would not necessarily be representative of the real average flux during the measurement and would be highly dependent on the distribution of flux. Thus, the average flux used in the model cannot be directly equated with the experimental flux, but should be useful for comparing relative fluxes of experiments that used beams with the same spatial distribution. With these considerations, we proceed with the description of our single point model of irradiance.

We assume that the concentration of neutral atoms is so small that photon attenuation can safely be neglected. In a similar manner, we assume that the cross-sectional area of the laser beam is constant within the ionization volume. These assumptions reduce the consideration of

the photon flux to the cross-sectional area of the laser beam intensity, which is described by a 2-D Gaussian profile. For our single point model, we further assume that the average flux of the beam can be described by the average flux in the area that contains 50 % of the photons[4].

The photon flux is the number of photons per unit area, which is related to laser pulse intensity in Eq. 5.16. The flux of laser i is given by

$$\phi_i[\text{photons}\cdot\text{cm}^{-2}] = \left(5\cdot 10^9\right)\cdot(\lambda_i[\text{nm}])\cdot(P_i[\mu\text{J}])\,/A[\text{cm}^2] \tag{5.16}$$

The wavelength (λ), pulse intensity (P_i), and area (A) of the laser beams are variables of the experimental conditions to be explored with the model. Empirically, we characterize the intensity of a laser beam using the average total beam energy per pulse and the spatial distribution of a laser beam in terms of the $1/\text{e}^2$ width in both the vertical and horizontal direction (the full width at which the intensity of the laser beam has fallen to approximately 13.5 % of the maximum intensity). For normal Gaussian distributions the $1/\text{e}^2$ width is equivalent to 4σ, and thus 50% of the population will be within $\approx \pm 0.674\sigma$ of the peak of the distribution. We define the cross sectional area containing 50 % of the laser energy as $A_{50\,\%} = \pi\cdot(.674)r_H\cdot(.674)r_V$ where r_H and r_V are the horizontal and vertical radii corresponding to 1σ, respectively (one fourth of the corresponding $1/\text{e}^2$ radii expressed in cm). The average elliptical area of the laser beams in the ionization volume is $A_{4\sigma} = \pi\cdot 16\cdot r_H\cdot r_V$. We have not explored the spatial variation of ionization experimentally and, therefore, for all three laser beams $A_{4\sigma}$ is $0.016\,\text{cm}^2$. To compare the model predictions with the experimental results, we define the pulse energy per unit area relative to the experimental values of total beam intensity. The modified laser intensity describing the photon flux is given by

$$P_{avg.} = P_i\cdot 0.5\cdot\frac{A_{4\sigma}}{A_{50\%}} \cong 17.58\cdot P_i \tag{5.17}$$

This equation converts the experimental values of laser intensity and cross sectional area to an average model pulse energy ($P_{avg.}$) in the area containing 50 % of the laser intensity.

The model is strongly dependent on the laser lineshape. We require that the integral of the laser lineshape be normalized to unity. To explore the sensitivity of the predicted ionization probability as a function of wavelength, we have explored several functional forms of this lineshape. We have considered Gaussian lineshapes, a linear combination of multiple laser modes (several Gaussian modes separated by the mode spacing of the laser cavity), and an empirical lineshape. When a Gaussian function is used, the amplitude of the laser lineshape is generated to a number of standard deviations of the distribution (the default is $\pm 9\ \sigma$)[5] and set to zero everywhere outside of this to avoid unnecessary computation of very small numbers.

[4]We expect that this approximation is acceptable for resonance processes, which are linearly proportional to photon flux, as long as the atoms are not concentrated in some volume of the lasers not well described by the average. However, for non-resonant processes that are non-linear with respect to the photon flux, this approximation is inappropriate.

[5]This may appear to be a very large range, but the resonance cross sections change very rapidly away from the resonance centroid. Thus, depending on the mean wavelength of the laser relative to the resonance centroid, the wings of the laser spectral distribution are important.

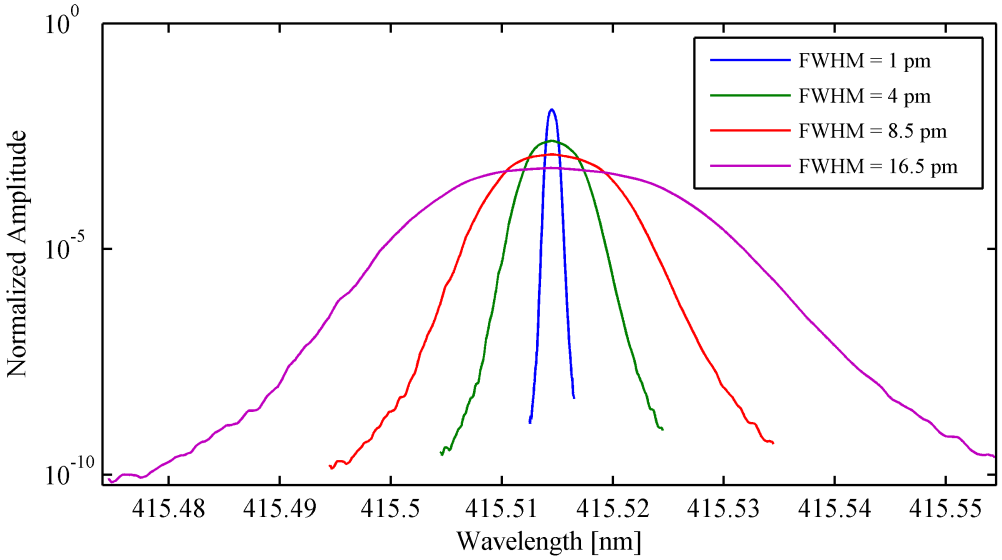

Figure 5.3: Empirical lineshapes for a frequency-doubled laser. The lineshapes were obtained by interpolating the output of the spectral distribution from the WS-7 wavemeter. It shows the original narrow bandwidth laser with a FWHM of 1 pm and other 3 curves that are the result of changing the scale of the abscissa and re-normalizing.

A representative empirical lineshape was obtained by averaging the spectral distribution output of the wavelength meter over several laser pulses (see Fig. 3.5). From this average, we can generate a laser lineshape of variable width for either the fundamental or frequency-doubled laser wavelengths. There are no data for the lineshape on the wings of broad bandwidth laser pulses, because only the central 10 pm of the laser pulses are available from the wavemeter. It is assumed that the lineshape on the wings of broad bandwidth pulses will follow the same shape as the distribution of narrow bandwidth laser pulses. To build the empirical lineshape of variable width, we take the narrow bandwidth lineshape, adjust the scale of the abscissa (the wavelength dependence), and re-normalize the integral of the lineshape to unity in order to create distributions with the desired FWHM in wavelength. Figure 5.3 shows 4 such lineshapes for a frequency-doubled laser beam (the amplitude is proportional to the square of the fundamental beam amplitude). The 1 pm curve is the result of frequency-doubling the original 3 pm line of the fundamental frequency and the other three curves are broadened lineshapes with FWHM of 4, 8.5, and 16.5 pm. This average lineshape is linearly interpolated between the experimental data points to increase the resolution of the lineshape to match the resolution of the atomic resonance lineshape.

The central wavelength of individual laser pulses may be fixed at a discrete value or randomly sampled from a distribution (theoretical or empirical) to reproduce the effects of pulse-pulse fluctuations or for averaging over a large number of pulses.

5.1.4 Instrument Assumptions

The model assumes a perfect instrument. This assumption includes unit efficiency for the sputtering, extraction, transport, and detection of atoms and ions. The result of this assumption is that the instrumental bias is considered to be negligible. This is not, in fact, true, but measurements have demonstrated that the instrument bias does not have a significant role in the result. For example, we've shown from the uranium oxides species (see Fig. 4.33) that the instrumental bias in the measured isotope ratio is less than 0.3 %. In addition, any bias present from instrument inefficiencies would be constant for the variations in model parameters explored and could be applied after the model computations.

5.1.5 Model Processes for Ion Formation

Empirically, we have a observed several processes for forming ions under resonant ionization conditions. In addition, under all ionization conditions we have a non-negligible background of non-resonant ions at the masses of the atomic uranium ions.

3-color, 3-photon Ionization – The desired pathway for ionization is by a transition induced by a photon of 722.202 nm to an autoionizing state from the second excited state. This pathway is included in the model by building a predicted cross section and calculating a rate for the transition based on the cross section, the incident photon flux of the appropriate laser pulse, and the population of the second excited state. The proper calculation of the ionization cross section requires integration of the probability of transitions to autoionizing states as well as continuum states and involves detailed angular momentum and radial descriptions of the wavefunctions, which is complex for uranium. We are most interested in the wavelength dependence of the first resonance transition, thus we have simply approximated the autoionizing cross section as a discrete transition where the last photon absorbed carries the atom to a discrete autoionizing state above the ionization limit and indeed decays by ionization. This neglects the contribution of the unbound states in the ionization continuum to the cross section, see Sec. 2.2.6.2. This approach will also neglect some differences in the ionization cross section of even and odd isotopes from angular momentum factors[36] involved in ionization to continuum states.

2-color, 3-photon Ionization – Experimental measurements have also confirmed the presence of at least a few other non-negligible ionization pathways that must be considered. Primarily, we must consider the 2-color, 3-photon ionization pathway (detailed in Sec. 4.3.4) for ionization out of the second excited state into the ionization continuum via absorption of a photon from the first laser beam. The experiments show a significant probability for ionizing U atoms with only the first and second resonance laser present in the ionization volume (Fig. 4.29). The ion signal for this process depends linearly on the intensity of the first laser and can contribute as much as 32 % of the ion signal. During typical measurements, however, this fraction is closer to 10 %. This is the most likely process because it is the only additional pathway involving single-photon excitation that results in the energy of the excited atom being above the

Resonance ^{238}U [nm]	Resonance ^{235}U [nm]	Lifetime or Width	Doppler Estimate [pm]
415.514	415.5068	57(6) ns	2.05
829.091	829.087	215(20) ns	4.08
722.202	722.200	52(2) pm	3.57

Table 5.1: Atomic parameters for ^{235}U and ^{238}U explored in the model. References for lifetimes or widths may be found in Table 3.1.

ionization potential for uranium. It is included in our model by estimating a rate for this process using a cross section and the photon flux from the laser for the first transition (415 nm), acting on the population of the second excited state. The calculation and results of this estimate are discussed in Sec. 5.3.1.2.

Non-Resonant Background – Experimentally, we observe a small probability for producing photoions at the masses of U ions when the laser for the first transition is tuned far from resonance. The ion signal for this off-resonance process is on the order of 1 % of the total ion signal when all three resonance lasers are tuned on-resonance. By studying the dependence of this ion signal on the power in the first laser, we have generated a functional form for this ion signal as a function of total laser intensity (Sec. 4.1.5.1). We will discuss the empirical cross section estimates to this ionization source below.

5.2 Cross Section and Laser Parameters

This section is a summary of the values used to calculate the atomic cross sections and laser irradiances used in the model. The range of parameters is meant to incorporate the variation of conditions explored in the experimental work already presented. Table 5.1 gives the wavelengths of the resonance transitions used in ^{235}U and ^{238}U, the lifetime or width of the excited states, and an estimate of the Doppler broadening in wavelength. Our initial estimate of the Doppler broadening, based on a general rule of thumb for ion sputtering, assumes a Maxwell-Boltzmann distribution at a temperature of 3 times the boiling temperature of UO_2.

Table 5.2 is a summary of the laser parameters explored in the model. It lists the range of laser wavelengths, the range of laser pulse energies, and the range of bandwidths studied. It also includes the measured values for the pulse-to-pulse fluctuations in wavelength and pulse timing of the lasers (see Sec. 3.1.5.2 and 3.1.5.3).

Laser No.	Wavelength [nm]	Pulse Energy [μJ]	Bandwidth [pm]	Wavelength Fluctuation [pm]	Time Fluctuation [ns]
1	415.48−415.54	0−250	1−10	2−4	14
2	829.08−829.10	0−1000	3	3	14
3	722.200	0−700	3	3	14

Table 5.2: Laser parameters explored in the model.

5.3 Modeling Results

5.3.1 Ionization Cross Section Estimates

We recognize three ionization processes that contribute to the formation of ions at the masses of atomic uranium in our experiments and that are not calculated easily from first principles using the available empirical data. The processes are: (1) the non-resonant ionization that occurs when only the first resonance laser is present in the ionization volume, (2) the 2-color, 3-photon ionization pathway, and (3) ionization through the 722.202 nm autoionizing state. Each of these cross sections can be estimated by examining the dependence of the ionization probability on the intensity of the laser involved in the process.

5.3.1.1 One-Color, Off-Resonance Ionization Process

We discussed the contribution of ion signal in the atomic uranium masses from a one-color, multi-photon off-resonance process in Sec. 4.1.5.1. Our functional fit of the dependence of the ionization probability on laser beam intensity of this process suggests that we can approximate this ion signal by modeling a two-photon absorption process. Two 2.9 eV photons are insufficient to ionize atomic uranium from the ground state or to photodissociate uranium oxide molecules from their ground states. This requires that the neutral species ionized in this 1-color process either be in an excited state prior to irradiation, or that additional photons from the laser beam are involved in excitation steps that do not limit the rate of the two-photon excitation step. We have made the assumption that the neutral species ionized by this process is not depleting the number of available ground state uranium atoms in the laser beam volume.

We begin with an estimate of the cross section for the two-photon excitation step that dominates the rate of this process. The estimate for the ion signal produced by this 1-color process is

$$N_{ion} = \sigma_{1C} I_x^2 N_0 \tag{5.18}$$

where σ_{1C} is the two-photon absorption cross section, I_x^2 is the squared-irradiance of the laser beam involved, and N_0 is the fraction of species available for this process. We assume that the cross section is constant over the bandwidth of the laser beam and thus use the total flux of the beam. Neglecting the possibility of higher-order multi-photon absorption, we estimate a

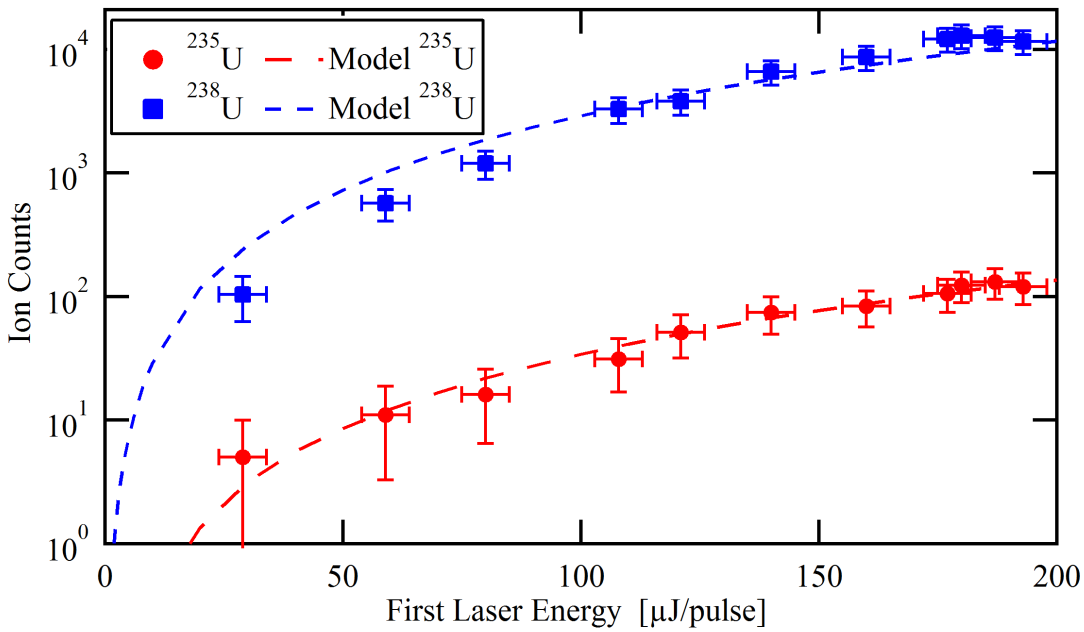

Figure 5.4: One-color ionization process as a function of beam intensity of the first laser. The data were obtained with only the first laser beam present at a wavelength far from the resonance wavelength. The model predictions are based on the cross section estimate for the process of 8.5×10^{-35} cm^2 and multiplied by a factor of 1.5×10^5 to convert the predicted probability into predicted ion counts.

two-photon absorption cross section for this process of $\sim 8.5 \times 10^{-35}$ cm^4. This estimate was obtained by fitting the cross section to the data from Exp. #6, already presented in Fig. 4.11. The resulting model prediction for this 1-color process is shown in Figure 5.4 alongside the data from Exp. #6. For review, the experiment was performed using only the first laser beam with a wavelength far from the uranium resonances while varying the intensity of this laser and was measured from the SRM 960 target (natural isotope abundance). Because the model predicts a probability, the predictions were multiplied by 1.5×10^5 in order to convert this probability into predicted counts. It was found that the model predictions better approximated the experimental results when the cross section for ^{235}U was increased by a factor of 1.6 relative to ^{238}U, consistent with the average increase in cross section in the other transitions studied as a result of angular momentum considerations.

The process for producing ions using only a single wavelength was also modeled using a 1-color, 3-photon process. In this process, it was hypothesized that an intermediate step involving the absorption of a single photon was also necessary to produce ions. This required

the numerical integration of the following equations,

$$\frac{dN_1}{dt} = -\sigma_X I_X N_1 \tag{5.19}$$

$$\frac{dN_2}{dt} = \sigma_X I_X N_1 - \sigma_{1C} I_X^2 N_2 \tag{5.20}$$

$$\frac{dN_{ion}}{dt} = \sigma_{1C} I_X^2 N_2 \tag{5.21}$$

where N_i represents the population of level i, σ_X is the single-photon absorption cross section for the photons from laser X, and the other symbols are explained in Eq. 5.18. The model predictions for this 3-photon ionization pathway agree with the 2-photon prediction as long as the cross section $\sigma_X \geq 5 \times 10^{-16}\,\mathrm{cm}^2$. Typical cross sections for resonance transitions are on the order of 10^{-12} to $10^{-14}\,\mathrm{cm}^2$, scattering cross sections are typically $10^{-16}\,\mathrm{cm}^2$, and cross sections for ionization into the continuum are on the order of $10^{-18}\,\mathrm{cm}^2$.

We expect that our use of a single average laser intensity for modeling the ionization probability of non-resonant ions is not appropriate. Rather than calculate the rate of the off-resonance signal directly from the estimated cross section and laser parameters, we can also correct the on-resonance model predictions empirically when trying to model specific experimental data. This correction is performed by adding the measured off-resonance ion signal from the specific experiment as a percent of the measured on-resonance signal after the computation of ionization probability. This enables us to include the total estimate of off-resonance ions in the model predictions instead of just the 1-color, off-resonance ion signal. Fortunately, for the two experiments we are most interested in modeling directly, we have empirical measurements of the total off-resonance ion signal. For the experiments performed on the natural U standard (SRM 960), when the total energy of the laser beam was 75 μJ the off-resonance ^{238}U signal was 1.0(1) % of the maximum on-resonance ^{238}U signal. When the energy per pulse was increased to 150 μJ the off-resonance ^{238}U signal increased to 2.6(2) % of the on-resonance ^{238}U signal. Using the difference in predicted off-resonance cross sections of 1.6 estimated earlier in this section suggests that the off-resonance signal at the mass of ^{235}U would be approximately 4.3 % of the maximum on-resonance ion signal. The off-resonance background should be quantified more carefully in additional experiments to determine the actual values of both the ^{235}U to ^{238}U off-resonance ion signals.

5.3.1.2 Two-Color, Three-Photon Ionization Cross Section

We must also estimate the ionization cross section for the two-color, three-photon pathway described in Fig. 4.29b. This is accomplished by setting the model parameters to mimic the experimental setup for on-resonance ionization conditions apart from the absence of the third laser beam. We must define an ionization rate (W_{2C}) that represents the excitation of atoms from the second excited state into the ionization continuum due to absorption from the first laser. This should be negligibly-dependent on wavelength, so we set the rate for this transition as a constant cross section (σ_{2C}) times the sum of the spectral irradiance in the first laser (I_1). We do not have

an experiment that quantifies the dependence of this ionization process on the intensity of the first laser, but we have a number of data points across several experiments where the laser used to excite the autoionizing transition was not present. These data points provide insight into the magnitude of the cross section for this process.

Specifically, we have an experimental measurement taken using broad bandwidth conditions in the first two laser beams with 315 μJ/pulse in the first resonance beam (Exp. #22) where we can compare the ion signal generated when the intensity of the third laser beam was reduced to zero. We find that the ion signals when only the first two lasers were present for ^{235}U and ^{238}U were measured to be 13.0(2) % and 12.4(2) %, respectively, of their maximum ion signal with all three lasers present. We do expect some difference in ionization probability between the two isotopes because of the differences in angular momentum, for this measurement the difference is a factor of approximately 1.05. Using this single measurement to fit a cross section value to the model predictions, results in $\sigma_{2C} = 7.25 \times 10^{-17}$ cm^2, which is fairly close to the theoretical cross section for absorption into the continuum of 10^{-18}. This cross section estimate is used below for estimating the autoionizing cross section.

5.3.1.3 Autoionizing Cross Section

The autoionizing state, by definition, prefers to decay by electron emission. Thus, the partial width for the de-excitation of the autoionizing state back to the second resonance state is small relative to the total width of the autoionizing resonance. The total width of the autoionizing state is described by

$$\Gamma = \sum_i \Gamma_i = \Gamma_{\gamma\gamma} + \sum_{\gamma'} \Gamma_{\gamma\gamma'} + \Gamma_{e^-} \tag{5.22}$$

where the total width Γ is the sum of the partial widths of all possible decay modes (Γ_i). The widths on the right-hand side of Eq. 5.22 correspond to the partial width of the autoionizing state to decay back to the second excited state ($\Gamma_{\gamma\gamma}$), the sum of all other possible photon transitions ($\Gamma_{\gamma\gamma'}$), and the partial width for electron emission (Γ_{e^-}). Neglecting Doppler broadening, the peak cross section (when $E = E_0$) is described by

$$\sigma_{\gamma\gamma} = \frac{g_2}{g_1} \frac{\lambda_0^2}{2\pi} \cdot \frac{\Gamma_{\gamma\gamma}}{\Gamma} \tag{5.23}$$

where g_2/g_1 is the ratio of the level degeneracies, λ_0 is the transition wavelength, and $\Gamma_{\gamma\gamma} = \Gamma - \sum_{\gamma'} \Gamma_{\gamma\gamma'} - \Gamma_{e^-}$.

Using the the experimental data from Exp. #22, already described in Sec. 4.3.3, we estimate $\sigma_{\gamma\gamma} = 1.16 \times 10^{-15}$ cm^2. This estimate was obtained by fitting the model prediction to the ion signals from both ^{235}U and ^{238}U simultaneously, including differences in the angular momenta. This cross section estimate corresponds to a partial lifetime for decay of the state to the second excited state of $\sim$3.8 μs. This can be compared to the average total lifetime of the autoionizing state of $\sim$5.5 ps and the average lifetime of the second excited state of $\sim$215 ns. The partial width corresponding to this cross section is $\Gamma_{\gamma\gamma} = \Gamma \cdot 1.45 \times 10^{-6}$. Figure 5.5 shows the data

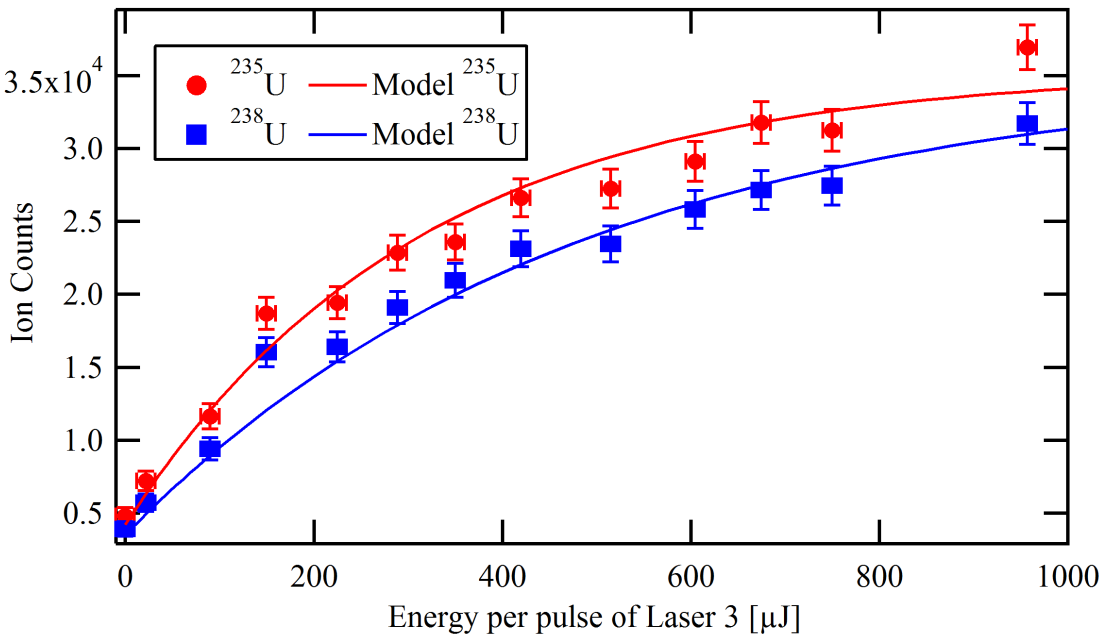

Figure 5.5: Ion signal for ^{235}U and ^{238}U as a function of the intensity of the third laser under on-resonance ionization conditions. The data are from Exp. #22. The model predictions are for $\sigma_{\gamma\gamma} = 1.16 \times 10^{-15}$ cm^2, and include the angular momentum considerations for excitation to the discrete autoionizing state.

from Exp. #22 along with the model predictions of ionization probability based on $\sigma_{\gamma\gamma} = 1.16 \times 10^{-15}$ cm^2, where we have included the isotope specific angular momentum considerations for excitation to the discrete autoionizing state ($J = 8$). We have not considered the contribution to the cross section or the angular momentum algebra that arises from excitation directly into the continuum, but the probability for excitation into the continuum must be several orders of magnitude smaller than excitation into the discrete autoionizing state (see Sec. 2.2.6.2).

5.3.2 Relative Ionization Probability

We now present the results of model predictions for the ionization probability of ^{235}U relative to that for ^{238}U. We begin with a set of model parameters that produced the closest fit to the experimental measurements and then explore the effects produced by variation of different model parameters to examine the predicted sensitivity of various experimental parameters.

5.3.2.1 Isotope Ratio as a Function of First Laser Wavelength Under Narrow Bandwidth Conditions

The results of an experiment (#9) designed to study the wavelength dependence of the first resonance transition under narrow bandwidth conditions have already been presented (see Sec. 4.2.1). Here, we will describe the input parameters used in the model to provide an output that closely approximates the observed variation in measured isotope ratio from Exp. #9 . All of the model input parameters were set to discrete values (no stochastic variations allowed). Using a simple Gaussian lineshape for the laser spectral distributions we set the bandwidths of the first, second, and third lasers to 1, 3, and 2 pm, respectively. The wavelength of the first laser beam was varied for each iteration of the model from 415.480 to 415.540 nm. The second and third lasers were fixed at 829.089 and 722.200 nm, respectively. The experiment was performed with the third laser tuned to 722.344 nm, and the cross section at this wavelength is about 62.5 % of the peak cross section at 722.200 nm. Thus, we manually reduced the peak cross section used in the model for the resonance at 722.200 nm by 62.5 %. The average mean wavelength variation from pulse-to-pulse of all three lasers was set to 2 pm, as observed experimentally. We include this as an average affect in the model, meaning we sum the Gaussian used for the laser lineshape with the average mean variation, yielding another Gaussian with different normalization. Including the mean wavelength variation in this manner will miss non-linear effects caused by the laser wavelength and time-dependent amplitudes both varying from pulse to pulse. The Doppler broadening of the atomic cross sections were set to the estimates as given in Table 5.1. The intensities for all three laser beams were converted from their total beam intensities to average beam intensities, although it was discovered through iterations on laser beam intensity that the best result of the model was achieved for an input value of 30 μJ for the total intensity of the first laser beam, compared to a value of 150 μJ measured during the experiment. We will discuss the difference between experimental and model beam intensity below. The peaks of the laser pulses were all fixed to arrive at the same time and were taken as Gaussian distributions with FWHM of 20 ns. This distribution was summed with another Gaussian distribution of 14 ns (FWHM) to approximate the average of the pulse amplitude over many laser pulses. This linear approximation to what is certainly a non-linear dependence on the relative laser pulse timing may contribute to the difference between experimental beam intensity and model-suggested values of beam intensity.

The empirical value of the ^{238}U off-resonance ion signal is 2.6(2) % of the maximum on-resonance ion signal. We do not have a direct measurement of the ^{235}U off-resonance ion signal relative to its maximum for this experiment, but our functional form of the off-resonance background suggests that the off-resonance ion signal for ^{235}U should be about 1.6 times larger than the ^{238}U ion signal. Thus, we begin with an estimate of the ^{235}U off-resonance ion signal that is 4.3 % of the maximum on-resonance ion signal. The empirical off-resonance ion signal is included in the model result by computing the ionization probability for each isotope independently and then adding the off-resonance ion signal estimates to their respective ionization

probabilities. The model predicted $^{235}U/^{238}U$ ratio then becomes

$$(^{235}U/^{238}U)_{predicted} = \frac{N_0^{235}}{N_0^{238}} \frac{(N_{ion}^{235} + N_{off}^{235})}{(N_{ion}^{238} + N_{off}^{238})} \tag{5.24}$$

where N_i is the factions of of atoms in state i, the superscripts identify the isotope, and the states considered are the initial abundance (0), the model prediction ionization probability (*ion*), and the off-resonance ion signal estimate (off). This approach assumes that the off-resonance ion signal is not depleting the reservoir of available ground state uranium atoms in the ionization volume.

The experimental data and the model prediction for the $^{235}U/^{238}U$ ratio from this set of input parameters are shown together in Figure 5.6 as a function of wavelength in the first resonance laser. Note that the certified value of this isotope ratio is 0.0072(1). There are five different regions of interest within the wavelength range studied that represent different contributions of each isotope to the measured ratio. Starting from the left of the figure there is a region from 415.495 to about 415.500 nm in the model result with a relatively small slope that represents the laser interacting primarily with the tails of the ^{235}U resonance. Next is the region that appears as a peak in the region between 415.500 and 415.510 nm that represents the wavelength range where the laser interacts strongly with the ^{235}U resonance (located at the up arrow), maximizing its ionization probability. In this wavelength range, the laser ionizes only a small fraction of the ^{238}U atoms (about 4 %). The decreasing slope to the right of this peak is the beginning of the region between the two resonances *(i.e.*, near the isosbestic point 415.5105 nm). This is the region in which the measured isotope ratio demonstrates a very large dependence on the wavelength of the laser beam. To the right of the isosbestic point is a region that displays a strong decrease of the measured isotope ratio. Here, the ^{238}U resonance (the down arrow) is dominating the ionization of uranium. Finally, at wavelengths above 415.520 nm, is again a region with a relatively slow change in the predicted isotope ratio that represents the laser interacting primarily with the tail of the ^{238}U resonance.

There is fairly good agreement between the model predictions and the experimental data. Discrepancies are most notable near the peaks of the isotope ratio in both maximum and minimum amplitude, but also in the curvature of the peaks. The model predictions vary very little near the peaks while the data appears to vary smoothly as a function of wavelength. Including stochastic variation of the wavelength and pulse-peak time in the model has been shown to increase the curvature of the predicted peaks as will be discussed later. The overall variation in magnitude of the isotope ratio is fairly well reproduced by the model, although this is strongly a function of average laser intensity that we know to be nearly arbitrary in the model. The widths of the peaks are in fairly good agreement with the experimental data. To aid the reader, in several of the following figures, the model predictions just described are included as a reference, shown as a solid blue line. Other model results, meant to display the sensitivity of model predictions to variations in model parameters, will be shown as dashed lines.

The predicted isotope ratio near the isosbestic point is close to the certified value and the model appears to predict a region with a smaller dependence of the ratio on wavelength than

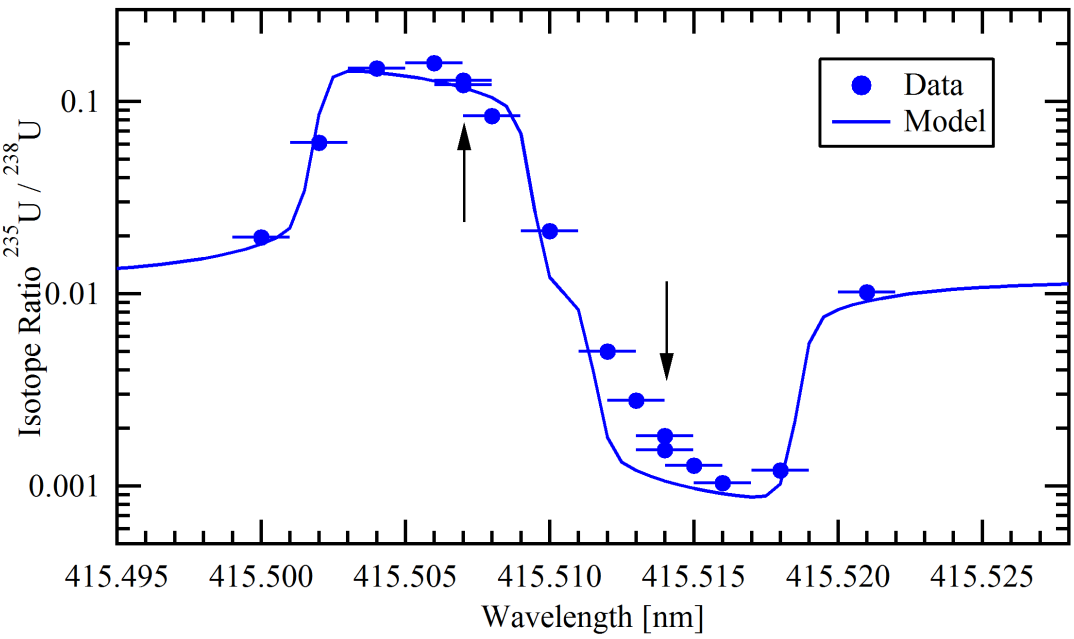

Figure 5.6: Experimental measurements (#9) and a model prediction of the measured $^{235}U/^{238}U$ ratio as a function of wavelength of the first resonance laser for narrow bandwidth conditions. The up arrow locates the mean wavelength of the ^{235}U resonance transition and the down arrow locates the mean wavelength of the ^{238}U resonance transition. The experimental data has been corrected for dead-time considerations, but not for off-resonance background. The error bars estimated by counting statistics for uncertainty in the measured isotope ratio are smaller than the data markers.

would be suggested by the experimental data. This result is misleading until the individual ionization probabilities are examined. For this bandwidth, the ionization probability for both isotopes is in the range of $40-50\,\%$ and thus the measurement at this wavelength would in fact not be close to saturating this transition for either isotope. The empirical individual ionization probabilities verify this conclusion and have already been shown in Fig. 4.16.

In the model inputs, we assumed that the off-resonance ion signal was not equal for each isotope. If, in fact, the off-resonance ion signal is susceptible to the same angular momentum considerations as the atomic U resonance transitions, then we expect a difference in the off-resonance ion signal contributions as large as a factor of 1.6. If the off-resonance ionization process was not subject to these angular momentum considerations we might expect an equal fraction of off-resonance ion signal for both isotopes. Figure 5.7 shows the same experimental data (Exp. #9) and the model prediction as a result of assuming a 1.6 factor increase in the ^{235}U off-resonance ion signal, and a model prediction with equal contributions of the off-resonance ion signal for each isotope. While the different input parameters result in differences in the maximum variation in the measured isotope ratio and have a relatively strong effect at wave-

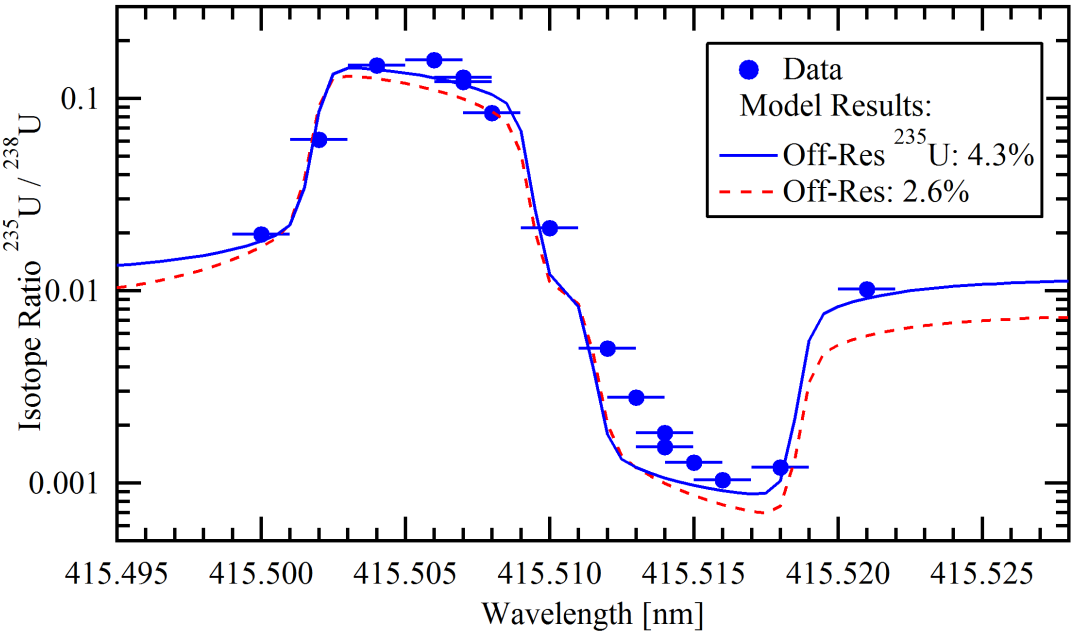

Figure 5.7: Experimental measurements (#9) and a model prediction of the measured $^{235}U/^{238}U$ ratio as a function of wavelength of the first resonance laser for narrow bandwidth conditions. First, a model prediction using inputs of 4.3 % off-resonance ion signal for ^{235}U and 2.6 % for ^{238}U. The second model used equal off-resonance ion signals for ^{235}U and ^{238}U as input parameters.

lengths far from both resonances, the general shape of the variation in isotope ratio as a function of wavelength is unaffected. In general, it can be expected that the off-resonance background will change as a function of target matrix and ionization conditions. Nevertheless, the results shown in Fig. 5.7 suggest that the general wavelength dependence of the isotope ratio will not be markedly affected.

5.3.2.2 Intensity

Figure 5.8 shows the measured $^{235}U/^{238}U$ ratio from Exp. #9 and the model results obtained using several values for the intensity of the first resonance laser as model inputs. The model suggests that laser intensity is a dominant parameter in determining the maximum variation of the measured isotope ratio. Note that the model intensity that best describes the experimental data is a factor of 5 smaller than the empirical total laser intensity in the ionization volume (150 μJ). This clearly suggests the need for better approximation of the spatial distribution of laser intensity, the atom density, and their superposition in the ionization volume, in order to better understand how the total beam intensity relates to the measured isotope ratio.

Notice that the shape of the peak regions change as a function of the assumed laser intensity,

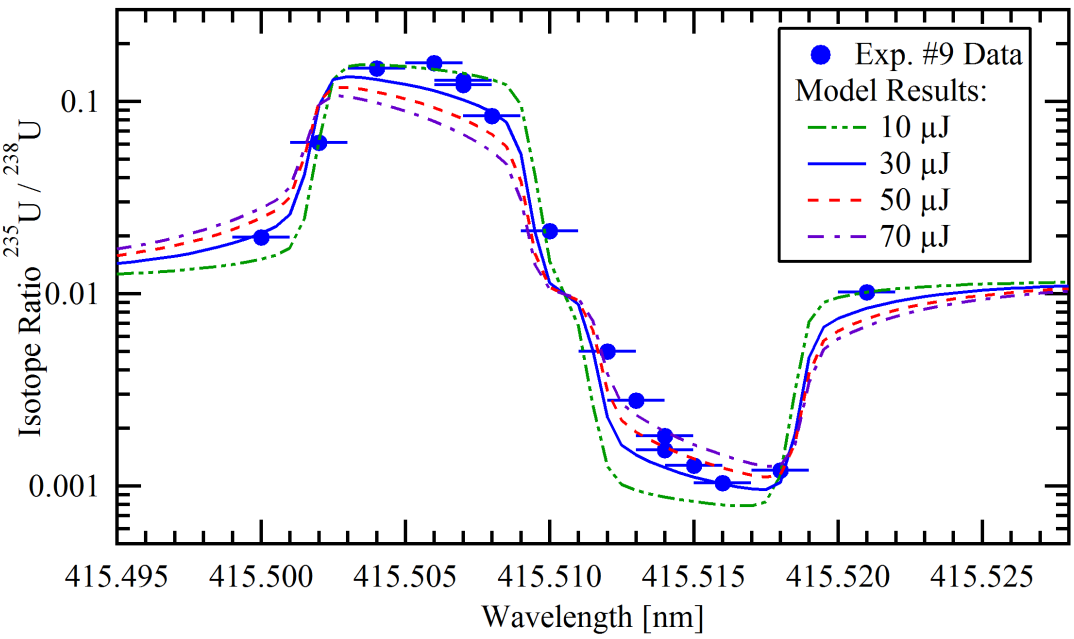

Figure 5.8: Isotope ratio versus wavelength of the first resonance laser for narrow bandwidth conditions for several model values of average laser intensity. Experimental data points are from Exp. #9.

which reflects the power dependence of the ionization probability. For example, in the peak between 415.500 and 415.510 nm, the ionization probability for ^{235}U is saturated even at the lowest average intensity shown here, but the probability for ionizing ^{238}U is very low. As the average intensity of the laser beam increases, the ionization probability for ^{238}U at those wavelengths increases, which depresses the predicted isotope ratio in that range. This is also the cause of the movement of the peak centers away from the isosbestic point, with higher intensities resulting in higher ion signals of the isotope not saturated at that wavelength.

The addition of the off-resonance ion signal after the calculation of ionization probability implies the variation of the laser beam intensity will produce proportionate variation in the contribution of non-resonant background. However, as pointed out above, the model predictions suggest that the average laser beam intensity in the ionization volume is much less than would be predicted from averaging the total beam intensity as we have done. This neglects variations of the atom density as a function of position in the ionization volume and of course the spatial distribution of laser intensity, both of which would produce nonlinear effects on the total ionization probability. Thus, the effect of saturating ionization of atoms near the high-intensity center of the laser beams is not accounted for. This has the effect of reducing the apparent laser intensity in the ionization volume as the excess photons near the center of the beam would have no atoms to ionize. In addition, the method used for distributing the amplitude of the laser pulse as an average intensity over many laser pulses likely over-predicts the overlap of the

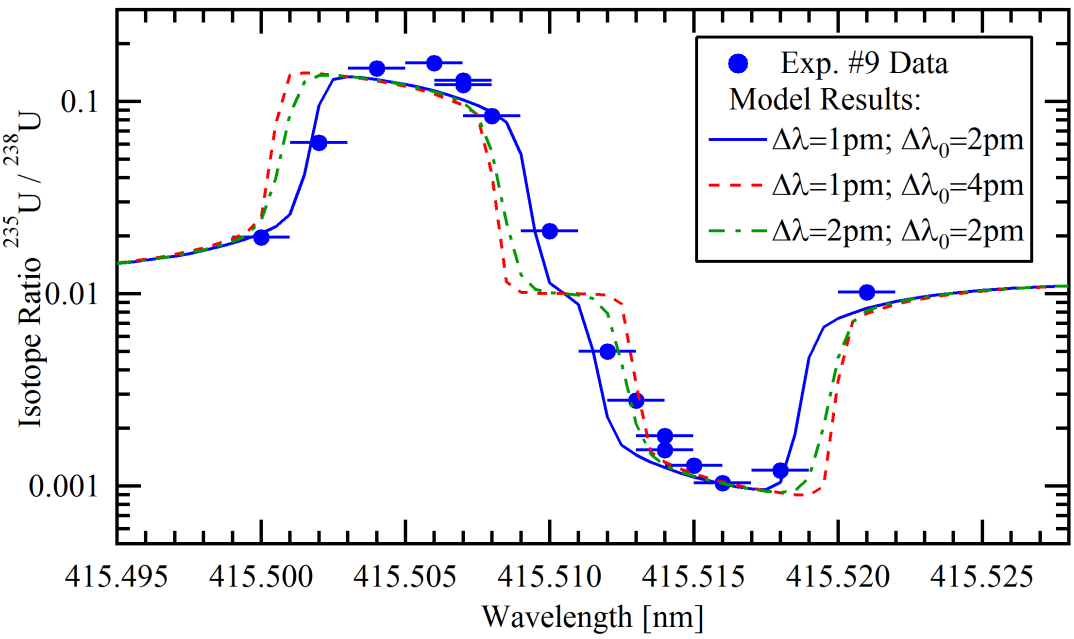

Figure 5.9: Isotope ratio versus wavelength of the first resonance laser for narrow bandwidth conditions for various values of laser bandwidth ($\Delta\lambda$) and mean wavelength variation ($\Delta\lambda_0$). Experimental data points are from Exp. #9.

time-dependent laser amplitudes relative to each other. Taken together, these effects reduce the effective intensity of the laser beams in the ionization volume.

5.3.2.3 Mean Wavelength Variation

Figure 5.9 shows the measured isotope ratio from Exp. #9 and the model predictions based on the empirical values of laser bandwidth ($\Delta\lambda$) and mean wavelength variation ($\Delta\lambda_0$), 1 and 2 pm, respectively. The mean wavelength produced in the narrow bandwidth laser cavity arrangement, has been observed to be distributed about the intended wavelength with a FWHM of ~ 2 pm. If we consider mean wavelength variations larger than 2 pm, we see that the peaks of the measured isotope ratio move away from the isosbestic point and are inconsistent with the experimental data. Note that we can find different combinations of bandwidth and mean wavelength variation that produce similar results. An example of this is shown by the two results with bandwidths of 1 and 2 pm and mean wavelength variations of 4 and 2 pm, respectively. These two results differ only slightly, which is a result of the difference in the combined Gaussian depending on the magnitudes of the individual parameters.

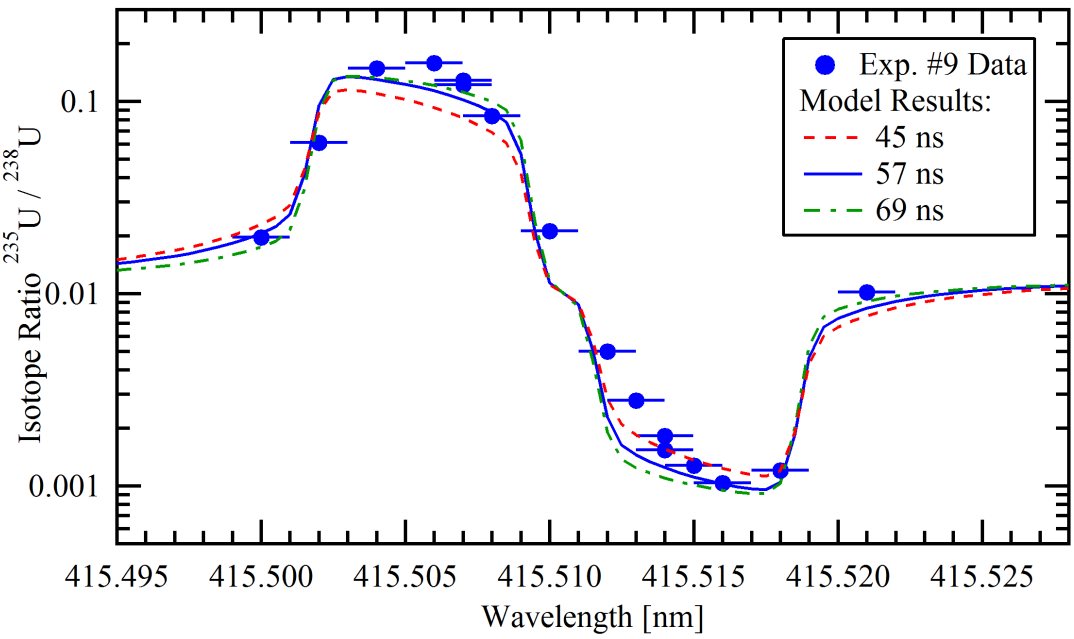

Figure 5.10: Isotope ratio versus wavelength of the first resonance laser for various average lifetimes of the first atomic resonance. Experimental data points are from Exp. #9.

5.3.2.4 Uncertainty in Mean Lifetime of the First Excited State

We tested the sensitivity of the model predictions as a function of the cross section dependence on the lifetime of the first excited state. The lifetime of this state is 57 ns. The stated experimental uncertainty is $\pm 10\,\%$[71]. We altered the model parameter for the excited state lifetime and estimated natural linewidth for the resonance as a result of a ± 12 ns discrepancy between the actual lifetime of the resonance and the lifetime reported in the literature. The model results are shown in Figure 5.10. While the model predictions change, the shape of the $^{235}U/^{238}U$ ratio distribution does not.

5.3.2.5 Doppler Broadening

The estimate used to approximate the Doppler broadening of the atomic resonances as a result of the atomization process have not been measured. We explored variation of the Doppler broadening to observe the sensitivity of the measured $^{235}U/^{238}U$ ratio to this parameter. If we assume that the values of laser bandwidth and mean wavelength fluctuation reported by the wavemeter are correct for our narrow bandwidth laser cavity, than the model predictions suggest the value of the Doppler broadening is very near the 2.05 pm used as our initial estimate in the model. A comparison between the distributions obtained with the 2.05 pm width used in the model and an increased width of 3 pm is shown in Figure 5.11. The increased Doppler width shifts the peaks of the isotope ratio away from the isosbestic point and results in poorer overall

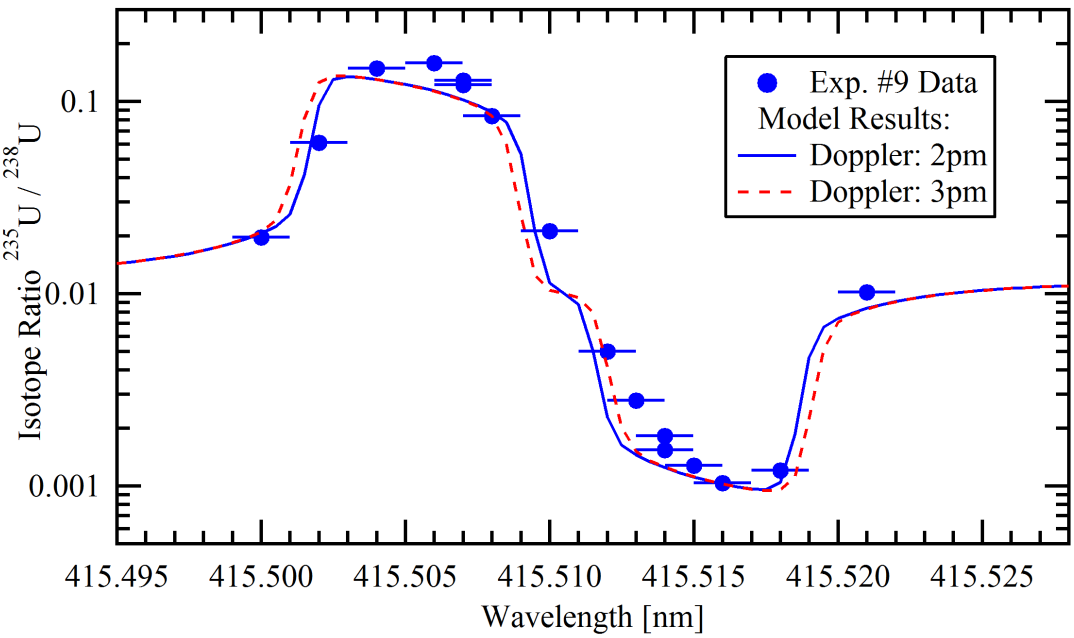

Figure 5.11: Isotope ratio versus wavelength of the first resonance laser for narrow bandwidth conditions for two Doppler broadened widths of the atomic resonances. Experimental data points are from Exp. #9.

fit to the experimental data. Further study of the variation of Doppler width demonstrated that, in general, nearly identical model predictions can be obtained for any arbitrary value of the laser bandwidth by increasing the Doppler width by 1 pm and reducing the laser bandwidth by 0.5 pm.

5.3.2.6 Stochastic Variation of Laser Parameters

The approximation that the mean wavelength variation and the laser pulse time distribution can be averaged over many laser pulses clearly neglects the nonlinear effects of the combination of those two parameters that, given the variations observed in those parameters empirically, must have an effect on the experimentally measured isotope ratio. While the discrete averaging of these parameters has allowed the gross understanding of the ionization probability as a function of wavelength, the comparison to experimental data is likely to fall short when the stochastic effects of laser performance are neglected. The model has been constructed in such a way as to allow the stochastic variation of a number of laser parameters, but thus far, we have only examined a limited number of cases using the stochastic sampling. In general, the stochastic sampling of model parameters will tend to produce more smoothly varying functions of laser wavelength. This is exemplified in Figure 5.12, which shows the experimental data from Exp. #9 and the results of two types of model predictions. The first is the reference model, shown

previously, where all model parameters are taken as discrete values describing the average over many laser pulses. The second result represents the average of 1000 computations at each wavelength where the laser wavelength and pulse time were randomly sampled from the empirical distributions (see Fig. 3.18 and Fig. 3.21). The distribution was sampled for each of the three laser beams in each computation. All other model parameters were fixed.

The two model predictions differ significantly. The stochastic model varies much more smoothly as a function of wavelength, as expected. The stochastic model reduces the width of the peaks and the maximum and minimum of the measured isotope ratio have moved closer to the isosbestic point. Clearly, the nonlinear effects of averaging laser wavelength and pulse timing are important to the measured isotope ratio and must be considered for better defining the actual values of laser parameters during the experiment. The effect of stochastic variation of laser timing on the model prediction will be strongly dependent on the intensity of the beams, as the superposition of pulses will be dependent on the pulse amplitude. This is a shortcoming of allowing the stochastic variation of laser timing in our single point model of laser beam intensity, which we know does not properly relate model beam intensity to experimental intensity. The stochastic variation of laser pointing stability (the movement of the beam center from pulse to pulse) has not been considered, but for significant variations in the beam position relative to the beam widths the effect would be very similar to the variation in laser pulse timing.

5.3.2.7 Bandwidth Variation

Our hypothesis is that by broadening the laser bandwidth of the first resonance laser we can saturate the resonance transition for both ^{235}U and ^{238}U at mean wavelengths near the isosbestic point, and that the measured isotope ratio will be less sensitive to the variations in mean wavelength that occur from pulse-to-pulse. Figure 5.13 shows model results for three values of the laser bandwidth. All other inputs are consistent with the closest fit model of 1 pm bandwidth already discussed and included in this figure. We have kept the mean wavelength fluctuations at 2 pm in these model calculations.

Clearly as the laser bandwidth increases, the peaks of the maximum and minimum isotope ratio move away from the isosbestic point and the peak shapes are more symmetric. For the larger bandwidths both isotopes are saturated in the region between the peaks, unlike that for the 1 pm bandwidth result. The peaks become more symmetric as the tails of the isotope not saturated in that wavelength region of the peak become less sensitive to wavelength. Generally, the peaks maintain the same variation in magnitude of the measured isotope ratio as the bandwidth is increased.

5.3.2.8 Comparison of Model Prediction with Broad Bandwidth Data

For experiment #10, we measured the $^{235}\mathrm{U}/^{238}\mathrm{U}$ ratio as a function of wavelength of the first resonance laser when that laser cavity was arranged to produce a broadened bandwidth of approximately 5 pm (see Sec. 4.2.1). The variation of the mean wavelength was observed to be distributed about the intended wavelength with a FWHM of 4 pm. However, the reported

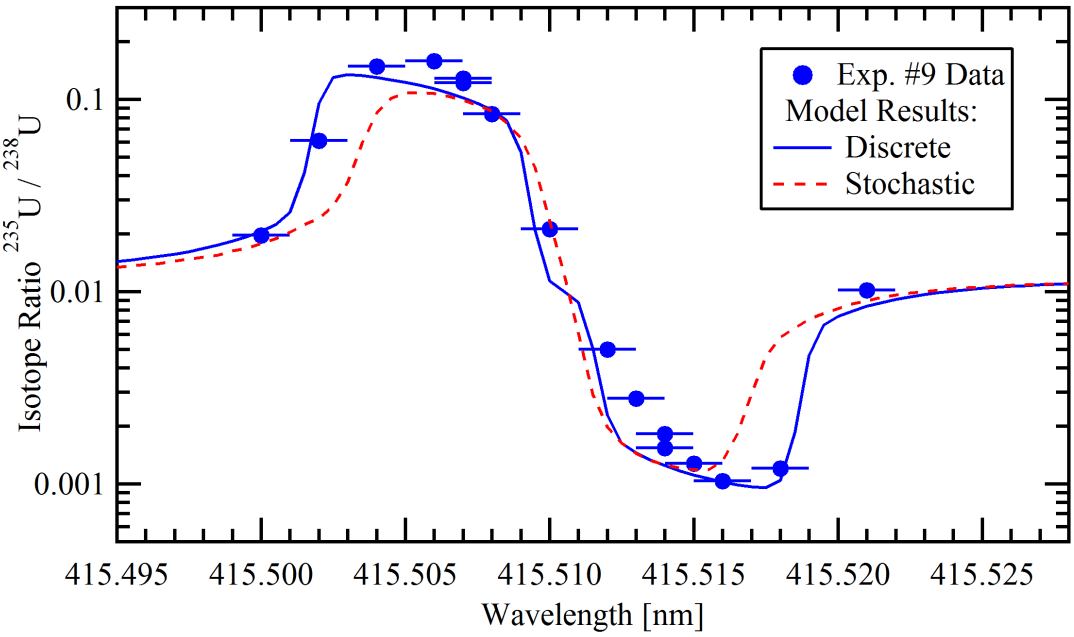

Figure 5.12: Isotope ratio versus wavelength of the first resonance laser for narrow bandwidth conditions. Experimental data points are from Exp. #9. Two model predictions are shown alongside the data, the first is the model result when all model parameters are input as discrete values. The second is a model prediction where the wavelength and time of the laser pulses were allowed to vary stochastically.

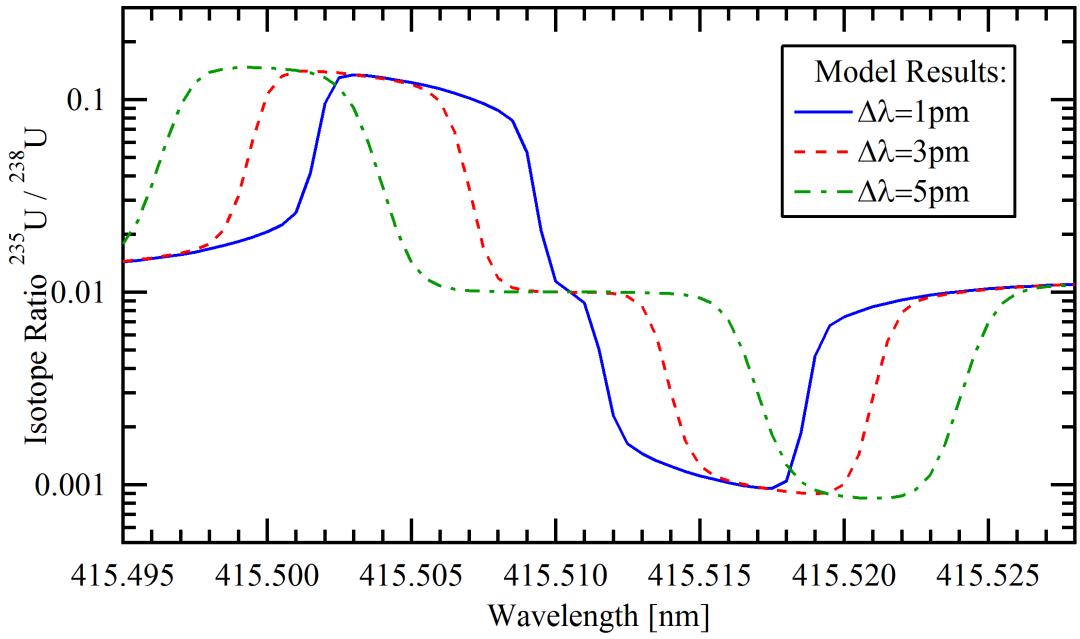

Figure 5.13: Isotope ratio versus wavelength of the first resonance laser for various bandwidth conditions. All results include 2 pm mean wavelength variation. The 1 pm bandwidth model result is the same as previously shown in Fig. 5.6.

bandwidth and mean wavelength from the wavemeter at this bandwidth are less reliable and should be considered with caution (see Sec. 3.1.2.3). The intensity of the first resonance laser was one-half the intensity of the laser used in Exp. #9, 75(8) μJ instead of 150(10) μJ, and thus the model used a value of 15 μJ for the beam intensity. The model predictions suggest that for a lower intensity the magnitude of the variation in isotope ratio should increase. The data from Exp. #10 are shown in Figure 5.14 along with a model prediction when the bandwidth was set to 5 pm and the variation in mean wavelength was taken as 4 pm. The model clearly does not reproduce the experimental data. Despite many different approaches and changes in parameters the current model cannot explain the distribution of measured isotope ratio observed in these data.

The current hypothesis for the discrepancy between the model results and the experimental data is that uncertainty in mean wavelength determination of the wavemeter and the reliance on the wavemeter result for the automated feedback system cause unknown variation in the mean wavelength. If the width of the distribution of mean wavelength is larger than the distribution reported by the wavemeter, it may help explain the discrepancy between the model predictions and the broad bandwidth experimental data obtained with the laser system used in this work. This would allow the averaging of the measured isotope ratio over a larger wavelength range and in turn provide the smoothly varying function observed in 5.14. Other possible causes for the discrepancy involve variations in the experimental parameters not well characterized in the model, such as non-linear effects in the combination of laser timing, spatial distribution, and wavelength variation.

5.3.2.9 Broad Bandwidth Experimental Data with the New Laser System

After the experiments discussed in this work were performed, a new laser system was installed for use on CHARISMA. These lasers include several improvements realized through the implementation of a single, common pump laser for all three tunable cavities, Q-switches for improving the relative timing of the laser pulses, and intracavity frequency doubling, which improves the intensity and stability of the spectral distribution for broad bandwidth laser beams. With kind permission, we present unpublished results obtained on the measured $^{235}U/^{238}U$ ratio as a function of first laser wavelength for a broad bandwidth laser beam of ~ 9 pm at 500 μJ total beam intensity[81]. This experiment uses the same wavemeter, with the same limitations. The fluctuation in mean wavelength of the new laser system for this beam was measured to be 0.65 pm FWHM. The calculation assumed a bandwidth of 6.5 pm, a fluctuation in mean wavelength of 0.65 pm (FWHM), and a beam intensity of 200 μJ. The variation of relative laser pulse timing for the new lasers was measured as $\sim$4 ns (FWHM). To correct for an apparent systematic error in the experimentally reported wavelength, the model predictions have been shifted in wavelength by +2.5 pm. This is consistent with the difficulty of the wavelength meter in determining the mean wavelength of the spectral distribution for broad bandwidth pulses and a shift of this size is consistent with the error associated with the manual calibration of the wavemeter (see Sec. 3.1.2.3). Both the model predictions and the experimental data demonstrate a wide wavelength range (approx. 415.508 to 415.515 nm) for which there appears to be very little

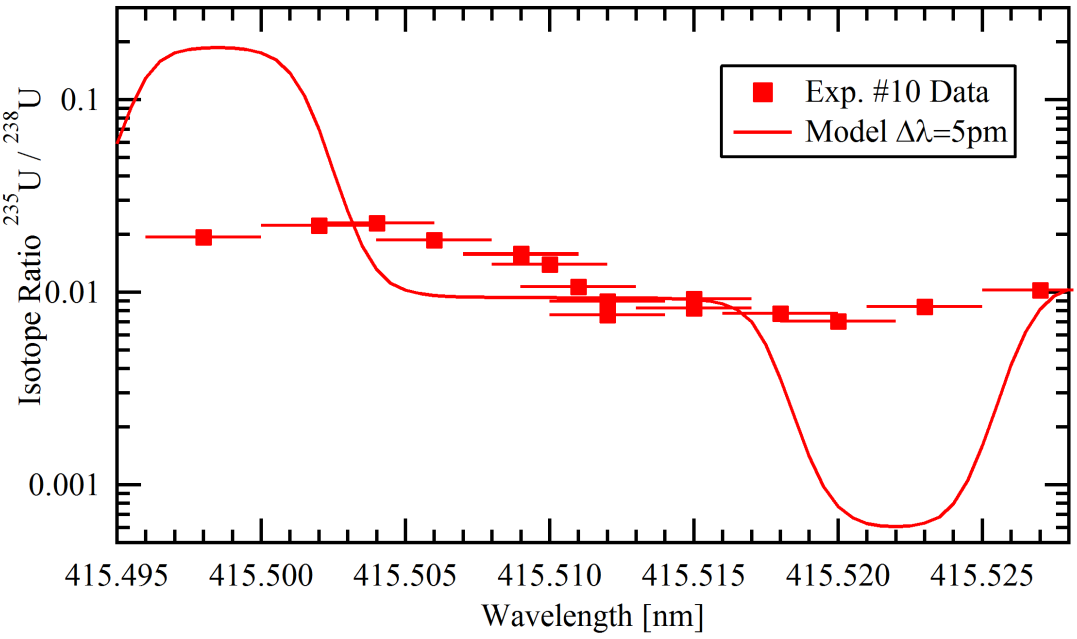

Figure 5.14: Isotope ratio versus wavelength of the first resonance laser for various bandwidth conditions. Experimental data points are from Exp. #10. Model predictions include 4 pm mean wavelength variation.

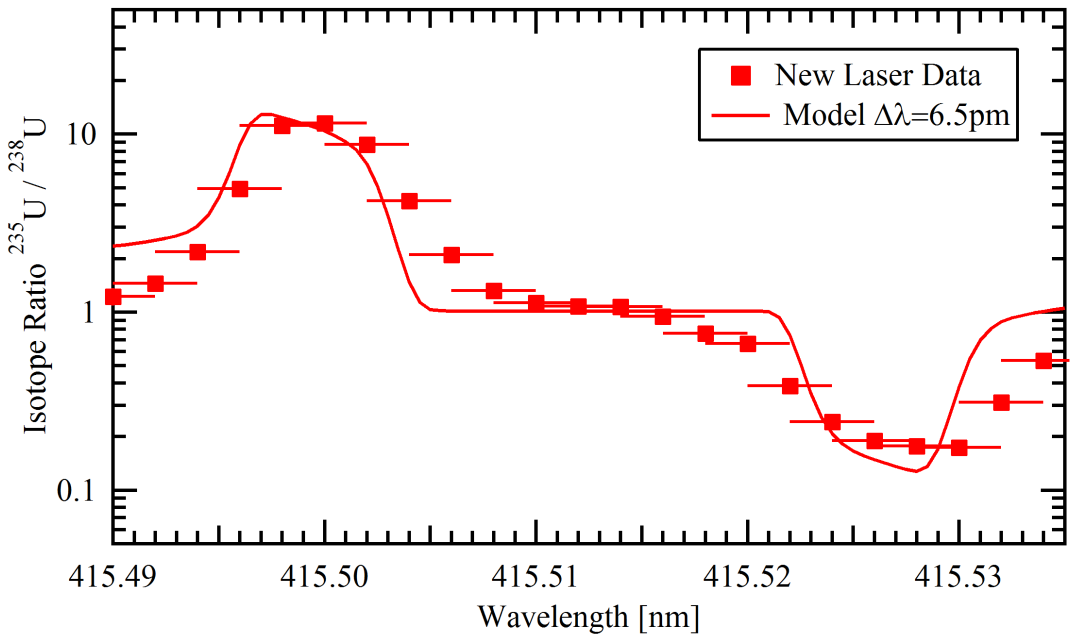

Figure 5.15: Isotope ratio versus wavelength of the first resonance laser for broad bandwidth conditions. Unpublished data[81].

sensitivity of the measured isotope ratio to mean wavelength of the first resonance laser. This supports our hypothesis that the measured laser parameters for the old laser system when producing a broad bandwidth beam were not accurate. Given the assumptions and limitations used in the model calculations, the rate equation model is successful at predicting the effect of laser bandwidth with the new laser beams.

Chapter 6

Conclusions and Future Work

6.1 Conclusions

The research presented in this dissertation demonstrates that the quantification of uranium isotope ratios using RIMS is viable to a precision of better than 0.5 % ($\pm 2\sigma$). This was accomplished through the use of broad bandwidth laser beams aided by automated feedback control of laser wavelength. This methodology was exhibited for ion sputtering of uranium oxide materials, including U_3O_8, without sample preparation. We have shown that the physical differences in the isotopes of uranium, such as the large isotope shift and angular momentum considerations, do not prevent reproducible excitation and ionization of the isotopes relative to one another. The laser systems and the ancillary technology necessary to provide such reproducibility are available. Measurement of a target of unknown isotopic abundance can be compared to the measurement of an isotope standard to provide a corrected result, which reduces the contributions of systematic errors to the total measurement uncertainty below the current level of precision. The findings of this work can be used to describe the limits of performance necessary for an instrument designed to perform routine measurements of uranium isotope ratios.

The approach in this work to measuring uranium isotope ratios is based on the simultaneous ionization of multiple isotopes of uranium with nearly equal ionization probabilities using a 3-color, 3-photon ionization scheme. Saturating the transitions of multiple uranium isotopes requires bandwidths on the order of the isotope shift, but does not guarantee equal ionization efficiency for all isotopes. If the ionization of all available neutral atoms in the irradiation volume is not complete, preferential ionization of one isotope over another is likely as a result of differences in cross sections and angular momenta. The effect on the measurement result by the enhancement of one isotope over another is mitigated by using an isotope standard, provided the instrumental parameters do not change significantly between measurements of the standard and the unknown. The need to analyze two targets requires stable operation of the instrument systems over the time required to perform all necessary measurements. In this work, we have demonstrated the use of automated feedback systems to successfully control the variation in mean laser wavelength and relative pulse timing for essentially an indefinite length of time. Other critical laser parameters not equipped with feedback systems, such as beam intensity and pointing accuracy, were successfully monitored for deviations from their nominal values.

The non-resonant photoion signals are shown to be non-negligible compared to the resonant uranium ion signal measured from uranium oxide materials using the 3-color, 3-photon ionization scheme. Non-resonant signals show very little dependence on the wavelength of the laser beams. The exact amount of non-resonant background at the masses of atomic uranium ions is dependent on both target composition and specific laser parameters for a given experiment. Thus, the non-resonant signal must be quantified for each target under actual experimental conditions. If the non-resonant signal is dominated by the photodissociation of molecular species into atomic U^+, then the background for each even-A isotope should be a common fraction of the abundance of each isotope in the target. The non-resonant background for odd-A isotopes may be enhanced by the differences in angular momentum caused by non-zero nuclear spins.

Poor performance of the wavelength meter for characterizing the broad spectral distributions produced by the laser system hinders accurate determination of the actual spectral distributions

used. However, the reproducibility of the measured $^{235}U/^{238}U$ ratio for analytical sessions on the order of hours, indicates that the wavemeter when used with the automated feedback system provides a reproducible distribution of mean wavelength over an indefinite period, even for broad laser spectral distributions. This behavior is sufficient for producing accurate measurements of the isotope ratio, but does not provide the information required for reliable calculation of ionization probability.

The rate equation model illustrates the dominant laser parameters that define the uranium isotope ionization probabilities. The model calculations display consistent features for the measured isotope ratio as a function of the first laser wavelength over a large range of values for the laser parameters studied. It supports the conclusion that current experimental parameters are sufficient to provide reproducible isotope ratios, by predicting a range of wavelengths that can saturate the transition to the first excited state in both $^{235}U/^{238}U$. Differences between model predictions and experimental data likely come from some of the simplifying assumptions used in the model and the uncertainty of characterization of the experimental parameters. The difficulty of obtaining an accurate determination of the spectral distribution of broad bandwidth lasers appears to be an important factor in resolving discrepancies between measured isotope ratios and model predictions. Use of discrete distributions to represent the average variations of mean wavelength and pulse timing, neglects the nonlinear combination of fluctuations in these parameters and does not produce smoothly varying functions as expected from random sampling of the distributions. The limitations of using a point model to represent the laser irradiance are evident when stochastic variations of laser wavelength and timing are included. Under these conditions, the unrealistic irradiance used in the model significantly affects the results. Further model development should include more realistic distributions of the spatially-dependent irradiance and the neutral atom distributions and should improve agreement between the model calculations and the experimental data.

6.2 New Laser System

While the laser system used in the work is capable of achieving reproducible measurements of the U isotope ratios, there remains considerable room for improvement. Particularly, improvements in relative laser pulse timing and intensity of the laser used for the ionizing step should make measurements more robust. Likewise, improved reproducibility of the spectral distribution and more accurate definition of the mean wavelength for broad bandwidth lasers should produce more consistent results from experiment to experiment.

Some of these improvements were realized with the installation of a new laser system for use on CHARISMA. The new system differs from the one already described in several properties. All three tunable Ti:Sapph cavities are now pumped using a single, high-power diode-pumped solid state laser. The new pump laser has significantly better pulse-to-pulse reproducibility of its irradiance. The tunable cavities now have the capability to be Q-switched, which is a method used to control the power output from the laser cavity with nanosecond time resolution. Finally, the new laser system is arranged to perform frequency-doubling inside the tunable cavities,

which provides significantly higher intensity of second-harmonic light and improved spectral irradiance.

Taken together, the improvements have been shown to produce laser beams more favorable to resonance ionization than the old laser system. The variation in peak time is now ≤ 4 ns, with an average pulse length of about 15 ns. Relative timing of the lasers in a given pulse is often better than 4 ns because the pulses from the tunable cavities tend to vary together in time as a result of the common pump laser. Overall, the laser system provides higher irradiance by almost a factor of two for some wavelengths, with less pulse-to-pulse fluctuation. Spectral distributions are broader than those produced by the old system, even when using a 40X beam expander. For broad bandwidth beams, reproducibility of the spectral distribution from pulse-to-pulse has improved significantly and the distribution varies more smoothly as a function of wavelength than distributions produced with the old system. These enhancements and their effect on the precision and accuracy of the measured uranium isotope ratios are currently being quantified.

6.3 Instrument Requirements

The results of this work define requirements for an instrument capable of achieving precision and accuracy in the measured $^{235}\mathrm{U}/^{238}\mathrm{U}$ ratio of 0.5 %. In general, the mass spectrometric methods required for these measurements are well understood and thus, we will focus on the properties of the laser system required for high-quality resonance ionization of uranium atoms.

The main factors that determine the resonance ionization probability are the distributions of laser beam irradiance as functions of time, position, and wavelength. For perfect laser systems, the distributions of these functions would be identical for every pulse. In practice, this is never the case and variation of these distributions from pulse to pulse induces variation in the ionization probability. To first order, variations in the distributions are dominated by fluctuation of the mean value and not the shape of the distributions. However, the effect on ionization probability due to variation of the means will depend strongly on the shape of the distributions. Isotope ratio measurements of high precision depend not only on the variation of distributions from pulse to pulse, but also on the long-term stability of these distributions over a period of hours.

The ionization scheme used here requires coordination of three laser beams with the cloud of neutral atoms. Distributions of irradiance in time and space for the three laser beams must not only coincide with the atoms, but must also be synchronized relative to one another. In terms of wavelength, the spectral distribution of each laser must provide sufficient irradiance to saturate the corresponding transition in the isotopes of interest.

Timing Relative timing of the laser pulses should be nearly simultaneous. The intent is to saturate the two bound-bound transitions for a time long enough to ionize all the atoms out of the second excited state. This requires a few nanoseconds because not all of the atoms will be in the second excited state simultaneously. This is one reason that pulse lengths on the order of several nanoseconds are ideal for resonant ionization. For our system the variation in laser timing,

about 14 ns, was a significant fraction of the pulse length, of ~ 20 ns. This did not prevent reproducible measurement of the isotope ratios, but clearly reduced the ionization probability of atoms for some laser pulses compared to others. When ionization probabilities are reduced by poor temporal overlap of the laser beams we expect an enhancement of the ionization of ^{235}U over that of ^{238}U as a result of the cross section and angular momentum differences. Pulse-to-pulse fluctuations in laser timing prevented investigation of the dependence of the measured isotope ratios on the relative timing of laser pulses. Improved relative timing with the new laser system essentially ensures that every instrument cycle produces beams with good superposition in time.

Position Similar to the relative laser timing, the laser beams must be well overlapped in space. The laser pulses are short (15-20 ns) and spot sizes are large compared to the velocity of the freely-expanding neutral atoms after sputtering ($\sim 1\,\mu$m/ns) so that atoms can be considered stationary. Measured isotope ratios do not show a large dependence on the relative position of the beams, but individual atoms must be excited from the ground state into an ion from essentially a single point within the ionization volume. This requires photons from each laser to be present at that point. Temperature stabilization of the laser system using regulated heaters improved the pointing stability of the laser beams. Typical variation of the beam centers is less than $\pm 100\,\mu$m[82], which is on the order of 10 % of the typical beam diameter. Variation in the laser position significantly larger than this, would likely degrade the reproducibility of the isotope ratio because of variation in the relative fraction of available atoms that are ionized. In principle, observation of the laser beam positions and shapes on a beam analyzer could be used to exclude measurements in which the beam position varied outside an acceptable range.

The cross-sectional area of the beams should vary smoothly as a function of position and provide good coverage of the cloud of neutral atoms. For our instrument, elliptical areas of about $1 \times 1.5\,\text{mm}^2$ are preferred for the extraction of ions into the mass spectrometer. If practical, diffuse beams are preferred to tightly focused beams of the same overall cross section to provide more uniform irradiance over the ionization volume. It is possible to employ collimating apertures to ensure that beam size does not increase with increasing irradiance, and to prevent formation of ions on the edges of beams, which are regions where irradiance is low and ionization probability varies significantly from pulse to pulse.

Wavelength The isotopes to be resonantly ionized define the spectral distribution required for each laser. One must then ensure that this distribution is reproducible from pulse-to-pulse. Application of broad bandwidth laser beams relaxes the requirements on the permissible pulse to pulse variation of mean wavelength (*i.e.*, even with a shift in mean wavelength, the spectral distribution still provides sufficient irradiance near the resonance to saturate the transition). Experiments presented in Chapter 4 clearly demonstrate a reduced dependence of the isotope ratio on wavelength for broadened spectral distributions in both the first and second transitions. The remaining question then becomes, how broad of a bandwidth is required to provide a reproducible measurement of the isotope ratio despite the presence of pulse-to-pulse variations in

mean wavelength?

From the experimental data and the model predictions a bandwidth of ≥ 5 pm is sufficient to saturate the first transition of both ^{235}U and ^{238}U at a single mean wavelength despite an isotope shift of 7 pm. For this bandwidth, and if our wavemeter can be believed, then a reproducible isotope ratio can be obtained even with a width for the distribution of mean wavelength as large as 4 pm. Although the wavemeter is inaccurate in describing the mean wavelength, it appears to be consistent, allowing the feedback system to maintain the same average wavelength over analytical sessions.

For the second transition, the isotope shift is smaller (about 4 pm). In addition, we were able to use an irradiance well above saturation without a significant increase to the non-resonant ion signal. The measured isotope ratio displays a dependence on the wavelength of the second laser that is almost an order of magnitude smaller than the dependence on the wavelength of the first laser. Since the wavelength of the second transition is produced in the fundamental frequency range of the tunable Ti:Sapph cavities, the bandwidth is nominally broader than for the first transition, which is produced by frequency-doubling. Our experiments demonstrated that a bandwidth of about 3 pm with variation in mean wavelength of about 2 pm from pulse to pulse enabled the measurement of the ^{235}U/^{238}U ratio to a precision of better than 0.5 %. For the 722.200 nm transition from the second excited state to the autoionizing state, the large width of the autoionizing state precludes the need to worry about laser bandwidth or isotope shift.

Integrated Irradiance Given the above considerations for the distributions and mean variations in the irradiance as a function of time, position and wavelength for the three beams, we can now discuss the total intensity required for the ionization of ^{235}U and ^{238}U simultaneously. The irradiance of each beam should provide sufficient saturation of the transition for each isotope such that the ion count rate depends very weakly on small changes in beam irradiance. An optimized irradiance should also aim to minimize the non-resonant ion signal. We assume that the beams have a cross sectional area described by a 2-D Gaussian with a total area of 1.5 mm^2. The first transition can be saturated for both isotopes with fairly low irradiance. We see that as little as 25 μJ per pulse is sufficient when the bandwidth of the laser is ~ 5 pm (Fig. 4.24). The second transition requires significantly more intensity to produce saturation, but this is still readily achievable. For this transition, Fig. 4.26 shows that nearly 400 μJ per pulse is necessary when the laser bandwidth is ~ 6 pm. Finally, the ionization step requires very high irradiance and saturation of this transition was not possible. For a laser bandwidth of 3 pm in the third laser the autoionizing transition is predicted to require approximately 1200 μJ per pulse for saturation. This intensity is feasible with the new laser system.

6.4 Future Work

The results of this work justify the remaining research and engineering needed to develop the measurement of uranium isotope ratios by RIMS into a routine technique. Important questions remain about the utility of this approach for specific applications. There are several avenues for

exploration: The yield of neutral ground state uranium atoms from a variety of targets using different desorption methods should be studied, with the aim of increasing the efficiency of uranium measurements. The new laser system should be used to improve the precision and accuracy of this broad bandwidth approach. Further development of the computational model is needed. The utility of this approach for a variety of practical targets such as U in the presence of atomic isobars, like Pu should be quantified. Finally, the approach of simultaneous ionization using broad bandwidths should be expanded to other elements with significant isotope shifts.

One of the most crucial issues remaining that will define the scenarios for which RIMS is useful is the total detection efficiency of the technique. Total detection efficiency for a particular species is defined as the number of ions detected divided by the total number of atoms removed from the target. Uranium oxides are challenging matrices for RIMS due to the strong tendency for U to desorb as molecular UO_x, and the efficiency of desorbing neutral ground state atoms has not been optimized. RIMS regularly demonstrates efficiencies for other elements on the order of a few percent. For uranium atoms liberated from oxygen-containing matrices, the current efficiency is on the order of 10^{-4}[79][1]. The factor limiting the efficiency is the yield of neutral atomic uranium atoms. We have not yet studied methods for improving the neutral yields for atomic uranium, but several directions remain open. Several groups have demonstrated increased efficiency for liberating neutral U and Pu atoms from oxide materials using Ti as a reducing medium[78, 77]. Evidence also suggests that laser desorption methods may be more efficient than ion sputtering for creating neutral atoms[83, 79]. Variation in laser desorption methods, such as wavelength and pulse length, can be explored to optimize the desorption process to improve neutral yields.

The new laser system provides more reproducible distributions of irradiance as a function of time and wavelength. The precision and accuracy of the measured result achievable with the new system remain to be quantified. Likewise, the increase in irradiance should make it possible to saturate the ionization step in our scheme and reduce the enhancement of ^{235}U compared to the even-A uranium isotopes. With the reduction in variation of mean wavelength from pulse to pulse for broad bandwidth beams produced by the new laser system, it may be worth re-evaluating the use of the very narrow autoionizing transition of 722.344 nm, because of the larger peak cross section.

The rate equation model can be improved upon significantly. There are two main improvements that should be included: (1) more realistic spatial distributions of laser irradiance and neutral atom densities in the ionization volume to provide a weighted average of the relative ionization probability and (2) the stochastic variation of irradiance as a function of time, position, and wavelength using empirical probability distribution functions. Realistic spatial distributions will provide amplitudes that more closely approximate experimental conditions. This will enable the model to reproduce the compounding effects of variations in the laser parameters. Additionally, the inclusion of realistic spatial irradiance distributions will improve the calculated values of the cross sections estimated using least square fits to the empirical data.

[1] Efficiencies for U isotope ratio analysis by SIMS instruments are on the order of 0.5 % and for multi-collector ICP-MS can be on the order of 1 %.

The cross section for the final step of the 2-color, 3-photon ionization process (Fig. 4.29) could be improved by performing an experiment to study the ionization dependence of this process on the irradiance of the first laser beam. Finally, improved characterization of broad spectral distributions should be pursued, particularly for the distribution of wavelength outside the current limited range of ± 5 pm from the mean wavelength.

RIMS lends itself to applications in the presence of interfering isobars due to its ability to selectively ionize the species of interest. We have not quantified the selectivity of the 3-color, 3-photon uranium ionization scheme against common isobaric interferences that might be expected in nuclear materials. Using multi-element standards with known compositions of elements that contain uranium isobars can help to quantify the selectivity of this resonance ionization scheme. This will help determine the practical limits for measuring uranium isotopes in the presence of these other elements.

Large isotope shifts are a common feature of the atomic spectra of the actinides. The approach of using broad bandwidth laser beams for overcoming the influence of the shifts on the measured isotope ratio of other actinides should be possible. Work is currently underway to expand the use of this broad bandwidth approach to measure isotope ratios in Pu and Eu. Other actinide elements, such as Th, are also attractive for this approach.

Bibliography

[1] K. Mayer, M. Wallenius, I. Ray, Nuclear forensics - a methodology providing clues on the origin of illicitly trafficked nuclear materials, Analyst 130 (4) (2005) 433–441.

[2] F. Szasz, The day the sun rose twice: the story of the Trinity Site nuclear explosion, July 16, 1945, Univ of New Mexico Press, 1984.

[3] D. L. Donohue, Strengthened nuclear safeguards, Anal. Chem. 74 (1) (2002) 28 A–35 A. URL http://pubs.acs.org/doi/abs/10.1021/ac021909y

[4] S. F. Boulyga, J. S. Becker, J. L. Matusevitch, H.-J. Dietze, Isotope ratio measurements of spent reactor uranium in environmental samples by using inductively coupled plasma mass spectrometry, Int. J. Mass Spectrom. 203 (1-3) (2000) 143 – 154.
URL http://www.sciencedirect.com/science/article/B6VND-423RH4V-F/2/e67da7045e15f16e12b43551bc384757

[5] K. Moody, I. Hutcheon, P. Grant, Nuclear Forensic Analysis, CRC, 2005.

[6] S. Boulyga, J. Becker, Isotopic analysis of uranium and plutonium using icp-ms and estimation of burn-up of spent uranium in contaminated environmental samples, J. Anal. At. Spectrom. 17 (9) (2002) 1143–1147.

[7] X. Hou, P. Roos, Critical comparison of radiometric and mass spectrometric methods for the determination of radionuclides in environmental, biological and nuclear waste samples, Anal. Chim. Acta 608 (2007) 105–139.

[8] G. Hurst, M. Payne, S. Kramer, J. Young, Resonance ionization spectroscopy and one-atom detection, Rev. Mod. Phys. 51 (4) (1979) 767–819.

[9] J. Young, R. Shaw, D. Smith, Resonance ionization mass spectrometry, Anal. Chem. 61 (22) (1989) 1271–1279.

[10] S. Raeder, S. Fies, H. Tomita, K. D. A. Wendt, Selective isotope determination of uranium using hr-rims, 4th Int. Conf. on Laser Probing - LAP 2008, AIP Conf. Proceedings 1104 (2009) 96–101.

[11] K. Wendt, N. Trautmann, Recent developments in isotope ratio measurements by resonance ionization mass spectrometry, Int. J. Mass Spectrom. 242 (2-3) (2005) 161–168.

[12] N. Erdmann, J.-V. Kratz, N. Trautmann, G. Passler, Resonance ionization mass spectrometry of ion beam sputtered neutrals for element- and isotope-selective analysis of plutonium in micro-particles, Anal. Bioanal. Chem. 395 (6) (2009) 1911–1918.
URL http://dx.doi.org/10.1007/s00216-009-2906-6

[13] M. R. Savina, M. J. Pellin, C. E. Tripa, I. V. Veryovkin, W. F. Calaway, A. M. Davis, Analyzing individual presolar grains with charisma, Geochim. Cosmochim. Acta 67 (17) (2003) 3215–3225.

[14] J. Levine, M. Savina, T. Stephan, N. Dauphas, A. Davis, K. Knight, M. Pellin, Resonance ionization mass spectrometry for precise measurements of isotope ratios, Int. J. Mass Spectrom. 288 (2009) 36–43.

[15] S. Boulyga, K. Heumann, Determination of extremely low 236u/238u isotope ratios in environmental samples by sector-field inductively coupled plasma mass spectrometry using high-efficiency sample introduction, J. Environ. Radioact. 88 (1) (2006) 1–10.

[16] S. Richter, A. Alonso, W. De Bolle, R. Wellum, P. Taylor, Isotopic "fingerprints" for natural uranium ore samples, Int. J. Mass Spectrom. 193 (1999) 9–14.

[17] S. Richter, S. A. Goldberg, Improved techniques for high accuracy isotope ratio measurements of nuclear materials using thermal ionization mass spectrometry, Int. J. Mass Spectrom. 229 (3) (2003) 181 – 197.
URL http://www.sciencedirect.com/science/article/pii/S1387380603003385

[18] R. Martinelli, T. Hamilton, R. Williams, S. Kehl, Separation of uranium and plutonium isotopes for measurement by multi collector inductively coupled plasma mass spectroscopy, J. Radioanal. Nucl. Chem. 282 (2009) 343–347, 10.1007/s10967-009-0150-3.
URL http://dx.doi.org/10.1007/s10967-009-0150-3

[19] Y. Ranebo, P. Hedberg, M. Whitehouse, K. Ingenerid, S. Littmanna, Improved isotopic sims measurements of uranium particles for nuclear safeguard purposes, J. Anal. At. Spectrom 24 (2009) 277–287.

[20] M. May, R. Abedin-Zadeh, D. Barr, A. Carnesale, P. Coyle, J. Davis, W. Dorland, W. Dunlop, S. Fetter, A. Glaser, et al., Nuclear forensics. role, state of the art, program needs (2008).

[21] J. Fassett, J. Travis, Analytical applications of resonance ionization mass spectrometry (rims), Spectrochimica Acta Part B: Atomic Spectroscopy 43 (12) (1988) 1409–1422.

[22] J. Fassett, L. Moore, J. Travis, J. DeVoe, Laser resonance ionization mass spectrometry, Science 230 (1985) 262–267.

[23] CONF-840449-10, Oak Ridge National Lab., TN (USA), Assessment of resonance ionization mass spectrometry for analytical chemistry and spectroscopy.

[24] Z. Ma, R. Thompson, K. Lykke, M. Pellin, A. Davis, New instrument for microbeam analysis incorporating submicron imaging and resonance ionization mass spectrometry, Rev. Sci. Instrum. 66 (1995) 3168.

[25] D. Donohue, J. Young, D. Smith, Spectral studies of actinide elements by resonance ionization mass spectrometry, Appl. Spectrosc. 39 (1) (1985) 93–97.

[26] J. Blaise, J. Wyart, Energy levels and atomic spectra of actinides, Tables Internationales de Constantes, 1992.
URL http://www.lac.u-psud.fr/Database/Contents.html

[27] J. Blaise, L. Radziemski Jr, Energy levels of neutral atomic uranium (ui), J. Opt. Soc. Am 66 (7) (1976) 644–659.

[28] D. Donohue, D. Smith, J. Young, H. McKown, C. Pritchard, Isotopic analysis of uranium and plutonium mixtures by resonance ionization mass spectrometry, Anal. Chem. 56 (1984) 379–381.

[29] L. Green, F. Sopchyshyn, Quantification of uranium isotopes by multiphoton ionization time-of-flight mass spectrometry, Int. J. Mass Spectrom. Ion Processes 89 (1) (1989) 81–95.

[30] N. Erdmann, M. Betti, F. Kollmer, A. Benninghoven, C. Gruning, V. Philipsen, P. Lievens, R. E. Silverans, E. Vandeweert, Resonance and nonresonant laser ionization of sputtered uranium atoms from thin films and single microparticles: Evaluation of a combined system for particle trace analysis, Anal. Chem. 75 (13) (2003) 3175–3181.
URL http://dx.doi.org/10.1021/ac0264426

[31] D. Goeringer, W. Christie, R. Valiga, Investigation of matrix effects on the neutral fractions ejected from ion-bombarded, uranium-containing solids using resonance ionization mass spectrometry, Anal. Chem. 60 (4) (1988) 345–349.

[32] S. L. Ziegler, B. A. Bushaw, Ultratrace uranium fingerprinting with isotope selective laser ionization spectrometry, Anal. Chem. 80 (15) (2008) 6029–6033.

[33] R. Wunderlich, G. Wasserburg, I. Hutcheon, G. Blake, Systematics of the odd-even effect in the resonance ionization of os and ti, Conference Series - Institute of Physics 128 (1992) 127–127.

[34] A. Maitland, M. Dunn, Laser physics, Out-of-Print Books on Demand/UMI, UMI, 1992.
URL http://books.google.com/books?id=dhYxQAAACAAJ

[35] M. Payne, S. Allman, J. Parks, Effect of hyperfine structure on ionization efficiencies in stepwise ionization using broad bandwidth lasers, Spectrochim. Acta, Part B 46 (11) (1991) 1439–1457.

[36] P. Lambropoulos, A. Lyras, Theory of resonant ionization by broad-band radiation in the determination of isotopic abundances, Physical Review A 40 (4) (1989) 2199–2202.

[37] I. Rabi, Space quantization in a gyrating magnetic field, Physical Review 51 (8) (1937) 652–654.

[38] M. G. Hurst, G. S. Payne, Principles and Applications of Resonance Ionisation Spectroscopy, A. Hilger, 1988.

[39] M. Payne, L. Deng, N. Thonnard, Applications of resonance ionization mass spectrometry, Rev. Sci. Instrum. 65 (1994) 2433–2459.

[40] X. Huang, Y. Yung, A common misunderstanding about the voigt line profile, Journal of the Atmospheric Sciences 61 (13) (2004) 1630–1632.

[41] S. N. Dixit, P. Lambropoulos, Theory of photoelectron angular distributions in resonant multiphoton ionization, Phys. Rev. A 27 (2) (1983) 861–.
URL http://link.aps.org/abstract/PRA/v27/p861

[42] A. Coste, R. Avril, P. Blancard, J. Chatelet, D. Lambert, J. Legre, S. Liberman, J. Pinard, New spectroscopic data on high-lying excited levels of atomic uranium, J. Opt. Soc. Am 72 (1982) 103–109.

[43] V. Letokhov, Laser photoionization spectroscopy, Academic Press, 1987.
URL http://books.google.com/books?id=dOXvAAAAMAAJ

[44] W. Fairbank Jr, A seat-of-the pants approach to ris theory, in: AIP Conference Proceedings, Vol. 388, 1997, p. 457.

[45] P. Lambropoulos, Topics on Multiphoton Processes in Atoms, Elsevier, 1976.

[46] G. Janes, I. Itzkan, C. Pike, R. Levy, L. Levin, Two-photon laser isotope separation of atomic uranium: spectroscopic studies, excited-state lifetimes, and photoionization cross sections, IEEE J. Quant. Electron.;(United States) QE-12 (1976) 111–120.

[47] U. Fano, Effects of configuration interaction on intensities and phase shifts, Physical Review 124 (6) (1961) 1866–1878.

[48] U. Fano, J. Cooper, Line profiles in the far-uv absorption spectra of the rare gases, Phys. Rev. 137 (5A) (1965) 1364–1379.

[49] G. Bekov, V. Letokhov, O. Matveev, V. Mishin, Observation of a long-lived autoionization state in the spectrum of the gadolinium atom, JETP Lett. 28 (1978) 283–285.

[50] P. Lambropoulos, P. Zoller, Autoionizing states in strong laser fields, Phys. Rev. A 24 (1) (1981) 379–397.

[51] P. Schumann, K. Wendt, B. Bushaw, High-resolution triple-resonance autoionization of uranium isotopes, Spectrochim. Acta, Part B 60 (11) (2005) 1402–1411.
URL http://www.sciencedirect.com/science/article/B6THN-4H9990T-2/2/c9eb03295df71a49e8f9a6a67f7e2852

[52] W. Childs, O. Poulsen, L. Goodman, High-precision measurement of 235u ground-state hyperfine structure of laser-rf double resonance, Opt. Lett 4 (1979) 4–1.

[53] L. Balling, J. Wright, Use of angular-momentum selection rules for laser isotope separation, Appl. Phys. Lett. 29 (1976) 411.

[54] D. Suter, The physics of laser-atom interactions, Cambridge studies in modern optics, Cambridge University Press, 1997.
URL http://books.google.com/books?id=NySULTHe3PwC

[55] A. Edmonds, Angular momentum in quantum mechanics, Princeton landmarks in mathematics and physics, Princeton University Press, 1996.
URL http://books.google.com/books?id=0BSOg0oHhZ0C

[56] A. Lyras, B. Zorman, P. Lambropoulos, Theory of doubly resonant ionization by broad-band radiation applied to the determination of isotopic abundances, Phys. Rev. A 42 (1) (1990) 543–.
URL http://link.aps.org/abstract/PRA/v42/p543

[57] W. Fairbank Jr, M. Spaar, J. Parks, J. Hutchinson, Anomalous odd-to even-mass isotope ratios in resonance ionization with broad-band lasers, Physical Review A 40 (4) (1989) 2195–2198.

[58] R. Wunderlich, I. Hutcheon, G. Wasserburg, G. Blake, Laser-induced isotopic selectivity in the resonance ionization of os, Int. J. Mass Spectrom. Ion Processes 115 (2-3) (1992) 123–155.

[59] M. Thompson, The velocity distribution of sputtered atoms, Nuclear Instruments and Methods in Physics Research Section B: Beam Interactions with Materials and Atoms 18 (1-6) (1986) 411–429.

[60] F. Lama, J. Strain, P. Townsend, D. Bolus, D. Mapper, Energy and angular distribution of ar sputtered uo 2, Radiat. Eff. Defects Solids 99 (1) (1986) 301–311.

[61] N. Shimizu, S. R. Hart, Isotope fractionation in secondary ion mass spectrometry, J. Appl. Phys. 53 (3) (1982) 1303–1311.
URL http://link.aip.org/link/?JAP/53/1303/1

[62] V. Shutthanandan, J. Zhang, P. Ray, Energy and mass dependence of isotopic enrichment in sputtering, Applied Physics A: Materials Science & Processing 76 (7) (2003) 1093–1097.

[63] W. Demtroder, Atoms, Molecules and Photons: An Introduction to Atomic- Molecular- and Quantum Physics, Graduate Texts in Physics, Springer, 2010.
URL http://books.google.com/books?id=vbc5mA7OEuYC

[64] D. Mills, Nonlinear optics: basic concepts, Springer-Verlag, 1991.
URL http://books.google.com/books?id=7M3vAAAAMAAJ

[65] A. Schawlow, C. Townes, Infrared and optical masers, Physical Review 112 (6) (1958) 1940–1949.

[66] I. Veryovkin, W. Calaway, M. Pellin, Ion optics of a new time-of-flight mass spectrometer for quantitative surface analysis, Nucl. Instrum. Methods Phys. Res., Sect. A 519 (1-2) (2004) 353–362.

[67] J. Wiza, et al., Microchannel plate detectors, Nucl. Instrum. Methods 162 (1-3) (1979) 587–601.

[68] A. K. Ray, V. K. Mago, B. Lal, P. R. K. Rao, New odd-parity rydberg and autoionization levels in uranium i, J. Opt. Soc. Am. B 7 (2) (1990) 145–151.
URL http://josab.osa.org/abstract.cfm?URI=josab-7-2-145

[69] M. Miyabe, M. Oba, I. Wakaida, Highly excited odd-parity levels of atomic uranium, Journal of Physics - London-B Atomic Molecular and Optical Physics 33 (21) (2000) 4957–4972.

[70] M. Smyth, L. Green, F. Sopchyshyn, P. Leeson, Identification of new high-lying odd energy levels of uranium by resonance ionization mass spectrometry, J. Phys. B: At., Mol. Opt. Phys. 24 (1991) 4887.

[71] E. Miron, R. David, G. Erez, S. Lavi, L. A. Levin, Laser spectroscopy of u i using stepwise excitation and fluorescence detection, J. Opt. Soc. Am. 69 (2) (1979) 256–264.
URL http://www.opticsinfobase.org/abstract.cfm?URI=josa-69-2-256

[72] T. Stephan, J. Zehnpfenning, A. Benninghoven, Correction of dead time effects in time-of-flight mass spectrometry, J. Vac. Sci. Technol., A 12 (1994) 405.

[73] W. Siekhaus, A. Nelson, The optical properties of a polished uranium surface and its epitaxial oxide, and the rate of oxide growth determined by spectrophotometry, Actinides 2005- Basic Science, Applications and Technology 893 (2005) 349–355.

[74] F. Capone, Y. Colle, J. Hiernaut, C. Ronchi, Mass spectrometric measurement of the ionization energies and cross sections of uranium and plutonium oxide vapors, J. Phys. Chem. A 103 (50) (1999) 10899–10906.

[75] S. Senanayake, G. Waterhouse, A. Chan, T. Madey, D. Mullins, H. Idriss, Probing surface oxidation of reduced uranium dioxide thin film using synchrotron radiation, The Journal of Physical Chemistry C 111 (22) (2007) 7963–7970.

[76] R. Wunderlich, I. Hutcheon, G. Wasserburg, G. Blake, Systematics of isotope ratio measurements with resonant laser photoionization sources, Applied Spectroscopy in Materials Science 11 1636 (1992) 211.

[77] R. Eichler, S. Hubener, N. Erdmann, K. Eberhardt, H. Funk, G. Herrmann, S. Kohler, N. Trautmann, G. Passler, F. Urban, An atomic beam source for actinide elements: Concept and realization, Radiochim. Acta 79 (4) (1997) 221–233.

[78] M. Nunnemann, N. Erdmann, H. Hasse, G. Huber, J. Kratz, P. Kunz, A. Mansel, G. Passler, O. Stetzer, N. Trautmann, et al., Trace analysis of plutonium in environmental samples by resonance ionization mass spectroscopy (rims), J. Alloys Compd. 271 (1998) 45–48.

[79] K. B. Knight, M. R. Savina, B. H. Isselhardt, I. D. Hutcheon, S. G. Prussin, M. J. Pellin, Uranium resonance ionization mass spectrometry in natural u silicate, in press,, Radiochim. Acta.

[80] B. W. Shore, M. A. Johnson, Effects of hyperfine structure on coherent excitation, Phys. Rev. A 23 (4) (1981) 1608–.
URL http://link.aps.org/abstract/PRA/v23/p1608

[81] M. R. Savina, D. G. Willingham, Unpublished results (2011).

[82] J. Levine, M. Savina, T. Stephan, M. Pellin, Improvements in rims isotopic precision: Application to in situ atom-limited analyses, 4th Int. Conf. on Laser Probing - LAP 2008 1104 (2009) 90–95.

[83] G. Nicolussi, M. Pellin, K. Lykke, J. Trevor, D. Mencer, A. Davis, Surface analysis by snms: Femtosecond laser postionization of sputtered and laser desorbed atoms, Surf. Interface Anal. 24 (6) (1996) 363–370.

Appendix A

Experimental Parameters

This appendix provides a quick access to the details of experiments described in this dissertation. The table includes the experiments in order as introduced in the text along with the relevant experimental parameters. The included columns are:

- The number used to reference this experiment in the text.

Name - A short description of the experimental result, typically describing the variable studied.

Date - Date experiment was performed

Target - Interrogated sample: U500, CRM 125-A, or SRM 960.

Pulses - Number of acquisition cycles of the instrument, usually defined as number of laser pulses or desorption events.

WavelengthX - Wavelength of laser X in order of excitation, in nm.

BX - Bandwidth of laser X, in pm. Laser 3 was always generated using a 40x beam expander, so the bandwidth is 1.3 GHz or 2.2 pm at 722.2 nm.

PowerX - Power of laser X in mW.

Instrumental - Other relevant instrumental parameters which are important to the result. Usually ion gun parameters such as primary ion current, aperture size, and raster area. LX: refers to the vertical and horizontal elliptical diameters of the Xth laser beam.

Other - Notes for other parameters not included in table.

#	Name	Date	Target	Pulses	λ_1	B1	λ_2
1	On Resonance Mass Spectrum	8/21/09	U500	10^5	415.5105	~ 5	829.089
2	Off Resonance Mass Spectrum	“	“	“	415.561	“	“
3	Dark Counts	6/28/08	-	$2 \cdot 10^5$	-	-	-
4	SIMS Eject On/Off	8/21/09	U500	10^5	-	-	-
5	Laser Combinations: Off Res.	2/11/09	960	10^5	418.007	1	829.091
6	1-color Off Resonance	2/11/09	960	10^5	417.757	1	NO
7	Sputter Rates: U500	05/26/09	U500	10^5	415.5105	5	829.089
8	Sputter Rates: CRM 125A	05/28/09	125A	10^5	415.5105	5	829.089
9	Ratio vs. Wavelength: Narrow	6/28/08	960	10^5	Range	1	829.089
10	Ratio vs. Wavelength: Broad	7/03/08	960	10^5	Range	5	829.089
11	Second Resonance 235	2/09/09	960	$4 \cdot 10^4$	415.507	1	Range
12	Second Resonance 238	6/30/09	960	$1.5 \cdot 10^5$	415.514	1	Range
13	2nd Res. Wavelength-Broad	5/19/09	U500	10^5	415.5105	5	Range
14	Third Res. Wavelength 238	2/08/09	960	$4 \cdot 10^4$	415.514	1	829.091
15	Third Res. Detail Scan 238	2/09/09	960	$4 \cdot 10^4$	415.514	1	829.091
16	Third Res. Detail Scan 235	2/09/09	960	$4 \cdot 10^4$	415.507	1	829.087
17	Power of 1st Laser -Narrow	7/01/08	960	$1.5 \cdot 10^5$	415.507	1	829.09
18	Power of 1st Laser -Broad	9/19/10	U500	$5 \cdot 10^4$	415.5105	5	829.089
19	Power of 2nd Laser -Narrow	7/01/08	960	$1.5 \cdot 10^5$	415.507	1	829.087
20	Power of 2nd Laser -Broad	9/19/10	U500	$5 \cdot 10^4$	415.5105	5	829.089
21	Power of 3rd Laser -Narrow	7/01/08	960	$1.5 \cdot 10^5$	415.507	1	829.09
22	Power of 3rd Laser -Broad	9/19/10	U500	$5 \cdot 10^4$	415.5105	5	829.089
23	Power of 2nd Laser, no 3rd	9/19/10	U500	$5 \cdot 10^4$	415.5105	5	829.089
24	LaserPath - 532 nm	6/26/08	960	$2 \cdot 10^5$	415.514	1	829.091
25	2-color, 2-photon Scheme	08/31/07	960	$2 \cdot 10^5$	436.328	1	367.798
26	Var. Enrichments-CRM125A	2/26/09	125A	10^5	415.5105	5	829.089
27	Var. Enrichments-SRM 960	2/12/09	960	$4 \cdot 10^5$	415.5105	5	829.089
28	Oxide Isotope Ratios	2/27/09	U500	10^5	415.5105	5	829.089
29	Laser 2 Relative Position	05/20/09	U500	10^5	415.5015	5	829.089
30	Isotopically Selective Ratio	2/12/09	960	10^5	415.5105	5	829.089
31	Ratios on U500	2/27/09	U500	10^5	415.5105	5	829.089
32	Ratios: U010, U500, & U970	10/28/09	Range	10^5	415.5105	5	829.089

#	B2	λ_3	Power 1	Power 2	Power 3	Instrumental	Other
1	9(2)	722.200	75	650	500	3.8μA, 20×20 μm	grainC_2:2
2	“	“	“	“	“	“	OffRes:3
3	-	-	-	-	-	Detector Noise Only	-
4	-	-	-	-	-	3.8μA, 20×20 μm	-
5	3	722.202	210	710	610	3.0μA, 50×50 μm	2/12/09
6	-	NO	Range	NO	NO	30 μm , 3 μA	
7	8	722.200	75	480	620	300 μm, 20 μm, 3.5 μA	Gold-coat
8	8	722.200	80	651	647	300 μm, 20 μm, 3.5 μA	
9	3	722.344	150	900	540	Off-Res = 2.7(2) %	
10	3	722.344	75	900	600	Off-Res = 1.0(1) %	See log
11	3	722.202	200	825	610	10 × 10 μm	Analog
12	3	722.344	150	910	470		Digital
13	8	722.200	120	565	590	19 μm , 3.7 μA	
14	3	Range	130	790	630	10 × 10 μm	Analog
15	3	Range	190-170	805	630	“	Analog
16	3	Range	200	805	610	“	Analog
17	3	722.344	0-180	920	550	L1: 1.38(2)×1.20(2) mm	
18	6	722.202	Range	640	950	L1: 1.50(1)×0.90(1) mm	
19	3	722.344	150	98-920	540	L2: 1.60(5)×1.40(5) mm	
20	6	722.202	315	Range	950	L2: 1.18(1)×1.01(1) mm	
21	3	722.344	150	920	12-540	L3: 1.80(5)×3.2(1) mm	
22	6	722.202	315	640	Range	L3: 1.40(1)×1.01(1) mm	
23	6	-	310	Range	-		
24	3	532	150	900	2100		
25	1	N/A	18	230	N/A	Desorption via Nd:YAG	
26	3	722.2	75	780	620	4.1μA	
27	3	722.2	75	780	610	Exp.#4:1,4,7,10	
28	3	722.2	75	725	510	300 ns, 20μm, 2.0-5.0 μA	
29	6	722.200	75	480	620	20μm, 4.6μA	
30	3	722.2	75	780	610		
31	3	722.2	75	725	510	300 ns, 20μm, 2.0-5.0 μA	
32	6	722.202	190	590	570	3.0 μA, 10 × 10 μm	

Appendix B

Isotope Ratio Model Code

This appendix contains the MATLAB code for our rate equation model of relative ionization probability of uranium isotopes. The code, as presented, is arranged for the simplest stochastic calculations, options included for other model parameters (such as using an empirical laser lineshape) are included in the code as comments (anything following a % sign is a comment in the code).

The file structure is as follows:

1. Isotopestatsbuilder.m
    (a) fconv.m
    (b) transitionsfirst.m (-second, -third)
        i. hyperfinecomponents.m
    (c) CG1.m (-2, -3)
        i. ClebschGordan.m
            A. Wigner3j.m
2. IRmeans.m
3. IRrand.m
4. odesolver1.m
5. laserparams.m
6. Stochastic Sampling:
    (a) timefetch.m
    (b) wavelengthfetch.m

B.1 Isotopestatsbuilder.m

```
function isotopestatsbuilder

   %Specify the parameters of the isotopes of interest.
   %234, 235, 236 and 238.
   % Si refers to cross section of resonance i,...
   % gi is the degeneracy of the level (# of states in level).
   %% % Build Profiles for these isotopes % %%
   m=1;
   wb = waitbar(0,'Please wait...');
   for isoS = [235,238,234,236];
   isoA = isoS;
```

```
%% % Integration Range and Delta step-size must match IR.m %%%
%These are stored and can be read directly into IR.m%
DeltaWavelength1=0.0000004;
DeltaWavelength2=0.0000005;
DeltaWavelength3=0.0001;
% For middle sum use:
P=[415.410+(DeltaWavelength1/2):DeltaWavelength1:415.630...
-(DeltaWavelength1/2)];
Q=[829.059+(DeltaWavelength2/2):DeltaWavelength2:829.130...
-(DeltaWavelength2/2)];
R=[722.000+(DeltaWavelength3/2):DeltaWavelength3:722.400...
-(DeltaWavelength3/2)];
J1=6; J2=7; J3=8; J4=8;
Sioncont=1e-20;
%% %% Start Isotope Parameters %%%%
if isoA == 235,
% Angular Momentum Vectors
I=7/2;
% Degeneracy of Excited States (2J+1)*(2I+1)
g1=104; g2=120; g3=136; g4=136;
% Centroid of Resonances
L1 = 415.5068; L2 = 829.087; L3 = 722.200;
% FWHM Natural Width of Resonance for Lorentzian [nm]
Gamma1 = 0.0000016; Gamma2 = 0.0000017; Gamma3 = 0.052;
% FWHM Width of Resonance for Gaussian based on Doppler of 4kK [nm]
band1 = 0.00205; band2 = 0.00408; band3 = 0.00357;
elseif isoA == 238,
% Angular Momentum Vectors
I=0;
% Degeneracy of Excited States (2J+1)*(2I+1)
g1=13; g2=15; g3=17; g4=17;
% Centroid of Resonances
L1 = 415.514; L2 = 829.091; L3 = 722.200;
% FWHM Natural Width of Resonance for Lorentzian [nm]
Gamma1 = 0.0000016; Gamma2 = 0.0000017; Gamma3 = 0.052;
% FWHM Width of Resonance for Gaussian based on Doppler of 4kK [nm]
band1 = 0.00205; band2 = 0.00408; band3 = 0.00357;
elseif isoA == 234,
% Angular Momentum Vectors
I=0;
% Degeneracy of Excited States (2J+1)*(2I+1)
g1=13; g2=15; g3=17; g4=17;
% Centroid of Resonances
L1 = 415.5054; L2 = 829.086; L3 = 722.200;
```

```
% FWHM Natural Width of Resonance for Lorentzian [nm]
Gamma1 = 0.0000016; Gamma2 = 0.0000017; Gamma3 = 0.052;
% FWHM Width of Resonance for Gaussian based on Doppler of 4kK [nm]
band1 = 0.00205; band2 = 0.00408; band3 = 0.00357;
elseif isoA == 236,
% Angular Momentum Vectors
I=0;
% Degeneracy of Excited States (2J+1)*(2I+1)
g1=13; g2=15; g3=17; g4=17;
% Centroid of Resonances
L1 = 415.509; L2 = 829.088; L3 = 722.200;
% FWHM Natural Width of Resonance for Lorentzian [nm]
Gamma1 = 0.0000016; Gamma2 = 0.0000017; Gamma3 = 0.052;
% FWHM Width of Resonance for Gaussian based on Doppler of 4kK [nm]
band1 = 0.00205; band2 = 0.00408; band3 = 0.00357;
else disp ('Not a U isotope');
end
%% %%%%%%% Build Resonance Profiles %%%%%%%%%%
%% Sigma for Gaussian distribution (S_b)
B1 = band1/(2*sqrt(2*log(2)));
B2 = band2/(2*sqrt(2*log(2)));
B3 = band3/(2*sqrt(2*log(2)));
%% Peak Cross Section - Normalization Factors [cm^2]%%%
F1 = (1/4)*(L1*1e-7)^2*(Gamma1/DeltaWavelength1);
F2 = (1/4)*(L2*1e-7)^2*(Gamma2/DeltaWavelength2);
F3 = (1/4)*(L3*1e-7)^2*(Gamma3/DeltaWavelength3);
%Build resonance arrays by convolution of Lorentzians and Gaussian
%% 1st Resonance Profile
if I==0
S2a = zeros(1,length(P));
S2b = zeros(1,length(P));
for j = 1:length(P)
S2a(j) = (DeltaWavelength1/(2*pi))*...
(Gamma1/((P(j)-L1)^2+(Gamma1/2)^2));
S2b(j) = (DeltaWavelength1/sqrt(2*pi*B1^2))*...
exp(-((P(j)-L1).^2/(2*B1^2)));
% S2b(j)= (DeltaWavelength1/(2*pi))*...
(band1/((P(j)-L1)^2+(band1/2)^2));
end
% Fast convolve (fconv.m) , can use Matlab's...
%built-in conv.m using conv(),but its slower!
S2c = fconv(S2a,S2b);
% Multiply Lineshape by Peak Cross Section %
S2d = F1*S2c;
```

```
% Set a cutoff so the cross section doesn't go to 10^-200!%
CS1 = 1e-10*max(S2d);
S2 = CS1*(S2d<CS1)+S2d.*(S2d>CS1);
else
% For odd isotopes when I!=0 %
% Call for number of transitions (modes1) and the shift in energy
for each and then call for the Clebsch-Gordan coefficients (CG1)
[modespacing1 modes1]= transitionsfirst;
modesB1 = CG1;
% Initialize Arrays fpr Building Cross Section
% Build as convolution of the sum of natural linewidths...
% and a single gaussian
S2m = zeros(modes1,length(P));
S2n = zeros(1,length(P));
S2a = zeros(1,(2*length(P)-1));
% Build each mode cross section and doppler profile, then convolve.
for j = 1:length(P)
for i=1:modes1
S2m(i,j) = modesB1(i)*(DeltaWavelength1/(2*pi))...
*(Gamma1/((P(j)-(L1+modespacing1(i)))^2+(Gamma1/2)^2));
end
S2n(j) = (DeltaWavelength1/sqrt(2*pi*B1^2))...
*exp(-(P(j)-L1).^2/(2*B1^2));
end
S2o=sum(S2m,1);
S2a = fconv(S2o,S2n);
S2b = S2a/((2*J1+1)*(2*I+1));
% Multiply Cross Section Lineshape by Peak Cross Section
S2d = F1*S2b;
CS1 = 1e-10*max(S2d);
S2 = CS1*(S2d<CS1)+S2d.*(S2d>CS1);
end
%% Build 2nd Resonance Profile
if I==0
S3a = zeros(1,length(Q)); S3b = zeros(1,length(Q));
for k = 1:length(Q)
S3a(k) = (DeltaWavelength2/(2*pi))...
*(Gamma2/((Q(k)-L2)^2+(Gamma2/2)^2));
S3b(k) = (DeltaWavelength2/sqrt(2*pi*B2^2))...
*exp(-((Q(k)-L2).^2/(2*B2^2)));
end
S3c = fconv(S3a,S3b);
S3d = F2*S3c;
CS2 = 5e-7*max(S3d);
```

```
S3 = CS2*(S3d<CS2)+S3d.*(S3d>CS2);
else
% For odd isotopes when I!=0 %
[modespacing2 modes2]= transitionssecond;
modesB2 = CG2;
% Initialize Arrays
S3m = zeros(modes2,length(Q));
S3n = zeros(1,length(Q));
S3a = zeros(1,(2*length(Q)-1));
for k = 1:length(Q)
for i2=1:modes2
S3m(i2,k)= modesB2(i2)*(DeltaWavelength2/(2*pi))*...
(Gamma2/((Q(k)-(L2+modespacing2(i2)))^2+(Gamma2/2)^2));
end
S3n(k) = (DeltaWavelength2/sqrt(2*pi*B2^2))...
*exp(-(Q(k)-L2).^2/(2*B2^2));
end
S3o = sum(S3m,1);
S3a=fconv(S3o,S3n);
S3b = S3a/((2*J2+1)*(2*I+1));
S3d = F2*S3b;
CS2 = 5e-7*max(S3d); %3e-17
S3 = CS2*(S3d<CS2)+S3d.*(S3d>CS2);
end
%% Build 3rd Resonance Profile
if I==0
Siona = zeros(1,length(R)); Sionb = zeros(1,length(R));
for l = 1:length(R)
Siona(l) = (DeltaWavelength3/(2*pi))...
*(Gamma3/((R(l)-L3)^2+(Gamma3/2)^2));
Sionb(l) = (DeltaWavelength3/sqrt(2*pi*B3^2))...
*exp(-((R(l)-L3).^2/(2*B3^2)));
end
Sionc = fconv(Siona,Sionb);
Siond = F3*Sionc*1.4e-9;
Sion = Siond+Sioncont;
else % For odd isotopes, when I!=0 %
[modespacingion modesion]= transitionsthird;
modesBion = CG3;
Sionm = zeros(modesion,length(R));
Sionn = zeros(1,length(R));
Siona = zeros(1,(2*length(R)-1));
for l = 1:length(R)
for i3=1:modesion
```

```
Sionm(i3,l)= modesBion(i3)*(DeltaWavelength3/(2*pi))*...
(Gamma3/((R(l)-(L3+modespacingion(i3)))^2+(Gamma3/2)^2));
end
Sionn(l) = (DeltaWavelength3/sqrt(2*pi*B3^2))...
*exp(-(R(l)-L3).^2/(2*B3^2));
end
Siono = sum(Sionm,1);
Siona = fconv(Siono,Sionn);
Sionb = Siona/((2*J3+1)*(2*I+1));
Siond = F3*Sionb*1.4e-9;
Sion = Siond+Sioncont;
end
%% % Save Resonance Parameters as UisoA.mat...
%in folder 'Uresonances' % %%
SAVEPATH=strcat(pwd,filesep,'Uresonances');
SAVEFILENAME=strcat(SAVEPATH,filesep,['U',num2str(isoA),'.mat']);
save (SAVEFILENAME, 'g1', 'g2', 'g3', 'g4', 'S2', 'S3', 'Sion')
m=m+1;
waitbar(m/length(isoS),wb)
end
SAVEPATH=strcat(pwd,filesep,'Uresonances');
SAVEFILENAME=strcat(SAVEPATH,filesep,'Uwavelengths.mat');
save(SAVEFILENAME,'DeltaWavelength1','DeltaWavelength2',...
'DeltaWavelength3','P','Q','R')
close(wb);
end
```

B.1.1 fconv.m

```
function [y]=fconv(x, h)

   %FCONV Fast Convolution
   % [y] = FCONV(x, h) convolves x and h, and normalizes the output
   % to +-1.
   %
   % x = input vector
   % h = input vector
   %
   % See also CONV
   %
   % NOTES:
   %% 1) I have a short article explaining what a convolution is.  It
   % is available at http://stevem.us/fconv.html.
   %
```

```
%Version 1.0
%Coded by:  Stephen G. McGovern, 2003-2004.
Ly=length(x)+length(h)-1; %
Ly2=pow2(nextpow2(Ly)); % Find smallest power of 2 that is > Ly
X=fft(x, Ly2); % Fast Fourier transform
H=fft(h, Ly2); % Fast Fourier transform
Y=X.*H; %
y=real(ifft(Y, Ly2)); % Inverse fast Fourier transform
y=y(1:1:Ly); % Take just the first N elements
%y=y/max(abs(y)); % Normalize the output
```

B.1.2 transitionsfirst.m (-second, -third)

```
function [Transitions,NumberofTransitions]=transitionsfirst

% I=7/2; J_GS=6; J_ES=7;
GS = [5/2 7/2 9/2 11/2 13/2 15/2 17/2 19/2];
E1S = [7/2 9/2 11/2 13/2 15/2 17/2 19/2 21/2];
GS_E = Hyperfinecomponents(0,415.510);
E1S_E = Hyperfinecomponents(1,415.510);
T=length(GS);
for i=2:T %dF=-1,0,+1
TransitionF0(i-1) = E1S_E(i-1)-(GS_E(i));
end
for j=3:T
TransitionFneg1(j-2)= E1S_E(j-2)-GS_E(j);
end
for k=1:T
TransitionFpos1(k)= E1S_E(k)-GS_E(k);
end
Transitions= [TransitionF0 TransitionFneg1 TransitionFpos1];
NumberofTransitions=length(Transitions);


function [Transitions,NumberofTransitions]=transitionssecond

% I=7/2; J_E1S=7; J_E2S=8;
E1S = [7/2 9/2 11/2 13/2 15/2 17/2 19/2 21/2];
E2S = [9/2 11/2 13/2 15/2 17/2 19/2 21/2 23/2];
E1S_E = Hyperfinecomponents(1,829.09);
E2S_E = Hyperfinecomponents(2,829.09);
T=length(E1S);
for i=2:T %dF=-1,0,+1
TransitionF0(i-1) = E2S_E(i-1)-(E1S_E(i));
end
```

```
   for j=3:T
   TransitionFneg1(j-2)= E2S_E(j-2)-E1S_E(j);
   end
   for k=1:T
   TransitionFpos1(k)= E2S_E(k)-E1S_E(k);
   end
   Transitions= [TransitionF0 TransitionFneg1 TransitionFpos1];
   NumberofTransitions=length(Transitions);


function [Transitions,NumberofTransitions]=transitionsthird

   % I=7/2; J_GS=8; J_ES=8;
   E2S = [9/2 11/2 13/2 15/2 17/2 19/2 21/2 23/2];
   E3S = [9/2 11/2 13/2 15/2 17/2 19/2 21/2 23/2];
   E2S_E = Hyperfinecomponents(2,722.2);
   E3S_E = Hyperfinecomponents(3,722.2);
   T=length(E2S);
   for i=1:T %dF=-1,0,+1
   TransitionF0(i) = E3S_E(i)-E2S_E(i);
   end
   for j=2:T
   TransitionFneg1(j-1)= E3S_E(j-1)-E2S_E(j);
   end
   for k=1:T-1
   TransitionFpos1(k)= E3S_E(k+1)-E2S_E(k);
   end
   Transitions= [TransitionF0 TransitionFneg1 TransitionFpos1];
   NumberofTransitions=length(Transitions);
```

B.1.3 Hyperfinecomponents.m

```
function [Efnm]=Hyperfinecomponents(S,lambda)

   %Hyperfinecomponents.m
   %Returns energy of individual hyperfine components...
   %for each level in state S in MHz relative to...
   %the isotope shift in order of increasing angular momentum.
   I = 3.5;
   if S==0
   J=6; dvis=0;
   A = -60.559; B=4104.15;
   elseif S==1
   J=7; dvis=12511.97;
   A = -108.172; B=2074.4;
```

```
elseif S==2
J=8; dvis=14913.8;
A = -105.639; B=3269.7;
elseif S==3
J=8; dvis=12880;
A = 60; B=4382.5;
end
F=J-I:J+I;
C=zeros(1,length(F));
Ef=zeros(1,length(F));
for f=1:length(F);
C(f) = (F(f)*(F(f)+1))-(I*(I+1))-(J*(J+1));
Aterm = A*C(f)/2;
Bterm = B*(3*C(f)*(C(f)+1)-(4*I*J*(I+1)*(J+1)))...
/(8*I*J*(2*J-1)*(2*I-1));
Ef(f)=Aterm+Bterm; %+dvis
end
c=2.997e8; %Speed of Light [m/s]
lambda1=lambda*1e-9;
Efm=-(Ef*1e6).*(lambda1^2/c);
Efnm=Efm*1e9;
```

B.1.4 CG1.m (-2, -3)

```
function [SCGcoefs]=CG1

GS = [5/2 7/2 9/2 11/2 13/2 15/2 17/2 19/2];
ES = [7/2 9/2 11/2 13/2 15/2 17/2 19/2 21/2];
T=length(ES);
% ClebschGordan(j1,j2,j,m1,m2,m) returns
% the Clebsch-Gordan coefficient
% <j1,j2,m1,m2|j1,j2,j,m>
%%% For linearly polarized light, where dm=0 %%%
%j1=GS;j=ES; j2=[0 -1 1];m1=-max:max m2=0; m=m1;
for ji=2:T %For dF=0, states =
mi=-1*ES(ji-1):ES(ji-1);
for i=1:length(mi)
CG1(ji-1,i)=ClebschGordan(GS(ji),0,ES(ji-1),mi(i),0,mi(i));
end
for jj=3:T %For dF=-1
mj=-1*ES(jj-2):ES(jj-2);
for j=1:length(mj)
CG2(jj-2,j)=ClebschGordan(GS(jj),1,ES(jj-2),mj(j),0,mj(j));
end
```

```
    for jk=1:T %For dF=+1
    mk=-1*GS(jk):GS(jk);
    for k=1:length(mk)
    CG3(jk,k)=ClebschGordan(GS(jk),1,ES(jk),mk(k),0,mk(k));
    end
    end
    end
    end
    CG1_2=CG1.^2;
    CG2_2=CG2.^2;
    CG3_2=CG3.^2;
    SCG1=sum(CG1_2,2);
    SCG2=sum(CG2_2,2);
    SCG3=sum(CG3_2,2);
    SCGcoefs=[SCG1' SCG2' SCG3'];


function [SCGcoefs]=CG2

    E1S = [7/2 9/2 11/2 13/2 15/2 17/2 19/2 21/2];
    E2S = [9/2 11/2 13/2 15/2 17/2 19/2 21/2 23/2];
    T=length(E2S);
    % ClebschGordan(j1,j2,j,m1,m2,m) returns the
    % Clebsch-Gordan coefficient
    % <j1,j2,m1,m2|j1,j2,j,m>
    %%% For linearly polarized light, where dm=0 %%%
    %j1=E1S;j=E2S; j2=[0 -1 1];m1=-max:max m2=0; m=m1;
    for ji=2:T %For dF=0, states =
    mi=-1*E2S(ji-1):E2S(ji-1);
    for i=1:length(mi)
    CG1(ji-1,i)=ClebschGordan(E1S(ji),0,E2S(ji-1),mi(i),0,mi(i));
    end
    for jj=3:T %For dF=-1
    mj=-1*E2S(jj-2):E2S(jj-2);
    for j=1:length(mj)
    CG2(jj-2,j)=ClebschGordan(E1S(jj),1,E2S(jj-2),mj(j),0,mj(j));
    end
    for jk=1:T %For dF=+1
    mk=-1*E1S(jk):E1S(jk);
    for k=1:length(mk)
    CG3(jk,k)=ClebschGordan(E1S(jk),1,E2S(jk),mk(k),0,mk(k));
    end
    end
    end
    end
```

```
    CG1_2=CG1.^2;
    CG2_2=CG2.^2;
    CG3_2=CG3.^2;
    SCG1=sum(CG1_2,2);
    SCG2=sum(CG2_2,2);
    SCG3=sum(CG3_2,2);
    SCGcoefs=[SCG1' SCG2' SCG3'];


function [SCGcoefs]=CG3

    E2S = [9/2 11/2 13/2 15/2 17/2 19/2 21/2 23/2];
    E3S = [9/2 11/2 13/2 15/2 17/2 19/2 21/2 23/2];
    T=length(E3S);
    % ClebschGordan(j1,j2,j,m1,m2,m) returns...
    % the Clebsch-Gordan coefficient
    % <j1,j2,m1,m2|j1,j2,j,m>
    %%% For linearly polarized light, where dm=0 %%%
    %j1=GS;j=ES; j2=[0 -1 1];m1=-max:max m2=0; m=m1;
    for ji=1:T %For dF=0, states =
    mi=-1*E3S(ji):E3S(ji);
    for i=1:length(mi)
    CG1(ji,i)=ClebschGordan(E2S(ji),0,E3S(ji),mi(i),0,mi(i));
    end
    for jj=2:T %For dF=-1
    mj=-1*E3S(jj):E3S(jj);
    for j=1:length(mj)
    CG2(jj-1,j)=ClebschGordan(E2S(jj),1,E3S(jj),mj(j),0,mj(j));
    end
    for jk=1:T-1 %For dF=+1
    mk=-1*E2S(jk):E2S(jk);
    for k=1:length(mk)
    CG3(jk,k)=ClebschGordan(E2S(jk),1,E3S(jk+1),mk(k),0,mk(k));
    end
    end
    end
    end
    CG1_2=CG1.^2;
    CG2_2=CG2.^2;
    CG3_2=CG3.^2;
    SCG1=sum(CG1_2,2);
    SCG2=sum(CG2_2,2);
    SCG3=sum(CG3_2,2);
    SCGcoefs=[SCG1' SCG2' SCG3'];
```

ClebschGordan.m

```
% ClebschGordan.m by David Terr, Raytheon, 6-17-04
% Modified on 11-9-04
% ClebschGordan(j1,j2,j,m1,m2,m) returns the Clebsch-Gordan
coefficient <j1,j2,m1,m2|j1,j2,j,m>.
% This program requires first downloading Wigner3j.m.
%For Linearly Polarized Light j2=1, m2=0;


function cg = ClebschGordan(j1,j2,j,m1,m2,m)

% error checking
if ( 2*j1 ~= floor(2*j1) || 2*j2 ~= floor(2*j2) || 2*j ~=...
floor(2*j) || 2*m1 ~= floor(2*m1) || 2*m2 ~=...
floor(2*m2) || 2*m ~= floor(2*m) )...
error('All arguments must be integers or half-integers.');
return;
end
if m1 + m2 ~= m
warning('m1 + m2 must equal m.');
cg = 0;
return;
end
if ( j1 - m1 ~= floor ( j1 - m1 ) )
warning('2*j1 and 2*m1 must have the same parity');
cg = 0;
return;
end
if ( j2 - m2 ~= floor ( j2 - m2 ) )
warning('2*j2 and 2*m2 must have the same parity');
cg = 0;
return;
end
if ( j - m ~= floor ( j - m ) )
warning('2*j and 2*m must have the same parity');
cg = 0;
return;
end
if j > j1 + j2 || j < abs(j1 - j2)
warning('j is out of bounds.');
cg = 0;
return;
end
if abs(m1) > j1
warning('m1 is out of bounds.');
```

```
cg = 0;
return;
end
if abs(m2) > j2
warning('m2 is out of bounds.');
cg = 0;
return;
end
if abs(m) > j
warning('m is out of bounds.');
cg = 0;
return;
end
cg = (-1)^(j1-j2+m) * sqrt(2*j + 1) * Wigner3j(j1,j2,j,m1,m2,-m);
% Reference:  Clebsch-Gordan Coefficient entry of Eric Weinstein's
% http://mathworld.wolfram.com/Clebsch-GordanCoefficient.html
% Mathworld:
% http://mathworld.wolfram.com/Clebsch-GordanCoefficient.html
```

Wigner3j.m

```
% Wigner3j.m by David Terr, Raytheon, 6-17-04
% Compute the Wigner 3j symbol using the Racah formula [1].


function wigner = Wigner3j(j1,j2,j3,m1,m2,m3)

% error checking if ( 2*j1 ~= floor(2*j1) || 2*j2 ~=...
floor(2*j2) || 2*j3 ~= floor(2*j3) || 2*m1 ~=...
floor(2*m1)|| 2*m2 ~= floor(2*m2) || 2*m3 ~= floor(2*m3) )...
error('All arguments must be integers or half-integers.');
return; end
if ( j1 - m1 ~= floor ( j1 - m1 ) ) error('2*j1 and 2*m1
must have the same parity'); return; end
if ( j2 - m2 ~= floor ( j2 - m2 ) ) error('2*j2 and 2*m2
must have the same parity'); return; end
if ( j3 - m3 ~= floor ( j3 - m3 ) ) error('2*j3 and 2*m3
must have the same parity'); return; end
if j3 > j1 + j2 || j3 < abs(j1 - j2) error('j3 is out of bounds.');
return; end
if abs(m1) > j1 error('m1 is out of bounds.'); return; end
if abs(m2) > j2 error('m2 is out of bounds.'); return; end
if abs(m3) > j3 error('m3 is out of bounds.'); return; end
t1 = j2 - m1 - j3; t2 = j1 + m2 - j3; t3 = j1 + j2 - j3;
t4 = j1 - m1; t5 = j2 + m2;
```

```
tmin = max( 0, max( t1, t2 ) ); tmax = min( t3, min( t4, t5 ) );
wigner = 0;
for t = tmin:tmax wigner = wigner + (-1)^t /
(factorial(t)*factorial(t-t1)*factorial(t-t2) ...
* factorial(t3-t) * factorial(t4-t) * factorial(t5-t) ); end
wigner = wigner * (-1)^(j1-j2-m3) ...
* sqrt( factorial(j1+j2-j3)...
* factorial(j1-j2+j3) * factorial(-j1+j2+j3)...
/ factorial(j1+j2+j3+1) * factorial(j1+m1) * factorial(j1-m1)...
* factorial(j2+m2) * factorial(j2-m2)...
* factorial(j3+m3) * factorial(j3-m3) );
% Reference:  Wigner 3j-Symbol entry of Eric Weinstein's
Mathworld:  http://mathworld.wolfram.com/Wigner3j-Symbol.html
```

B.1.5 IRmeans.m

```
clear Means
W1 = (415.480:0.0005:415.540);
mW = 1;
wb = waitbar(0,'Please wait...');
NarrowM=zeros(length(W1),5);
BroadM=zeros(length(W1),5);
Pn=150;
Pb=75;
b1 = 0.001;
b2 = 0.005;
its = 100;
for mW = 1:length(W1)
NarrowM(mW,1)= W1(mW);
[NarrowM(mW,2),NarrowM(mW,3),NarrowM(mW,4),NarrowM(mW,5)]=...
IRrand(W1(mW),its,Pn,b1,2);
BroadM(mW,1)= W1(mW);
[BroadM(mW,2),BroadM(mW,3),BroadM(mW,4),BroadM(mW,5)]=...
IRrand(W1(mW),its,Pb,b2,1);
waitbar(mW/length(W1),wb)
mW=mW+1;
end
figure(3);
plot(NarrowM(:,1),NarrowM(:,3),BroadM(:,1),BroadM(:,3));
set(gca,'YLimMode','auto','YScale', 'lin')
xlabel ('Wavelength [nm]')
ylabel ('U-235 Ionization Probability')
figure(4);
plot(NarrowM(:,1),NarrowM(:,4),BroadM(:,1),BroadM(:,4));
```

```
   set(gca,'YLimMode','auto','YScale', 'log')
   xlabel ('Wavelength [nm]')
   ylabel ('U-238 Ionization Probability')
   figure(5);
   plot(NarrowM(:,1),NarrowM(:,5),BroadM(:,1),BroadM(:,5));
   set(gca,'YLimMode','auto','YScale', 'log')
   xlabel ('Wavelength [nm]')
   ylabel ('U-235:U-238 Isotope Ratio')
   close (wb);
```

B.2 IRrand.m

```
function [W M5 M8 MR] = IRrand(W1,its,P1,B1,fetch1)

   %% IR.m generates a model isotope ratio of two uranium isotopes
   %using numerical integration of simple rate equations of motion
   %for the population of the specific atomic resonances used.
   %Files required IR.m, odesolver1.m, isotopestats.m,
   %and laserparams.m
   %Include folder of atomic resonances or call to isotopestats.m
   %%
   clear global
   global P Q R P2 Q2 R2 TSPAN POWER1 POWER2 POWER3
   TIME1 TIME2 TIME3 BAND1 BAND2 BAND3...
   FWHMS1A FrequencyL1 FrequencyL2 FrequencyL3
   DeltaWavelength1 DeltaWavelength2 DeltaWavelength3 %INTERP1
   %% ===============Configurable Parameters =============== %%
   %% Which Ratio?  (Iso1/Iso2)
   Iso1 = 235;
   Iso2 = 238;
   Abund1 = 0.49696;%0.0073;
   Abund2 = 0.4971;%0.9927;
   %% Integration Time Span
   TSPAN = [0 100];
   %% Ion Flight Ditributions
   % % Pulselength = 15 ns FWHM
   % pl1 = 20; pl2= 10;
   % % Sigma^2 of pulses
   % st1 = (pl1/2)^2/(2*log(2));st2 = (pl2/2)^2/(2*log(2));
   % % Time distribution of laser power
   % t1 = 1/(sqrt(2*pi*st))*exp(-(t-TIME1)^2/(2*st));
   % t2 = 1/(sqrt(2*pi*st))*exp(-(t-TIME2)^2/(2*st));
   %%Wavelength interval for isotopestats and laserparams
   % Load DeltaWavelength1,2,3 and P, Q, R from Uwavelengths.mat)
```

```
load('Uresonances\Uwavelengths.mat');
% if exist('DeltaWavelength1','var') == 0
%Or if not pre-running resonances:
% DeltaWavelength1=0.0000004;
% DeltaWavelength2=0.0000005;
% DeltaWavelength3=0.0001;
% P = (415.450:DeltaWavelength1:415.570);
% Q = (829.050:DeltaWavelength2:829.130);
% R = (722.000:DeltaWavelength3:722.400);
% end
P2 = (min(P):DeltaWavelength1/2:max(P));
Q2 = (min(Q):DeltaWavelength2/2:max(Q));
R2 = (min(R):DeltaWavelength3/2:max(R));
% Central Wavelength or Range for Iteration and Ratio:
% WAVE1 = 415.507;
WAVE1 = W1*ones(its);
% WAVE1= (415.480:0.0005:415.540);
WAVE2 = 829.089;
% WAVE2=(829.070:0.001:829.120);
WAVE3 = 722.200; %.200
%WAVE3=(722.100:0.05:722.300);
% Laser Powers [mW]
%Narrow Powers:150,900,540
%Broad Powers:75,900,600
%Typical Now:  75, 650, 510
%Power sat-0:180,920,550
Power1 = P1*17.58;
POWER2 = 900*17.58;
POWER3 = 540*17.58;
% Power1 = W1*ones(its);
% Laser Bandwidth:  (FWHM in nm)
Fwhm1 = B1;%0.005;%001;
Fwhm2 = 0.003;
Fwhm3 = 0.00225;
FWHMS1A = 0.000;
% Convert to pm for Graphs
pmfwhm1 = Fwhm1*1000;
% Time dependence of Laser Pulse peak at t=30 width = 15
time1 = 50*ones(10);
time2 = 50;
time3 = 50;
% Sigma for Laser Gaussians
BAND1 = Fwhm1/(2*sqrt(2*log(2)));
BAND2 = Fwhm2/(2*sqrt(2*log(2)));
```

```
BAND3 = Fwhm3/(2*sqrt(2*log(2)));
%%==========End Configurable Parameters ==============%%
%% Set up Outputs %%
% Make plots for each LaserCenterLine?  (NO=0, YES=1)
MakePlot=0;
% Save plots for each LaserCenterLine?  (NO=0, YES=1)
SavePlot=0;
% Allocate Output Matrix
OutputData=zeros(length(WAVE1)*length(WAVE2)*length(WAVE3)...
*length(Power1)*length(time1)*length(time2)*length(time3),10);
% Initialize Waitbar
m=1;
%wb = waitbar(0,'Please wait...');
%% Load Atomic Resonances %%
%%%% For on the fly resonances use these calls to
isotopestats.m for the atomic parameters%%
% [g1i g2i g3i g4i S2i S3i Sioni] = isotopestats(Iso1);
% [g1ii g2ii g3ii g4ii S2ii S3ii Sionii] = isotopestats(Iso2);
%%For pre-calculated resonances look in MATLAB/Umodel/Uresonance
folder for UXXX.mat files%%
Filename1=[pwd,filesep,'Uresonances',filesep,...
'U',num2str(Iso1),'.mat'];
Filename2=[pwd,filesep,'Uresonances',filesep,...
'U',num2str(Iso2),'.mat'];
load(Filename1);
g1i=g1; g2i=g2; g3i=g3; g4i=g4; S2i=S2; S3i=S3; Sioni=Sion;
load (Filename2);
g1ii=g1; g2ii=g2; g3ii=g3; g4ii=g4; S2ii=S2; S3ii=S3; Sionii=Sion;
%% Load Laser Lineshape Distribution %%
% Filename3=[pwd,filesep,'NarrowLaserLineshape','.mat'];
% load (Filename3);
% % For a fundamental laser lineshape
% % LaserAmp1 = NarrowLineshape;
% LaserAmp2 = NarrowLineshape;
% LaserAmp3 = NarrowLineshape;
% % For a frequency doubled amplitude
% DoubledLaserLine1= (NarrowLineshape).^2;
% % For a frequency-doubled Laser Lineshape
% LaserAmp1 = DoubledLaserLine1;
%%Interpolate Laser Lineshape for Laser 1 to have length ...
% of integration parameters
% % Laser Wavelength Index Range
% W1 = 1:length(P2);
% % Index Value of the middle of Integration Range
```

```
% LaserW1 = mean(W1);
% % Convert bandwidth to indexwidth of ...
%wavelength range [pm to nm to index]
% bandwidth1nm = (1000*Fwhm1*40.1);
% % Find index limits for drawing lineshape
% Laser1Plus = LaserW1 + (bandwidth1nm*(length(LaserAmp1)/2));
% Laser1Minus = LaserW1 - (bandwidth1nm*(length(LaserAmp1)/2));
% % Scale index values for Laser Lineshape Array onto...
%the wavelength scale.
% LW1=Laser1Minus:bandwidth1nm:Laser1Plus-1;
%-1 for integers, -0 for decimals
%Fill in the middle values of laser lineshape which have non-zero
%values over range defined by LW.
% INTERP1=interp1(LW1,LaserAmp1,W1);
% % Set any NaN's to zero
% for in=1:length(INTERP1)
% if isnan(INTERP1(in))==1
% INTERP1(in)=0;
% end
% end
% % Interpolated laser lineshape from empirical shape
% INTERP1=INTERP1/sum(INTERP1);
%% %% Iterate over Wavelength, Power, Time %% %%
for j=1:length(WAVE1)
for k=1:length(WAVE2)
for l=1:length(WAVE3)
for o=1:length(Power1)
for a=1:length(time1)
for b=1:length(time2)
for c=1:length(time3)
FrequencyL1 = WAVE1(j)+wavelengthfetch(fetch1);
%%%1 for Broad, 2 for Narrow
FrequencyL2 = WAVE2(k)+wavelengthfetch(1);
FrequencyL3 = WAVE3(l)+wavelengthfetch(1);
POWER1 = Power1(o);
TIME1 = time1(a)+timefetch;
TIME2 = time2(b)+timefetch;
TIME3 = time3(c)+timefetch;
OutputData(m,1)=FrequencyL1;
OutputData(m,2)=FrequencyL2;
OutputData(m,3)=FrequencyL3;
OutputData(m,4)=POWER1/17.58;
OutputData(m,5)=TIME1;
OutputData(m,6)=TIME2;
```

```
OutputData(m,7)=TIME3;
IONS1=odesolver1(Iso1,Abund1,g1i,g2i,g3i,g4i,S2i,S3i,Sioni);
OutputData(m,8)= IONS1/Abund1;
IONS2=odesolver1(Iso2,Abund2,g1ii,g2ii,g3ii,g4ii,S2ii,S3ii,Sionii);
OutputData(m,9)=IONS2/Abund2;
OutputData(m,10)=IONS1/IONS2;
m=m+1;
% waitbar(m/length(OutputData),wb)
end
end
end
end
end
end
end
%% Mean of Run %%
W = mean(OutputData(:,1));
M5 = mean(OutputData(:,8));
M8 = mean(OutputData(:,9));
MR = mean(OutputData(:,10));
if MakePlot==1
subplot(1,2,2)
plot(P2,S2)
title(strcat('Center of resonance at:', num2str(L1)))
axis([min(P) max(P) 0 10])
set(gca,'YLimMode','auto', 'YScale', 'log') %linear
figure(2)
plot(ResponseData(:,1), ResponseData(:,2))
axis([min(P2) max(P2) 0 10])
xlabel('Laser Centerline')
set(gca,'YLimMode','auto')
set(gcf,'PaperUnits','inches','PaperPosition',[0 0 5.60 4.20])
print('-dpng', 'ResponseData.png', '-r100')
if SavePlot==1
set(gcf,'PaperUnits','inches','PaperPosition',[0 0 5.60 4.20])
print('-dpng',strcat('LaserAndResonanceProfiles.LaserCenterLineAt',
num2str(LaserCenterLine),'.png'), '-r100')
end
end
%% Close up shop %%
clear global;
%close(wb);
end
```

B.3 odesolver1.m

```
function [ions] = odesolver1...

(isotope,isotopeabund,g1a,g2a,g3a,g4a,S2a,S3a,Siona)

   global IONS isoA TSPAN oxide g1 g2 g3 g4...
   FrequencyL1 FrequencyL2 FrequencyL3 ...
   Z1 Z2 Z3 Z2C
   % Time of Integration
   tspan = TSPAN;
   % Initial Conditions for state populations
   y0 =[isotopeabund; 0; 0; 0];
   % Oxide abundance for isotope ionization probability
   oxide = isotopeabund;
   % Isotope statistics used for this iteration
   isoA = isotope;
   g1 = g1a; g2 = g2a; g3 =g3a; g4 = g4a;
   S2 = S2a; S3 = S3a; Sion =Siona;
   % Call laserparams.m for the laser line profiles
   [I1 I2 I3] = laserparams(FrequencyL1, FrequencyL2, FrequencyL3);
   % Contiuum cross section from 2nd excited state
   % S2C = 7.5e-19; on res235, L3=0mW, 13% 7.5e-19
   % No difference in first laser wavelength data
   % Integrate Cross Section and Laser Profile over wavelength
   Z1 = (S2*I1');
   Z2 = (S3*I2');
   Z3 = (Sion*I3');%*0.00000005;
   Z2C = (S2C*sum(I1)); % 2-color ionization rate
   if isoA==235
   Z2C = Z2C*1.23;
   end
   % Options for Solver
   %(Specify error tolerances and allow only positive values)
   options=odeset('RelTol',1e-6,'AbsTol',1e-8,'NonNegative',[1 2 3 4]);
   % Initialize a figure for the solver
   figure(1);
   % xlabel ('Time [ns]');
   % ylabel ('Abundance of Atoms in State N');
   % legend('N_0', 'N_1', 'N_2', 'N_{ion}');
   % Call the solver to solve equations in f
   ode15s (@f,tspan,y0,options);
   % Output the probability of ionization
   ions=IONS;
   end
```

```
%%Subfunction to be integrated%%
function [dydt] = f(t,y)
global IONS TIME1 TIME2 TIME3 POWER1 oxide g1 g2 g3 g4 Z1 Z2 Z3 Z2C
%% Time dependence of laser pulses
% Pulselength = 20 ns FWHM
% Sum of pulse width (pl) and timing fluctuations (plfluc)
pl = 20;%15; %New lasers (SPIRIT) = 15ns and 4ns
plfluc = 14; %4 ns
% Sigma^2 of laser pulse
st = (pl/2)^2/(2*log(2));
stfluc = (plfluc/2)^2/(2*log(2));
% Time distribution of laser power
t1 = 1/(sqrt(2*pi*(stfluc+st)))*exp(-(t-TIME1)^2/(2*(stfluc+st)));
t2 = 1/(sqrt(2*pi*(stfluc+st)))*exp(-(t-TIME2)^2/(2*(stfluc+st)));
t3 = 1/(sqrt(2*pi*(stfluc+st)))*exp(-(t-TIME3)^2/(2*(stfluc+st)));
tox = 1/(sqrt(2*pi*st))*exp(-(t-TIME1)^2/(2*st));
% Average Lifetime of first Resonance in ns
tau2 = 57;
% Average Lifetime of second Resonance in ns
tau3 = 215;
%% Rate Constants for absorption
W12 = t1*Z1;%*(g2/g1)
W23 = t2*Z2;%*(g3/g2)
W34 = t3*Z3;%*(g4/g3)
W2C = t1*Z2C;
% Rate Constants for stimulated emission
W21 = t1*Z1;
W32 = t2*Z2;
% Power dependent Non-resonant ionization factor 1
% Ions/pulse at 75mW(.5/0.0049)
% If:  flux^2*9e-35, flux^3*8e-51,flux1^1*1e-18
% flux1 = 5e9*415.5105*POWER1/(pi*0.06*0.075);
% Wnr = (tox*flux1^2*4.5e-36);
% WnAr = (t1*flux1^3*5.2e-51);
%% Rate Equations
dydt = [ -W12*y(1) + W21*y(2) + y(2)/tau2 %- Wnr*y(1) %-Wnr*oxide
W12*y(1) - W21*y(2) - W23*y(2) + W32*y(3) - y(2)/tau2 + y(3)/tau3
W23*y(2) - W32*y(3) - W34*y(3) - y(3)/tau3 - W2C*y(3)
W34*y(3) + W2C*y(3) ];%+ Wnr*y(1) ];%+ Wnr*oxide];
% Output the # of Ions created by end of pulse
IONS = y(4);
end
```

B.4 laserparams.m

```
function [I1,I2,I3] = ...

laserparams(FrequencyL1,FrequencyL2,FrequencyL3)

   global FWHMS1A P P2 Q2 R2 POWER1 POWER2 POWER3...
   INTERP1 BAND1 BAND2 BAND3 ...
   DeltaWavelength1 DeltaWavelength2 DeltaWavelength3
   % Number of Sigmas for Laser Lineshape for Modeled Lines
   NumberOfLaserSigmas= 11;
   %Multimode laser sigma = 11+(2*modes*(1000*modespacing));
   % Ellipsoidal area of lasers (a/b radii of minor/major in cm!)
   a= 0.068;% 13.5% width diameter in cm, reported in logbook as mm!
   b= 0.075;% These values are from pictures taken in 02/2009
   area1 = pi*a*b;
   %Flux[#photons/cm^2](Power[mW],wavelength[nm],...
   Energy/pulse[J]@1kHz=Power[mW]*10^-6/Area[pi*a*b])
   Flux1 = 5e9*415.5105*POWER1/area1;
   Flux2 = 5e9*829.089*POWER2/area1;
   Flux3 = 5e9*722.200*POWER3/area1;
   % Scatter
   FWHMS1 = FWHMS1A;%0.002;
   FWHMS2 = 0.002;
   FWHMS3 = 0.002;
   LaserScatter1=FWHMS1/(2*sqrt(2*log(2)));
   LaserScatter2=FWHMS2/(2*sqrt(2*log(2)));
   LaserScatter3=FWHMS3/(2*sqrt(2*log(2)));
   %% First Laser Profile %%
   % % Shift center frequency of NarrowLinshape to FrequencyL1
   % I1=zeros(1,length(P2));
   % I1a=zeros(1,length(P2));
   % I1b=zeros(1,length(P2));
   % [~,FreqIndex1] = min(abs(P2(1,:)-FrequencyL1));
   % MeanP2 = (round(length(P2)/2));
   % FreqShift1 = MeanP2-FreqIndex1;
   % Edge1=1+abs(FreqShift1);
   % for j = Edge1:length(P2)-Edge1
   % I1a(j-FreqShift1) = INTERP1(j);
   %%I1b(j)=(DeltaWavelength1/2)*(1/sqrt(2*pi*LaserScatter1^2))...
   %*exp(-((P2(j)-FrequencyL1)).^2/(2*LaserScatter1^2));
   % end
   % I1c = I1a+I1b;
   % I1d = I1c/sum(I1c);
   % I1 = Flux1*I1d;
```

```
% Gaussian Laser Lineshape %
[~,LeftLaserCellIndex1]=min(abs(P2(1,:)...
-(FrequencyL1-BAND1*NumberOfLaserSigmas)));
[~,RightLaserCellIndex1]=min(abs(P2(1,:)...
-(FrequencyL1+BAND1*NumberOfLaserSigmas)));
I1= zeros(1,length(P2));
for j = LeftLaserCellIndex1:RightLaserCellIndex1
I1(j) = (DeltaWavelength1/2)*(Flux1/sqrt...
(2*pi*(BAND1^2+LaserScatter1^2)))*exp(-((P2(j)-FrequecyL1)).^2...
/(2*(BAND1^2+LaserScatter1^2)));
end
%% Laser 2 and 3 Profiles %%
[~,LeftLaserCellIndex2]=min(abs(Q2(1,:)...
-(FrequencyL2-BAND2*NumberOfLaserSigmas)));
[~,RightLaserCellIndex2]=min(abs(Q2(1,:)...
-(FrequencyL2+BAND2*NumberOfLaserSigmas)));
I2= zeros(1,length(Q2));
for k = LeftLaserCellIndex2:RightLaserCellIndex2
I2(k) = (DeltaWavelength2/2)*(Flux2/sqrt(2*pi*...
(BAND2^2+LaserScatter2^2)))*exp(-((Q2(k)-FrequencyL2)).^2...
/(2*(BAND2^2+LaserScatter2^2)));
end
[~,LeftLaserCellIndex3]=min(abs(R2(1,:)...
-(FrequencyL3-BAND3*NumberOfLaserSigmas)));
[~,RightLaserCellIndex3]=min(abs(R2(1,:)...
-(FrequencyL3+BAND3*NumberOfLaserSigmas)));
I3 = zeros(1,length(R2));
for l = LeftLaserCellIndex3:RightLaserCellIndex3
I3(l)=(DeltaWavelength3/2)*(Flux3/sqrt(2*pi*...
(BAND3^2+LaserScatter3^2)))*exp(-((R2(l)-FrequencyL3)).^2...
/(2*(BAND3^2+LaserScatter3^2)));
end
% %% FWHM Measurement for First Laser Pulse %%
% Find the index of the maximum
MaxI1=find(I1==max(I1));
% Find the index of the HWHW
[~,HWHMI1] = min(abs(I1-I1(MaxI1)/2));
% This is the FWHM in [nm] for [pm just multiply by 1000
FWHM=(P2(MaxI1)-P2(HWHMI1))*2;
```

B.5 Stochastic Sampling

B.5.1 timefetch.m

```
function [s] = timefetch

   clear Dist
   %% Load Distribution to Sample %%
   load('timedistributions.mat')
   Dist = Timedist2; %Variable from .mat file
   lengthdist=length(Dist);
   % Number of Bins = sqrt(Number of Points)
   Nbins=round(sqrt(lengthdist))+1;
   [counts,bincenter] = hist(Dist,Nbins);
   %% Plot ditribution %%
   %bar(binedge,counts)
   %% Create CDF from PDF %%
   Y=zeros(Nbins);
   for i=2:Nbins
   Y(i) = Y(i-1) + counts(i);
   end
   Y = Y/length(Dist);
   %% Sample Randomly from Distribution %%
   r = rand;
   t = find(Y>r);
   if isempty(t)
   t=1;
   end
   s = bincenter(t(1));
   %s = binedge(t(1)-1)+(rand*(smax-binedge(t(1)-1)));
   end
```

B.5.2 wavelengthfetch.m

```
function [s] = wavelengthfetch(freqrange)

   %freqrange is fundamental (1) or doubled beam (2)
   clear Dist
   %% Load Distribution to Sample %%
   load('laserdistributions.mat')
   Dist = Narrowdist; %Broaddist
   lengthdist=length(Dist);
   % Number of Bins = sqrt(Number of Points)
   Nbins=round(sqrt(lengthdist))+1;
```

```
[counts,bincenter] = hist(Dist,Nbins);
%% Plot ditribution %%
%bar(binedge,counts)
%% Create CDF from PDF %%
Y=zeros(Nbins);
for i=2:Nbins
Y(i) = Y(i-1) + counts(i);
end
Y = Y/lengthdist;
%% Sample Randomly from Distribution %%
r = rand;
t = find(Y>r);
if isempty(t)
t=1;
end
s = bincenter(t(1))/freqrange;
end
```

Appendix C

Clebsch-Gordan Coefficients for the First Excitation Step of ^{235}U

The resonance ionization scheme we use involves exciting the ground state atoms of uranium ($J = 6$) to an excited state at 24,066 cm^{-1} with $J = 7$. The nuclear spin of ^{235}U is $I = 7/2$. The coupling of atomic and nuclear spins in ^{235}U lead to F being a good quantum number for the system (where $F = I \oplus J$) . This leads to eight possible angular momentum levels within each state with $F_g = [19/2, 17/2, ..., 5/2]$ and $F_e = [21/2, 19/2, ..., 7/2]$ where the subscripts g and e refer to the ground state and excited state respectively. In addition, each of these levels will be composed of $2(F+1)$ degenerate magnetic substates m_F. This leads to 104 total substates in the ground state and 120 total substates in the first excited state (and 126 each in the second excited and autoionizing states). The selection rules for allowed dipole transitions for linear polarized light are $\Delta F = 0, \pm 1$, $m_F = 0$.

In the allowed dipole transition probabilities for *odd* isotopes the dipole matrix element in the transition probability (or Rabi oscillation) can be related to the dipole matrix element of the transition probability for even isotopes by the Wigner-Eckart Theorem [54, 35, 55], which states that the two different matrix elements are related by the Clebsch-Gordan coefficients (C-G) for the transition,

$$\sum_{m_g, m_e} \left| \left\langle F_g, m_g \left| D_{odd} \right| F_e, m_e \right\rangle \right|^2 = C(j_1, j_2, j, m_1, m_2, m)^2 \left\| D_{even} \right\|^2$$

where $C(j_1, j_2, j, m_1, m_2, m)$ are the C-G coefficients and are defined by $C(F_g, 1, F_g + \Delta F, m, 0, m)$ because F_e is fixed by the transition considered. Also, $m_g = m_e$ because $\Delta m = 0$. The C-G coefficients are symmetric about $m_F = 0$. They are plotted here as a graph for each possible ΔF and show the squared C-G value as a function of m_F for each value of F_g. Also included are three tables, below the figures, containing the values for the squares of the C-G coefficients for transitions between F_g and F_e, as a reference. Finally, Table C.4 contains the sum of the squared C-G coefficients from all three ΔF showing that the coefficients are normalized. Clearly, symmetry can be invoked to reduce the number of states (*i.e.*, equations) involved by at least a factor of 2, and the C-G coefficients vary fairly smoothly as a function of m_F for a given ΔF.

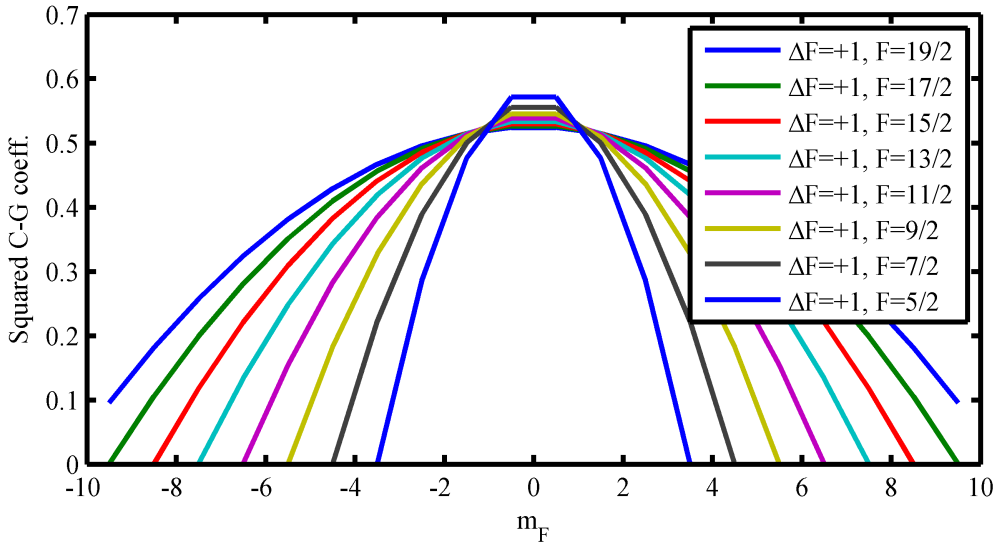

Figure C.1: Squared Clebsch-Gordan Coefficients for $\Delta F = +1$, $\Delta m = 0$

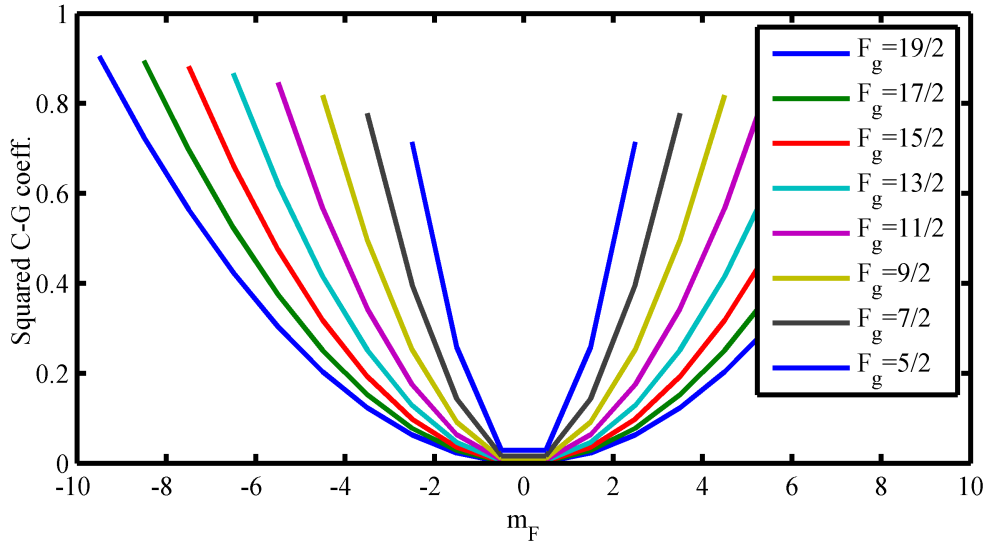

Figure C.2: Squared Clebsch-Gordan Coefficients for ΔF=0, Δm=0

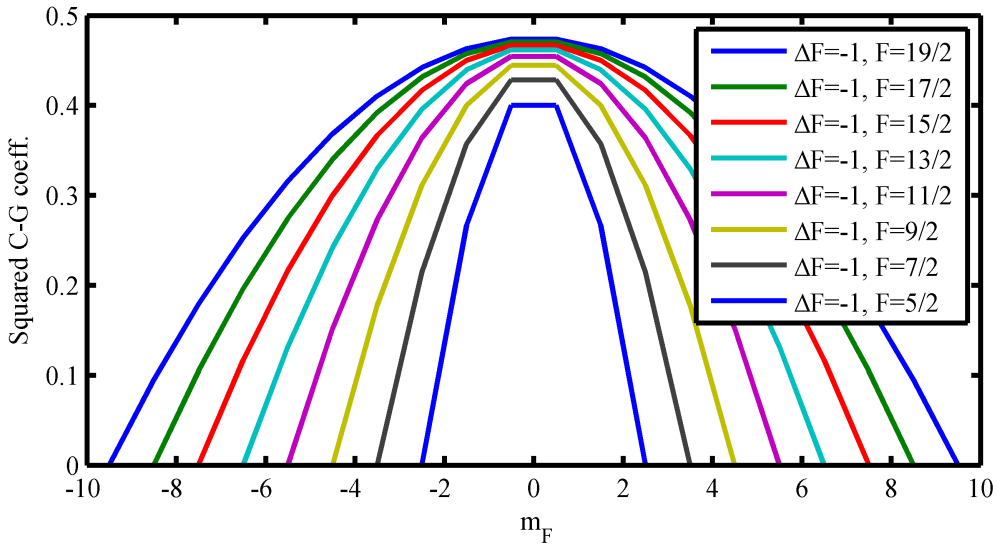

Figure C.3: Squared Clebsch-Gordan Coefficients for $\Delta F = -1$, $\Delta m = 0$

Table C.1: Squared Clebsch-Gordan Coefficients for $\Delta F = +1$, $\Delta m = 0$

$F_g =$	$19/2$	$17/2$	$15/2$	$13/2$	$11/2$	$9/2$	$7/2$	$5/2$
$m_F = -19/2$	0.0952	0	0	0	0	0	0	0
$-17/2$	0.1809	0.1052	0	0	0	0	0	0
$-15/2$	0.2571	0.1988	0.1176	0	0	0	0	0
$-13/2$	0.3238	0.2807	0.2205	0.1333	0	0	0	0
$-11/2$	0.3809	0.3508	0.3088	0.2476	0.1538	0	0	0
$-9/2$	0.4285	0.4093	0.3823	0.3428	0.2820	0.1818	0	0
$-7/2$	0.4666	0.4561	0.4411	0.4190	0.3846	0.3272	0.2222	0
$-5/2$	0.4952	0.4912	0.4852	0.4761	0.4615	0.4363	0.3889	0.2857
$-3/2$	0.5142	0.5146	0.5147	0.5142	0.5128	0.5090	0.5000	0.4761
$-1/2$	0.5238	0.5263	0.5294	0.5333	0.5384	0.5455	0.5556	0.5714
$1/2$	0.5238	0.5263	0.5294	0.5333	0.5384	0.5455	0.5556	0.5714
$3/2$	0.5142	0.5146	0.5147	0.5142	0.5128	0.5090	0.5000	0.4761
$5/2$	0.4952	0.4912	0.4852	0.4761	0.4615	0.4363	0.3889	0.2857
$7/2$	0.4666	0.4561	0.4411	0.4190	0.3846	0.3272	0.2222	0
$9/2$	0.4285	0.4093	0.3823	0.3428	0.2820	0.1818	0	0
$11/2$	0.3809	0.3508	0.3088	0.2476	0.1538	0	0	0
$13/2$	0.3238	0.2807	0.2205	0.1333	0	0	0	0
$15/2$	0.2571	0.1988	0.1176	0	0	0	0	0
$17/2$	0.1809	0.1052	0	0	0	0	0	0
$19/2$	0.0952	0	0	0	0	0	0	0

Table C.2: Squared Clebsch-Gordan Coefficients for $\Delta F = 0$, $\Delta m = 0$

$F_g =$	$19/2$	$17/2$	$15/2$	$13/2$	$11/2$	$9/2$	$7/2$	$5/2$
$m_F = -19/2$	0.9047	0	0	0	0	0	0	0
$-17/2$	0.7243	0.8947	0	0	0	0	0	0
$-15/2$	0.5639	0.6966	0.8824	0	0	0	0	0
$-13/2$	0.4235	0.5232	0.6628	0.8667	0	0	0	0
$-11/2$	0.3032	0.3746	0.4745	0.6205	0.84625	0	0	0
$-9/2$	0.2030	0.2508	0.3177	0.4153	0.5664	0.8182	0	0
$-7/2$	0.1228	0.1517	0.1922	0.2513	0.3427	0.4949	0.7778	0
$-5/2$	0.0626	0.0774	0.0980	0.1282	0.1748	0.2525	0.3968	0.7143
$-3/2$	0.0225	0.0278	0.0353	0.0462	0.0629	0.0909	0.1429	0.2571
$-1/2$	0.0025	0.0031	0.0039	0.0051	0.0069	0.0101	0.0158	0.0286
$1/2$	0.0025	0.0031	0.0039	0.0051	0.0069	0.0101	0.0158	0.0286
$3/2$	0.0225	0.0279	0.0353	0.0462	0.0629	0.0909	0.1428	0.2571
$5/2$	0.0626	0.0774	0.0980	0.1282	0.1748	0.2525	0.3968	0.7143
$7/2$	0.1228	0.1517	0.1922	0.2513	0.3427	0.4949	0.7778	0
$9/2$	0.2030	0.2508	0.3177	0.4154	0.5664	0.8182	0	0
$11/2$	0.3032	0.3746	0.4745	0.6205	0.8462	0	0	0
$13/2$	0.4235	0.5232	0.6628	0.8667	0	0	0	0
$15/2$	0.5639	0.6966	0.8824	0	0	0	0	0
$17/2$	0.7243	0.8947	0	0	0	0	0	0
$19/2$	0.9047	0	0	0	0	0	0	0

Table C.3: Squared Clebsch-Gordan Coefficients for $\Delta F = -1$, $\Delta m = 0$

$F_g =$	$19/2$	$17/2$	$15/2$	$13/2$	$11/2$	$9/2$	$7/2$	$5/2$
$m_F = -19/2$	0	0	0	0	0	0	0	0
$-17/2$	0.0947	0	0	0	0	0	0	0
$-15/2$	0.1789	0.1045	0	0	0	0	0	0
$-13/2$	0.2526	0.1960	0.1167	0	0	0	0	0
$-11/2$	0.3157	0.2745	0.2167	0.1318	0	0	0	0
$-9/2$	0.3684	0.3398	0.3000	0.2417	0.1515	0	0	0
$-7/2$	0.4105	0.3921	0.3667	0.3297	0.2727	0.1778	0	0
$-5/2$	0.4421	0.4313	0.4167	0.3956	0.3636	0.3111	0.2143	0
$-3/2$	0.4631	0.4575	0.4500	0.4396	0.4242	0.4000	0.3571	0.2667
$-1/2$	0.4736	0.4705	0.4667	0.4615	0.4545	0.4444	0.4286	0.4000
$1/2$	0.4736	0.4705	0.4667	0.4615	0.4545	0.4444	0.4286	0.4000
$3/2$	0.4631	0.4575	0.4500	0.4396	0.4242	0.4000	0.3571	0.2667
$5/2$	0.4421	0.4313	0.4167	0.3956	0.3636	0.3111	0.2143	0
$7/2$	0.4105	0.3921	0.3667	0.3297	0.2727	0.1778	0	0
$9/2$	0.3684	0.3398	0.3000	0.2417	0.1515	0	0	0
$11/2$	0.3157	0.2745	0.2167	0.1318	0	0	0	0
$13/2$	0.2526	0.1960	0.1167	0	0	0	0	0
$15/2$	0.1789	0.1045	0	0	0	0	0	0
$17/2$	0.0947	0	0	0	0	0	0	0
$19/2$	0	0	0	0	0	0	0	0

Table C.4: Sum of the squared C-G coefficients from all three types of transition

$F_g =$	$19/2$	$17/2$	$15/2$	$13/2$	$11/2$	$9/2$	$7/2$	$5/2$
$m_F = -19/2$	1	0	0	0	0	0	0	0
$-17/2$	1	1	0	0	0	0	0	0
$-15/2$	1	1	1	0	0	0	0	0
$-13/2$	1	1	1	1	0	0	0	0
$-11/2$	1	1	1	1	1	0	0	0
$-9/2$	1	1	1	1	1	1	0	0
$-7/2$	1	1	1	1	1	1	1	0
$-5/2$	1	1	1	1	1	1	1	1
$-3/2$	1	1	1	1	1	1	1	1
$-1/2$	1	1	1	1	1	1	1	1
$1/2$	1	1	1	1	1	1	1	1
$3/2$	1	1	1	1	1	1	1	1
$5/2$	1	1	1	1	1	1	1	1
$7/2$	1	1	1	1	1	1	1	0
$9/2$	1	1	1	1	1	1	0	0
$11/2$	1	1	1	1	1	0	0	0
$13/2$	1	1	1	1	0	0	0	0
$15/2$	1	1	1	0	0	0	0	0
$17/2$	1	1	0	0	0	0	0	0
$19/2$	1	0	0	0	0	0	0	0